UNIVERSIDAD COMPLUTENSE DE MADRID

FACULTAD DE CIENCIAS FÍSICAS

Departamento de Física Atómica, Molecular y Nuclear

TESIS DOCTORAL

Mass composition studies from the Azimuthal asymetry in the risetime of the surface detector signals of the Pierre Auger Observatory

Estudios de composición en masa a partir de la asimetría azimutal en el risetime de las señales del detector de superficie del observatorio Pierre Auger

MEMORIA PARA OPTAR AL GRADO DE DOCTOR

PRESENTADA POR

Ignacio Andrés Minaya Flores

Directores

Fernando Arqueros Martínez
Diego García Pinto

Madrid, 2017

Universidad Complutense de Madrid
Facultad de Ciencias Físicas
Departamento de Física Atómica, Molecular y Nuclear

Mass Composition Studies from the Azimuthal Asymmetry in the Risetime of the Surface Detector Signals of the Pierre Auger Observatory

Estudios de composición en masa a partir de la asimetría azimutal en el risetime de las señales del detector de superficie del Observatorio Pierre Auger

Memoria para optar al grado de Doctor en Física presentada por:
Ignacio Andrés Minaya Flores

Trabajo codirigido por:
Dr. Fernando Arqueros Martínez
Dr. Diego García Pinto

Enero de 2016

Dedicado a mis padres,
a mi hermano,
y a tí, Maiko.

Contents

List of Figures

Appendix A

Resumen

Este trabajo ha sido desarrollado en el marco de la Colaboración Pierre Auger, que actualmente opera el Observatorio más grande del mundo para el estudio de rayos cósmicos con energías por encima de 10^{17} eV. El Observatorio está compuesto por un Detector de Superficie (SD), que consiste en 1660 estaciones que miden la componente muónica y electromagnética de las cascadas, y por un Detector de Fluorescencia (FD) que mide su desarrollo longitudinal.

Particularmente, esta tesis está dedicada a un estudio completo y actualizado de la asimetría observada en la estructura temporal de las señales del SD con respecto a la dirección de llegada de la cascada atmosférica, con el fin de obtener información acerca de la composición en masa de los rayos cósmicos de ultra-alta energía ($> 10^{18}$ eV). Para caracterizar la estructura temporal se usa el parámetro risetime $t_{1/2}$, definido como el tiempo que la señal integrada tarda en crecer desde el 10% hasta el 50%. Para este estudio se ha usado la muestra de datos reales detectados por el SD entre Enero de 2004 y Octubre de 2014. Además, se ha contado con más de 6×10^5 eventos generados mediante simulaciones Monte Carlo usando distintos modelos hadrónicos, en partícular QGSJETII-04 y EPOS-LHC. Esta librería se ha usado para validar el método y extraer información de la composición en masa.

Para llevar a cabo el análisis primero se seleccionan eventos en intervalos de energía E y ángulo zenital θ. Para cada intervalo se ha calculado el valor medio del risetime dividido por la distancia radial de la estación correspondiente $\langle t_{1/2}/r \rangle$, y su dependencia con el ángulo polar ζ ha sido modelada para extraer la amplitud de la asimetría. Para una E primaria dada, la amplitud de asimetría alcanza un máximo en el valor $(\sec\theta)_{\max}$, que depende de la masa del primario.

Este método no puede ser aplicado evento a evento debido a que el número de

estaciones del SD en eventos individuales no es suficiente para medir la asimetría. Por lo tanto, el análisis se lleva a cabo a partir de valores medios del risetime para grupos de eventos con intervalos dados de ζ, θ y E. Además, dado que la asimetría depende de la distancia radial, se ha desarrollado el análisis en dos subintervalos por separado, 500 - 1000 m y 1000 - 2000 m.

Se ha llevado a cabo un estudio detallado de las incertidumbres sistemáticas en el parámetro $(\sec\theta)_{\max}$. Estas incertidumbres, expresadas en términos de la separación entre los primarios protón y hierro, representan menos de un 16% y un 21% para los intervalos radiales 500 - 1000 m y 1000 - 2000 m respectivamente.

Los resultados de $(\sec\theta)_{\max}$ obtenidos para datos se encuentran entre las predicciones de MC para protón y hierro, indicando un aumento suave de la composición en masa con la energía en acuerdo con otros estudios de la Colaboración Pierre Auger.

Para interpretar estos resultados en términos de composición en masa, los valores obtenidos de $(\sec\theta)_{\max}$ se convierten en valores del número másico A. Para EPOS-LHC los análisis en ambos intervalos radiales dan lugar a predicciones compatibles de composición en masa. Sin embargo, se observan resultados inconsistentes cuando se usa el modelo QGSJETII-04. Por lo tanto, este análisis ha demostrado que el observable $(\sec\theta)_{\max}$ es también útil para realizar test en modelos de interacción hadrónica.

Teniendo también en cuenta otros resultados de la Colaboración Auger como los obtenidos con cascadas inclinadas y con las medidas de la profundidad de producción de muones, puede concluirse que ninguno de los modelos hadrónicos da una descripción completamente satisfactoria de los datos, y por lo tanto hay que resolver estas deficiencias en el conocimiento del modelado de las cascadas atmosféricas para poder progresar en el análisis de composición mediante el parámetro $(\sec\theta)_{\max}$.

Se ha encontrado que los valores de $(\sec\theta)_{\max}$ están fuertemente correlacionados con la profundidad del máximo de la cascada $X_{\max}$. Usando $(\sec\theta)_{\max}$ como medida de $X_{\max}$ se obtienen resultados de composición en masa en ambos intervalos radiales totalmente compatibles con los obtenidos con el FD. Esto confirma que $(\sec\theta)_{\max}$ es un estimador de masa fiable y robusto.

Appendix B

Summary

This work has been carried out in the framework of the Pierre Auger Collaboration that is presently operating the largest Observatory in the world for the study of cosmic rays with energies over 10^{17} eV. The Observatory is provided with a Surface Detector (SD) consisting of 1660 stations that measure the muonic and electromagnetic components of the showers, and a Fluorescence Detector (FD) that record their longitudinal development.

In particular, this thesis is devoted to study the asymmetry in the time structure of the SD signals with respect to the shower direction, aiming to obtain information about the mass composition of ultra-high energy cosmic rays ($> 10^{18}$ eV). To characterize the time structure, the risetime parameter $t_{1/2}$ has been used, which is defined as the time that it takes for the integrated signal to rise from 10% to 50%. For this study, the sample of data collected by the SD between January 2004 to October 2014 has been used. In addition more than 6×10^5 MC simulated events have been generated using several models of hadronic interaction, in particular QGSJETII-04 and EPOS-LHC. This MC library has been used to validate the method and extract information on the mass composition.

To carry out the analysis, events are firstly split in intervals of energy E and zenith angle θ. For each interval, the average value of the risetime divided by the core distance of the corresponding station $\langle t_{1/2}/r \rangle$ has been computed, and its dependence with the polar angle ζ has been modelled to extract the amplitude of the asymmetry. For a given primary E, the asymmetry amplitude reaches a maximum at a $(\sec\theta)_{\max}$ value that depends on the primary mass.

This method cannot be applied on a shower-by-shower basis because the number of SD stations in individual events is not enough to measure the asymmetry. Therefore,

the analysis is carried out from average values of the risetime from sets of events in given intervals of ζ, θ and E. Moreover, since the asymmetry depends on the core distance, the analysis has been performed in two radial subintervals separately, 500 - 1000 m and 1000 - 2000 m.

A detailed study of the systematic uncertainties in the $(\sec\theta)_{\max}$ parameter has been carried out. Expressed in terms of the separation between proton and iron primaries these uncertainties amount less than 16% and 21% for the radial intervals 500 - 1000 m and 1000 - 2000 m respectively.

The results of $(\sec\theta)_{\max}$ found in data are in between MC predictions for proton and iron nuclei, indicating a smooth increase of the mean mass with energy in agreement with other studies of the Pierre Auger Collaboration.

To interpret the results in terms of mass composition, the obtained values of $(\sec\theta)_{\max}$ are translated into mass number A values. For EPOS-LHC the analyses in both radial intervals lead to compatible predictions on mass composition. However, inconsistent results are found when asumming the QGSJETII-04 model. Thus, the reach of the $(\sec\theta)_{\max}$ observable extends to providing a test of hadronic interactions models.

Taking also into account other results of the Auger Collaboration like those of the inclined showers and the measurements of the muon production depth, it can be concluded that neither model provides a completely satisfactory description of the data and therefore these deficiencies in the understanding of shower modelling must be resolved to progress on the mass analysis through the $(\sec\theta)_{\max}$ parameter.

The $(\sec\theta)_{\max}$ values are found to be strongly correlated with the shower maximum depth $X_{\max}$. Using $(\sec\theta)_{\max}$ as a measure of $X_{\max}$ lead to mass composition results fully compatible with those obtained with the FD in both radial intervals. This confirms that $(\sec\theta)_{\max}$ is a robust and reliable mass estimator.

Chapter 1

Introduction

Although the discovery of cosmic rays took place one hundred years ago, nowadays, some of their most important properties are still unknown. In particular, their origin, production mechanism and mass composition are specially debated for cosmic rays with energies above 10^{18} eV, the so-called Ultra-High-Energy Cosmic Rays (UHECRs). These fascinating particles have energies of several orders of magnitude larger than the highest energy reached by the most energetic man made particle accelerator: the Large Hadron Collider (LHC). However, these cosmic rays cannot be detected directly because their flux decreases dramatically as the energy increases. Instead, their study is performed through the measurement of the properties of the particle showers that they generate when colliding with atmospheric nuclei, the so-called Extensive Air Showers (EASs). These secondary particles can be sampled using detectors at ground level, allowing the inference of the properties of the primary particle that generate them. To this end, several detectors have been built at ground level with very large instrumented surfaces to make possible the study of the most energetic cosmic rays with that extremely low flux.

At present, the Pierre Auger Observatory, located in the province of Mendoza (Argentina), is the largest detector created to study the nature of UHECRs. It was designed as a hybrid observatory, composed by an array of 1660 surface detectors covering an extension of 3000 km^2 overlooked by 27 fluorescence detectors. The Cherenkov tanks of the Surface Detector (SD) record the secondary particles reaching the ground, while the telescopes of the Fluorescence Detector (FD) collect the fluorescence light emitted by the N_2 molecules in the atmosphere that have been excited by the charged particles of the shower. The Pierre Auger Observatory combines for the first time two detection techniques to obtain information about EASs, and its hybrid design grants a large

statistics and a better control of the systematic uncertainties involved in both detection techniques.

Given the importance of the kind of particles composing UHECRs to the correct interpretation of their properties, several methods have been developed to extract information about the mass composition from the observed EASs. Different parameters sensitive to the mass composition have been developed. The most reliable one is the atmospheric depth of the maximum of the longitudinal profile of an EAS, X_{max}, which can be measured directly with the FD. However, the FD only operates during moonless and clear nights with a duty cycle of $< 13\%$, in comparison with the $\sim$100% of the SD. Therefore, there is a large number of events containing only SD information, which can also be useful in the determination of the mass composition. In this thesis, a method to extract information of the mass composition of UHECRs using SD events is presented. This method is based on the observed asymmetry in the time structure of signals with respect to the direction of an incoming air shower. This asymmetry is mainly due to the differences in the path travelled by particles reaching the ground, and its amplitude depends on the zenith angle θ of the incoming cosmic ray. As will be explained in this work, the dependence of the azimuthal asymmetry with respect to the zenith angle allows the definition of $(\sec\theta)_{\mathrm{max}}$, which is an SD parameter sensitive to the mass composition of the primary cosmic ray.

This thesis is organized as follows: a brief introduction of this field and the main features of UHECRs and the EASs produced in the atmosphere are described in chapter 2. An overview of the Pierre Auger Observatory with a description of the SD and FD and also of the recent upgrades of the Observatory is given in chapter 3. A study of the asymmetry in the features of the EASs using Monte Carlo simulated showers is performed in chapter 4. Once the mass sensitive parameter $(\sec\theta)_{\mathrm{max}}$ is defined, the results of the asymmetry analysis applied to the latest SD data of the Pierre Auger Observatory are shown in chapter 5, as well as their interpretation in terms of mass composition. The comparison with the results obtained by other methods and the implications on the validity of models of hadronic interactions are also discussed here. Finally, chapter 6 summarizes the main results obtained throughout this work.

Chapter 2

Ultra-High-Energy Cosmic Rays

2.1 Introduction

Cosmic rays are extraterrestrial particles which are continuously hitting the atmosphere of the Earth. Despite their discovery was nearly one hundred years ago, some of their most important properties such as origin, production mechanism and mass composition are still a mystery, even more for those with energies above 10^{18} eV, that is, the Ultra-High-Energy Cosmic Rays. As the low flux of these high-energy particles does not allow their direct detection, it is necessary to study them through the extensive air showers they induce in the atmosphere.

In this chapter a brief summary about cosmic rays and the physics behind them is presented. After a historical introduction in section 2.2, the features of the energy spectrum are described in section 2.3. Their possible origin and the propagation effects suffered in their travel to the Earth are explained in sections 2.4 and 2.5 respectively. In addition, in section 2.6 the EASs and their components are described in detail. Finally, several methods based on different techniques to measure the composition of UHECRs are briefly explained in section 2.7.

2.2 History

One year after the discovery of X-Rays by Röntgen in 1895, Becquerel, during an experiment with phosphorescent materials, discovered the radioactivity. Thereafter, the radiation from the radioactive elements in the ground were thought to be the cause of the ionization of air, assuming a terrestrial origin. In 1912 Victor Hess measured an increase in the air ionization with height during several balloon flights, indicating thus

an extraterrestrial origin [1]. Millikan, using electroscopes sunk in lakes, supported this result probing that the ionization decreased with air (or water) depth, and named this radiation as cosmic rays [2]. The study of high-energy particles made possible a significant progress in the particle physics with the discoveries of unknown particles. Anderson, in 1932, discovered the positron in a cloud chamber [3]. Four years later, in 1936, Neddermeyer and Anderson observed for the first time the muon when they noticed that some particles in presence of magnetic fields showed the same charge than an electron but they were more penetrating [4]. This was confirmed by Street and Stevenson in a cloud chamber experiment [5]. The Bristol group discovered the pion in 1947 [6], demonstrating the origin of muons in the disintegration of the pion and invalidating the original beliefs of Millikan that cosmic rays were actually gamma rays.

One more significant step in the knowledge of cosmic rays was given by Pierre Auger and co-workers in 1939 [7], following the idea of Rossi a few years before [8]. Using multiple Geiger counters at the same altitude but widely separated in space, they registered an amount of coincidences above random expectations. They interpreted these coincidences as secondary particles reaching the ground generated by the collision of a high-energy cosmic ray in the atmosphere, and called this phenomenon as Extensive Air Shower. P. Auger calculated that some of these detected particle showers were caused by cosmic rays with energies around 10^{15} eV, inspiring the studies of EASs with arrays of particle detectors. J. Linsley observed in 1963 the first event with an energy of 10^{20} eV [9] in the Volcano Ranch, the first large scale array (with an extension of 8.1 km^2) composed by 19 scintillator detectors [10]. The discovery of this ultra-high-energy event promoted even more the construction of larger arrays, like Haverah Park [11] (12 km^2 of water Cherenkov tanks), Yakutsk [12] (18 km^2), SUGAR [13] (70 km^2), AGASA [14] (100 km^2). The Pierre Auger Observatory [15] and the Telescope Array [16] are also instrumented with surface detectors of 3000 km^2 and 700 km^2 respectively.

In addition to the construction of larger arrays, new detection methods were also proposed in 1962 by K. Suga [17] and A.E. Chudakov [18]. They suggested the possibility of using the atmosphere as a calorimeter where the energy of shower particles was deposited, exciting the N_2 molecules upon their passage through it and causing them to radiate fluorescence light. The first detection of fluorescence light from a cosmic ray shower took place in the INS-Tokyo experiment in 1969, measuring signals from an air shower with energy of 10^{19} eV [19]. Seven years later, in Volcano Ranch, a coincidence between ground array detection and fluorescence emission from air showers was registered for the first time [20]. Some successful experiments based on the

fluorescence technique are Fly's Eye observatory (two detection buildings which allow stereoscopic observation of air showers) and its successor HiRes [21]. The Pierre Auger Observatory [22] and Telescope Array [23] use presently this technique. Also, future experiments like the satellite mission JEM-EUSO [24] aims to detect the atmospheric fluorescence from space.

2.3 Energy spectrum

Cosmic rays are continuously striking the atmosphere but the rate of impacts depends strongly on their energy, going from several particles per m^2 and per second at 10^{11} eV to one particle per km^2 and per century at 10^{20} eV (see Fig. 2.1). The energy spectrum follows a power law:

$$\frac{dJ}{dE} \propto E^{\gamma}\,, \tag{2.1}$$

where J is the flux, E the energy and γ is the spectral index of the power law.

At the lowest energies cosmic rays can be directly detected with balloons or satellites thanks to its high flux [26, 27, 28], but when the energy grows (above 10^{14} eV) their detection is only possible studying the showers generated in the atmosphere. The first experiments which obtained data in the extremely energetic region of the spectrum were AGASA [29, 30, 31, 32] and HiRes [33, 34, 35]. However, the results of both experiments, based on different techniques as mentioned before, were dominated by a very limited statistics and thus large fluctuations. With the construction of the Pierre Auger Observatory [36], which combines for the first time both techniques, the spectrum at the highest energies was finally measured with better statistics and reduced uncertainties.

As it can be observed in Fig. 2.1, the energy spectrum shows a power law index at lower energies of $\gamma \sim -2.7$. However, at higher energies there are two clear deviations of this value: the first one, at $\sim 10^{15}$ eV, is referred to as the *knee* [37], and the second one, at $\sim 10^{18}$, is referred to as the *ankle* [38]. The variations in the shape of the spectrum could reflect changes in the acceleration mechanisms as well as in the hadronic interaction models or in composition. The features are described in detail in the following.

2.3.1 The knee

At around 4×10^{15} eV the spectral index changes from $\gamma \sim -2.7$ to $\gamma \sim -3.0$. There are several theories to explain this feature. The most accepted one proposes that the

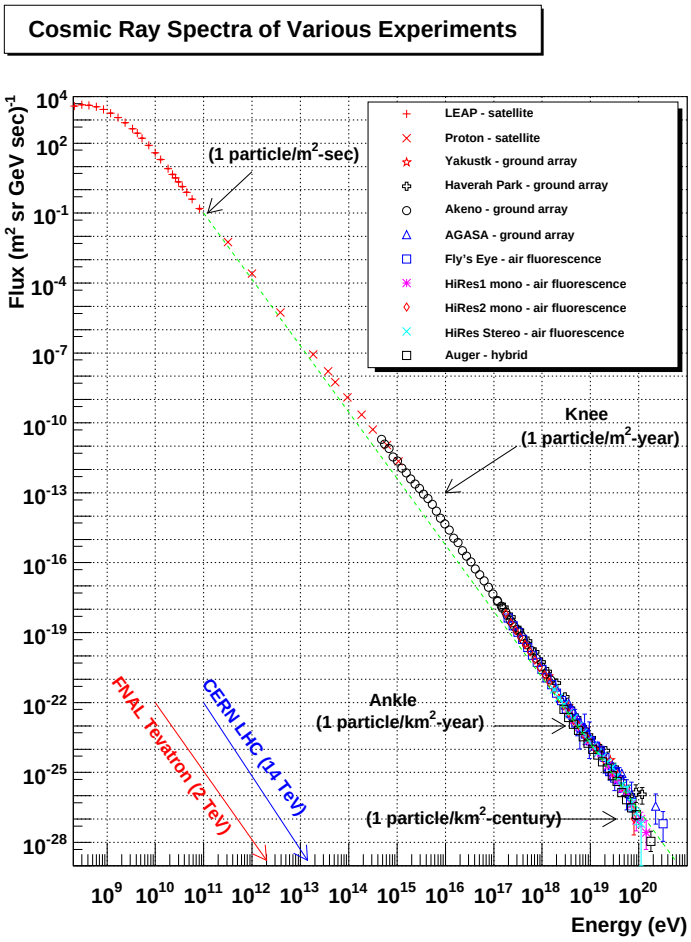

Figure 2.1: Energy spectrum of cosmic rays measured by different experiments; the highest energy terrestrial accelerators are also marked. Figure taken from [25].

change in the knee region is due to the maximum energy reached by the galactic cosmic ray accelerators (see section 2.4). Another plausible models try to explain it through the leakage of galactic cosmic rays due to the limitation of the galactic magnetic fields to confine them when they reach a certain energy or through interactions of cosmic rays with background particles in the Galaxy [40].

Akeno [30], Fly's Eye [38] and more recently KASKADE-Grande [41] have observed a second change in the slope at energies around 8×10^{16} eV (the so-called second knee), where the spectral index changes to $\gamma \sim -3.3$. This feature is perfectly consistent with the fact that, as the maximum energy reached is proportional to the charge of the

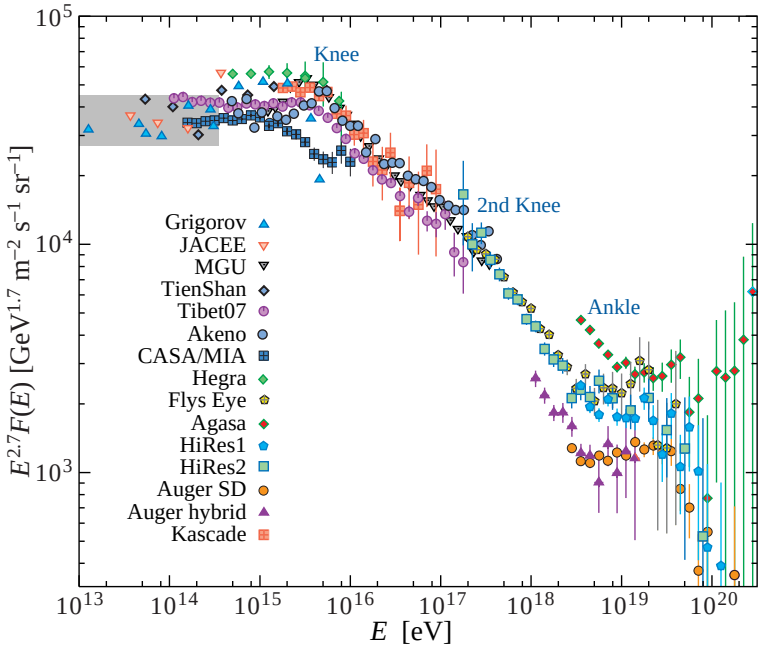

Figure 2.2: Energy spectrum of cosmic rays measured by different experiments. The flux is multiplied by $E^{2.7}$ in order to better appreciate the changes in the spectral index. Figure taken from [39].

particle Z, heavier particles would be accelerated to higher energies. Thus, this second knee might indicate the maximum energy of the flux of the heavy galactic component.

2.3.2 The ankle

The ankle is the point where the spectral index turns again to $\gamma \sim -2.7$. Several models try to describe this spectral feature as follows:

• The *dip model* [42, 43] assumes that the transition from galactic to the extragalactic components takes place at lower energies. Then, the ankle corresponds to the point where there is no more galactic component and, thus, the flux is completely dominated by the extragalactic one, purely composed by protons [44, 45]. These protons interact with the intergalactic Cosmic Microwave Background (CMB) and lose energy through electron-positron pair creation:

$$p + \gamma_{\mathrm{CMB}} \rightarrow p + e^{+} + e^{-} \ , \tag{2.2}$$

showing a lack of events at higher energies. The transition for the *dip model* is rep-

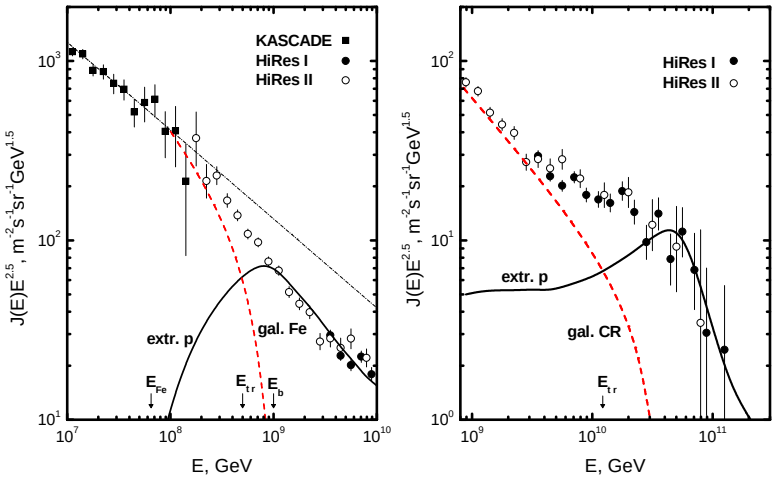

Figure 2.3: Transition in the dip (left panel) and ankle (right panel) models. In both cases a solid line gives the calculated spectrum of extragalactic protons, the dashed line represents the spectrum of galactic iron and $E_{\rm tr}$ is the energy of intersection of galactic and extragalactic spectra. In the left panel $E_{\rm Fe}$ gives the position of iron knee and $E_{\rm b}$ $= 1 \times 10^{18}$ eV is the energy where transition from galactic to extragalactic cosmic rays is completed. Figures taken from [42].

resented in the left panel of Fig. 2.3. For this model the predicted elongation rate[1] from different models of interaction shows a reasonable agreement with HiRes data but does not agree with the Auger data (see left panel of Fig. 2.4), especially with the two highest energy points [42].

• The *ankle model* [38] assumes that this spectral feature corresponds to the beginning of the transition to extragalactic component, contributing both components equally (see the right panel of Fig. 2.3). However, this model presents discrepancies between the expected values of the elongation rate from different interaction models and the measurements of data for HiRes, Fly's Eye and Pierre Auger [42], as can be observed in right panel of Fig. 2.4.

• The *mixed composition model* [46, 47, 48, 49, 50, 51, 52] is the only model that allows a non pure composition for the highest energies. It is based on the argument that any acceleration mechanism operating in the gas involves the different nuclei and thus the primary flux must have mixed composition. It is the same principle than the *ankle model* but considering mixed composition. The mass composition predicted for a version

[1]The elongation rate is the variation of the depth of the atmosphere at which the maximum number of particles is reached ($X_{\rm max}$) with the logarithmic energy, as will be explained in section 2.6.2.

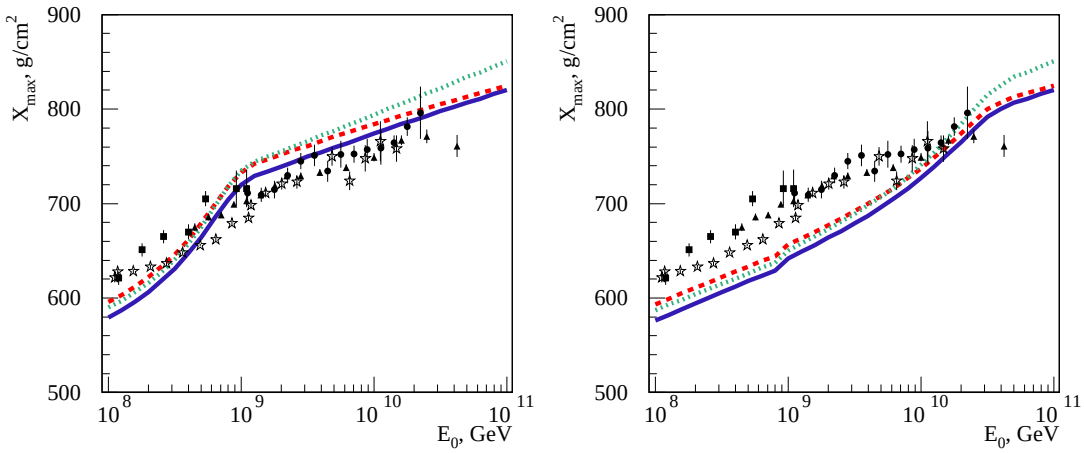

Figure 2.4: Elongation rate for the dip model (left panel) and ankle model (right panel). Points are data measurements of Fly's Eye (stars), HiRes-Mia (squares), HiRes (circles) and Auger (triangles). Lines represent the calculated elongation rates for different hadronic interaction models. Figures taken from [42].

of this model evolves from almost pure iron composition at $E \sim 3 \times 10^{17}$ eV to a lighter composition due to enrichment by protons and light nuclei of extragalactic origin. At an energy of 3×10^{18} eV the transition to pure extragalactic component is completed and the evolution of the chemical composition proceeds further due to photo-disintegration of the nuclei. Finally at $E \sim 1.3 \times 10^{19}$ eV all nuclei are disappearing faster than before, and the composition becomes strongly proton-dominated at $E \geq 3 \times 10^{19}$ eV. Therefore, in this model the ankle is again the transition region between galactic and extragalactic origin, as is displayed in Fig. 2.5. This model predicts an abundance of heavy elements of ∼10%, which is compatible with the current observations of the Pierre Auger Observatory.

The latest study of KASKADE-Grande, analysing the energy spectrum of light elements, provides evidences for an ankle-like structure at the energy $E = 10^{17.08 \pm 0.08}$ eV, where the spectral index changes from $\gamma = -3.25 \pm 0.05$ to $\gamma = -2.79 \pm 0.08$ [53]. This result might indicate that this is the energy where the transition from galactic to extragalactic origin of cosmic rays starts.

2.3.3 The GZK cutoff

One year after the discovery of the CMB by Penzias and Wilson in 1965 [54], Greissen [55], and independently Zatsepin and Kuzmin [56], realised that cosmic rays with

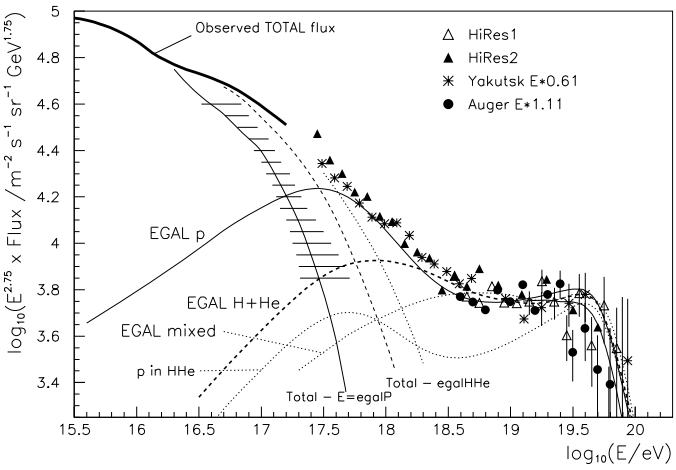

Figure 2.5: The upper end of the cosmic ray spectrum. Data from HiRes, from preliminary Auger exposure (energy scaled by factor 1.11 to match HiRes), and Yakutsk (energy scaled by 0.61). Thick line shows mean of data points below 10^{17} eV and hatched area shows probable fall-off of Galactic flux if the rigidity spectrum of Si-Fe component falls off as steeply as other components appear to do in the KASCADE spectra. The expected flux of cosmic rays from universal sources accelerating protons (*EGAL p*) subject to energy losses en route (CMB and estimated starlight-infrared interactions), a primordial mix of H and He (*EGAL H+He*) and a normal mixed composition from [46] (*EGAL mixed*) are shown. *Total-egal* curves show the flux required from other sources (presumably Galactic) to make up the observed total. The data suggest that the flux may be falling even before the expected GZK drop (seen in the curves near 5 $\times 10^{19}$ eV), presumably due to accelerators maximum energy. Figure taken from [44].

high energies could lose energy interacting with photons of that CMB by pion photoproduction via Δ^+ resonance:

$$p + \gamma_{\mathrm{CMB}} \rightarrow \Delta^+ \rightarrow p + \pi^0 \ , \tag{2.3}$$

$$p + \gamma_{\mathrm{CMB}} \rightarrow \Delta^+ \rightarrow n + \pi^+ \ . \tag{2.4}$$

Supposing a common universal origin of UHECRs, this phenomenon implies a strong suppression in the energy spectrum at energies around 6×10^{19} eV. This effect, the so-called GZK cut, might be the responsible for the shape of the energy spectrum at the

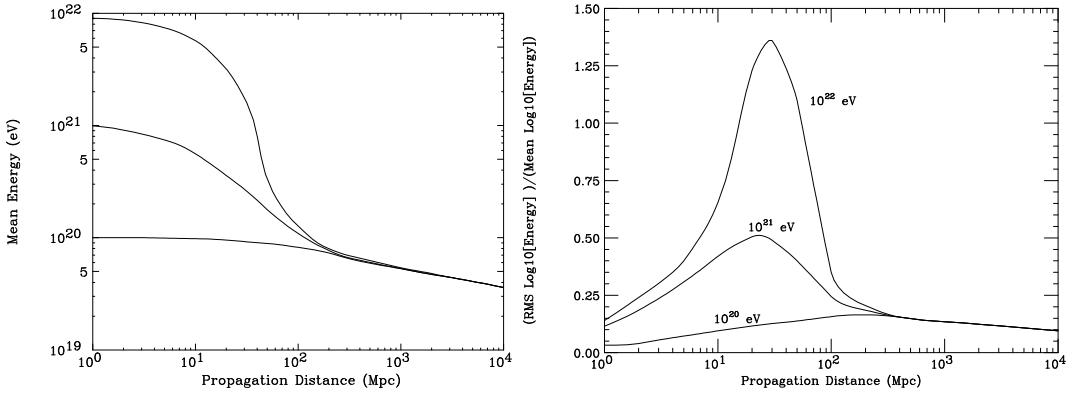

Figure 2.6: Left panel: mean energy of protons as a function of propagation distance through the CMB; curves are for energy at the source of 10^{22} eV, 10^{21} eV and 10^{20} eV. Right panel: fluctuation of the energy of a proton propagating through the CMB for the same three energies. Figures taken from [57].

highest energies, and also puts a limit for the distances at which the sources of the cosmic rays detected above this energy limit can be located (see left panel of Fig. 2.6). As an example, observed cosmic rays with energies larger than 10^{20} eV cannot be originated from distances larger than about 100 Mpc, or otherwise the cosmic ray would interact with the CMB and could not be detected due to the attenuation. Thus, all particles originated from distances larger than 100 Mpc would be detected with the same energy.

In the interaction of a nucleon with the CMB a significant amount of energy can be lost in a single collision. As a consequence, the fluctuation of the energy of a nucleon about the mean as a function of distance is large. This fluctuation about the mean is shown in the right panel of Fig. 2.6.

This spectral suppression at the end of the spectrum as an evidence of the GZK cutoff has been observed by HiRes [58], Telescope Array [59] and the Pierre Auger Observatory [60], but it has not been observed in the AGASA data [32]. However, although HiRes and the Pierre Auger Observatory have measured this suppression, the spectrum obtained with their studies are not compatible: HiRes observes the dip compatible with the pair production dip and the flux suppression due to the GZK cutoff, which indicate a proton dominated composition [42, 61], while the Auger spectrum cannot be described by a pure proton model, using thus a mixed pure proton and iron spectrum [46]. In order to fix these disagreements in the spectrum, more statistics of energetic cosmic rays are required.

2.4 Origin of cosmic rays

There is still a lot of unsolved questions about the origin and acceleration mechanisms of cosmic rays. Most of the low-energy cosmic rays, up to some GeV, have their origin in the Sun (known thanks to the characteristic night-day variations shown in their spectrum) and below 1 EeV they are considered to have a galactic origin [62, 63, 64]. However, the origin of the most energetic ones is still unknown.

Many theories have been proposed to explain the origin of UHECRs. The first one, elaborated by E. Fermi in 1949, was a model based on an acceleration mechanism through collisions between particles and magnetic clouds in movement [65]. However, the predicted maximum energy by his model was not enough to explain the highest energies observed in the spectrum. His model was the base for the currently accepted acceleration model, the Diffusive Shock Acceleration Mechanism (DSAM) [66] or first order Fermi acceleration, which is based on collisions between particles and front shocks (as those in the expanding supernova remnants SNRs [44]). In this model, particles cross through the shock fronts in both directions due to the deflections by magnetic anomalies, obtaining energy in every cross until they escape the remnant. The maximum energy achievable for a particle of charge Z through this mechanism is:

$$E_{\max} \sim \beta Z B R \,, \tag{2.5}$$

where β is the velocity of the front shock relative to the speed of light. This model gives the characteristic power-law spectrum and allows a maximum energy larger than the one predicted by the original Fermi model. However, it is still limited by the size of the acceleration object R and the magnetic field strength B, explaining the acceleration of cosmic rays in SNRs up to 10^{15} eV (or up to 10^{18} eV according to some theories [67, 44]).

Since this model is not able to explain the highest observed energies, like values larger than 10^{19} eV, those energetic cosmic rays are thought to have their origin out of our Galaxy [68, 69, 70]. M. Hillas argued that there are only a few astrophysical objects able to accelerate particles to those energies [71] (see Fig. 2.7). One of these objects could be the Active Galactic Nuclei (AGNs), which have jets with magnetic fields of six orders of magnitude larger than SNRs. However, those jets are finites, implying again a maximum energy, which in this case is 1 EeV. For higher energies there is no successful theoretical model yet, but there are some suggestions of their origin like pulsars, galaxy clusters, powerful radio galaxies, Gamma Ray Bursts (GRBs), or supermasive black holes which could accelerate particles in their perpendicular jets to their rotational plane up to 10^{21} eV [72, 73].

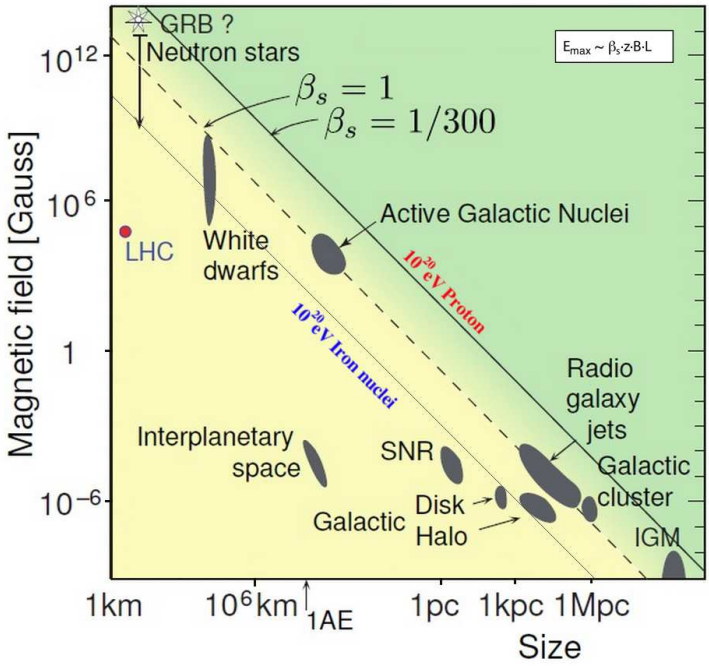

Figure 2.7: Hillas Plot [71] representing size and magnetic field strengths of the astrophysical objects in which UHECRs could be accelerated. Objects below the corresponding lines are not able to accelerate protons or iron nuclei to an energy of 10^{20} eV. Figure adapted from [74].

2.5 Effects on the propagation

In addition to the GZK cutoff at highest energies, there are other effects to take into account in the propagation of UHECRs, like the energy loss of protons interacting with the CMB through pair production with an energy threshold about 10^{18} eV:

$$p + \gamma_{\mathrm{CMB}} \rightarrow p + e^{+} + e^{-} \ . \tag{2.6}$$

Although these loses are insignificant compared with the photo-pion production ones, this mechanism is thought to be the dominating process in the region between the second knee and the ankle and determines the shape of the energy spectrum.

Other effect is the interaction between heavy nuclei and the CMB, and also with the intergalactic Infrared Background Radiation (IBR), through photodisintegration and

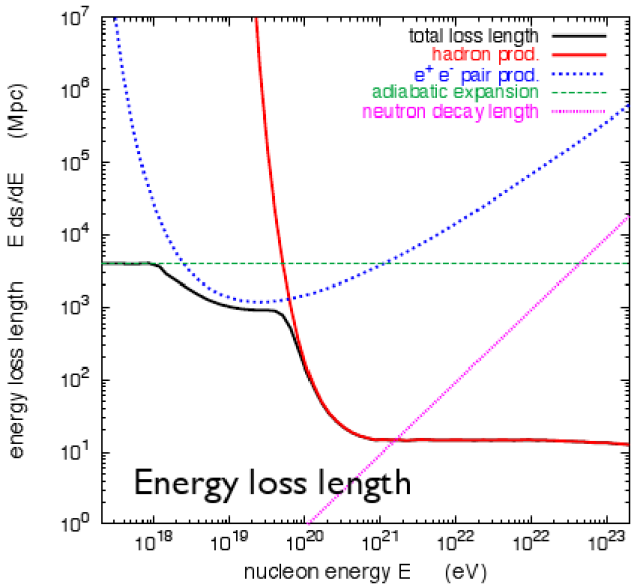

Figure 2.8: Energy loss length as a function of nucleon energy. The hadron production corresponds to the GZK effect. Figure taken from [77].

pair production with similar energy thresholds [75, 76]:

$$N^A + \gamma_{\mathrm{CMB}} \rightarrow N^{A-1} + n \,, \tag{2.7}$$

$$N^A + \gamma_{\mathrm{CMB}} \rightarrow N^A + e^+ + e^- \,. \tag{2.8}$$

In Fig. 2.8 the mean path lengths for the main mechanisms of energy losses suffered by UHECRs as they propagate to the Earth are presented.

Furthermore, cosmic rays also suffer interactions with the galactic and extragalactic magnetic fields. The isotropy in the arrival distribution due to the effect of the galactic magnetic field makes harder the source identification. However, at the highest energies the angular deflection of this highly energetic cosmic rays passing through galactic or extragalactic magnetic fields is minimal, which implies that their arrival direction should point to their origins and therefore it should be easier to correlate the incoming UHECRs with some astrophysical sources. Nevertheless, this prediction is quite difficult to check due to the limited knowledge of the strength of this magnetic fields, the charge of the UHECRs and the location of the sources. In Fig. 2.9 the effect of a magnetic field of 1 nG in the trajectories of protons originated from a point source with different

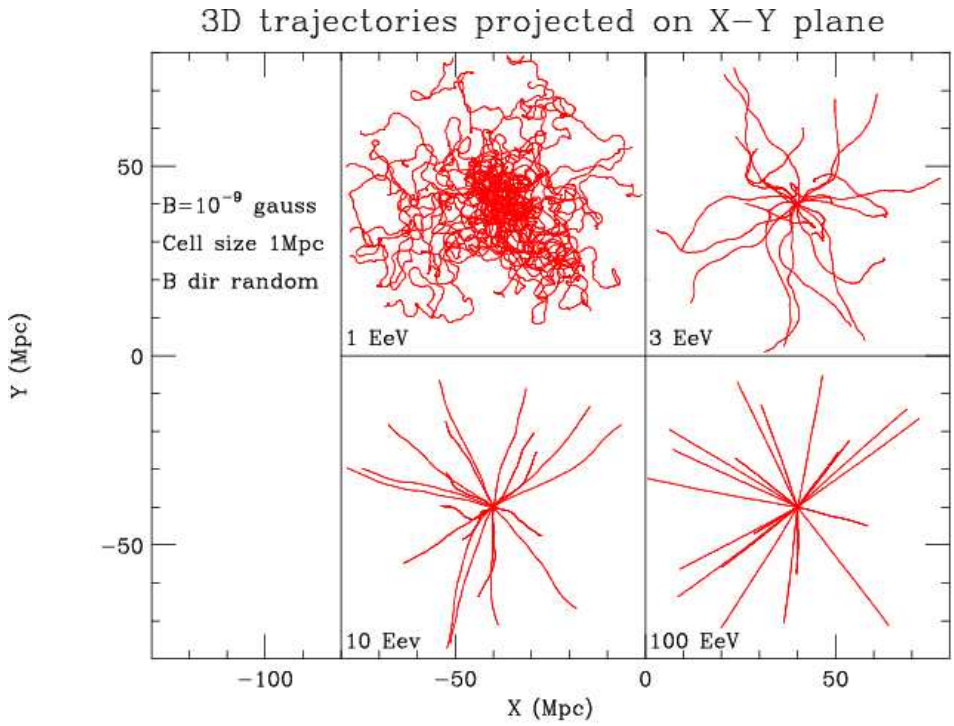

Figure 2.9: Projected view of 20 trajectories of proton primaries originated in a point source for several energies. Trajectories are plotted until they reach a physical distance from the source of 40 Mpc. Figure taken from [57].

energies is represented. As can be observed in this figure, the propagation of cosmic rays can pass from diffusive to rectilinear propagation (even in the presence of a weak magnetic field) when the primary energy increases from 1 to 100 EeV.

The Pierre Auger Collaboration has made several analyses of this anisotropy trying to correlate the most energetic events with nearly Active Galactic Nuclei (AGNs). The first study was made with cosmic rays from 1 January 2004 to 31 August 2007 with energies larger than 57 EeV and the position of AGNs at distances shorter than 75 Mpc, showing 27 events in circles of 3.2°. For 22 of these 27 events the circle contains an AGN position, which was compatible with the scenario of UHECRs accelerated in nearby extragalactic sources as AGNs [78]. However, an updated study using the 69 events detected above the same energy threshold until 31 December 2009 reduced down this correlation from 69% to 38% (compared with 21% expected for isotropic cosmic rays) [79]. A recent analysis, with 62 correlated events of 103 UHECRs detected with energies greater than 55 EeV until 21 December 2011, gives a probability of 0.13%

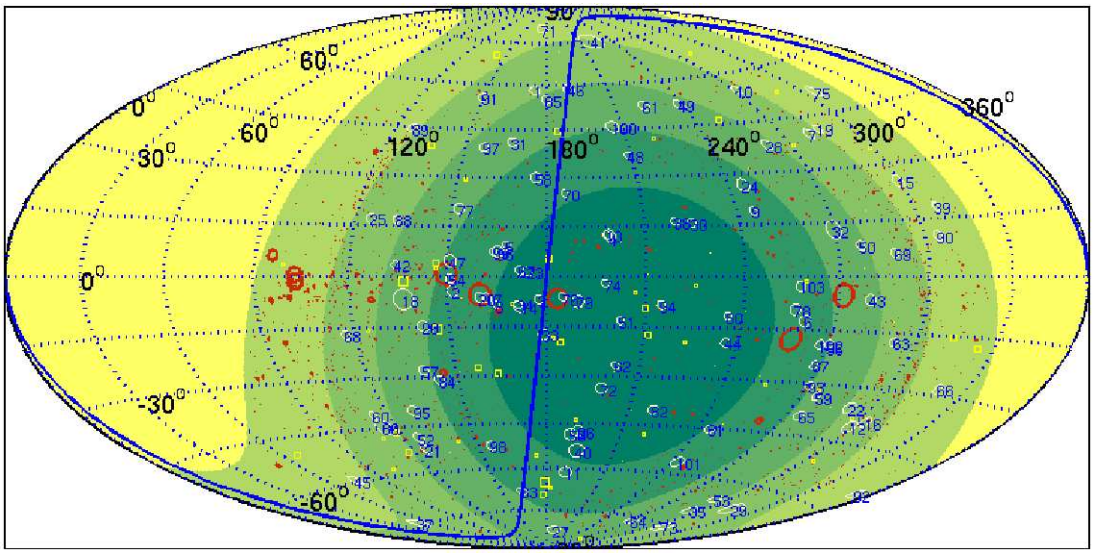

Figure 2.10: Aitoff projection of the sky in supergalactic coordinates. The blue solid line represents the galactic plane. The 103 arrival directions of cosmic rays with energy $\geq$ 55 EeV detected by the Pierre Auger Observatory from January 1 of 2004 to December 21 of 2011 are shown as white circles with diameters proportional to their energy, normalized to 3.0° in diameter for E = 55 EeV. The white squares represent the events with energies between 42 and 55 EeV, their sides are linearly scaled with their energies between 0° for E = 42 EeV and 3.0 ° for E = 55 EeV. The red circles represent the positions of AGN from the VCV 13th edition catalogue normalized to a diameter of 6.0° for a red shift of 0.001. The AGN shown are located within a distance of 200 Mpc from the Earth. Figure taken from [82].

that this degree of correlation results from an isotropic distribution of the sources of UHECRs within a distance of 200 Mpc from the Earth. This probability is even lower using the Swift-BAT 58-month hard X-ray catalogue [80] instead of the previously used Veron-Cetty and Veron (VCV) 13th edition catalogue [81], showing only 29 correlated events, corresponding to a probability less than 0.05% [82, 83]. Fig. 2.10 represents the arrival directions of those UHECRs in supergalactic coordinates. Nowadays, the search for the anisotropy is actually an open field of research in continuous development.

2.6 Extensive Air Showers

The flux of particles with energies beyond 10^{15} eV is not large enough to allow direct measurements with sufficient statistics due to the limited effective area of detectors aboard balloons or satellites. However, when a cosmic ray of these energies strikes the atmosphere, it interacts with the molecules of air, developing a cascade of secondary particles composed mainly by electrons and positrons ($e^{\pm}$), photons (γ), pions ($\pi^{\pm}$) and muons ($\mu^{\pm}$). As already mentioned the result of this process is the Extensive Air Shower, and its detection allows the indirect measurement of the properties of the primary cosmic ray at ground. Even at relatively low energies ($\sim 10^{14}$ eV) EASs spread several km^2 and, due to this wide spatial distribution, large arrays of detectors are needed. The different detection techniques of the EASs will be described in the next chapter.

The incident particle suffers a nuclear interaction with the air molecules, producing a large number of hadrons, mainly pions, which give rise to further hadronic interactions. In every generation, approximately a third of the energy is transferred to an electromagnetic cascade by the fast decay of neutral pions into two photons. This electromagnetic component dissipates $\sim 90\%$ of the energy of the primary particle through ionization of air molecules. In addition, a muonic cascade is generated through the decay of charged pions and kaons into muons. Along all these processes the atmosphere acts as a calorimeter in which the energy of the primary nucleon decreases, and then only a small fraction of the primary energy (corresponding to the fraction carried by neutrinos, muons and a few nucleons) reaches the ground level. A scheme of the main processes involved in the development of the EASs is shown in Fig. 2.11.

There are thus three components in the extensive air showers: the hadronic component (p, n, and not decayed $\pi^{\pm}$ and $K^{\pm}$), the electromagnetic component ($e^{\pm}$ and γ) and the muonic component ($\mu^{\pm}$). These components are described in detail in the next subsections. A complete review on the phenomenology of EASs can be found in [84, 85].

2.6.1 Hadronic component

Hadronic interactions are dominant in the early stages of the air shower development. About 1% of the particles in an extensive air shower are pions, kaons and baryons travelling very close to the shower axis. Neutral and charged pions give rise to the electromagnetic and the muonic component respectively, as will be explained in the next subsections.

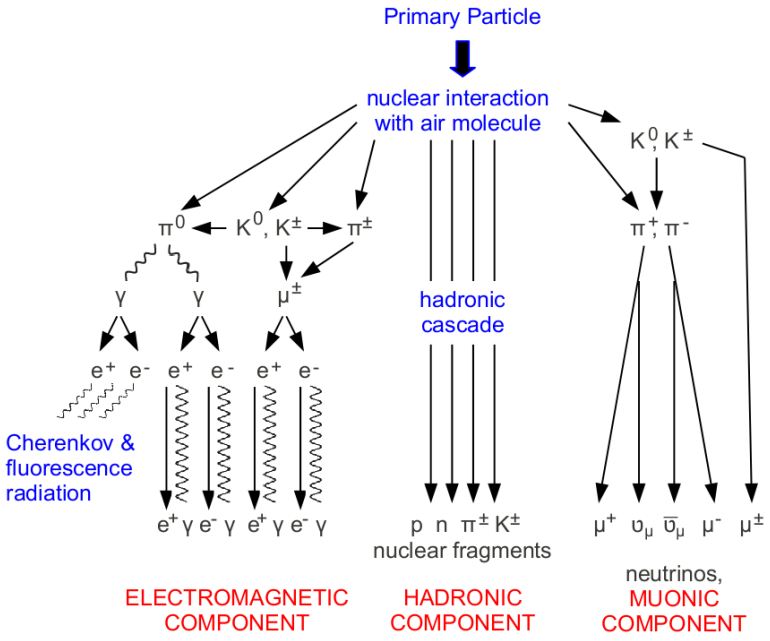

Figure 2.11: Schematic diagram of the processes involved in the EASs.

As has been pointed out, the information about the primary energy or the particle type is derived from the properties of the EAS, and the results are interpreted using Monte Carlo (MC) calculations of the shower development. While the properties of the electromagnetic interactions are well understood, the hadronic interactions at ultra-high energies are still not well known. Several models are used to describe hadronic interactions such as Quark-Gluon String Model with Minijet Production (QGSJET) [86], Energy Parton Off-shell Splitting (EPOS) [87] and SIBYLL [88]. The EPOS model has been updated using recent data from the LHC [89, 90, 91], however there is a lack of experimental data for UHECRs since even the LHC is not able to reach such high energies and thus an extrapolation from lower energies is needed. As a consequence, the assumed models for hadronic interactions give rise to the main source of uncertainties in EAS simulations. Since some parameters of the primary cosmic rays are inferred from the comparison of shower data and MC simulations, in particular the primary mass, the lack of knowledge in hadronic interactions is the main source of systematic uncertainties in the measurement of these parameters.

The present knowledge of hadronic processes is given by the fundamental theory

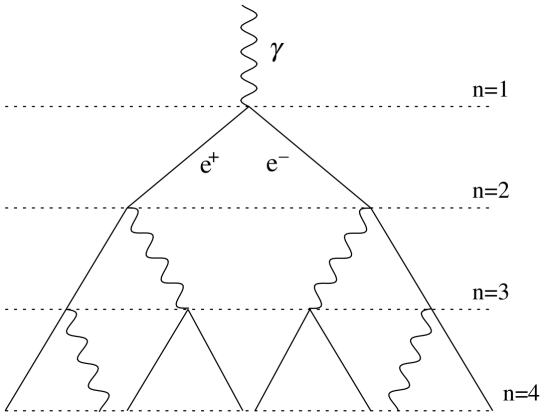

Figure 2.12: Scheme of Heitler model for an electromagnetic shower. Figure taken from [93].

of quantum chromodynamics (QCD). However, soft collisions with small momentum transfer, which dominate in the non-diffractive inelastic processes of the hadronic component and have an important role in the EASs, cannot be calculated using the QCD.

2.6.2 Electromagnetic component

As already mentioned, neutral pions decay into two gamma rays ($\pi^0 \rightarrow \gamma + \gamma$). On the other hand, charged pions might also decay before interacting giving rise to an electron. Both gamma rays and electrons of high energy develop in the atmosphere an electromagnetic shower. A pure electromagnetic shower can be well described by the Heitler model [92]. As represented in Fig. 2.12, a primary photon gives rise to an e^+ - e^- pair which generates photons through bremsstrahlung. In every new generation, the number of particles is doubled and the energy is equally shared between all of them, decreasing the energy of each particle in every step. Thereby, after n generations the number of particles is 2^n, each one with an energy of $E_0/2^n$, where E_0 is the primary energy (i.e., the energy of the particle which initiates the shower). This growing process stops when the particle energy reaches a critical value E_c (which in air is $\sim$ 85 MeV) because in the photonic component the Compton scattering starts to dominate over the pair production while, in the electrical component, collisions dominate over the bremsstrahlung radiation. As a consequence, losses due to ionization dominate and the cascade dissipates its energy in the atmosphere.

Thus, the electromagnetic component develops fast, reaches a maximum in number

of particles, and then starts to attenuate. From the Heitler model it is deduced that the maximum number of shower particles is $N_{\max} = E_0/E_c$, and it is reached at an atmospheric slant depth[2] $X_{\max}$:

$$X_{\max} = \lambda_r \cdot \ln\left(\frac{E_0}{E_c}\right) , \tag{2.9}$$

where λ_r is the radiation length of air for electrons. Then, the number of particles in the shower maximum is proportional to the primary energy and the depth of maximum is proportional to the logarithm of the primary energy.

The maximum number of particles in an iron shower of energy E is reached at higher altitude in the atmosphere than the one in a proton shower with the same energy. This can be understood from the superposition theorem, which postulates that, as a first approximation, a nucleus of mass number A and energy E is equivalent to the superposition of A independent nucleons, each with energy E/A. This theorem implies that the energy of the sub-showers are E/A instead of E, and as a consequence $X_{\max}$ becomes smaller for iron ($A_{Fe} = 56$) than for proton.

Besides, from expression (2.9), the rate of increase of $X_{\max}$ with $\log E_0$ (which is the so-called elongation rate) can be obtained:

$$D_{10} = \frac{\mathrm{dX_{max}}}{\mathrm{d\log E_0}} = 2.3\lambda_r \ [\mathrm{g\,cm^{-2}/decade}] . \tag{2.10}$$

This law is confirmed by more complex models. Taking into account that the radiation length of air for electrons is 37 $\mathrm{g\,cm^{-2}}$, the Heitler model predicts an increase in $X_{\max}$ of 85 $\mathrm{g\,cm^{-2}}$ per decade in energy for pure electromagnetic showers.

Nowadays, thanks to quantum electrodynamic, the knowledge of electromagnetic processes of EASs is quite precise, unlike hadronic ones. Heitler proposed the first model of electromagnetic showers, but since then some authors have developed more sophisticated analytical models. Greisen gave a formula for the total number of charged particles in an electromagnetic shower initiated by a photon of energy E_0 as a function of depth t in units of radiation lengths [94]:

$$N_e(E_0, t) = \frac{0.31}{\sqrt{\ln\left(\frac{E_0}{E_c}\right)}} \cdot e^{t(1-\frac{3}{2}\ln(s))} , \tag{2.11}$$

[2]The slant depth is defined as the atmospheric depth measured along the shower axis as $X = \int_z^\infty \rho(z')dz'$, where ρ is the density of the atmosphere at distance z' from ground measured along the shower axis.

where:

$$s \approx \frac{3t}{t + 2\left(\frac{E_0}{E_c}\right)} \tag{2.12}$$

is the so-called age of the shower, and is defined to be $s = 0$ at the origin of the shower, $s < 1$ when the number of particles is growing, $s = 1$ at the shower maximum, and $s > 1$ when the shower attenuates.

Gaisser and Hillas [95] proposed the following parameterization for the longitudinal development of the electromagnetic component of an EAS initiated by a nucleus:

$$N_e(X) = N_{\max}\left(\frac{X - X_0}{X_{\max} - X_0}\right)^{\frac{X_{\max}-X_0}{\lambda}} \cdot e^{\frac{X_{\max}-X}{\lambda}}\ , \tag{2.13}$$

where $N_{\max}$ is the number of particles at $X_{\max}$, and X_0 and λ are parameters that depend on the point of first interaction and on the shower development

Besides, the decrease of the particle density as a function of the distance from the shower axis can be described by a Lateral Distribution Function (LDF). Nishimura, Kamata and Greisen gave the following equation (NKG formula [96]) to express the density of particles at a distance r in a plane perpendicular to the shower axis:

$$\rho_e(r) = \frac{N_e}{2\pi r_{\mathrm{M}}^2}\frac{\Gamma\left(\frac{9}{2} - s\right)}{\Gamma(s)\Gamma\left(\frac{9}{2} - 2s\right)}\left(\frac{r}{r_{\mathrm{M}}}\right)^{s-2} \cdot \left(1 + \frac{r}{r_{\mathrm{M}}}\right)^{s-\frac{9}{2}}\ , \tag{2.14}$$

where N_e is the total number of particles, $\Gamma(s)$ is the gamma function, s the age parameter and r_{M} is the Molière radius ($\sim$ 100 m at the Pierre Auger Observatory altitude). Although this NKG formula was obtained for pure electromagnetic showers, it provides a good description of the lateral distribution of $\mathrm{e}^{\pm}$ at all stages of shower development, and can be extended to describe showers initiated by a nucleus.

2.6.3 Muonic component

Following an approach similar to that of Heitler, air showers initiated by hadrons can be modelled [93]: a proton interacting with a nucleus creates a certain number of pions, i.e., multiplicity, with and average value increasing with E_0. About 2/3 of these generated pions are charged while 1/3 are neutral pions. The neutral ones create the electromagnetic component, as explained before, and the charged pions are the responsible for the muonic component, as it is shown in Fig. 2.13. Charged pions interact producing more pions until their energies fall below a critical value E_c^{μ} ($\sim$ 20

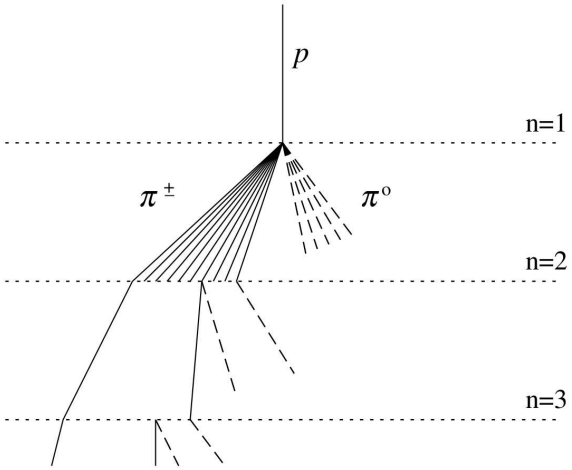

Figure 2.13: Scheme for a hadronic shower. The charged pions initiate the muonic component and the neutral pions initiate the electromagnetic component. Note that not all pion lines are shown after the n = 2 level. Figure taken from [93].

GeV). At this stage the charged pions decay into muons and neutrinos:[3]

$$\pi^+ \rightarrow \mu^+ + \nu_\mu \ , \tag{2.15}$$

$$\pi^- \rightarrow \mu^- + \nu_\mu \ . \tag{2.16}$$

Kaons are also involved in the muonic component because they mostly decay directly into muons, but they also have a probability of 28.5% to decay into charged pions:

$$K^\pm \rightarrow \mu^\pm + \nu_\mu \ , \tag{2.17}$$

$$K^\pm \rightarrow \pi^\pm + \pi^0 \ . \tag{2.18}$$

Muons amount to about 10% of the charged particles in the shower. As muons are heavier than electrons their radiative losses through their travel to the ground are significantly smaller (i.e. muons have a smaller cross section than electrons). They have almost rectilinear trajectories and only lose a small fraction of their energy by ionizating collisions. The low scattering suffered by muons implies that their arrival times at ground are shorter than the arrival times of electromagnetic particles. In

[3]These neutrinos are part of the invisible energy.

addition, muons are not able to generate cascades of particles, so there are no new generations of muons and, as a consequence, for high energies and vertical showers the number of muons reaching the ground is smaller than the amount of electrons.

Using the approach to Heitler model for air showers initiated by a proton, the number of muons in the shower can be calculated as follows:

$$\ln(N_\mu) = \beta \cdot \ln\left(\frac{E_0}{E_c^\mu}\right) \ , \tag{2.19}$$

where β is:

$$\beta = \frac{\ln(\frac{2}{3}\langle m\rangle)}{\ln\langle m\rangle} = 0.85 \ , \tag{2.20}$$

being $\langle m\rangle$ the number of generated pions.

Introducing the value of $E_c^\mu \simeq 20$ GeV in the expression (2.19), the number of muons can be expressed as follows:

$$N_\mu \sim 10^4 \left(\frac{E_0}{1\text{PeV}}\right)^{0.85} \ . \tag{2.21}$$

The $X_{\max}$ value for the muonic component can be parametrised as follows. Defining N_{ch} as the number of charged pions, in the first interaction the process $\frac{1}{2}N_{\text{ch}}\pi^0 \rightarrow N_{\text{ch}}\gamma$ takes place, and each generated photon produces an electromagnetic shower of energy $E_0/(3N_{\text{ch}})$. Using this value as the primary energy, and starting at the path length traversed where the interaction with the air molecule took place, i.e. X_0,[4] the expression of $X_{\max}$ for a proton initiated shower is:

$$X^p_{\max} = X_0 + \lambda_r \ln\left(\frac{E_0}{3N_{\text{ch}}E_c}\right) \ . \tag{2.22}$$

The number of charged pions, N_{ch}, in the first interaction can be obtained from p-p data [93], obtaining then:

$$X^p_{\max} = 470 + 58\log\left(\frac{E_0}{1PeV}\right) \ [\text{g cm}^{-2}] \ . \tag{2.23}$$

It is possible to extrapolate these results to a shower generated by a massive nuclei using the superposition model, obtaining:

$$N^\mu_{\text{A}} = N^\mu_{\text{p}} \cdot A^{0.15} \ , \tag{2.24}$$

[4] X_0 follows the expression $X_0 = \lambda_I \ln 2$, where λ_I is the interaction length in air.

$$X^A_{\max} = X^p_{\max} - \lambda_r \ln A \, . \tag{2.25}$$

The first expression means that the number of muons in the shower depends on the mass of the primary particle: at a given primary energy, a heavier nucleus creating the EAS leads to a larger amount of muons. This is due to the fact that, since a heavy nucleus has less energy per nucleon than a light one of equal primary energy, it reaches the E^μ_c faster, and then lose less energy to electromagnetic components. Then, an iron shower will have a factor of $(56)^{0.15} = 1.8$ more muons than a proton shower of the same energy. In the second expression it can be noticed that $X_{\max}$ of iron showers is smaller than proton showers by $\lambda_r \cdot \ln 56 = 150$ g cm^{-2} at all energies (i.e., proton showers reach the maximum deeper in the atmosphere than iron showers).

The LDF of muons, which are non-affected by Coulomb scattering unlike electrons and photons, gives information about the trajectories of the parent pion. Greisen gave one of the first parameterizations of the muon LDF at a depth t [97]:

$$\rho_\mu(t, r) = N_\mu(t) \left(\frac{r}{r_{\rm G}} \right)^{-0.75} \left(1 + \frac{r}{r_{\rm G}} \right)^{-2.5} \, , \tag{2.26}$$

where r_G is analogous to the Molière radius in the LDF for electromagnetic cascades. The value of $r_G = 320$ m is larger than $r_M \sim 100$ m, which means that muons spread to larger distances from the shower core than electrons. This fact makes muon to be the main part of the particle density at large distances to the core. Consequently, muons dominate for inclined showers, where the electromagnetic component is rapidly attenuated in the atmosphere (more rapidly at higher values of zenith angle) due to the large amount of atmospheric path travelled [98].

2.7 Mass composition of UHECRs from the properties of the EASs

As it was pointed out above, a direct measurement of the primary mass of low-energy cosmic rays is possible. Results show a composition similar to that observed in the intergalactic medium, with protons and α particles dominating over other nuclei. However, for the most energetic cosmic rays, the mass composition studies must be done through the properties of the EASs which correlate with the mass of primary particle. In the present thesis a novel procedure based on the azimuthal asymmetry of the rise-time of the signals of the surface detector of the Pierre Auger Observatory is used to infer the mass composition of cosmic rays at the highest energies (see chapters 3 and

4). The corresponding results will be compared with those obtained from other mass sensitive parameters that are described in detail next.

2.7.1 Mass-sensitive observable $X_{\max}$

The most reliable method to extract information about the mass composition is based on the $X_{\max}$ parameter, defined above as the atmospheric depth at which the shower reaches the maximum development. As previously explained, for a given primary energy E, the $X_{\max}$ value of light nuclei is larger than that of heavy ones. Therefore, $X_{\max}$ can be used as a parameter sensitive to the primary mass composition. Furthermore, simulations indicate that showers initiated by heavy primaries fluctuate less than those generated by light nuclei. For instance $\sigma(X_{\max})$ for iron showers is smaller than the one of protons by about 40 $\mathrm{g\,cm^{-2}}$. Therefore $\sigma(X_{\max})$ can also be used to measure the mass composition.

As described in the next chapter, the shower maximum depth can be directly measured by fluorescence telescopes. For instance in the Pierre Auger Observatory, this parameter can be measured with an accuracy of better than 20 $\mathrm{g\,cm^{-2}}$. The results of Auger [99] using the latest data set of the $\langle X_{\max}\rangle$ evolution with energy of the two first moments of $X_{\max}$ are shown in Fig. 2.14, suggesting a change of behaviour in the ankle region when the data are compared with the model lines corresponding to the most recent interaction models QGSJETII-04 [100], EPOS-LHC [101] and SYBILL 2.1 [102]. In the left panel it can be observed that the slope of the data is different than the expected one for a pure composition. Besides, in the right panel, it can be seen that the $X_{\max}$ distribution gets narrower towards high energies, as it would be expected from a composition heavier at growing energies [99]. The dependence of $\langle X_{\max}\rangle$ with E measured by other experiments is shown in Fig. 2.15.

The generalized superposition model allows to establish a relationship between mass and energy expressing the mean value of $X_{\max}$ [104, 105] as:

$$\langle X_{\max}\rangle = X_0 + D_{10}\cdot\log\left(\frac{E}{E_0 A}\right) + \zeta\cdot\ln A + \delta\cdot\ln A\cdot\log\left(\frac{E}{E_0 A}\right)\ , \tag{2.27}$$

where X_0 is the mean depth at maximum of proton showers at energy E_0, D_{10} is the elongation rate (2.10) and η and δ are parameters dependent on the assumed hadronic interaction model. From this equation a conversion to the two first moments of $\ln A$ can be derived:

$$\langle X_{\max}\rangle = \langle X_{\max}\rangle_p + f_E\cdot\langle\ln A\rangle\ , \tag{2.28}$$

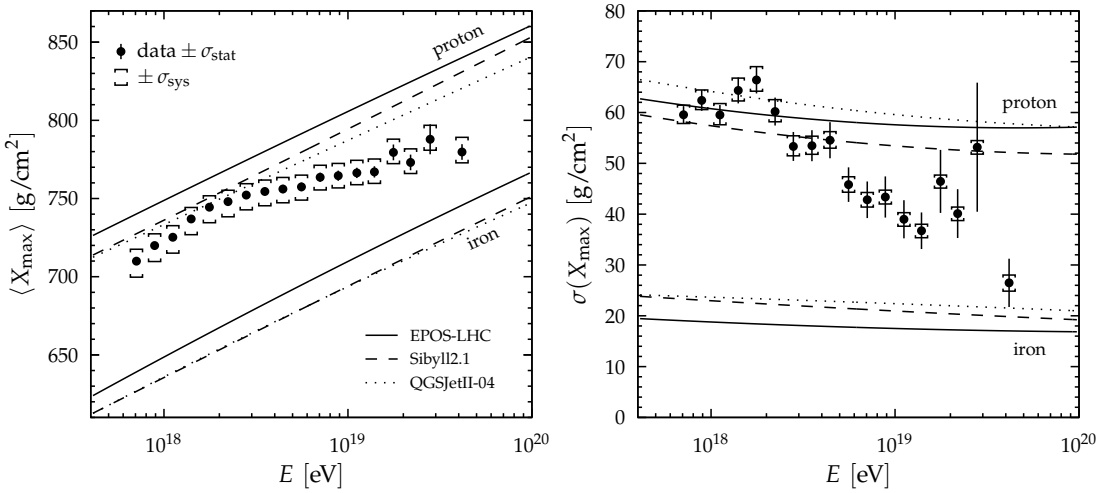

Figure 2.14: Energy evolution of the first two central moments of the $X_{\max}$ distribution from the measurements of the Pierre Auger Observatory compared to air-shower simulations for proton and iron primaries. Figure taken from [99].

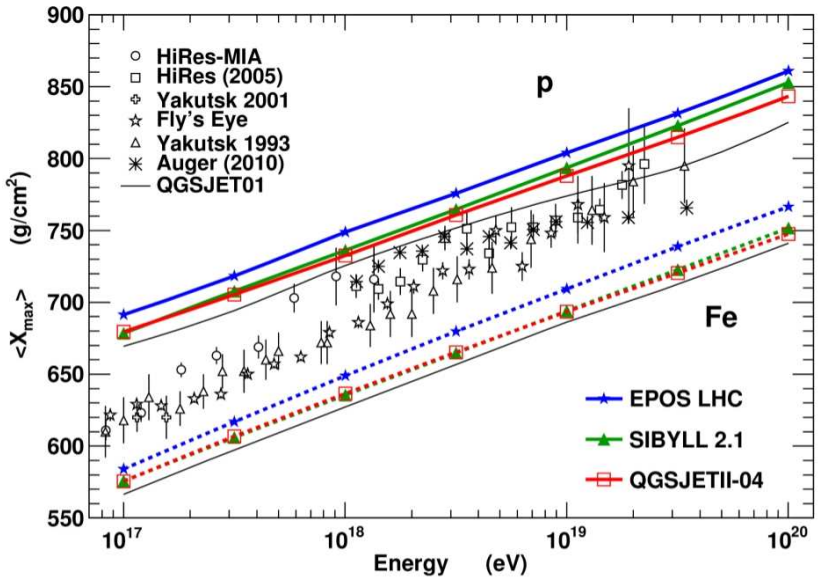

Figure 2.15: Variation of $X_{\max}$ with energy measured by different experiments as well as predictions from different models. Figure taken from [103].

$$\sigma^2(X_{\max}) = \langle \sigma^2_{\rm sh} \rangle + f_E^2 \cdot \sigma^2_{\ln A} \ , \tag{2.29}$$

where $\langle X_{\max} \rangle_p$ is the mean value of $X_{\max}$ for a proton, $\langle \sigma^2_{\rm sh} \rangle$ represents the shower-to-shower fluctuation, the variance $\sigma^2_{\ln A}$ reflects the dispersion in $\ln A$ coming from the mass distribution of the composition and f_E is an energy-dependent parameter expressed as a function on D_{10}, E, E_0 and η. In Fig. 2.16 the results of the same data set used in Fig. 2.14 in terms of $\langle \ln A \rangle$ and variance $\sigma^2(\ln A)$ (named as $V(\ln A)$ in this figure) are represented. As can be observed in the figure, the inferred composition is strongly dependent on the hadronic model used for the analysis, but all of them have the same behaviour suggesting an evolution from light to medium composition with a minimum in the average $\ln A$ just before the ankle (i.e. between 2 and 3 EeV). Results interpreted with EPOS-LHC point to the heaviest average composition, with $\ln A$ compatible with nitrogen at the highest energies. The variance of $\ln A$ derived using EPOS-LHC and SIBYLL 2.1 suggests a flux of cosmic rays composed by different nuclei at low energies and dominated by a single type of nucleus above $10^{18.7}$ eV, where the variance is close to zero. Besides, the interpretation of the results with QGSJETII-04 leads to unphysical variances (i.e., $\sigma^2(\ln A) < 0$) above $10^{18.4}$ eV. This implies that this hadronic model is disfavoured by the data of the Pierre Auger Observatory unless one allows for a systematic bias that is twice as large as the estimated uncertainties.

Although the $X_{\max}$ parameter is an useful observable for mass composition studies, it can only be measured using fluorescence telescopes, which have a low duty cycle, as will be explained in the next chapter. Because of this statistic limitation, and also looking for an independent measure to make a cross-check, the array of surface detectors is used to obtain other mass sensitive parameters.

2.7.2 Muons at ground level and its mass information

As the Heitler model indicates, at a given primary energy a shower generated by a heavy nuclei has more muons at ground level than a proton-induced shower. However, that difference is affected by large fluctuations. In addition, as will be discussed in section 2.7.4, there are discrepancies between the predicted number of muons and the one observed at ground level in real showers. These two facts make very difficult to discriminate directly between primaries only measuring the number of muons at ground. Nonetheless, several analyses based on the muon content have been developed for different experiments to obtain relative information about the mass composition of the primary particle; for example, HiRes/MIA noticed an overestimation of the muon density but predicted a change to a lighter composition from 10^{17} to 10^{18} eV [106], while

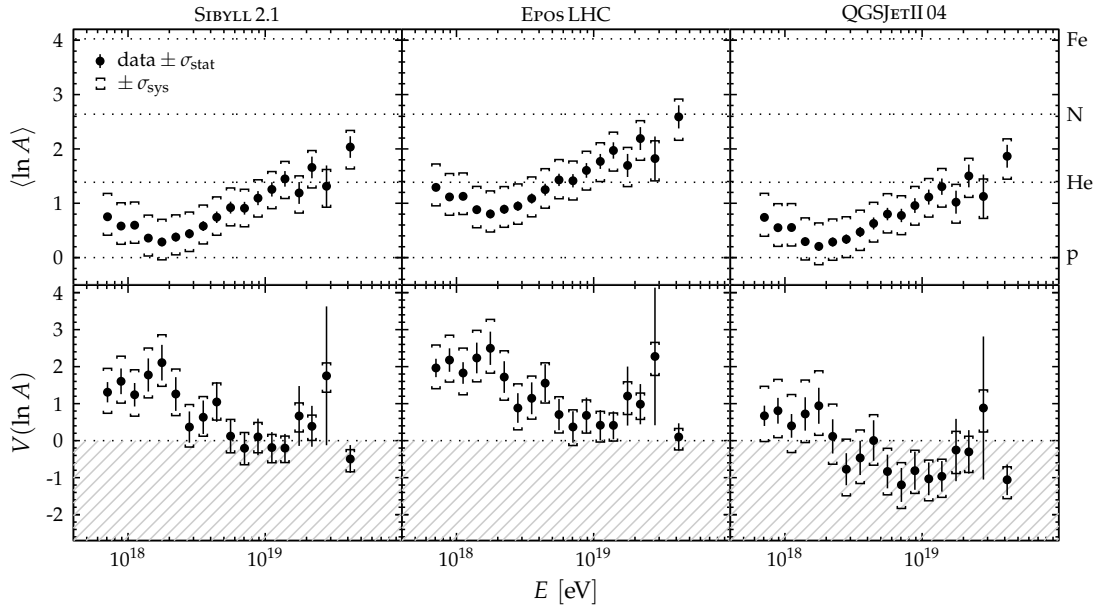

Figure 2.16: Average of the logarithmic mass (top panels) and its variance $\sigma^2(\ln A)$ (named as $V(\ln A)$ in bottom panels) estimated from Auger data using different interaction models. The non-physical region of negative variance is indicated as the gray dashed region. Figure taken from [99].

AGASA, studying the muon density at 1000 m, predicted a decreasing A composition between $10^{17.5}$ to 10^{19} eV [107, 108].

The Pierre Auger Observatory has developed methods for mass composition based on the features of the muonic component. One of them, the so-called Muon Production Depth (MPD) method [109, 110] relies on the idea that muons at ground level carry information about their production point. Assuming that muons are produced in the shower axis and travel following straight lines it is possible to measure the atmospheric depth at which a muon is produced, X^μ, from its arrival time. In this way it is possible to obtain the X^μ distributions related with the development of the muon component, and the corresponding maximum $X^\mu_{\rm max}$ (similar to the $X_{\rm max}$ value for the EM component) is a parameter sensitive to the mass composition of showers. However, this method can only be applied to showers with $E > 20$ EeV in a restricted angular interval $55° - 65°$ using the information of stations at core distances between 1700 and 4000 m.

An example of a typical X^μ distribution is shown in left panel of Fig. 2.17 for a proton simulated event with $E = 10^{19}$ eV and $\theta = 60°$. The MPD distributions

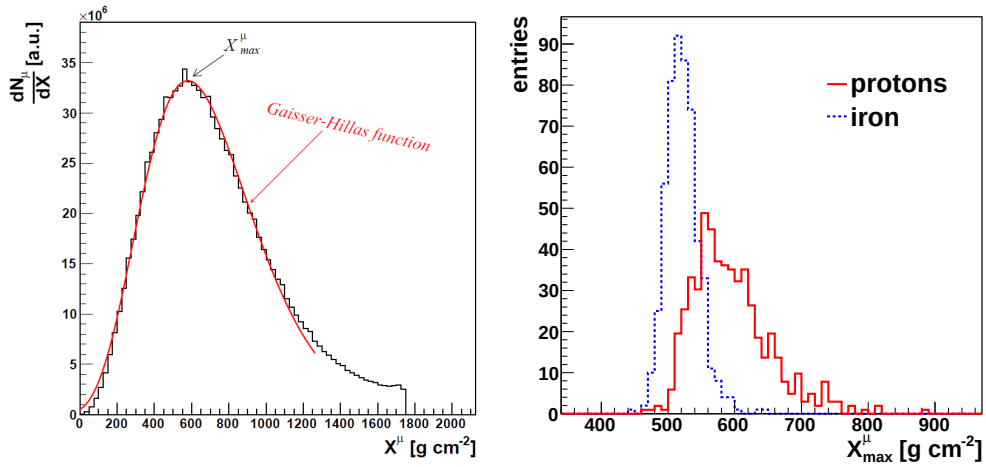

Figure 2.17: Left panel: fit of a Gaisser-Hillas function to a typical MPD distribution of a simulated proton event with $E = 10^{19}$ eV and $\theta = 60°$. Figure taken from [110]. Right panel: $X^{\mu}_{\rm max}$ distributions for proton and iron showers simulated at 30 EeV with EPOS-LHC with θ between 55° and 65°. The mean value and the RMS of the distributions show a clear dependence upon the mass of the primary cosmic ray. For the construction of these MPDs, only muons reaching the ground at distances greater than 1700 m have been considered. Figure taken from [109].

predicted by MC simulations for proton and iron primaries of $E = 3 \times 10^{19}$ eV and θ between 55°and 65°are shown on the right panel of Fig. 2.17. As can be seen, the $X^{\mu}_{\rm max}$ of showers generated by iron nuclei will develop higher, faster and with less shower to shower fluctuations than proton nuclei showers. The behaviour of $X^{\mu}_{\rm max}$ as a function of the energy is studied for data and compared with the predicted results of MC simulations for different primaries in order to extract information about the mass composition of UHECRs. As can be seen in Fig. 2.18 data are bracketed by theoretical expectations for p and Fe, however these results results are fully incompatible with the EPOSLHC predictions. This can be due to the modification in the EPOS-LHC model of the rapidity gap distribution of p-p interactions measured in LHC [111]. These results will be compared in chapter 5 with those presented in this thesis using a different technique, and the interpretation in terms of mass composition will be also discussed.

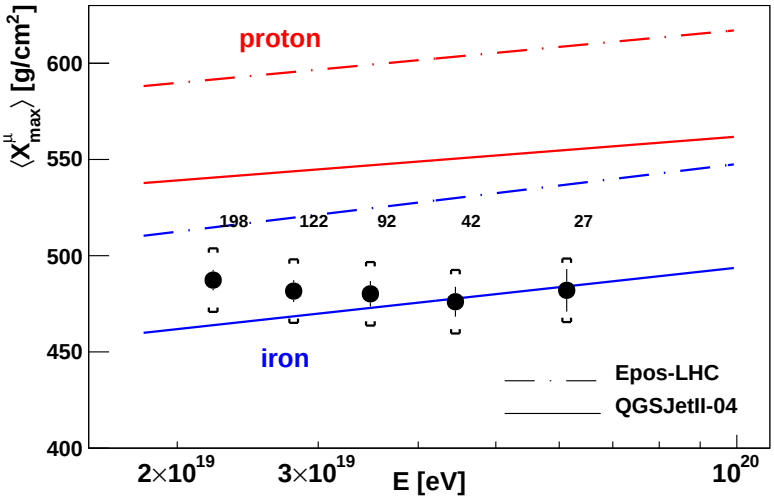

Figure 2.18: $X^{\mu}_{\max}$ as a function of energy. The prediction of different hadronic models for proton and iron are shown. Numbers indicate the amount of selected data in each energy bin and brackets represent the systematic uncertainty. Figure taken from [109].

2.7.3 Mass-sensitive parameter risetime $t_{1/2}$

As it was explained before, the electromagnetic particles of an EAS suffer multiple scattering while the muons travel in almost straight lines, generating a difference in the arrival times of particles reaching the ground between the electromagnetic and the muonic component. To measure the spread in the arrival time of the particles a fixed segment of the total integrated signal over time is chosen. Haverah Park fixed this segment [11], defining the risetime $t_{1/2}$ as the time of increase from 10% to 50% of the total integrated signal. While the selection of this interval does not have a physical reason, it has an important advantage: the 10% to 50% interval allows to extract information from both muonic and electromagnetic component. If the interval is chosen below 30% level the muonic component dominates over the electromagnetic one, while if it is chosen up to 50% is the opposite case.

The $t_{1/2}$ fluctuations between showers were observed to be larger than the expected from sampling uncertainties [112]. This fact gave rise to the development of different analyses to extract information about composition from the risetime. For example, $t_{1/2}$ measurements at Haverah Park of a data set of cosmic rays with primary energy of 10^{19} eV, re-analysed in [113], lead to a result of $\sim$ 20% proton + 80% iron composition.

Several methods had been carried out at the Pierre Auger Collaboration. The Leeds group [114, 115] has developed a procedure to suppress the dependence of risetime on

both distance to the shower core r and the zenith angle θ. For that, a Δ parameter is defined as:

$$\langle \Delta_i \rangle = \sum_i^N \frac{t_{1/2} - t_{1/2}^{\text{benchmark}}(r,\theta)}{\sigma_{1/2}(r,\theta,S)} \,, \tag{2.30}$$

where i refers to each surface detector, $\sigma_{1/2}$ is the uncertainty of the risetime (it will be explained in detail in section 4.3) and $t_{1/2}^{\text{benchmark}}$ is the benchmark function, which represents the risetime values evaluated from a fit to the average risetime as a function of r for showers at a fixed energy. It is obtained fitting the function in the range of energies from $10^{18.9}$ to $10^{19.2}$ and for values of $\sec\theta < 1.4$, $r > 1400$ m and signals above a certain level. Thanks to it, the values of Δ do not depend on r or θ but depends on the mass sensitive observable X_{max}. Using hybrid events, this dependence of Δ on X_{max} was found to be linear, allowing to measure the maximum depth with the SD data and its dependence with energy.

Another method [116, 117] parametrizes the risetime as a function of the distance to the core (assuming a quadratic dependence [118]) in order to obtain the risetime at 1000 m and compare it with the simulated values for different primaries.

Finally, the Auger Collaboration has adopted a method based on the azimuthal asymmetry in $t_{1/2}$ that is the objective of this thesis, and will be extensively explained in the following chapters.

2.7.4 Muon discrepancy

As already mentioned, the determination of the mass composition relies on comparisons with MC predictions and thus on models of hadronic interactions that need to be extrapolated to energies inaccesible to accelerators. This results in a large spread in the predictions of the muon production in air showers [119]. The hybrid nature of the Pierre Auger Observatory provides an ideal experimental set-up for testing and constraining models of high-energy hadronic interactions.

A comparison between ground signals obtained by Monte Carlo simulations of hadronic models and hybrid data collected by the Pierre Auger Observatory shows significant discrepancies. In the left panel of Fig. 2.19, the ratio between the expected and the measured signal at 1000 m ($S(1000)$) as a function of the zenith angle is shown for QGSJETII-04 and EPOS-LHC simulated showers with different compositions and 411 hybrid events with energies $10^{18.8} < E < 10^{19.2}$ eV [120]. The discrepancy between the measured and the simulated $S(1000)$ value, larger than the uncertainty in the FD

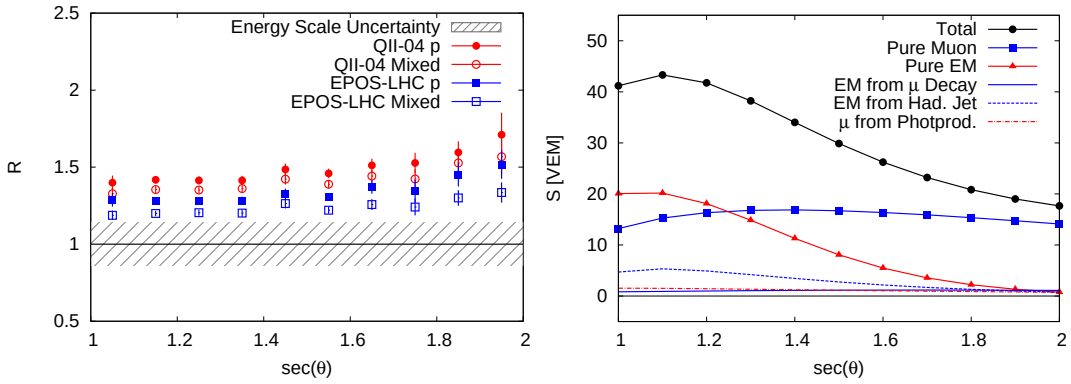

Figure 2.19: Left panel: the average ratio R of the $S(1000)$ of observed events to that in simulated events as a function of zenith angle for mixed or pure proton composition; the gray band represents the impact of the 14% systematic uncertainty in the FD energy scale. Right panel: contributions of different components to the average signal as a function of zenith angle, for stations at 1 km from the shower core, in simulated 10 EeV proton air showers illustrated for QGSJETII-04. Figures taken from [120].

energy scale at all angles, grows with zenith angle, suggesting a lack of predicted muons in simulations for all the models.

This discrepancy can be analysed adjusting the ground signal in the simulations to fit the measured ground signal in the data. To this end, two rescaling factors are introduced: a rescaling factor of the primary energy R_E, which uniformly rescales the total ground signal of the event, and a muonic rescaling factor R_μ, which rescales only the muonic contribution to the ground signal. For each event i, a rescaled $S(1000)$ is simulated as a function of R_E, R_μ and the primary particle type j. Then, the two rescaling factors are fitted minimizing the signal discrepancy. The likelihood function to be maximized is $\prod_i P_i$, with the contribution of each event i expressed as:

$$P_i = \sum \frac{p_j(X_{\max,i})}{\sqrt{2\pi\sigma_{i,j}^2}} e^{\frac{1}{2}\left(\frac{S_{\rm resc}(R_E,R_\mu)_{i,j}-S(1000)_i}{\sigma_{i,j}}\right)^2}, \tag{2.31}$$

where $p_j(X_{\max,i})$ is the probability that the i^{th} event comes from primary type j for the given $X_{\max}$ of the event (calculated using the mix of p, He, N and Fe which best-fits the observed $X_{\max}$ distribution), $\sigma_{i,j}^2$ is the total variance and the rescaled signal $S_{\rm resc}(R_E, R_\mu)_{i,j}$ is expressed in terms of the electromagnetic and muonic signals as

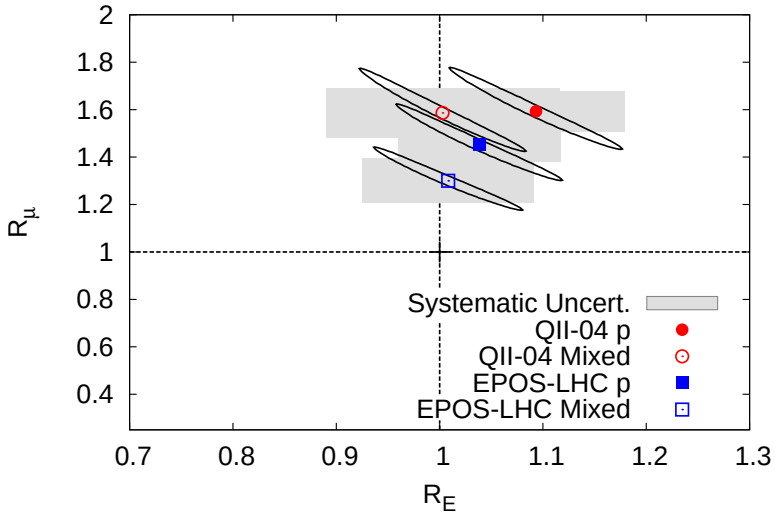

Figure 2.20: The best-fit values of R_E and R_μ for QGSJETII-04 and EPOS-LHC, for mixed and pure proton compositions. The ellipses show the 1σ statistical uncertainties and the gray boxes show the systematic uncertainties. Figure taken from [120].

follows:

$$S_{\rm resc}(R_E, R_\mu)_{i,j} = R_E S_{EM,i,j} + R_E^\alpha R_\mu S_{\mu,i,j} \ , \tag{2.32}$$

where α determines the energy scaling of the muonic signal and has the value of 0.89 independent of composition [121]. The right panel of Fig. 2.19 shows the different contributions in the signal of a 10 EeV EAS.

Finally, the variance of $S(1000)$ with respect to $S_{\rm resc}$ has three contributions: the shower-to-shower variance in the ground signal ($\sigma_{\rm shwr}$, typically 16% of $S_{\rm resc}$ for proton initiated showers and 5% for iron ones), the variance due to limitations in reconstructing the shower ($\sigma_{\rm rec}$, typically 12% of $S_{\rm resc}$), and the variance due to prediction limitations in the MC simulations ($\sigma_{\rm sim}$, typically 10% of $S_{\rm resc}$ for proton initiated showers and 4% for iron initiated showers). The total variance is then:

$$\sigma^2_{i,j} = \sigma^2_{\rm shwr,i,j} + \sigma^2_{\rm rec,i} + \sigma^2_{\rm sim,i,j} \ . \tag{2.33}$$

The results of the fit for R_E and R_μ are shown in Fig. 2.20. As can be observed, there are differences between models and compositions. Since the best fit of $R\mu$ is the closest to unity, the smallest signal deficit corresponds to the mixed composition case with EPOS-LHC. The size of the muonic signal, which is 15% larger for EPOS-

LHC than for QGSJETII-04 for pure proton (and 20% for mixed composition), is the main difference between the ground signals predicted by the two models. EPOS-LHC benefits more than QGSJETII models when a mixed composition is used because the mean primary mass determined from the $X_{\max}$ data for EPOS-LHC is larger [105].

Summarizing, the simulated hadronic signal is a factor 1.3 - 1.6 smaller than the observed one using the last hadronic models. Furthermore, this discrepancy doubles the value of the estimated systematic and statistical uncertainties combined in quadrature, even for the best case of mixed composition using EPOS-LHC. Thus, the present shower models do not describe correctly the muonic ground signal. This has to be taken into account in the interpretation of the results for any analysis in which the hadronic models are required.

Chapter 3

The Pierre Auger Observatory

3.1 Introduction

The Pierre Auger Observatory [22, 122] is the largest detector all over the world designed to study the properties of UHECRs with a high statistical significance. It is located near the town of Malargüe, in the Province of Mendoza (Argentina), at an altitude of 1400 m above sea level (see Fig. 3.1).

The observatory is provided with a Surface Detector and a Fluorescence Detector. The Surface Detector (SD) consists in 1660 water Cherenkov tanks separated by 1.5 km on a triangular grid, covering a total area of about 3000 km^2. The Cherenkov light emitted by the particles as they travel through the water of the tanks provides a measurement of the lateral distribution of the shower. The Fluorescence Detector (FD) that overlooks the SD consists in 24 telescopes split in four buildings surrounding the surface array. The FD measures the longitudinal development of EASs by recording the fluorescence light generated in the atmosphere by the shower particles. The energy threshold of these detectors is of about $10^{18.5}$ eV for the SD and of about $10^{18.0}$ for the FD. The hybrid operation makes possible to detect simultaneously cosmic rays with both detectors allowing a large statistics, a better control of the systematic uncertainties and useful cross-checks for detector calibration and data consistency.

In addition other instruments have been installed. In the first place HEAT and AMIGA are extensions of FD and SD respectively that lower the energy threshold down to 10^{17} eV. Radio antennas are also being used (AERA) as well as microwave detectors (AMBER, EASIER, MIDAS). The location of these components inside the Pierre Auger Observatory is also shown in Fig. 3.1.

While writing this thesis the Pierre Auger Collaboration has agreed to carry out

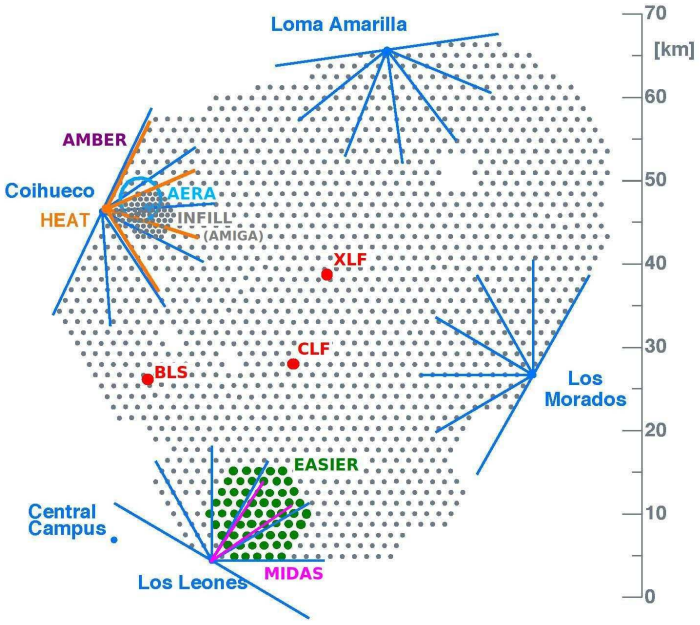

Figure 3.1: Situation of the components of the Pierre Auger Observatory. The water Cherenkov tanks of the SD are represented as gray dots. The blue solid lines represent the field of view of each telescope of the four FD buildings (Coihueco, Los Leones, Loma Amarilla and Los Morados). HEAT, the radio system AERA, the microwave detection prototype AMBER and the infill array of the AMIGA extension are installed next to Coihueco. MIDAS and the surface detectors instrumented with EASIER antennas are close to Los Leones. The Balloon Launching Station (BLS) as well as the XLF and CLF stations (which are instruments for monitoring the properties of the atmosphere) are also shown inside the array. Figure adapted from [123].

a major upgrade of the Observatory by adding plastic scintillators on top of the SD stations in order to enhance their capability to distinguish the muonic and electromagnetic component of the signals. This *AugerPrime* upgrade will improve significantly the determination of the mass of the primary cosmic rays. Although it will not be described here, more details can be found in [124].

This chapter is organized as follows: the performance of the FD and SD detectors are described in sections 3.2 and 3.3 respectively, explaining their design, calibration, trigger system and event reconstruction. The detector enhancements already installed (and those still in deployment) are briefly described in section 3.4.

3.1.1 The Pierre Auger Collaboration framework: $\overline{\text{Off}}\underline{\text{line}}$

In order to carry out the analyses of the data collected by the observatory, the Pierre Auger collaboration developed in C++ the Offline Software Framework [125, 126] , usually named $\overline{\text{Off}}\underline{\text{line}}$. It consists of three principal components:

· Detector description: Containing information about the configuration and performance of the observatory, and also about the atmospheric conditions as a function of time.

· Event model: All simulation and reconstruction information is gathered in this component.

· Framework: The different tasks can be divided into several sequences of self contained processing steps. These tasks are developed by algorithms, the so-called modules. Each module is able to read information from the detector description and/or the event, process the information and write the results back into the event. These modules can be configured and structured by a XML file.

This framework will be the basis for the reconstruction and simulation tasks of the EASs detected by the Pierre Auger Observatory, explained in detail alongside this chapter.

3.2 Fluorescence Detector

As mentioned above, the Fluorescence Detector of the Pierre Auger Observatory is a set of four "eyes" or buildings with a sky coverage of 180° in azimuth, each surrounding and overlooking the array of surface detectors. Their names come from the small hills where they are located: Los Leones, Los Morados, Loma Amarilla and Coihueco. As can be seen in the left panel of Fig. 3.2, each building contains six identical telescopes designed to collect the light emitted in the UV wavelength region (300 - 400 nm). This light is due to the de-excitation of the N_2 molecules of the atmosphere previously excited by the particles from the EAS [127, 128]. These telescopes have a field of view (FoV) of 30° in azimuth and 28.6° in elevation, and have been designed following the Schmidt technique to achieve a high optical quality, reducing the coma aberration as well as keeping the spot size for any viewing angle within an angular spread of 0.5°. An updated and detailed description of the FD of the Pierre Auger Observatory can be found in [129].

The components of the telescopes are: an 0.85 m radius diaphragm with a corrector ring that doubles the aperture area of the telescope and keeps the properties of the Schmidt system [130, 131]; a spherical mirror with a radius of curvature of 3.4 m and

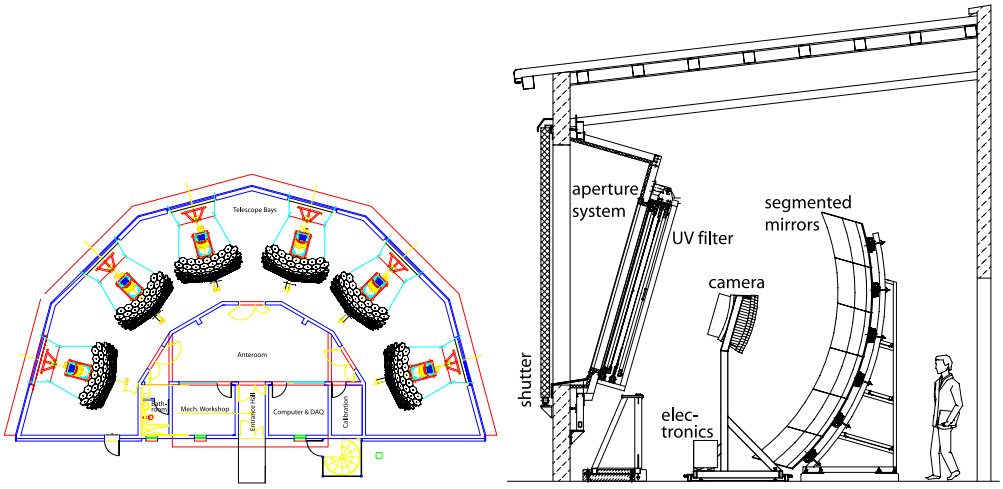

Figure 3.2: Left panel: schematic layout of the building with six fluorescence telescopes. Right panel: schematic view of a fluorescence telescope of the Pierre Auger Observatory. Figures taken from [129].

square shape (3.8 m × 3.8 m); a UV-filter to reduce the background light and a camera in the focal point composed of 440 photomultipliers (PMTs) Photonis XP3062 arranged in a pixel matrix of 22 rows by 20 columns, each one with a FoV of about 1.5°. Due to the spacing between PMTs, each photomultiplier tube is surrounded by a system of Winston cones to optimize the light collection. Finally, 20 front-end boards (each one serving 22 pixels of a camera column), located below the camera, receive the analogue signals of the PMTs and digitize them at 10 MHz using a large dynamic range of 12 bit ADCs. In the right panel of Fig. 3.2 an schematic representation of a fluorescence telescope with its components is shown.

The FD can be only operated during nights with moon fraction below 60% and under stable atmospheric conditions, which implies a duty cycle $< 13\%$. To check this conditions it is necessary an atmospheric monitoring system, performed by several devices deployed in the Pierre Auger Observatory. The pressure, temperature and humidity are recorded by weather stations at ground and also by balloon flights [132]. There is one Laser Imaging Detection And Ranging (LIDAR) station in each FD building, consisting of a pulsed laser beam of 355 nm and a receiver telescope to measure the backscattered photons versus time, allowing to detect clouds and aerosols by analysing the backscattered light from laser pulses [133]. Additionally, there are infrared cameras installed on the top of each FD building to map the cloud coverage over each site taking images every 5 minutes [134]. Another laser-based systems used to study the

atmosphere are the Aerosol Phase Function (APF) monitor, the Central Laser Facility (CLF) and the eXtreme Laser Facility (XLF) [135]. In addition other systems as meteorological radio soundings [136], the star monitor Photometric Robotic Atmospheric Monitor (FRAM) [137], the Horizontal Attenuation Monitor (HAMs) [138] and an octocopter [139] are used for complementary information and cross-checks. The location of some of these instruments is shown in Fig. 3.1. The atmospheric data are stored in SQL databases for a simple accessibility in the reconstruction procedure.

3.2.1 FD calibration

The signals of the PMTs measured in FADC counts have to be converted into light flux. This is necessary for the determination of the longitudinal profile and energy of the showers. An absolute end-to-end calibration allows obtaining the corresponding conversion factor. This is achieved using a portable calibrated diffuse light consisting in a 375 nm light UV LED inside a diffusing cylindrical box that is mounted in front of the telescope aperture. This tool (the so-called drum) provides a uniform illumination of the PMTs camera [140] and thus the calibration factor to convert FADC counts into absolute photon number can be directly obtained with an uncertainty of 9.5%. This calibration is repeated for all telescopes every year.

In addition, in order to avoid variations in the absolute calibration constants due instability of the optical components, another relative calibration is also performed before and after each night of data-taking. Furthermore, a cross-check of the absolute calibration of the FD is performed using the scattered light from the remote vertical laser beams of 337 nm and 355 nm.

3.2.2 FD trigger

The trigger of the FD is the mechanism which allows to distinguish background from event candidates. It is composed of four levels [141, 142], two of them implemented at hardware level and the other two at software level.

- First Level Trigger:
The First Level Trigger (FLT), implemented in the front-end board, makes decisions at pixel level. It compares the collected digitized signal over 1000 ns (10 consecutive time bins) with a threshold, which is continuously adjusted to maintain a pixel trigger rate of 100 Hz. If the sum is larger than a threshold then the pixel is flagged as triggered.

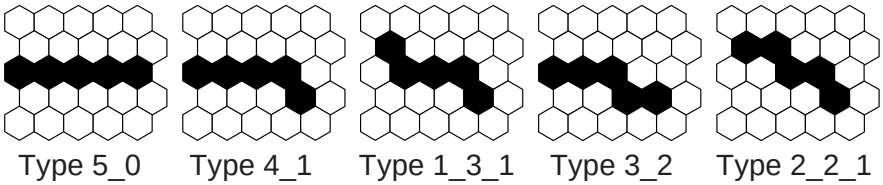

Figure 3.3: Fundamental types of pattern regarded as straight track segments for SLT. Figure taken from [129].

- Second Level Trigger:
The Second Level Trigger (SLT), implemented in a separated board, reads the pixel triggers in all channels and looks for patterns similar to the track generated by the fluorescence light of an EAS (like those shown in Fig. 3.3). It is possible that some light track does not pass through the center of some pixels and thus some PMTs within the shower track do not record enough light to trigger. To avoid that effect as well as that of defective PMTs, only 4 out of the 5 triggered pixels are required for the pattern recognition algorithm. This level of trigger has a rate of about 0.1 Hz per mirror.

- Third Level Trigger:
The Third Level Trigger (TLT) is implemented in a computer called Mirror PC which is associated to each telescope. The TLT is an algorithm that looks for time correlation within the pixel tracks to reject background events like those generated by muon impacts on the camera, lightnings or randomly triggered pixels. The rate for this level is of about 0.02 Hz per mirror with a fraction of true showers rejected below 0.7%.

- Hybrid trigger (T3):
Candidate events passing the TLT trigger in all telescopes are sent to a computer (the Eye PC), where an event builder merges coincident events from adjacent telescopes. Here, a hybrid trigger, called T3, is sent to the Central Data Acquisition System (CDAS), which acts as an external trigger for the SD, aiming to record hybrid events at low energies (below $10^{18.5}$ eV) where the array is not fully efficient and would not generate an independent trigger. At these energies hybrid events occur within 20 km of the FD buildings, triggering no more than one or two SD stations. With this trigger a preliminary shower reconstruction is performed, obtaining basic shower parameters like the ground impact time and the shower direction with a simple online reconstruction. When these data arrive at the CDAS, the SD is requested for signals

recorded close to the calculated impact time. With each T3 trigger the SD stations which are located near the FD building are read out. Finally, the FD and SD data are merged offline allowing hybrid analysis.

3.2.3 FD reconstruction

In the following, the different steps of the reconstruction of shower parameters using FD data are briefly explained. First, the geometrical reconstruction provides the direction of the cosmic ray and the impact point at the ground. Later, this information together with the longitudinal development of the showers is used to reconstruct the primary energy.

- Geometrical reconstruction:

The plane containing the shower axis and the position of the triggered FD building is defined as the Shower Detector Plane (SDP) [143] (see Fig. 3.4). The first step in the geometrical reconstruction is to determine the SDP by minimizing the angular distances from the pointing directions of triggered pixels. Once it is determined, the next step is to obtain the direction of the shower axis within the SDP using the arrival times information. The shower axis can be characterized by two parameters: R_p, which is the perpendicular distance from the camera to the track, and χ_0, which is the angle between the track and the horizontal line in the SDP. Each pixel observing the track has a pointing direction defined by χ_i (the angle with respect the horizontal line). If t_0 is the time when the shower front on the axis passes the point of closest approach to the camera, R_p, then the light arrives at the i^{th} pixel at the time:

$$t_i = t_0 + \frac{R_p}{c} \tan\left(\frac{\chi_0 - \chi_i}{2}\right) \ . \tag{3.1}$$

The geometrical parameters are determined by fitting the data points to equation (3.1). Although it can be calculated using only arrival times of the FD telescopes, a more accurate reconstruction can be obtained combining those times with timing information of SD stations, as can be seen in Fig. 3.5, where the fit to equation (3.1) is compared with the fit of the same equation adding the term corresponding to the arrival time of the SD station. This hybrid procedure allows to obtain an angular resolution of the FD better than 0.6° (on average) at energies above $10^{18.5}$ eV [144].

- Energy reconstruction:

At a given atmospheric depth, the amount of fluorescence light emitted isotropically

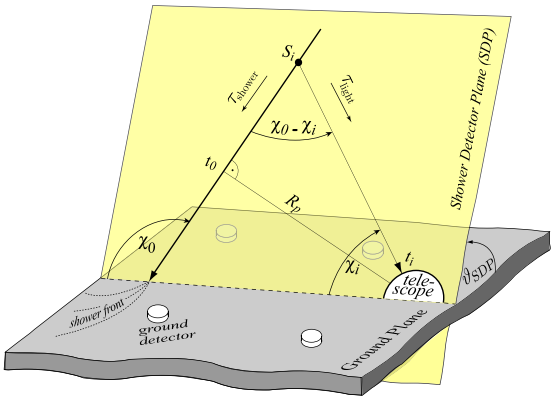

Figure 3.4: Illustration of the geometrical shower reconstruction from the observables of the Fluorescence Detector. Figure taken from [143]

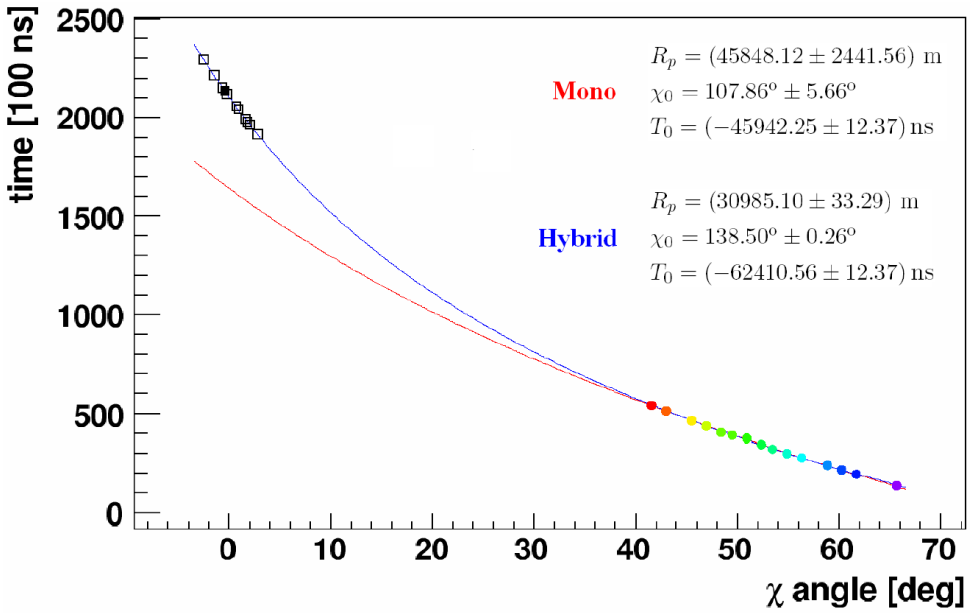

Figure 3.5: Example of reconstructed shower axis. FD data (colour points) and SD data (squares) are superimposed to the monocular (red line) and hybrid (blue line) reconstruction fits. The full square indicates the SD station with the highest signal. This is a typical event in which the monocular reconstruction does not work well. Figure taken from [129].

is proportional to the energy deposited by the particles of the shower at that altitude. It is possible then to convert the light flux at the telescope aperture, collected by every single pixel, into the energy deposited as a function of the slant depth. The relationship between fluorescence emission and energy deposition is given by the so-called fluorescence yield, defined as the number of fluorescence photons emitted per unit deposited energy. This parameter has been measured in dedicated laboratory experiments. The Auger collaboration is currently using the precise yield reported by AIRFLY [145], in good agreement with previous measurements [146] as presented in [147]. The fluorescence yield varies with atmospheric conditions, and thus its dependence with pressure, temperature and humidity are needed for an accurate reconstruction of the energy profile [148, 149, 150]. The assumed fluorescence yield and its dependencies have a relevant impact in the energy scale of any experiment using fluorescence telescopes as discussed in [151, 149].

In a real shower not only the fluorescence light, but also the air-Cherenkov radiation, reaches the telescope. For a given geometry this Cherenkov light is also proportional to the shower energy providing complementary information. In addition it is necessary to take into account the scattered Cherenkov light [152] and multiple-scattered light [153] as well as the attenuation suffered by the light in its path to the detector. The method used by the Auger collaboration to reconstruct the profile of energy deposition that includes all these ingredients, is described in detail in [154].

If the FoV of the telescopes is wide enough to observe the complete shower profile, the total energy deposited by the electromagnetic component can be obtained by integrating the energy deposited at each level; however, this is not the typical case, so it is usually required to extrapolate to depths out of the range of the FoV.

The reconstructed profile of deposited energy is fitted to a Gaisser-Hillas function [95] and integrated to obtain the calorimetric energy:

$$E_{\rm cal} = \int_0^\infty f_{\rm GH}(X)\mathrm{d}X \ . \tag{3.2}$$

The Gaisser-Hillas function is expressed as:

$$f_{\rm GH}(X) = \frac{\mathrm{d}E(X)}{\mathrm{d}X} = \left.\frac{\mathrm{d}E(X)}{\mathrm{d}X}\right|_{X_{\rm max}} \cdot \left(\frac{X - X_0}{X_{\rm max} - X_0}\right)^{\frac{X_{\rm max}-X_0}{\lambda}} \cdot e^{\left(\frac{X_{\rm max}-X}{\lambda}\right)} \ , \tag{3.3}$$

where $\left.\frac{\mathrm{d}E(X)}{\mathrm{d}X}\right|_{X_{\rm max}}$ is the total energy deposited at an atmospheric slant depth $X_{\rm max}$ (defined in the previous chapter as the atmospheric depth at which the maximum number of particles in the shower is reached), while X_0 and λ are shape parameters without

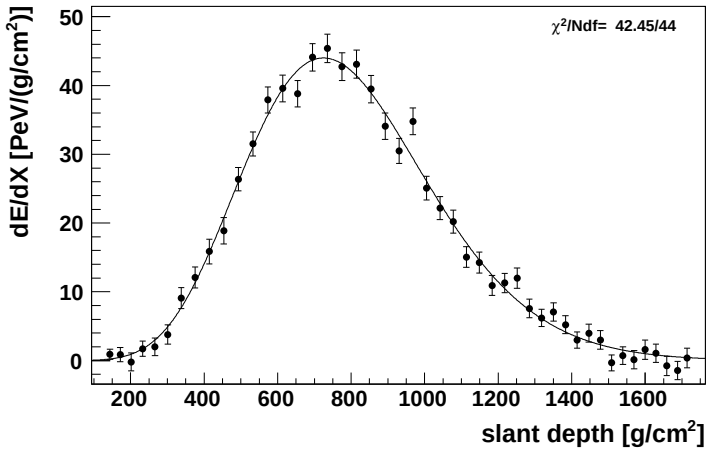

Figure 3.6: Example of a reconstructed energy deposit profile with the Gaisser Hillas fit; the energy reconstruction for this shower was $(3.0 \pm 0.2) \cdot 10^{19}$ eV. Figure taken from [129]

a direct physical interpretation (since the Gaisser-Hillas function is a phenomenological function). In Fig. 3.6 an example of the Gaisser Hillas fit to the energy deposit profile is shown.

The calorimetric energy of the shower does not include the energy carried by particles that do not generate fluorescence light like neutrinos and muons below the ground [155]. This so-called "invisible energy" has been parametrised (see left panel of Fig. 3.7) as [156, 157]:

$$\frac{E_{\mathrm{inv}}}{1\mathrm{EeV}} = 0.174 \cdot \left(\frac{E_{\mathrm{cal}}}{1\mathrm{EeV}}\right)^{0.914} . \tag{3.4}$$

For energies above 10^{18} eV, the fraction of the invisible energy is about 15% of the total energy, decreasing with energy (see right panel of Fig. 3.7). The total energy of the primary cosmic ray as measured by the FD is therefore:

$$E_{\mathrm{FD}} = E_{\mathrm{cal}} + E_{\mathrm{inv}} . \tag{3.5}$$

3.3 Surface Detector

As has already been introduced, the SD is an array of Water-Cherenkov Detectors (WCDs) in a triangular grid of 1660 tanks separated by 1500 m covering more than 3000

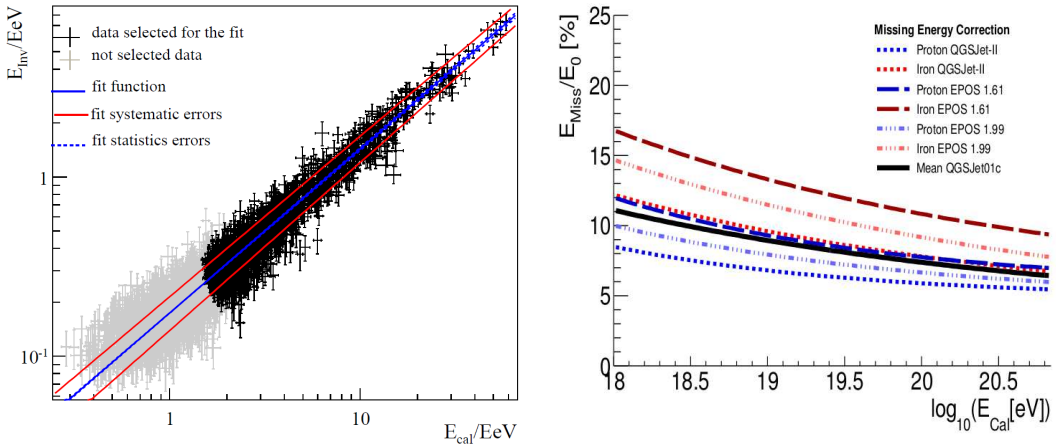

Figure 3.7: Left panel: fit of E_{inv} vs E_{cal} on the golden hybrid events above $10^{18.3}$eV. Figure taken from [157]. Right panel: invisible energy as a function of calorimetric energy for different hadronic models. Figure taken from [156].

km^2. The WCDs are cheaper than scintillators, as well as more sensitive to showers arriving at large zenith angles, increasing therefore the sky coverage. Additionally, these detectors can operate for a long period of time with both high stability and low maintenance.

The WCDs exploit the fact that charged particles moving faster than the speed of light in the medium generate Cherenkov light. At ground level, shower particles are mainly photons and electrons with energies below 10 MeV, and also muons in the GeV range. At these energies electrons and muons generate Cherenkov light inside the tank while photons are converted via pair production and Compton scattering into relativistic electrons and positrons, which can also produce Cherenkov light.

Each station (like the one shown in Fig. 3.8) consists of a cylindrical tank of polyethylene with a diameter of 3.6 m and a height of 1.55 m containing a Tyvek® liner filled with 12000 l of high purity water up to a height of 1.2 m; this liner is black on the outside (acting as a seal against background light) and its inner surface provides an excellent diffusive reflectance for Cherenkov light (about 98% depending on wavelength). The water volume is observed, through three clear plastic windows, by three 9″ XP1805 Photonis photomultiplier tubes (PMTs) [158] located at the top surface of the liner looking downwards. From each PMT two signals are extracted: one from the anode and another one from the last dynode (amplified by a factor of 32 to match the dynamic range) [159, 160]. The readout of these six signals from each tank is digi-

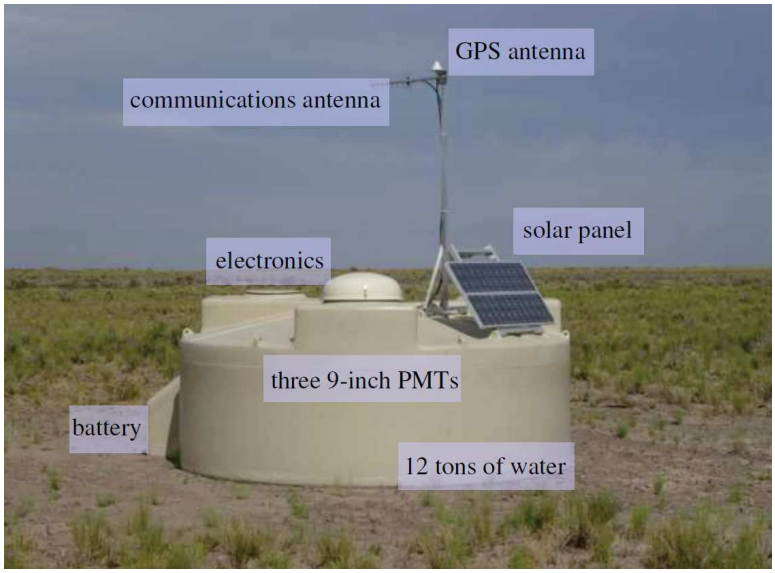

Figure 3.8: SD station of the Pierre Auger Observatory with its components labelled; the Tyvek® liner and the three PMTs are inside the tank.

tized at 40 MHz (25 ns bins) using a Flash Analog to Digital Converter (FADC) [161] and sent to a Programmable Logic Device (LPD). This device is operated by a CPU located in a box on the top of the tank that controls the electronics. The LPD selects the signals according to the trigger configuration and sends them to the closest of the four local communication towers, which are located at each fluorescence building. From there, signals go to the CDAS through a high capacity microwave link. Timing synchronization, which is essential to determine the shower direction, is obtained by a GPS Motorola unit installed in each local station. The GPS allows achieving a time precision of $\sim$8 ns. Two solar panels on the top of the tank, connected to two 12 V batteries, supply an electrical power of 10 W to feed the electronics. Therefore, each detector is autonomous and can operate independently of the other tanks of the array.

The SD is complete since June 2008 although it has been taking data in stable operation since January 2004 with a smaller number of tanks. A map of the active SD stations at present [162] is shown in Fig. 3.9. The status of each tank is monitored continuously [163]. In order to get a better understanding on the time resolution and the fluctuations in the signals, some position of the SD grid are provided by two (twins) or three (triplets) nearby detectors with a separation of $\sim$11 m.

An example of a complete SD event is illustrated in Fig. 3.10. It corresponds to a proton simulated event with an energy of $10^{19.25}$ eV and a zenith angle of 45°. In the

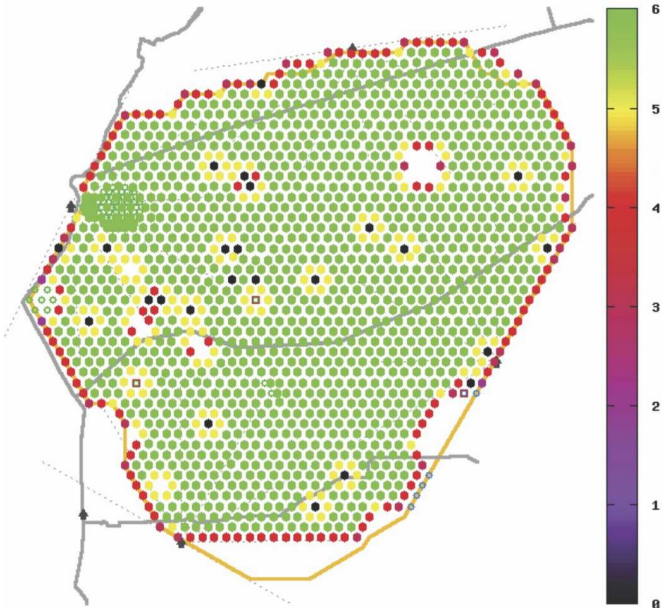

Figure 3.9: Map of the SD array with the current active detectors (coloured points). For each working detector, the colour indicates the number of surrounding active detectors. The high populated area in the upper left corner of the map is the infill, treated in detail in Section 3.4.1. Figure taken from [162].

left panel the reconstruction of the event inciding into the SD array is represented, while in the right panel the footprint of this event is shown. The straight line represents the incoming direction of the cosmic ray, the size of the triggered stations is proportional to the amount of signal registered by each tank, and the colour is related to the time of arrival: the yellow stations are first triggered while the red ones are the most delayed.

3.3.1 SD calibration

A certain amount of light generated by a particle in different tanks, or even in the same tank but at different times, does not usually give rise to exactly the same signal. This is due to the fact that the electronic signal in a given PMT not only depends on the light pulse induced by the particle, but also on the water quality, the PMT response and the liner reflectivity. Hence, in order to avoid variations between tanks, the signal measured at each one has to be normalized to a reference calibration unit.

Given the large number of detectors and their separated locations, a simple and automatic self-calibration procedure has been implemented in the local electronics.

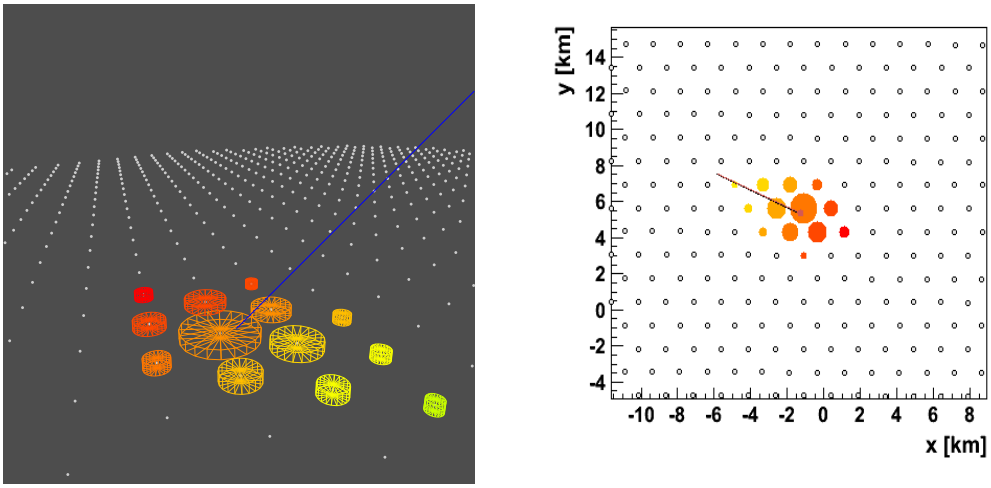

Figure 3.10: Left panel: reconstruction of a proton shower with $\log(E/\mathrm{eV}) = 19.25$ and $\theta = 45°$ inciding into the SD; the straight line represents the incoming direction of the primary particle, the untriggered tanks of the array are represented as white dots, while the triggered stations are coloured taking as a function of the time of arrival of the particles (yellow tanks are hit before the red ones) and have an area proportional to the signal intensity. Right panel: footprint of the same event at ground level.

The calibration unit is the so-called Vertical Equivalent Muon (VEM or $\mathrm{Q_{VEM}}$) defined as the signal produced by a vertical and central through-going (VCT) muon [164]. The goal of the calibration procedure is to determine with good accuracy the value of 1 VEM in electronics units (i.e., integrated channels). For that, the signals of atmospheric muons crossing the tanks (which have a high rate of ∼2500 Hz) are used. An example of the charge histogram corresponding to the sum of the 3 PMTs of a SD station obtained with atmospheric muons is shown as a solid black line in the left panel of Fig. 3.11. To select only VCT muons and establish the relation between a VEM and the peak of the histogram, a test detector consisting in a reference tank equipped with two movable scintillators have been used [165]. The charge from these VCT muons, measured by coincidences between the two scintillators of the reference tank, is represented with a red dashed line. The first peak is due to low-energy atmospheric muons, while the second one ($\mathrm{Q}^{peak}_{\mathrm{VEM}}$) is due to vertical through-going atmospheric muons. In comparison with the VEM peak of the VCT muons, this second peak corresponds to approximately at 1.09 VEM for the sum of the 3 PMTs (i.e., there is a conversion factor between both peaks of $\mathrm{Q}^{peak}_{\mathrm{VEM}} = 1.09\ \mathrm{Q_{VEM}}$) and 1.03 ± 0.02 VEM for each PMT; these values are

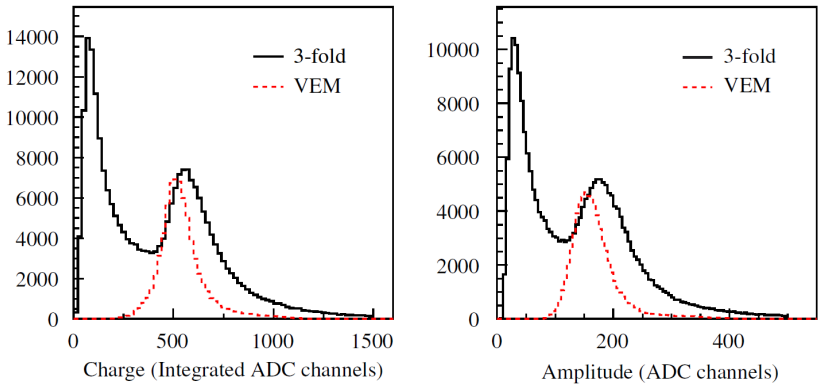

Figure 3.11: Charge (left panel) and pulse height (right panel) histograms from an SD station with 3-fold coincidences between all 3 PMTs. The dashed histogram is produced by an external muon telescope to select only vertical and central muons. The first peak is due to low-energy atmospheric muons. The second peak is due to vertical through-going atmospheric muons. Figure taken from [164].

different because each PMT measures a portion of the signal deposited closest to them but the sum of the 3 PMTs measures the total signal in the tank [166].

Moreover, to keep the same trigger condition for the whole array, the SD stations must have a reference unit for threshold levels. This reference is again provided by the atmospheric muons, which produce a peak in a pulse height histogram in a similar way that the peak produced in the charge histogram, as it is shown in the right panel of Fig. 3.11. The pulse height histogram for atmospheric muons is shown as a solid line. Muons also produce two peaks of equivalent interpretation; the second one, I_{VEM}^{peak}, is used as a common reference unit for threshold levels.

For the calibration to VEM units procedure, the initial end-to-end gains of the 3 PMTs, i.e. I_{VEM}^{peak}, must be roughly equivalent to ensure that the signals recorded from the 3 PMTs are similar in amplitude. Additionally, this calibration procedure must be able to convert the raw FADC traces into integrated channels, which requires to determine the baselines[1] of all six FADC inputs and the gain ratio between the dynode and the anode. Once the calibration is completed, the calibration constants I_{VEM}^{peak} and Q_{VEM}^{peak} are obtained with precision at the level of 3% and 6%, respectively.

[1]The baseline is the part of the trace which does not correspond with the air shower signal or coincident muons; it is a combination of an artificial constant off-set from zero, the undershoot and the electronic noise fluctuations.

They are calculated every minute and sent to CDAS with each triggering event [166], which allows the registration of a large amount of information about the state of each surface detector in the minute preceding the trigger of each recorded event, leading to an accurate calibration of the data. More details about the process of the calibration to VEM units can be found in [164].

3.3.2 SD trigger

When a particle hits a tank, it is mandatory to have a mechanism which allows the separation between particles coming from EASs and background particles. The trigger system (detailed in [167]) is designed to put constrains on the signals of the tanks in order to select only physical events generated by cosmic rays, allowing operation at a wide range of primary energies and incident angles from vertical to very inclined showers.

It consists of five levels. Two local triggers, levels 1 and 2 (called T1 and T2) implemented at the tanks. A level 3 (T3), implemented at the CDAS, is based upon the spatial and temporal correlation of the T2 triggers. All data satisfying the T3 trigger are stored for further analysis. The two last trigger levels (T4 and T5) are implemented offline in order to select physical events associated with cosmic rays and good quality events. In the following, these trigger levels are explained in detail:

- T1 level:

The T1 trigger is formed by two different modes. The first mode is a Time-over-Threshold trigger (ToT) that requires the signal to be larger than a threshold value of $0.2 \cdot \mathrm{I}^{peak}_{\mathrm{VEM}}$ in at least 13 bins of 25 ns/bin within a time window of 120 bins in coincidence in 2 out of 3 PMTs [168]. The second mode corresponds to a Simple Threshold trigger (TH) that requires the signal from the 3 PMTs to be larger than a given threshold value of $1.75 \cdot \mathrm{I}^{peak}_{\mathrm{VEM}}$ in at least one bin. The first-mode condition has a rate smaller than 2 Hz and is designed to identify small signals spread in time like those induced by low-energy showers with a strong electromagnetic component or by high-energy showers in tanks far from the shower core. The second-mode condition is designed to identify large and narrow signals corresponding to the muonic component of highly inclined showers and allows the reduction of the rate due to atmospheric muons from about 3 kHz to about 100 Hz.

An improved version of the ToT trigger, the ToTd trigger, was proposed in [169] in order to distinguish the composite signals produced by a sequence of several particles coming from an EAS from the background of isolated signals. A composite signal is

produced by several particles spread over a time much larger than 25 ns, while the background signals are produced by isolated particles or by a bunch of particles hitting the tank within a short period. It uses a deconvolution algorithm to suppress the exponential tail in the signal by a single particle, associated to the long decay time of the light in the water Cherenkov tanks. After the deconvolution, the trace appears in principle as a succession of narrow peaks, so counting the number of slots above a low threshold within a time window is an appropriate way to distinguish between one peak (random signal), two peaks (double random within the window), or several peaks (shower signal). It was successfully tested in [170] and it detects shower signals of lower amplitude than the ToT/TH combination does. However, some instabilities of the ToTd trigger rate were observed in stations where the response of the electronics was not stable. An alternative algorithm, designed to be much less sensitive than ToT/ToTd against a possible distortion of the signal by the electronic chain, is the so-called Multiplicity of Positive Steps (MoPS) [171]. The MoPS is based on the idea of detecting and counting the accumulation of successive increases (defined as positive steps) in the FADC traces, each step corresponding to the arrival of a particle. The algorithm requires at least a certain number of steps above a certain threshold within a time window. These new triggers are working officially since June 2013.

- T2 level:

The T2 trigger is also implemented in the station to reduce to about 20 Hz the rate of events per detector to be sent to the CDAS. ToT triggers are directly promoted to the second level T2 (T2 ToT) whereas TH triggers are needed to exceed a higher threshold of $3.2 \cdot \mathrm{I}_{\mathrm{VEM}}^{peak}$ in coincidence for 3 PMTs (T2 TH). This level is very useful to detect fast signals (< 200 ns) corresponding to the muonic component associated with horizontal showers.

- T3 level:

The T3 trigger, implemented at the CDAS, consists of two different modes and it is based on spacial and temporal coincidences of triggered stations passing the T2 level. The main mode is developed to assure the time coincidence of at least three tanks which have passed the ToT conditions with a minimum of compactness. It imposes that at least one of the tanks must have one of its closest neighbours and one of its second closest neighbours triggered. It is called "ToT2C$_1$&3C$_2$", where mC$_n$ means m triggered stations within the n$^{\mathrm{th}}$ ring, as can be seen in the example of the left panel of Fig. 3.12. Once the spatial coincidence is verified, timing criteria are imposed: each T2

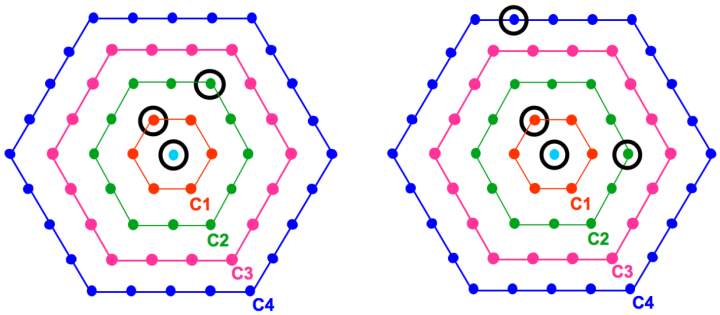

Figure 3.12: Example of T3 configurations: the 3-fold T3 mode ToT2C_1&3C_2 (left panel) and the 4-fold mode 2C_1&3C_2&4C_4 (right panel); see text for the definitions. Figure taken from [167].

must be within (6 + 5n) μs of the first one to be included in the event. Since the ToT as a local trigger has already very low background, this trigger selects mostly physical events generated by cosmic rays with a high efficiency: 90% of the selected events are cosmic ray showers, while the 10% remaining is caused by chance coincidences due to the permissive timing criteria. This mode is extremely helpful to detect vertical showers.

Additionally, to detect horizontal showers, which generate fast signals and have wide spread topological patterns, a different and more permissive mode is implemented. It requires a four-fold coincidence of any T2 with a moderate compactness requirement; i.e., among the 4 triggered tanks, one is let to be as far as 6 km away from the others within the appropriate time window. It is called "2C_1&3C_2&4C_4". The same timing criteria explained before are also applied. An example of such T3 configuration is shown on the right panel of Fig. 3.12. The efficiency of this trigger mode is smaller than 10%.

- T4 level:

The T4 trigger is applied offline to distinguish between physical events and the possible random coincidences from the stored T3 data sample. One of its two modes, the so-called 3ToT, was devised to select real vertical showers. It requires that at least 3 ToT stations are in a triangle of first neighbours, as shown in Fig. 3.13. This mode of trigger has an efficiency of more than 98%. The second T4 mode, the so-called 4C1, is needed to select very inclined showers (above 60°) and also the small fraction of vertical showers lost with the 3ToT condition. It requires a compact configuration of 4

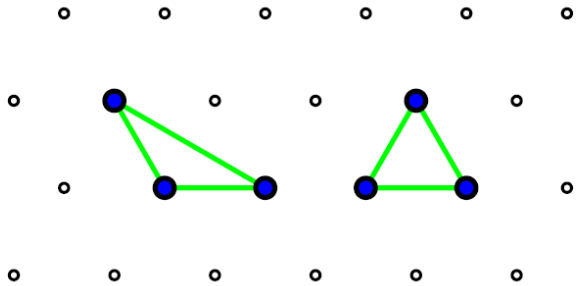

Figure 3.13: The two possible 3ToT compact configurations (with addition of all of the symmetry transformations of the triangular grid). Figure taken from [172].

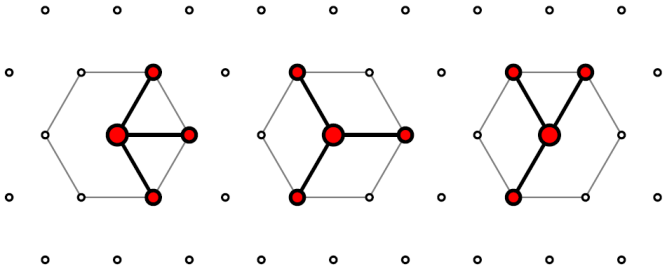

Figure 3.14: The three (minimal) 4C1 configurations (with addition of all of the symmetry transformations of the triangular grid). Figure taken from [172].

tanks with a T2 trigger each, i.e., the three stations are located in the first crown C_1, as shown in Fig. 3.14). This 4C1 trigger brings to $\sim$ 100% the efficiency for showers below 60°. For both modes, trigger times must be compatible with a plane shower front moving at the speed of light as a simple time compatibility criterion needed to avoid accidentally triggered stations.

- T5 level:

The T5 trigger is designed to select high-quality events ensuring a good reconstruction of the shower parameters. It rejects events with a deficient reconstruction due to showers inciding too close of the edge of the array, where a part of the shower is missed and the real core is located outside the array. One of its two modes, the 6T5 mode, requires the tank with the highest signal to be surrounded by at least 6 working stations, not necessarily triggered, at the time of triggering. This mode ensures ade-

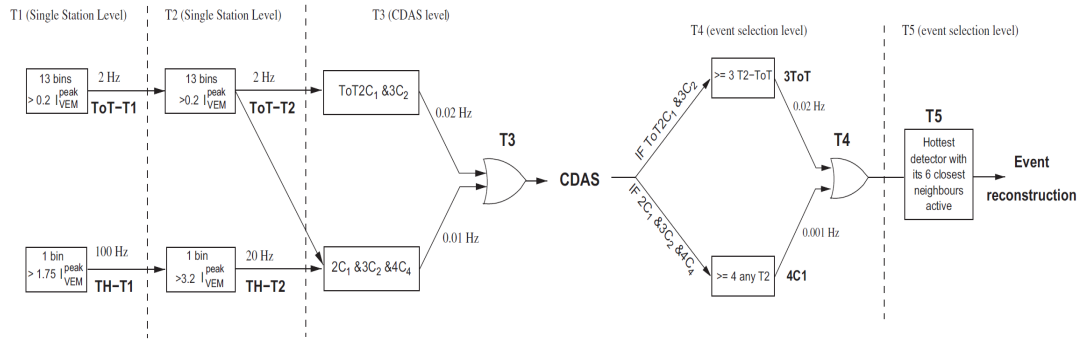

Figure 3.15: Schematics of the hierarchy of the trigger system of the Auger Surface Detector. Figure taken from [172].

quate containment of the event inside the array and allows a simple way to compute the detector acceptance counting active hexagons. To increase the statistics of selected events a different implementation, more permissive, which takes into account the non-working stations (about 1% of the tanks of the array is expected to malfunction at any time) is implemented. This mode, the so-called 5T5, requires the tank with the highest signal to be surrounded by at least 5 working stations among the 6 closest tanks.

The whole trigger chain of the SD, from T1 to T5, is summarized in Fig. 3.15.

3.3.3 SD event reconstruction

Once a T5 event has been identified, not all the triggered stations are considered for reconstruction. A first rejection is for events due to lightning, characterized by their oscillating signal: if the total signal in the station is lower than 1000 FADC counts and crosses the baseline more than 3 times, it is considered to be generated from a lightning, and thus that station is not taken into account. Additionally, the stations with the highest ID in the twin configurations (which are the last deployed tanks) are removed in order to keep the standard on-grid stations. Besides, lonely stations, defined as those stations with no neighbours within 1800 m or with only one within 5000 m, are rejected. A time constrain is also applied using an iterative reconstruction of the shower geometry and arrival time in order to check the compatibility between the start time of the signals with the one corresponding to a plane propagating at the speed of light. If the station delay, defined as the difference between the actual start time and the predicted one by the shower arrival time, is not between -1000 and 2000 ns,

it is considered as an accidental station and is then removed from the candidate list. Finally, events collected in time periods when there were CDAS software or hardware problems (usually referred to as "bad periods") are also rejected.

Thanks to the information recorded by SD tanks, it is possible to reconstruct properties of the primary cosmic ray such as the direction or the energy. Timing information from pulses in the surface detectors allows the reconstruction of the arrival direction of the shower and the front curvature. Besides, the signal size can be used to define a parameter which is related to the "size" of the shower at ground (the signal at a reference distance). With this estimator the reconstructed energy can be derived from parameterizations based on shower simulations as well as from calorimetric measurements using the FD. Moreover, mass composition can be studied using timing information of SD, as has been explained in the previous chapter.

- Geometrical reconstruction:

An EAS can be considered as a front of particles (determined by the arrival direction of the primary particle) propagating in straight line at the speed of light, c. In a first approximation, that front can be supposed to be a plane perpendicular to the shower axis $\hat{a}$, as represented in blue in Fig. 3.16. The axis direction can be obtained using an algorithm based on timing compatibility. With the plane front assumption, the expected time when the shower of particles passes through a specific tank located at $\vec{x_i}$, i.e., $t(\vec{x_i})$, can be obtained as:

$$c \cdot (t_0 - t(\vec{x_i})) = (\vec{x_i} - \vec{b}) \cdot \hat{a} \ , \tag{3.6}$$

where $\vec{b}$ is the signal-weighted barycentre of the triggered stations (a first estimation of the shower core position x_0) and t_0 is the arrival time of the estimated core position.

Assuming that the positions of the stations are known with absolute precision and the only deviations are due to statistical fluctuations in the start time σ_{t_i} [173], the shower plane can be obtained by minimizing the sum of squares of the time differences between the measured signal start time and the predicted one $t(\vec{x_i})$ given by the equation (4), i.e.,

$$\chi^2 = \sum_i \left[\frac{t_i - t(\vec{x_i})}{\sigma_{t_i}} \right]^2 = \sum_i \left[\frac{ct_i - ct_0 + \vec{x_i'}\vec{a}}{c\sigma_{t_i}} \right]^2 \ , \tag{3.7}$$

where $\vec{x_i'} = \vec{x_i} - \vec{b}$ and t_i is the signal start time of the station i. Decomposing vectors

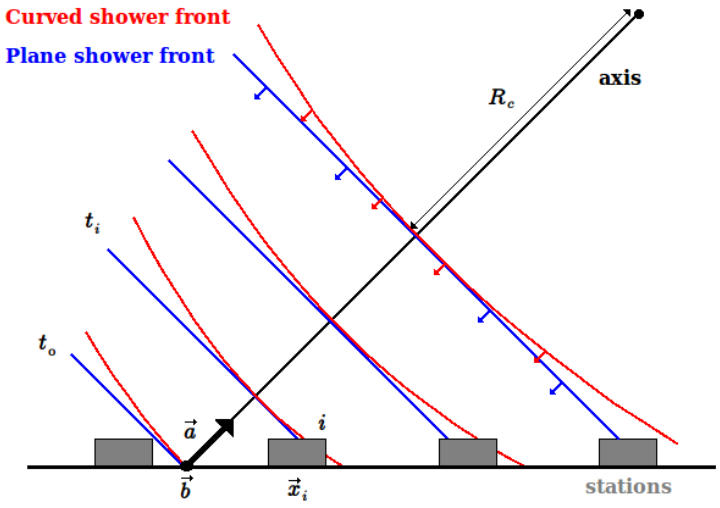

Figure 3.16: Shower geometry including parameters used in the SD reconstruction for a plane shower front (in blue) and a curved shower front (in red) propagating with the speed of light c.

in their coordinates $\vec{a} = (u, v, w)$ and $\vec{x_i'} = (x_i, y_i, z_i)$, χ^2 is given by:

$$\chi^2 = \sum_i \left[\frac{ct_i - ct_0 + x_i u + y_i v + z_i w}{c\sigma_{t_i}} \right]^2 . \tag{3.8}$$

However the axis implies a constraint due to its normalization:

$$\vec{a} \cdot \vec{a} = 1 \Rightarrow u^2 + v^2 + w^2 - 1 = 0 \Rightarrow w = \sqrt{1 - u^2 - v^2} . \tag{3.9}$$

This condition introduces a difficulty in solving the non-linear equation of χ^2. Nevertheless, an approximation can be performed: if all stations lay close to an horizontal plane, the z-component can be neglected and a linear solution for χ^2 can be obtained [172].

A more realistic approximation can be done considering a curved shower front with radius of curvature R_c (as shown in red in Fig. 3.16) propagating at the speed of light. For this hypothesis the expected arrival time $t(\vec{x_i})$ is expressed by:

$$c \cdot (t_0 - t(\vec{x_i})) = (\vec{x_i} - \vec{x_0}) \cdot \vec{a} + \frac{\rho_i^2}{2R_c} , \tag{3.10}$$

where $\rho_i = |\vec{a} \times (\vec{x_i} - \vec{b})|$ is the perpendicular distance to the axis. R_c can be obtained assuming that the propagation of the front is given by an expanded sphere centered at the position of the first interaction travelling at the speed of light[2]. With this assumption the equation, which will be used for the minimization procedure, is the following:

$$\chi^2 = \sum_i \left[\frac{c(t_i - t_{0,core}) - |R_c\vec{a} - \vec{x_i}|}{\sigma_{t_i}} \right]^2 . \tag{3.11}$$

In this case it is not necessary any further assumptions on the z_i values. Nonetheless, the curvature fit requires the position of the shower core, and therefore it is necessary to obtain it before the curvature shower front fit[3].

- The Lateral Distribution Function (LDF):

To obtain the primary energy of a cosmic ray it is necessary to know the number of particles reaching the surface array. This number of particles was estimated for the first time in the Volcano Ranch experiment integrating the signal over all distances using an empirical LDF. Afterwards, M. Hillas [174, 175], trying to avoid the large uncertainties in the energy estimation due to fluctuations in the shower development, proposed to use the signal at some reference distance from the core where the fluctuations of the particle density were smaller than those obtained in the total number of particles. This optimal distance depends on the spacing of the array [176].

For the Pierre Auger Observatory, the optimal distance is 1000 m [176]. At this distance the fluctuations on signal due to inaccuracies in the particular LDF selected are minimized (see Fig. 3.17). The expression of the LDF which predicts the dependence of the expected signal, S, as a function of r can be factorized as:

$$S(r) = S_{1000} \cdot f_{LDF}(r) , \tag{3.12}$$

where S_{1000} is the signal estimated at 1000 m from the shower core in VEM units and $f_{LDF}(r)$ is a shape function normalized as $f_{LDF}(1000) = 1$. Using stations at approximately the same distance to the shower core, the uncertainty of the signal σ_S has been parametrised as a function of the axis zenith angle θ as [177]:

$$\sigma_S(\theta) = f_S(\theta)\sqrt{S} = (0.32 + 0.42 \sec\theta)\sqrt{S} . \tag{3.13}$$

[2]This propagation does not need any assumption about the ground impact point [172].

[3]The shower core position is obtained from the Lateral Distribution Function (LDF) fit.

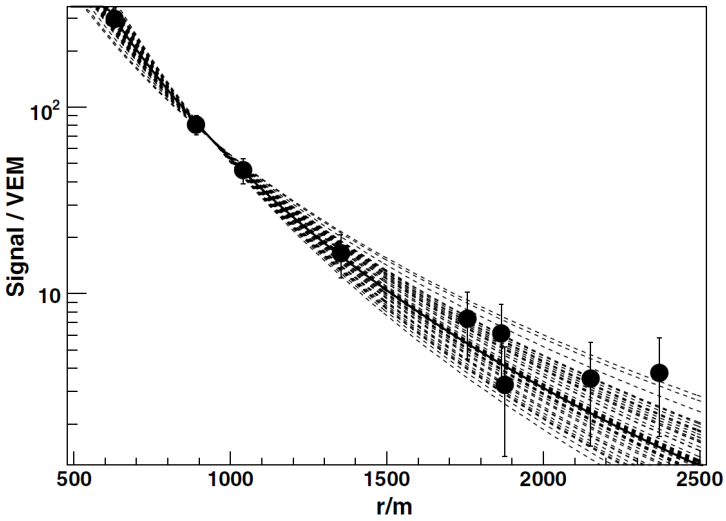

Figure 3.17: Station signals as a function of distance for a single simulated event (dots) and the reconstructed LDFs using 50 different values of β (dashed lines). Figure taken from [176].

Many different functional forms of the LDF have been studied, like a modified power law or a log-log parabola [172, 178, 179]. The Pierre Auger Observatory has adopted a slightly modified Nishimura Kamata Greisen (NKG) function, which has been demonstrated to be a good approximation [96, 94]:

$$f_{LDF}(r) = \left(\frac{r}{1000}\right)^{\beta} \cdot \left(\frac{r+700}{1700}\right)^{\beta+\gamma} . \tag{3.14}$$

The parameters β and γ that give the shape of the LDF and are related with the shower age [96, 94] are obtained through several iterative process as explained in [180, 181].

The final LDF is obtained with a fitting procedure implemented as a maximum likelihood method. The likelihood function is composed by four terms corresponding to the contribution of stations with low signal, high signal, saturated and zero-signal respectively:

$$L = \prod_i f_p(n_i, S(r)) \prod_i f_G(n_i, S(r)) \prod_i F_{sat}(n_i, S(r)) \prod_i F_{zero}(n_i, S(r)) , \tag{3.15}$$

where:

· n_i is the effective number of particles detected in the tank (muons, electrons and photons), estimated as $n_i = S \cdot p_S$, where S is the total signal (the sum of electromagnetic and muonic signals) and p_S depends on $f_S(\theta)$ (defined in equation (3.13)) as:

$$p_S = \begin{cases} f_S(\theta)^{-2} & \text{if } f_S(\theta) \geq 1 \\ 1 & \text{if } f_S(\theta) < 1 \end{cases}$$

· $S(r) = S_{1000} \cdot f_{LDF}(r)$.

· $f_{\mathrm{p}}(n_i, S(r)) = \frac{S(r)^{n_i} e^{-S(r)}}{n_i!}$ is the contribution for small signals assuming Poissonian distribution ($n < 30$ particles).

· $f_{\mathrm{G}}(n_i, S(r)) = \frac{1}{\sqrt{2\pi}\sigma_i} e^{-\frac{(n_i - S(r))^2}{2\sigma_i^2}}$ is the contribution for large signals assuming Gaussian distribution.

· $F_{\mathrm{sat}}(n_i, S(r)) = \int_{n_i}^{\infty} f_{\mathrm{G}}(n_i, S(r))\mathrm{d}n$ is the contribution for saturated signal [182, 183, 184], for which n_i represents a lower limit on the actual signal.

· $F_{\mathrm{zero}}(n_i, S(r))$ is the contribution for untriggered but active stations (i.e., stations without signal). It needs an assumption of $n_i > n_{\mathrm{thr}} \equiv 3$ which gives the expression $F_{\mathrm{zero}}(n_{\mathrm{thr}}, S(r)) = P(S < S_{\mathrm{thr}}) = \int_0^{S_{\mathrm{thr}}} f_p(n_i, S(r))\mathrm{d}S$.

From this maximization process the parameters of the LDF can be obtained, including accurate values of $S(1000)$, which is used to calculate the energy. An example of a reconstructed shower with its LDF is shown in Fig. 3.18.

- Energy reconstruction:

The hybrid nature of the Pierre Auger Observatory is extremely useful for an accurate measurement of the primary cosmic rays. As already explained, the FD is able to measure the total energy of the shower in a nearly model-independent way. Unfortunately the subsample of events recorded by the FD is very small due to their limited duty cycle. The SD provides a large statistics, however, any attempt to measure the primary energy with the only information of this detector is strongly dependent on the model assumed for the evolution of the shower. The strategy of the Pierre Auger

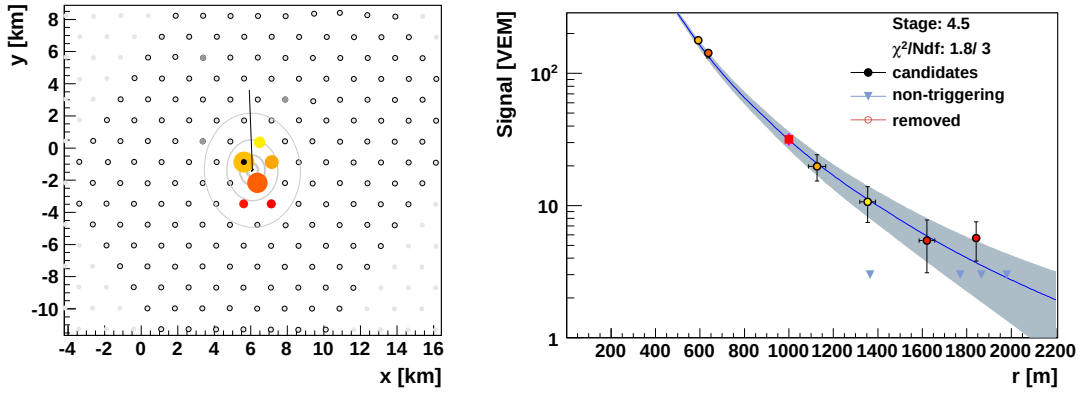

Figure 3.18: Left panel: footprint of an SD event (event #14165753) with an energy of $7.16 \cdot 10^{18}$ and $\theta = 42.4°$. Right panel: LDF of the reconstructed event, i.e., the signal of the six triggered stations represented as a function of the core distance. The $S(1000)$ value is also represented.

collaboration, recently also followed by the TA collaboration, is to calibrate the SD detector using the energy information of the so-called hybrid events, that is, those events simultaneously registered by both detectors with enough information to reconstruct accurately their parameters.

As already mentioned, for a given zenith angle, $S(1000)$ is correlated with energy [185]. In the first place $S(1000)$ has to be transformed into the angle independent parameter $S_{38°}$, defined as the $S(1000)$ signal that would be measured if the EAS arrives from a zenith angle of 38°. To this end, the Constant Intensity Cut (CIC) method [186] is used, that is:

$$S_{38°} = \frac{S(1000)}{CIC(\theta)} \,, \tag{3.16}$$

where $CIC(\theta)$ is the corresponding attenuation curve following the parametrization:

$$CIC(\theta) = 1 + a(\cos^2\theta - \cos^2 38°) + b(\cos^2\theta - \cos^2 38°)^2 \,, \tag{3.17}$$

with a and b being fitted parameters.

Then this $S_{38°}$ parameter is compared with the corresponding total energy as measured by the FD (see Fig. 3.19). For the 750 m spacing infill array (explained in the following section 3.4.1) the same procedure is applied but using the $S_{35°}$ parameter (that is normalized to 35°) [187]. For very inclined events, the N_{19} parameter, de-

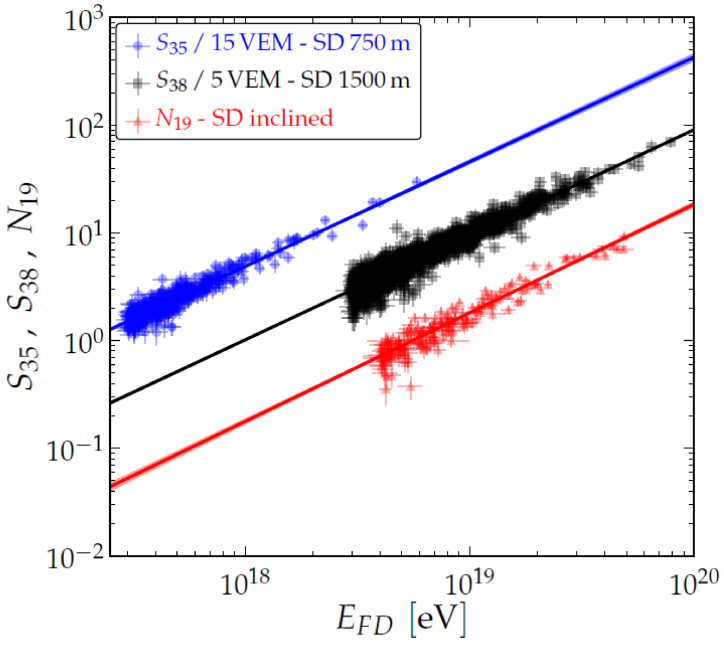

Figure 3.19: The correlation between the different energy estimators S_{38°, S_{35° and N_{19} and the energy determined by FD. Figure taken from [187].

fined as the muon content relative to simulated proton showers with an energy of 10^{19} eV [188] is used for this purpose. As can be observed in Fig. 3.19, the SD parameters (i.e., S_{38°, S_{35° and N_{19}) are strongly correlated with the calorimetric energy of the FD following the power law $E_{FD} = A \cdot S_{SD}^{B}$. Using a hybrid data sample composed by 1475 events with energies larger than $3 \times 10^{18} eV$ and θ values up to 60° collected between 1$^{\text{st}}$ January 2004 and 31$^{\text{th}}$ December 2012, the A and B parameters for the S_{38° (which is the most interesting one for this work) are $A = (0.190 \pm 0.005) \times 10^{18} eV$ and $B = 1.025 \pm 0.007$ with a correlation coefficient of 0.98 [189].

It is important to note that the FD uncertainties correlated between different showers should be propagated to the SD energy scale by shifting all FD energies coherently by their uncertainties. This means that the correlated uncertainties propagate entirely to the SD energies. The value of the total systematic uncertainty of the energy scale has been reduced in the last update from 22% [190] to 14% [189]. In table 3.1 all the contributions to this systematic uncertainty are summarized. The largest contributions to this 14% value are due to the calibration and profile reconstruction of the FD, followed by those from the atmosphere. The contribution of the absolute fluorescence

Systematic uncertainties on the energy scale	
Fluorescence yield	3.6%
Atmosphere	3.4% - 6.2%
FD calibration	9.9%
FD profile rec	6.5% - 5.6%
Invisible energy	3% - 1.5%
Stat. error of the SD calib. fit	0.7% - 1.8%
Stability of the energy scale	5%
Total	**14%**

Table 3.1: Systematic uncertainties on the energy scale. Table taken from [189].

yield, which was the largest one to the previous uncertainty of the energy scale (14% of the total 22%), has been reduced significantly down to an average value of 3.4%, which is the dominant component of the total uncertainty of 3.6% in the fluorescence yield (including the dependence on atmospheric parameters). The statistical errors of the SD calibration fit explained above represent the less important contribution to the total systematic uncertainty. More details of each individual contribution can be found in [189, 149].

3.4 Other instruments

To achieve a better understanding of astrophysical models of the origin of UHECRs it is mandatory to analyse their composition along the transition region, which starts at an energy of about 10^{17} eV (in the region of the second knee). Thus, it is necessary to lower the energy threshold of the Observatory. With this aim upgrades for both the SD and FD detectors have been developed. In addition, a very rich program of R+D is being developed to search for new techniques for the detection of UHECRs.

3.4.1 AMIGA

The Auger Muon and Infill for the Ground Array (AMIGA) is an extension of the Surface Detector of the Pierre Auger Observatory located in the regular SD array near the Coihueco site and covering 23.5 km^2. It consists of an array of 85 water Cherenkov tanks (the same tanks as the standard array) forming two grids: an array of 61 stations on a 750 m grid (the so-called infill) and another array of 24 stations on a 433 m grid,

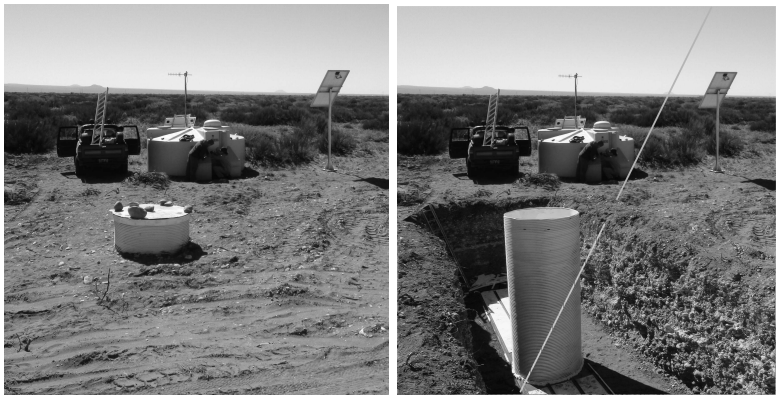

Figure 3.20: Left panel: SD infill station with its associated muon counter already buried. Right panel: photo-montage representing the detector concept: any muon with energy $\geq$ 1 GeV propagates through the soil and is capable of reaching the buried scintillator. Figures adapted from [193].

both with buried muon counters. As was explained in the previous chapter (see 2.7.2), the muon content at ground level carries mass composition information. The number of muons as a function of the distance to the shower axis (the muon LDF) is the main observable of AMIGA. The combination of the buried location of the scintillators and their strong shields suppresses the electromagnetic component, allowing the counting of muons with energies above 1 GeV; a photograph of these buried scintillators and the concept of AMIGA muon detection is shown in Fig. 3.20. AMIGA was designed to measure the mass composition, energy and arrival direction of cosmic rays from energies around $10^{17.5}$ eV with the 750 m distance grid and to below 10^{17} eV with the 433 m distance grid, and thanks to the near location of HEAT (see 3.4.2) low energy hybrid measurements can be obtained [191]. At present, only 14 fully operational scintillator modules buried at 2.3 m depth in a prototype hexagon grid (the so-called unitary cell, represented in Fig. 3.21) are taking data and have validated the detection technique and physics analysis [192].

3.4.2 HEAT

As cosmic rays with low energy have a shower maximum higher in the atmosphere, only tilted telescopes are able to observe the shower maximum depth. With this purpose the High Elevation Auger Telescope (HEAT) was built. It consists of three tilting fluorescence telescopes located near Coihueco, working similarly to the FD telescopes

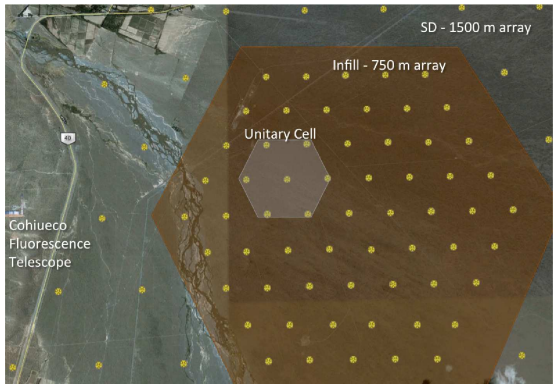

Figure 3.21: Map of the AMIGA array with brown background. The engineering array positions, where muon counters are already deployed, can be seen highlighted in gray (the unitary cell). Figure taken from [191].

but with an extended field of view (from 30° to 60° in elevation instead of from 1.5° to 30° of the standard fluorescence telescopes of the FD), lowering the energy threshold down to 10^{17} eV [194].

HEAT is taking data since May 2010 [195]. Its distance from Coihueco (only 170 m of distance between them) allows a high amount of showers to trigger both detectors. Operating on the default tilted mode (as shown in left panel of Fig. 3.22) makes both detectors to view different parts of the atmosphere, giving the possibility of studying different and complementary parts of the same shower. As an example, in the right panel of Fig. 3.22, the position of the shower maximum is registered by HEAT telescopes staying out of the Coihueco's field of view.

3.4.3 AERA

Particles of EASs emit radio pulses as they develop in the atmosphere. Broadband radio pulses from air showers are coherent in the VHF band (10-100 MHz) and thus have a signal power which scales with the square of the cosmic ray primary energy. The pulse characteristics can be used to probe the electromagnetic shower development and primary particle composition [197, 198, 199].

Recent experiments such as LOPES [200] and CODALEMA [201] have employed antennas triggered by particle detectors to demonstrate the detection technique and verify the dominant emission mechanism: the acceleration of shower particles in the Earth's magnetic field. The Auger Engineering Radio Array (AERA) of the Pierre Auger Observatory is expected to corroborate the feasibility of a large scale radio

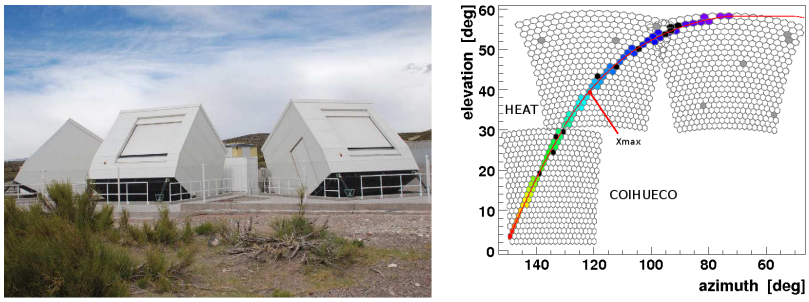

Figure 3.22: Left panel: photograph of HEAT in tilted mode with closed shutters. Figure taken from [196]. Right panel: event 9612495, an example of a low-energy event recorded in coincidence with Coihueco and two HEAT telescopes; camera image of the recorded signal with the arrival time of the light colour-coded (blue early, late red) and the $X_{\max}$ value as a red dot.

array for the detection of cosmic rays [202]. Located in the area of the infill array, AERA project consists of 160 self-triggered radio-detector stations covering an area of 20 km^2 and measuring the radio emission of secondary particles in air showers in the frequency range from 30 to 80 MHz (inside the VHF band), observing the longitudinal development of the shower with a 100% duty cycle.

Its first phase, called AERA24, started to operate on April 2011. It consisted of 24 logarithmic periodic dipole antennae (LPDAs) separated by 125 m and covering an area of 0.5 km^2. At present, AERA, still in development, is taking data with 124 detector stations in a stable configuration; one of these radio station is shown in Fig. 3.23.

Its location near AMIGA array will provide to the Pierre Auger Observatory with super-hybrid measurements using four independent detection techniques: fluorescence telescopes, water-Cherenkov detectors, muon counters and radio antennae. With an expected rate of radio events from UHECRs primaries of 5000 events per year, AERA will record several thousands of cosmic rays showers in the range of 10^{17} to 10^{19} eV. An example of an AERA event is shown in the right panel of Fig. 3.23.

3.4.4 Microwave detection

Radio emission in the microwave band is another alternative technique for the detection of UHECRs. The emission mechanism (the Molecular Bremsstrahlung Radiation or MBR [204]) produces unpolarized and isotropic signal which, together with the transparency of the atmosphere at these frequencies, allows the measurement of the

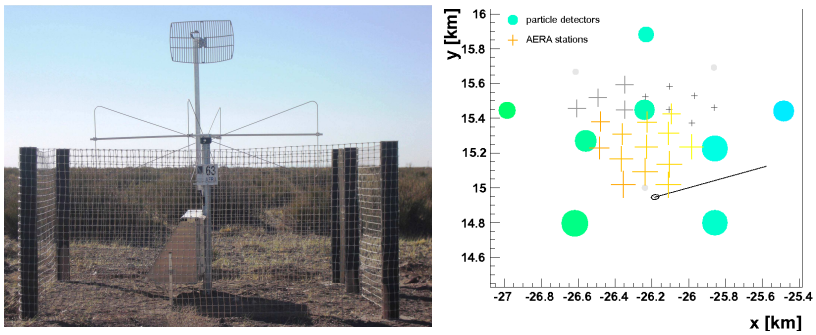

Figure 3.23: Left panel: radio station of AERA with a communication antenna for wireless data transfer, two butterfly antennas for the radio measurements (one aligned East-West and one North-South), a metal box for electronics, a solar panel and a battery for power supply, and a fence protecting against cattle; more details of the antennae set can be found in [203]. Right panel: footprint of measured AERA event triggered by the Auger surface detector; each coloured cross represents an AERA station with data, and the size of the bars represents the amplitude of the radio signal in the North-South and East-West polarization and the colour code the arrival time; the circles are the Auger surface detectors in the area of AERA24 where the line indicates the arrival direction and the core of the shower determined with the surface array. Figures taken from [202].

shower longitudinal profile with a duty cycle of detection close to 100% using relatively cheap equipment. In the Pierre Auger Observatory three detectors in the GHz band have been installed: MIDAS, AMBER and EASIER; all these instruments, which are being developed nowadays, use horn antennas as receivers, in C-band (3.4 - 4.2 GHz) and Ku-band (10.95 - 14.5 GHz) for AMBER, and only C-band for MIDAS and EASIER [123].

- AMBER:

The Air-shower Microwave Bremsstrahlung Experimental Radiometer (AMBER) is a radio telescope located in the Coihueco FD site (pointing in direction of the SD infill array) consisting of a 2.4 m low-emissivity off-axis parabolic dish and a 16 pixels camera imaging a section of 14° x 14° of the sky at 30° elevation angle (a picture is shown in the left panel of Fig. 3.24). AMBER's trigger system is a modified version of the T3 SD trigger, that reconstructs geometrically the SD event and gives the time at which the shower crossed its field of view. The reconstruction requires a precise synchronization between the timing of Auger and AMBER detectors. At present, AMBER has taken

Figure 3.24: Left panel: AMBER detector at the Coihueco FD site. Middle panel: MIDAS detector installed at the Pierre Auger Observatory next to Los Leones FD building. Right panel: EASIER detector installed at the SD. Figures taken from [123].

more than 18 months of data, but the analysis is still in progress. In the future the camera will be modified in order to increase the sensitivity by 40% lowering the noise temperature of the electronics and by increasing the efficiency of the focal surface, and the field of view will be extended to 17°.

- MIDAS:

The MIcrowave Detection of Air Showers (MIDAS) is a radio telescope installed next to the FD building Los Leones instrumented with a 5 m^2 parabolic dish and a camera of 53 pixels at its focal plane covering approximately 1.3° x 1.3° of the sky (as illustrated in the middle panel of Fig. 3.24). The main difference between AMBER and MIDAS is the trigger system: AMBER depends on the SD trigger while MIDAS incorporates its own two level-triggering system to identify incoming cosmic rays. MIDAS is taking data since the beginning of 2013.

- EASIER:

The Extensive Air Shower Identification with Electron Radiometer (EASIER) is a radio detector array located near the FD building Los Leones formed by antennae mounted on the tanks of the SD (as shown in the right panel of Fig. 3.24). The trigger system is dependent on the SD: when an EAS triggers the SD, the radio trace is automatically recorded alongside the SD data. EASIER began in April 2011 as a prototype with 7 SD tanks and was extended by 54 detectors in April 2012; at present, EASIER is an array formed by 61 detectors with 33 antennae oriented with a North-South polarization and the other 28 ones with East-West polarization, of which calibration is still in progress.

Taking data since 2011, only three radio signals in coincidence with EASs detected by the SD have been recorded; the first of these three GHz signals, measured in June 2011 in coincidence with a SD event corresponding to an energy of 13.2 EeV (event 12046376), was the first microwave detection of an EAS: the maximum of the signal was found to be more than 11 times larger than the noise fluctuations and occurred just one time bin (25 ns) before the signal in the water Cherenkov detector.

With the three microwave extensions of the Pierre Auger Observatory in the phase of stable data taking, only three unequivocal signals were detected. The ongoing analysis, the future upgrades and the further studies focused on the search for a fainter but longer signal (and also from more distant air showers) will help to a better understanding of the observed emissions. More technical information about these three detectors can be found in [205].

Chapter 4

Properties of the azimuthal asymmetry of SD signals

4.1 Introduction

While for vertical showers there is a circular symmetry around the axis of the signals recorded at ground, in inclined ones this symmetry is broken due to the differences in the path travelled by particles as they reach the SD tanks. This fact does not only generate an asymmetry in the total integrated signal but also implies an azimuthal asymmetry in the time structure of the traces. On the one hand this asymmetry has to be taken into account in many studies that use the SD traces of individual events, but on the other hand, it contains very valuable information about the development of the shower that can be useful for the determination of the mass composition of the cosmic rays, as it has been pointed out in [206, 207].

In this chapter the azimuthal symmetry of the SD signals and its correlation with the mass of the primary cosmic rays will be studied in detail with the assistance of Monte Carlo simulations. Firstly, in section 4.2 the asymmetry in both the signal intensity and time structure is described, and the different sources of the asymmetry and its dependence on the zenith angle and the core distance are studied. In this section the effect of the asymmetry on the core reconstruction will also be studied. In section 4.3 the risetime parameter and its asymmetry correction are described. In section 4.4 the library of Monte Carlo simulated showers used for this analysis as well as all the necessary quality cuts are described. In section 4.5 the analysis of the azimuthal asymmetry in the time structure is performed, allowing the definition of a parameter sensitive to the mass composition. In section 4.6 all the steps of the asymmetry analysis

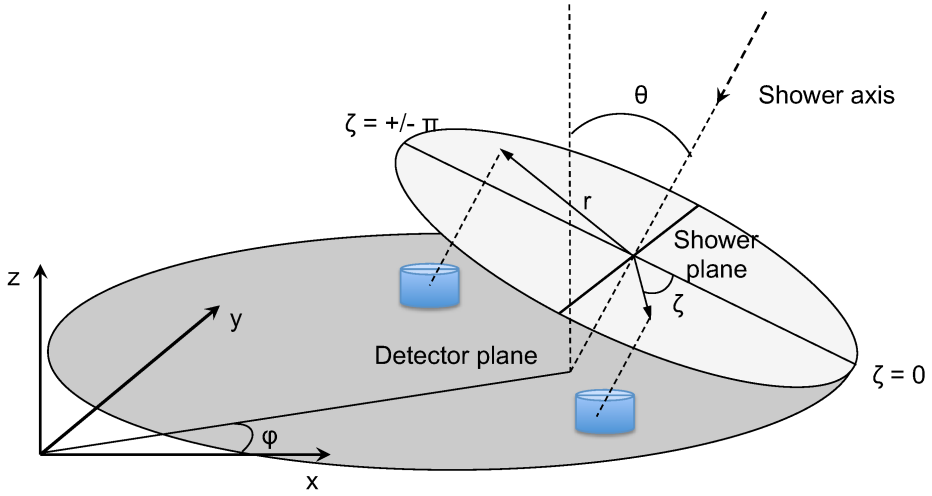

Figure 4.1: Schematic view of the shower geometry. The incoming direction of the primary particle defines two regions, "early" ($-\pi/2 < \zeta < \pi/2$) and "late" region ($\zeta > \pi/2$ or $\zeta < -\pi/2$). Note the different amount of atmosphere traversed by the particles reaching the detectors in each region.

required to get mass composition information of UHECRs are revisited and updated with respect to previous analyses [206, 207] using simulated shower samples. Finally, in section 4.7 the correlation between the mass sensitive parameter of the asymmetry analysis and the X_{max} observable is studied.

4.2 Asymmetry in EASs

Apart from statistical fluctuations, the properties of an extensive air shower at a given slant depth only depend on the distance to the shower axis, and therefore the footprint of a shower in a plane perpendicular to the axis has circular symmetry. For vertical showers the ground plane is perpendicular to the axis and consequently the signals in a surface array keep this circular symmetry. The footprint of inclined showers at ground level is an ellipse that, when projected on the shower plane, loses their circular symmetry. This is mainly due to the fact that the particles traverse different atmospheric depths depending on the azimuthal angle [208, 206], as illustrated in Fig. 4.1. The region with those detectors that are struck first as the shower propagates over the array, corresponding to $-\pi/2 < \zeta < \pi/2$, is the so-called "early" region, while the opposite one with detectors located at $\zeta > \pi/2$ or $\zeta < -\pi/2$ is the "late" region.

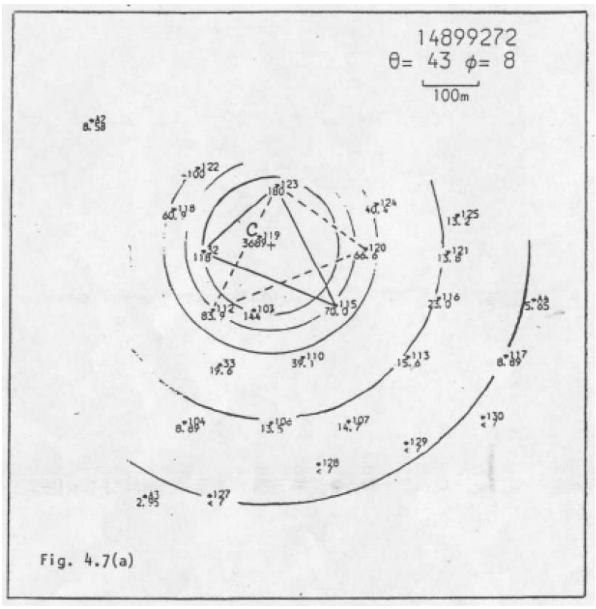

Figure 4.2: Data in the shower plane corresponding to the Event#14899272 collected by the Haverah Park array. The position of the axis is represented with a cross, and the corresponding detectors at the same distance to the axis are also shown. Figure taken from [209].

K. Greisen [97] was the first to point out that the attenuation of shower particles in the atmosphere would lead to a loss of circular symmetry in the signals intensities recorded by a detector at a single atmospheric depth. Experimental evidences of azimuthal asymmetry in the signal size were obtained by C.D. England [209] using data from the Haverah Park array, when detectors at the same distance to the shower core measured different density of particles. As an example, in Fig. 4.2 an inclined shower detected by the Haverah Park Array with a reconstructed energy of 3×10^{18} eV and $\theta = 43°$ is shown, representing the position of the axis with a cross. In this example a difference in the density of particles recorded by detectors located at the same distance to the core is observed.

On April 2002, an early examination of the FADC signals of the event #184599 recorded with the detectors of the Engineering Array of the Pierre Auger Observatory[1] led to the realization of an asymmetry not only in the size but also in the time distribution of the signals. The analysis of this event (detailed in [210]) showed that the

[1]The Engineering Array was a prototype of the Pierre Auger Observatory consisting of 32 surface detectors and 2 fluorescence telescopes created to validate the elements of the Observatory [22].

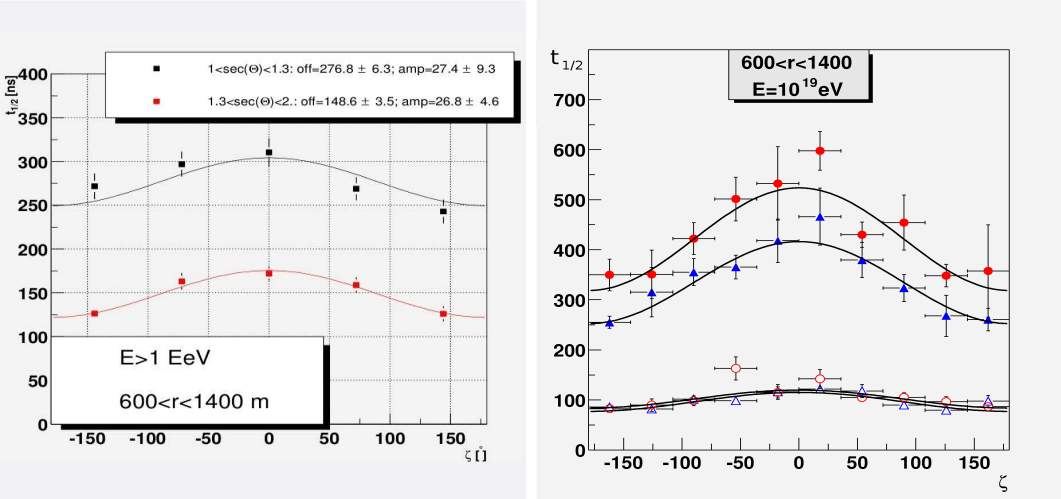

Figure 4.3: Left panel: risetime as a function of ζ in two bins of θ for events with energy above 1 EeV collected by the EA. Right panel: risetime as a function of ζ for $\theta = 35°$ (filled symbols) and $\theta = 60°$ (open symbols) using MC simulations with the hadronic model QGSJET01 for proton (red dots) and iron (blue dots) primaries. Figures taken from [211].

traces of the signals had different behaviour depending on their azimuthal angle: the late stations had shorter risetimes than the early ones. These features can be observed in more detail when using the information from a set of events within a given energy and zenith angle intervals. As an example, in Fig. 4.3, the risetime versus ζ of a sample of events is represented for two intervals of $\sec\theta$ (left panel). For comparison, in the right panel it is shown the equivalent plot as predicted by MC simulations. As can be observed the behaviour of proton showers (red dots) is different from that of iron ones (blue dots) suggesting the possibility of using the asymmetry in the time distribution as a tool for primary mass separation [211].

To understand the time asymmetry of the signals of a surface array it is necessary to know the behaviour of the various components of the EASs as a function of the incidence angle and the distance to the shower axis. For a vertical shower of 10 EeV, a signal of ~ 50 VEM is recorded at 1000 m from the shower axis. About 50% of the total signal is due to muons sufficiently energetic to traverse the detector without stopping. Electrons and photons are a factor of 10 and 100 more numerous than muons, respectively. They contribute with the other 50% of the total signal and, as their average energy is of ~ 10 MeV [212], are largely absorbed in the 3.2 radiation lengths of water inside the surface

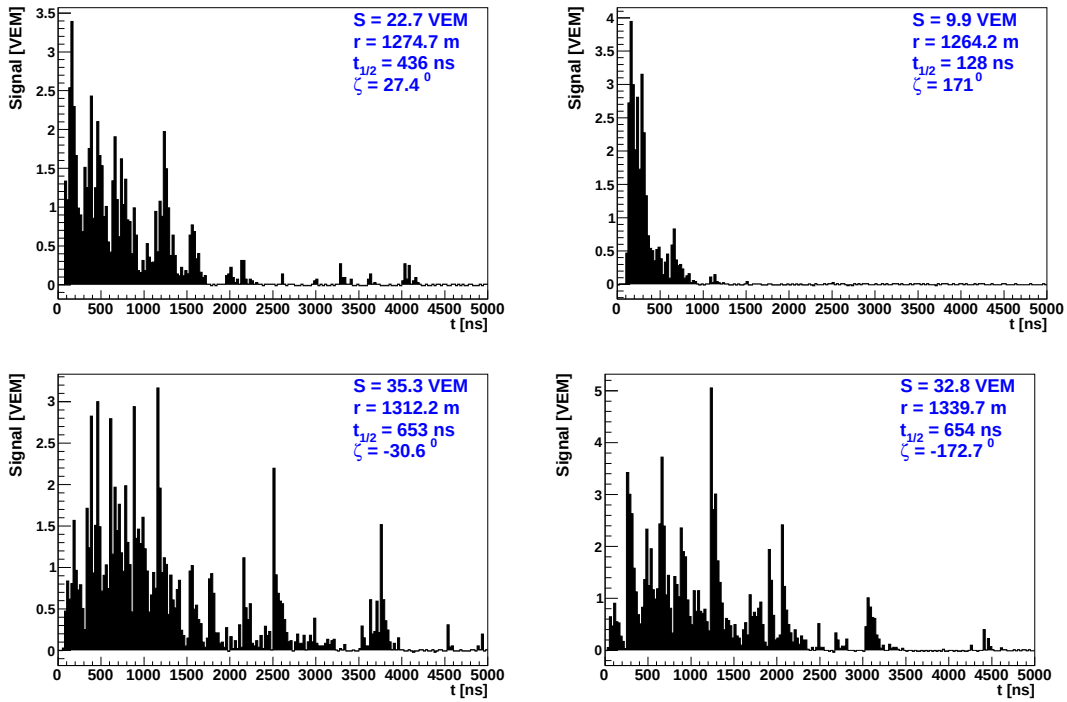

Figure 4.4: Top: signals for an event of 7.7 EeV and 52° in zenith. Bottom: signals for an event of 16.9 EeV and 15.7° in zenith. Left panels correspond to early stations while right panels correspond to late stations.

station.

In top panels of Fig. 4.4 the FADC signals from an inclined shower with an energy of 7.7 EeV and a zenith angle of 52°, recorded by the SD of the Pierre Auger Observatory, in early and late detectors are shown. Although both detectors are at approximately the same distance from the shower core (∼1300 m) the FADC signals are dramatically different in time-spread and in overall signal sizes. For comparison, at the bottom of the same figure, signals from a near vertical shower are also shown. In this case, the expected symmetry is evident.

To illustrate the contributions of the electromagnetic and muonic components to the total signal, simulated traces collected by the PMTs from different stations measuring the same event will be compared. The footprint of the selected event for this example is represented on top panel of Fig. 4.5. In this figure, the colour of the station represents the time of arrival: yellow corresponds to the first triggered tanks (early stations) and red represents the last triggered tanks (late stations). The event corresponds to a shower

initiated by an iron nuclei of $\log(E/\text{eV}) = 20.2$ and $\theta = 36.7°$ that has been simulated with the CORSIKA[2] code using the EPOS-LHC model for the hadronic interactions (see section 4.4 for more details). The traces of three chosen stations (which are marked with black dots in the footprint of the event) are shown on the bottom panels: left panel corresponds to a station in the early region, the central panel corresponds to a station with $\zeta \sim \pi/2$, and the right panel corresponds to a station in the late region. As can be seen, traces are more attenuated as the shower goes from early to late region. To illustrate the differences in the attenuation of the muonic and the electromagnetic component, their contributions to the total signal are shown in Fig. 4.6. Total traces (as shown in the bottom panels of Fig. 4.5) are displayed in the left panels of Fig. 4.5, while the contribution of the muonic component and the electromagnetic one ($e^{\pm}$ and photons) are shown on central and right panels, respectively. The station on the early region is represented in the upper plots, the station at $\zeta \sim \pi/2$ in the central plots, and the station on the late region in the lower panels. As can be observed, the early station has a total signal composed by the fast peak of the muonic component and the electromagnetic component more spread over time. On the other hand, the late station has basically the same muonic contribution (as has been explained before, the muonic component is less affected by attenuation) while the electromagnetic one has been attenuated, showing a smaller contribution to the total signal. This early-late asymmetry observed in the traces is the base of the asymmetry analysis developed in this thesis.

4.2.1 Main sources of asymmetry

The above mentioned asymmetry of the recorded signals is due to the combination of geometrical effects, related to the incidence angles of the particles on the detectors, and of the longitudinal evolution of the shower. Both sources of asymmetry are briefly explained in the following.

The geometrical contribution can be understood from Fig. 4.7: particles reaching the early region will be seen in the detection plane more vertical than the ones in the late region, leading to non-symmetric patterns on the ground that, when projected into the shower plane, give rise to eccentric circumferences [214]. Since the flux received in the early tanks is more vertical than that in the late ones, particles entering the top of the tank deposit larger signals in an early tank than in a late one, while particles entering the side of the tank lead to larger signals in a late tank than in a early one.

[2]COsmic Ray SImulations for KAscade, a physics computer software for simulation of EASs induced by high-energy cosmic rays [213]

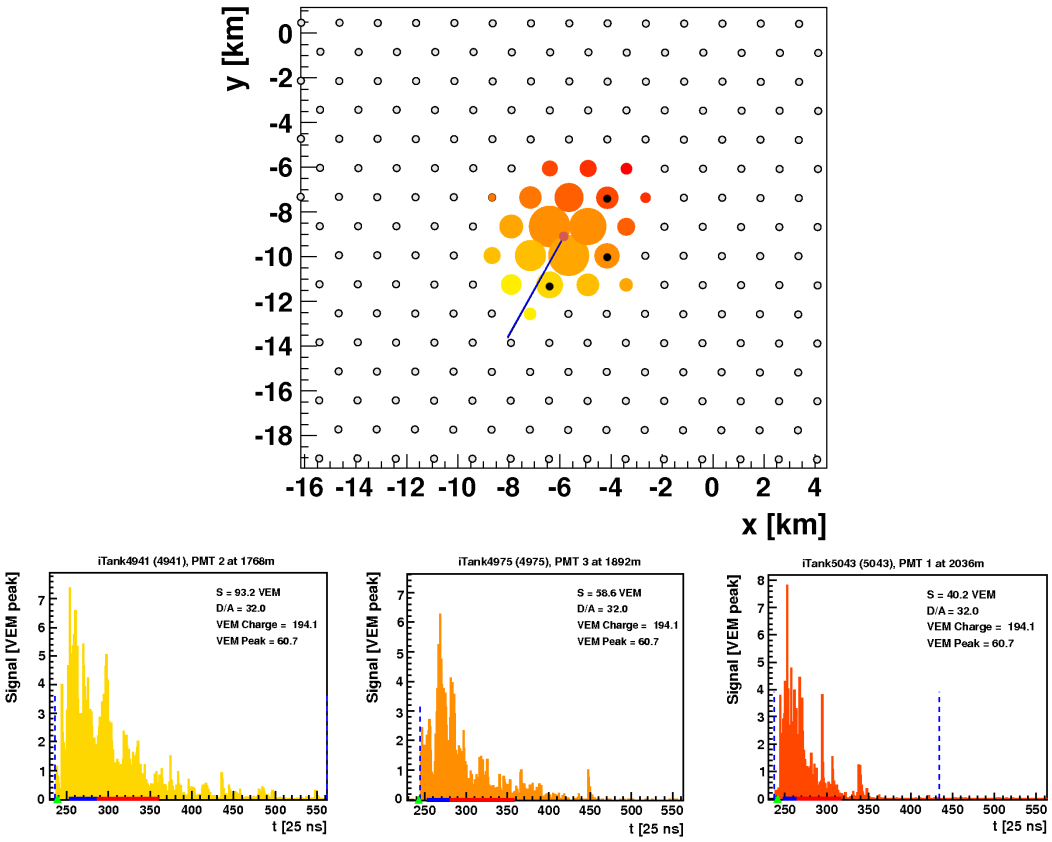

Figure 4.5: Top: footprint of an event (top panel). The straight line represents the incoming direction of the cosmic ray, the size of the triggered stations is proportional to the amount of signal registered by each tank, and the colour makes reference to the time of arrival: the yellow stations are the first triggered (early stations) and the red ones are the last triggered (late stations). Bottom: the traces of three selected stations on different locations, corresponding to the early region (left panel), the region with $\zeta \sim \pi/2$ (central panel) and the late region (right panel). The blue vertical dashed line marks the beginning and the end of the trace.

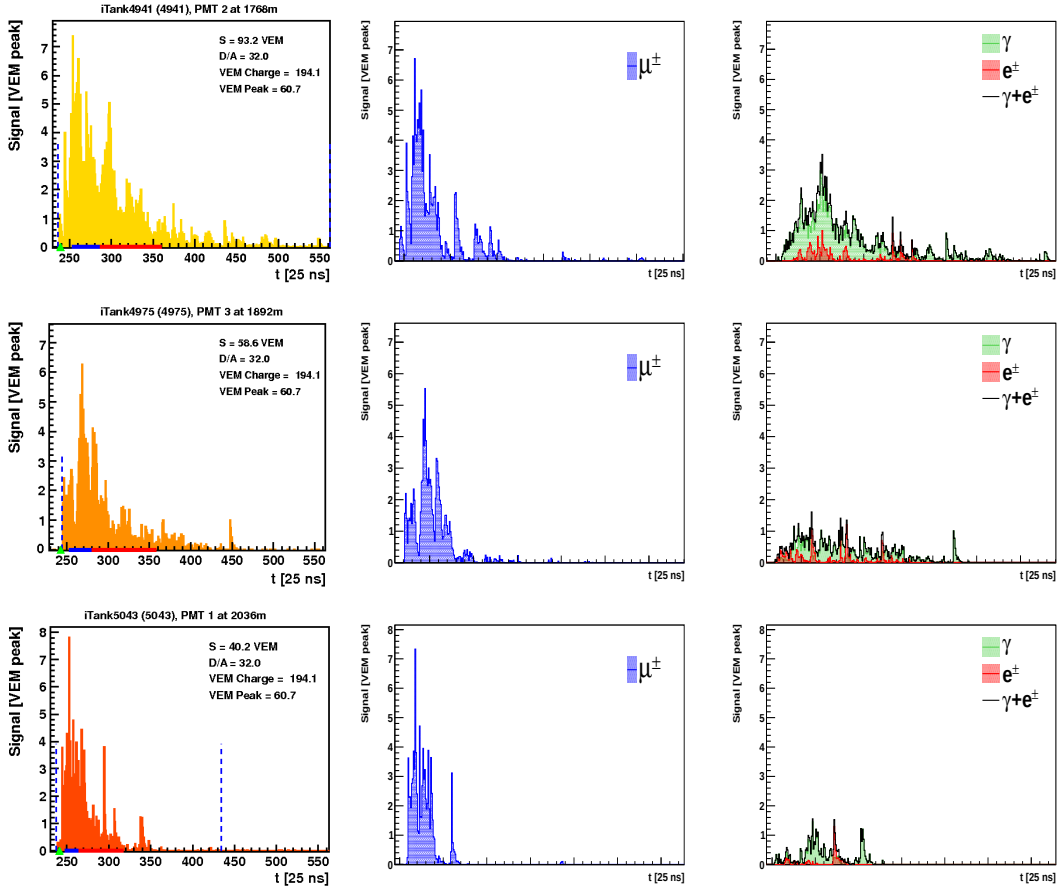

Figure 4.6: Traces of the stations selected in Fig. 4.5. The total reconstructed signal is shown on left panels, and the generated contribution of the muonic component and the electromagnetic one (composed by $e^{\pm}$ and photons) are shown on central and right panels, respectively. Upper panels correspond to the station on the early region, middler plots correspond to the station at $\zeta = \pi/2$, and lower panels correspond to the station on the late region.

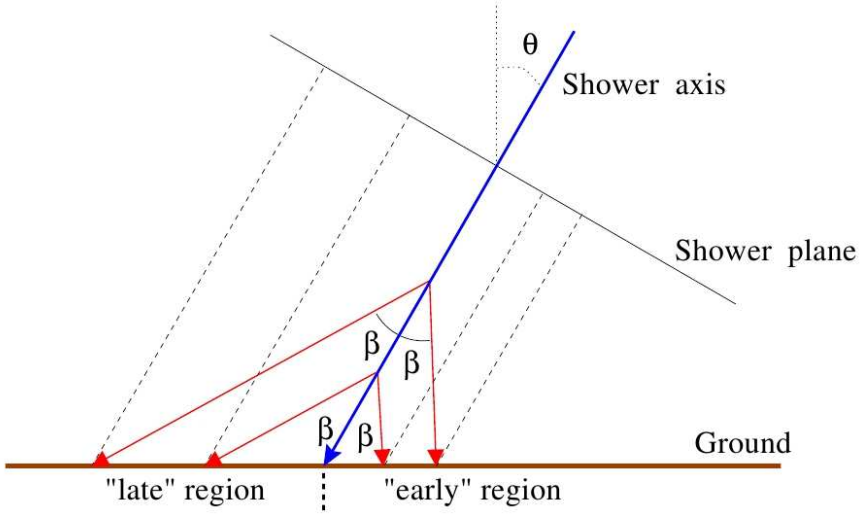

Figure 4.7: Particles going away from the shower axis with symmetric angles β; when projecting the ground densities on the shower plane, a purely geometric asymmetry appears. Figures taken from [214].

In [215] the contribution due to the geometrical effect of the total observed asymmetry in signals measured with the surface detectors of the Pierre Auger Observatory was analysed, leading to the conclusion that the geometrical effect dominates the observed asymmetry for zenith angles $\theta < 30°$.

The contribution of the longitudinal evolution of the shower consists mainly in the attenuation of the electromagnetic component of the shower as it crosses more atmosphere to reach late detectors [208], as has been previously shown (Fig. 4.6). The difference in path travelled by the particles is illustrated in Fig. 4.8. As can be observed, particles reaching a late station correspond to a portion of the shower older (i.e., larger stage of development) than those reaching the early stations. As a consequence, late tanks will measure a weaker signal than early ones because its electromagnetic component is more attenuated. This contribution is the main source of asymmetry for inclined showers with zenith angles $\theta > 30°$.

The observed asymmetry also includes an effect due to muons. On the one hand, as the Cherenkov light deposited by muons depends on their path in water, and they usually have enough energy to go through the tank, the signal produced by muons entering the side of the tank is larger than the one produced if they enter the top of the tank. This fact compensates the geometrical effect, so there is no geometrical

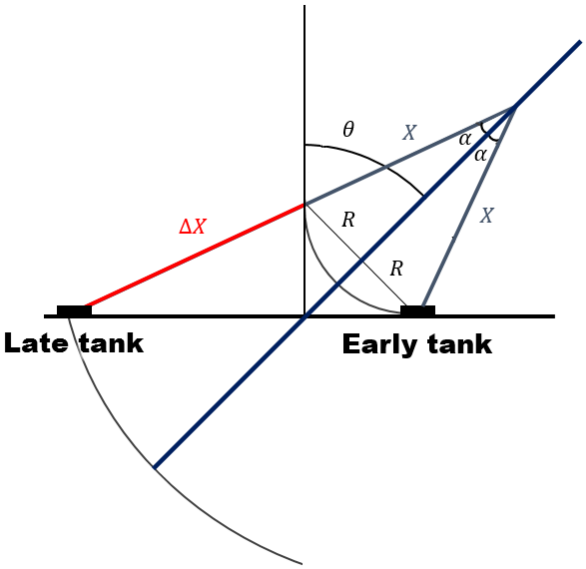

Figure 4.8: Difference in the path length ΔX travelled by particles at ground reaching a late and an early station, both at the same distance R from the shower axis measured at the shower plane and with the same angle α from the shower axis.)

asymmetry for muons. However, on the other hand, the solid angles into which muons are injected at the height of production are not uniformly populated, with the later detectors "seeing" more muons emitted closer to the shower axis than the early ones at the same distance to the core. Note that a shower generated by a heavy primary contains, on average, more muons and have a smaller electromagnetic component at the observation level than a shower created by a light nucleus.

A more detailed study of the sources of the asymmetry can be found in [207] and in references therein.

4.2.2 Asymmetry dependence on core distance and zenith angle

The asymmetry in both the signal intensity and the time structure is expected to show a dependence on the core position r because for measurements close to the shower axis, the path difference between late and early detectors is smaller compared to that for large core distances. Additionally, the time asymmetry must also depend on the zenith angle θ, as it is illustrated in Fig. 4.9. This dependence with θ can be described as follows: no asymmetry is expected for vertical showers (case a, left panel) but it appears

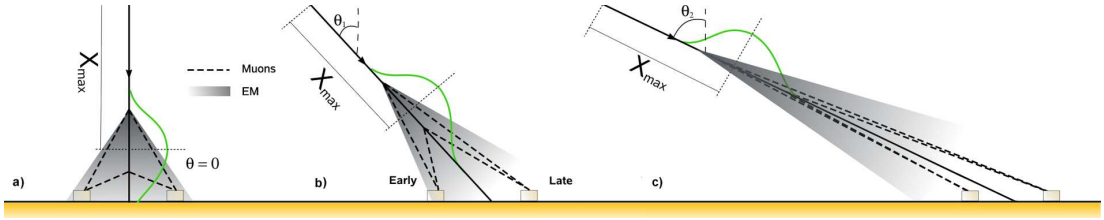

Figure 4.9: Schematic view of shower development when arriving at three different zenith angles. Figure taken from [206].

with growing zenith angle (case b, central panel). As the zenith angle keep growing the path difference between early and late region increases and thus asymmetry also increases. However for very large θ values (horizontal showers) the electromagnetic component is quenched due to the longer atmospheric path travelled and the signal is dominated by the muon component, that is not attenuated in the path between early and late regions. Thus, asymmetry disappears at large zenith angles (case c, right panel). In summary, as the zenith angle increases the early-late asymmetry increases until it reaches a maximum and then it decreases for more inclined showers.

The above mentioned differences between the behaviour of the electromagnetic and the muonic component for different θ values allow the use of the asymmetry in the time structure as an indicator of the stage of the shower evolution. Thus, like most of the other observables sensitive to the mass composition, the features of the time distribution of the signals measured by the SD are expected to be correlated with X_{max}, and therefore sensitive to the average mass of the primary particles.

4.2.3 Effect of the azimuthal asymmetry on the shower reconstruction

The azimuthal asymmetry has an impact on the reconstruction of the shower parameters, and more specifically on the reconstruction of the core position. To understand this effect it is necessary to note that for the reconstruction of the shower, using the SD data, a circular symmetry of the particle density in the shower plane is assumed. However, as has been previously explained, signals measured in the early region are larger than the ones measured in the late region at the same core distance; thus, the isodensity lines in the ground plane are eccentric ellipses and their projection to the shower plane are eccentric circumferences, as illustrated in Fig. 4.10. As can also be observed in this figure, the attempt to preserve the supposed cylindrical symmetry during reconstruction generates a shift between the real core position and the reconstructed

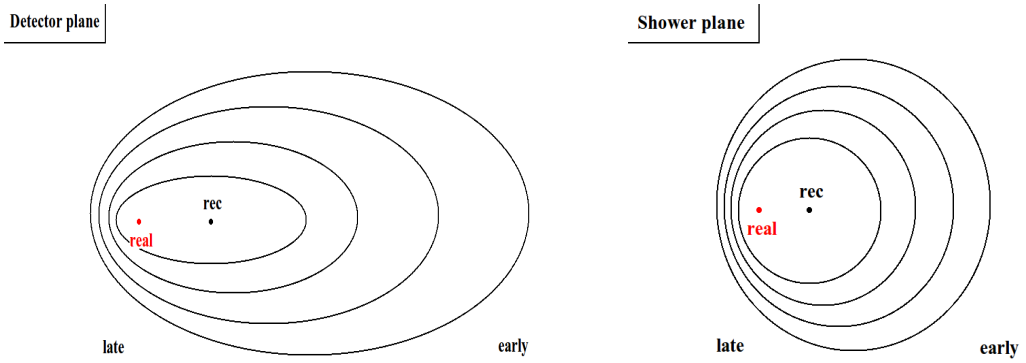

Figure 4.10: Shift between the real core position (red point) and the reconstructed position (black point) using the SD array for the detector plane (left panel) and the shower plane (right panel)

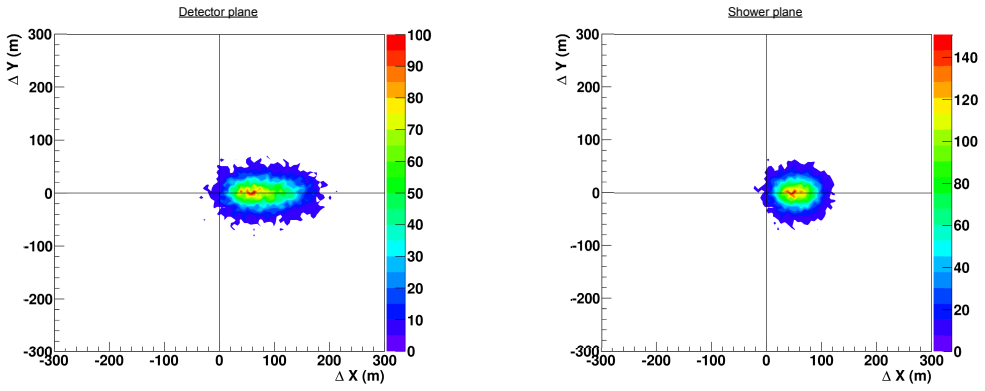

Figure 4.11: Histogram in two dimensions with the differences in the core position between the generated and the reconstructed one using Monte Carlo simulations (QGSJETII-03 hadronic model) in the detector plane (left panel) and in the shower plane (right panel).

one towards the early region.

The shift in the reconstructed core was also observed using hybrid events of the Pierre Auger Observatory by comparing the reconstructed core position using the FD with the reconstructed one using the SD, which is affected by the asymmetry [216]. To quantify the magnitude of this shift and its possible dependence on the zenith angle of the shower, Monte Carlo simulations were used. Using simulated showers it

is possible to compare the reconstructed core position with respect to the generated one. In Fig. 4.11 the differences between the true core position and the reconstructed one are shown for proton showers (with a mean energy of $10^{19.0}$ eV) using QGSJETII-03 [217] hadronic model. In this figure, the (0,0) point corresponds the axis of the shower in both planes. As can be seen, there is a clear shift towards the early region, as anticipated in Fig. 4.10.

To understand the shift it is mandatory to define first the relationship between the coordinate systems of the detector plane and the shower plane. The detector plane is defined by the coordinates $(X_{\rm dp}, Y_{\rm dp}, Z_{\rm dp})$ where, following the conventions of the Pierre Auger Observatory, $X_{\rm dp}$ matches with the East direction, $Y_{\rm dp}$ matches with the North direction and $Z_{\rm dp}$ is the altitude from the detector plane. The shower plane is defined by the coordinates $(X_{\rm sp}, Y_{\rm sp}, Z_{\rm sp})$, where $X_{\rm sp}$ is parallel to the direction of the shower axis, $Y_{\rm sp}$ is perpendicular to it and $Z_{\rm sp}$ matches with the shower axis. In Fig. 4.12 a scheme of these coordinate systems is shown, as well as the relationship between them. The steps for the coordinate transformation from the detector plane system to the shower plane system are the following:

- Firstly, a ϕ rotation of the system $(X_{\rm dp}, Y_{\rm dp})$ around the axis $Z_{\rm dp}$ is required to obtain $(X'_{\rm dp}, Y'_{\rm dp})$.

- Then, it is necessary to rotate the obtained system $(X'_{\rm dp}, Y'_{\rm dp})$ by an angle θ around $Y'_{\rm dp}$ to obtain $(X'_{\rm sp}, Y'_{\rm sp})$, where $Y'_{\rm sp} = Y'_{\rm dp}$.

- Finally, a translation is made along the shower axis to obtain $(X_{\rm sp}, Y_{\rm sp})$.

All these steps translates into the following coordinate transformation:

$$\begin{cases} X_{\rm sp} = (\cos\phi \cdot X_{\rm dp} + \sin\phi \cdot Y_{\rm dp})\cos\theta \\ Y_{\rm sp} = \cos\phi \cdot Y_{\rm dp} - \sin\phi \cdot X_{\rm dp} \end{cases} \tag{4.1}$$

As can be seen in Fig. 4.12, the coordinate $X_{\rm sp}$ is parallel to the direction of propagation of the shower while the $Y_{\rm sp}$ coordinate is perpendicular to it. Thus, the shift of the core position will be restricted to the X coordinate while the Y coordinate will be unaffected when the shower plane coordinate system is used. If ΔX_0 and ΔY_0 are defined as the shifts in the X and Y coordinates in the detector plane (i.e., $\Delta X_0 = X_{\rm real} - X_{\rm rec}$ and $\Delta Y_0 = Y_{\rm real} - Y_{\rm rec}$, respectively), then the shifts ΔX and ΔY in the shower plane are given by:

$$\begin{cases} \Delta X = (\cos\phi \cdot \Delta X_0 + \sin\phi \cdot \Delta Y_0)\cos\theta \\ \Delta Y = \cos\phi \cdot \Delta Y_0 - \sin\phi \cdot \Delta X_0 \end{cases} \tag{4.2}$$

For a better understanding of this shift the behaviour of each component can be studied as a function of energy and θ. The mean values of ΔY for three different energy

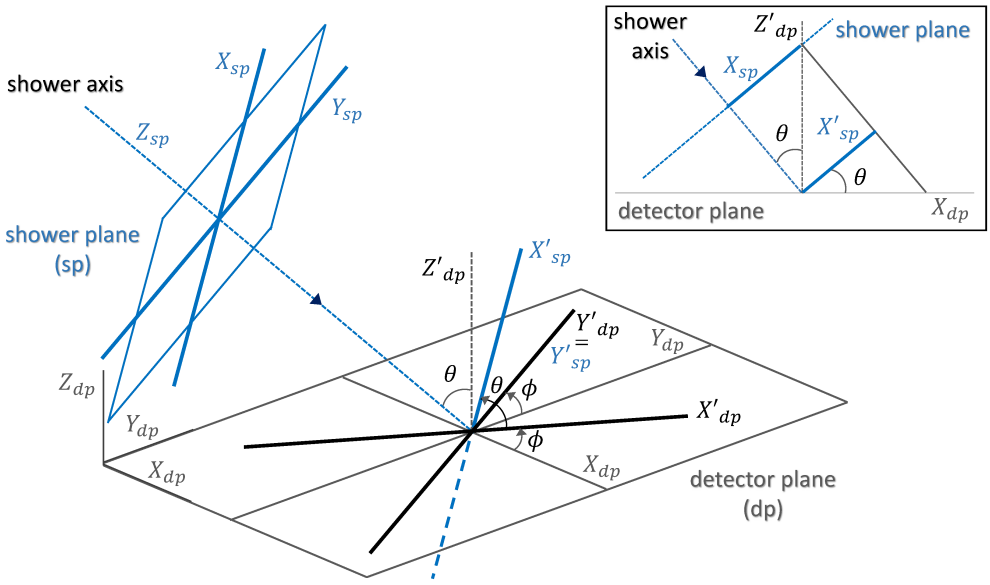

Figure 4.12: Scheme of the coordinate transformation required to work in the shower plane (sp) instead of the detector plane (dp). See text for a complete explanation of each step necessary to obtain the $(X_{\rm sp}, Y_{\rm sp})$ coordinates. Figure taken from [218].

bins as a function of $\sec\theta$ and both primaries (proton and iron) are shown in Fig. 4.13, and the same plots for $\Delta X$are shown in Fig. 4.14. As expected, the shift in the Y direction is compatible with 0 and it is independent of θ, E and primary type. On the other hand, the shift in the X coordinate depends on θ, E and primary type: the mean value of the shift increases until it reaches a maximum and then decreases (following the same explanation given for Fig. 4.9). To obtain the maximum shift a Gaussian fit was performed. The maximum shift increases with the primary energy. Additionally, the proton curve is always above the iron curve (as can be observed in Fig. 4.14), i.e., shift values in core position are larger for proton induced showers than for iron ones. This is due to the fact that iron showers are shallower than proton ones (i.e., the shower maximum $X_{\rm max}$ is higher in the atmosphere for iron showers, see section 2.6.2), which implies that their electromagnetic component will be more attenuated when it reaches the surface.

However, this shift has a very small effect in the $S(1000)$ estimation as it was shown in [219]. A systematically shifted core position implies that some stations will have an underestimated core distance and some others will have an overestimated one, and therefore the LDF fit will try to compensate this systematic effect. In [219]

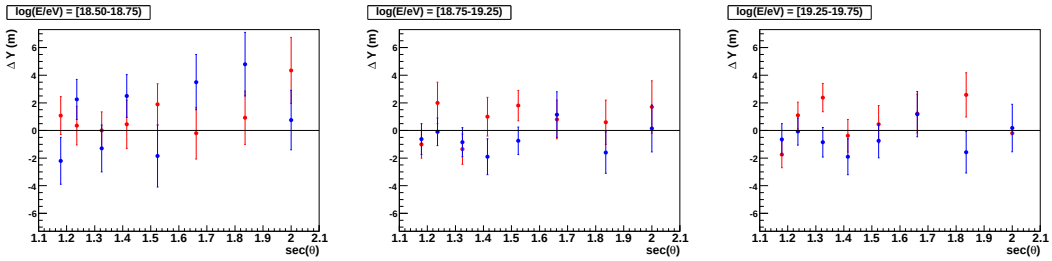

Figure 4.13: Shift in the Y component of the reconstructed core position in the shower plane vs $\sec\theta$ for proton (red dots) and iron (blue dots) primaries in three different energy bins.

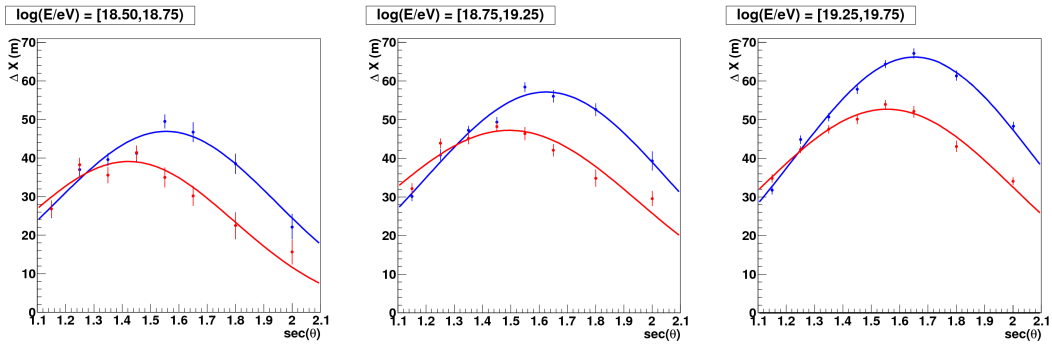

Figure 4.14: Shift in the X component of the reconstructed core position in the shower plane vs $\sec\theta$ for proton (red dots) and iron (blue dots) primaries in three different energy bins.

the influence of the reconstructed core position on $S(1000)$ for inclined showers was analysed, obtaining an effect smaller than 4% in the $S(1000)$ value.

As a conclusion, this shift in the core position has a dependence with the primary particle type, which could be helpful to extract mass composition information of UHECRs. Nevertheless, a large amount of golden events which passes both SD and FD reconstruction requirements would be necessary to this end, and this is not possible, at present, with the event statistics of Auger. However, this effect of the azimuthal asymmetry on the shower reconstruction has to be taken into account in the next chapter and it will be included as a source of systematic uncertainties. Other studies of the shift in the core position can be found in [220, 218].

4.3 The risetime parameter

As pointed out in section 2.7.3, the risetime $t_{1/2}$ is defined as the time of increase from 10% to 50% of the total integrated signal. This interval of the traces contains information of the fast peak of the muonic component as well as of the spread in arrival times of electromagnetic particles. Since the ratio of muon to electromagnetic components depends on the primary particle (iron showers have more muons than proton showers, which implies smaller $t_{1/2}$ values) the risetime is considered as a very useful tool for the composition analysis.

The risetime value in each station is calculated as the average value of the three PMTs. Its uncertainty $\sigma_{t_{1/2}}$ is estimated comparing measurements of the same event from stations with a similar distance to the core r [114]. To this end twins and triplets (sets of two or three stations located inside the SD array separated by $\sim$ 11 m) can be used, as well as the "pairs" (two stations belonging to the same event with a difference in r smaller than 100 m) [221, 112]. To remove the difference in the risetime values due to the different azimuthal angles of the pair stations, a preliminary asymmetry correction, which will be explained in the next section, is performed. This uncertainty of the risetime is observed to have a dependence on the signal size as expected, since the lower the number of contributing particles the larger the fluctuations in risetime. As described in [222], for a given zenith angle and r distance, $\sigma_{t_{1/2}}$ follows the expression:

$$\sigma_{t_{1/2}}(S) = \frac{j(r, \sec\theta)}{S} + k(r, \sec\theta) \ , \tag{4.3}$$

where S is the signal intensity, and j and k are functions of the core position and the zenith angle, and are parameterized using different expressions [222, 223, 224, 225]. This behaviour of $\sigma_{t_{1/2}}$ was confirmed through MC simulations using stations located within a ring at 1000 m from the shower core, considering pairs of stations located at $\zeta = \pm\pi/2$ (where there is no need for asymmetry correction) [222]. This risetime uncertainty will be taken into account in the next chapter for the evaluation of the systematic uncertainty of the mass sensitive parameter defined in section 4.6.2.

The analysis described in this thesis requires to measure the asymmetry of the risetime distributions as a function of the azimuthal angle. However, this measurement cannot be done on shower-by-shower basis, because it is not possible to sample the whole range of the azimuthal angles from early to late regions with a single event. Thus, a statistical approach is applied to characterize the asymmetry of the risetime as a function of the azimuthal angle, using to this end all the stations within a given radial interval from events at a given energy and zenith angle.

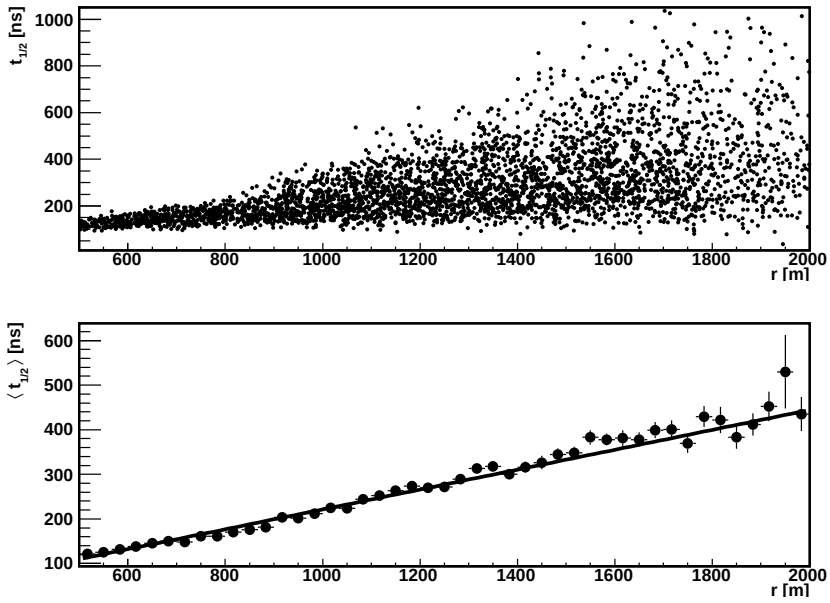

Figure 4.15: Top panel: $t_{1/2}$ vs. r for stations of real events with zenith angle $42^\circ < \theta < 48^\circ$ and energy $19.2 < \log(E/\mathrm{eV}) < 19.6$. Bottom panel: same figure than the top one but using mean values of $t_{1/2}$ in intervals of r. The solid line corresponds to a linear fit.

The risetime grows with the core distance r and, in a first approximation, follows a linear behaviour in the range of distances considered in the present analysis, as can be seen in Fig. 4.15. The variable that will be used to study the azimuthal asymmetry is $t_{1/2}/r$. Since the core distance dependence is compensated, an average value using all stations at different r values can be used, increasing the statistics of the analysis.

As will be discussed later, even if the risetime is divided by the core distance of the station, the time asymmetry depends on r. Note that the risetime difference between early and late stations is negligible close to the core position but increases at large distances.

4.3.1 Asymmetry correction of risetime

Although the asymmetry in the risetime of the SD traces contains very valuable information about the shower development as already mentioned, it might lead to incorrect results when the time structure of the shower front is needed, e.g., analyses using $t_{1/2}$ at 1000 m for composition studies [117]. In this section it will be shown a method for

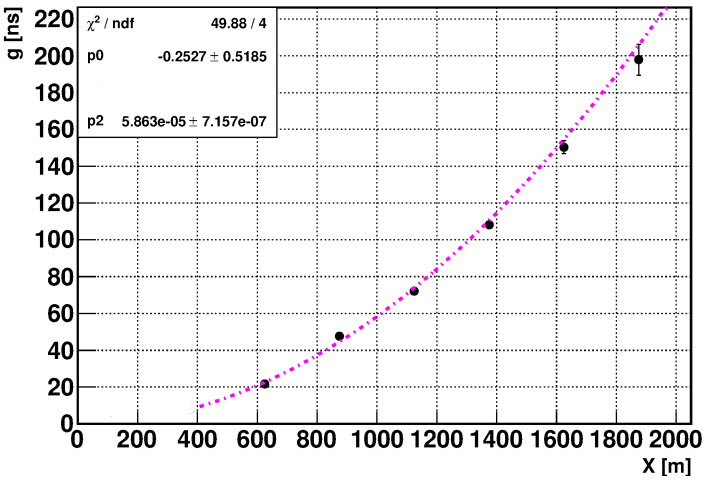

Figure 4.16: The correction factor g vs core distance r for $1.2 < \sec\theta < 1.4$.; p_0 and p_2 correspond to the value of A and B in equation (4.5) respectively, while p_1 is fixed to zero in the implemented function.

correcting the risetime measurements from this asymmetry effect. The Pierre Auger Collaboration developed a procedure that was implemented in the Offline module Risetime1000LLL.cc using data up to 2007 [226]. This correction was later updated in [222], but it was not included in the Offline. Following a similar approach as the one used in [222], the asymmetry correction has been updated here in collaboration with La Plata group (see [227] for details) using data from 2004 to 2013. The corrected risetime is expressed as:

$$f = m(r, \theta, \zeta) - g(r)\cos\zeta \ , \tag{4.4}$$

where m is the measured risetime and g the asymmetry correction factor that can be described with a second-degree polynomial function of r, with coefficients depending on θ:

$$g(r) = A(\sec\theta) + B(\sec\theta)r^2 \ . \tag{4.5}$$

In Fig. 4.16 an example of this parameterization is shown for events with zenith angle $1.2 < \sec\theta < 1.4$ and energy above $10^{18.45}$ eV. The A and B parameters can be parametrised with a third degree polynomial function on $\sec\theta$ (see Fig. 4.17). Once the asymmetry correction factor is obtained, it can be applied to correct the azimuthal

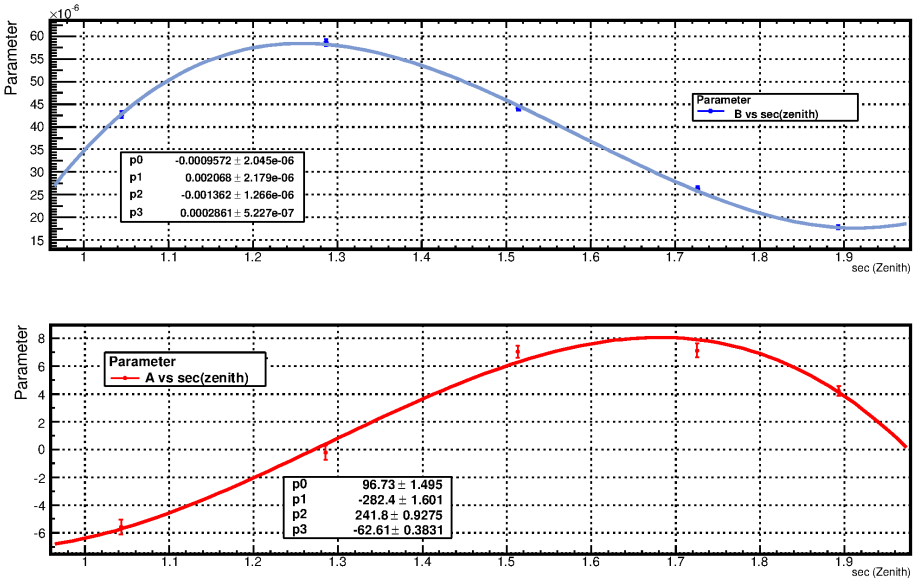

Figure 4.17: Dependence on zenith angle of the parameters A (bottom) and B (top).

asymmetry in the risetime. In Fig. 4.18 an example of the risetime vs azimuth angle with and without the asymmetry correction for events with $1.2 < \sec\theta < 1.4$ and 1000 m $< r <$ 1250 m is shown.

In order to check the effectiveness of the correction in the whole core distance range, risetime values with and without the correction at $\zeta = 0°$ and $\zeta = \pm 180°$ (where the maximum deviation in risetime values due to the asymmetry is observed) are compared with those at $\zeta = \pm 90°$ (where there is no asymmetry). The comparison between uncorrected and corrected risetimes are shown in Fig. 4.19 for the zenith angle interval $1.2 < \sec\theta < 1.4$. As it can be observed, the corrected risetimes are in full agreement with those measured at $\zeta = \pm 90°$ for core distances $r < 1400$ m (at larger r values the correction is also valid within statistical uncertainties). This comparison has been repeated in other bins of $\sec\theta$ with similar results, demonstrating the feasibility of the asymmetry correction for events with $1.0 < \sec\theta < 2.0$ and energy above $10^{18.45}$ eV. This asymmetry correction is then necessary to be applied for the studies using risetime of individual events.

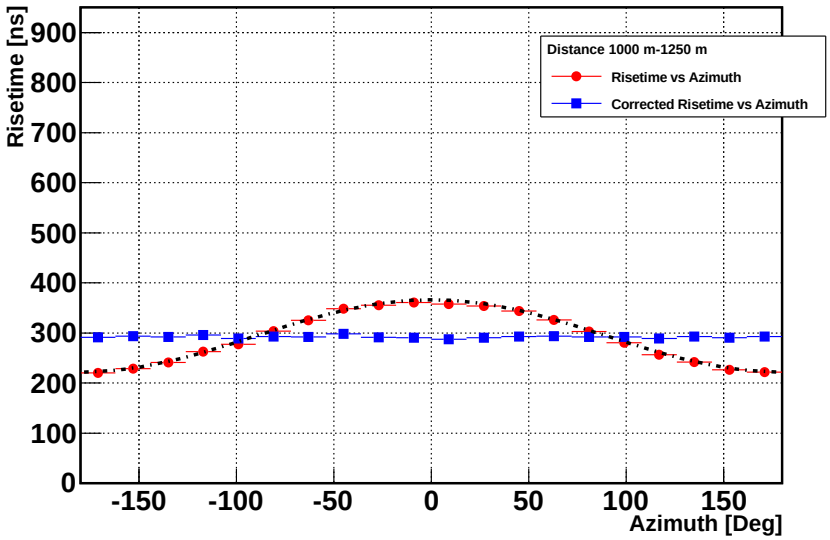

Figure 4.18: Azimuthal dependence on risetime for $1.2 < \sec\theta < 1.4$ and 1000 m $< r <$ 1250 m before and after applying the asymmetry correction.

4.4 MC library for the asymmetry analysis

All mass composition analyses have to rely on the comparison with theoretical predictions using available models of hadronic interactions. For the present analysis it has been generated a dedicated library of MC showers initiated by protons and iron nuclei in a wide angular and energy interval. The shower simulations have been carried out using the CORSIKA code with the interaction models QGSJETII-03, EPOS 1.99 [228], SIBYLL 2.1, EPOS-LHC and QGSJETII-04 with the following fixed values of zenith angle and energy:

- θ: 18°, 25°, 32°, 36°, 41°, 45°, 49°, 53°, 57°, 60°, 63°.

- $\log(E/\mathrm{eV})$: 18.00, 18.25, 18.50, 18.75, 19.00, 19.25, 19.50, 19.75, 20.00, 20.25.

The detector simulation and the event reconstruction was performed with the $\overline{\text{Off}}\underline{\text{line}}$ software. The EPOS 1.99 and SIBYLL 2.1 libraries were generated with CORSIKA version 6990 and $\overline{\text{Off}}\underline{\text{line}}$ version v2r7p7, and each one is composed by 40000 showers (20000 proton showers and 20000 iron ones). The QGSJETII-03 library, generated with CORSIKA version 6970 and $\overline{\text{Off}}\underline{\text{line}}$ version v2r6p1, contains 1×10^5 showers (60000 proton showers and 40000 iron ones). Finally, the libraries using the updated QGSJETII-04 and EPOS-LHC models were both generated with CORSIKA version

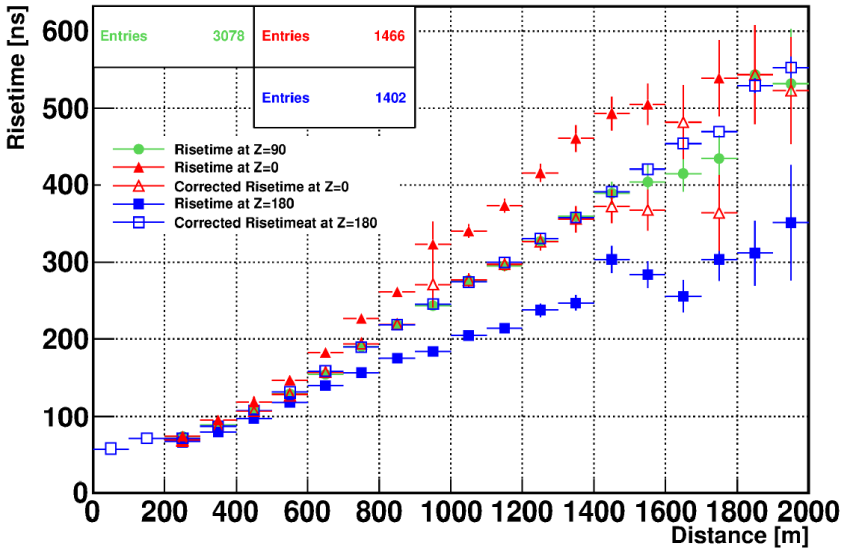

Figure 4.19: Dependence of $t_{1/2}$ vs r before and after applying the asymmetry correction for $1.2 < \sec\theta < 1.4$, for stations with $\zeta = 0°$ and $\zeta = \pm 180°$, compared with the value at $\zeta = \pm 90°$. In the plot legend, Z corresponds to ζ.

7370 and $\overline{\text{Off}}\underline{\text{line}}$ version v2r9p3, and each one is composed by 1.5×10^5 showers (75000 proton showers and 75000 iron showers). All these showers have been reconstructed using both SD and FD information in order to have hybrid (golden) simulated events. Some examples of hybrid reconstruction using the two recent models QGSJETII-04 and EPOS-LHC and both primaries are shown in Fig. 4.20.

To obtain reliable results in the analysis, it is mandatory to impose certain quality cuts to the events. Firstly, they have to fulfil the T5 trigger level condition (see section 3.3.2 for a description of this trigger), so that a good reconstruction of the shower parameters of high-quality events contained inside the array is ensured. To stay in the regime of full-efficiency of the SD, the shower energy has to be larger than 3.16 EeV (i.e., $10^{18.5}$ eV) and the zenith angle smaller than 62°. Moreover, to select only inclined showers (in which the attenuation effect is the dominant contribution of the asymmetry) the minimum value of θ has to be 30°. To reject events with a bad reconstruction, the χ^2/ndf value of the LDF fit is required to be smaller than 10, and at least 4 stations have to be triggered in each event.

Additionally, quality cuts have to be applied at the station level. It is required that the recorded signal is larger than 10 VEM (the Vertical Equivalent Muon unit has

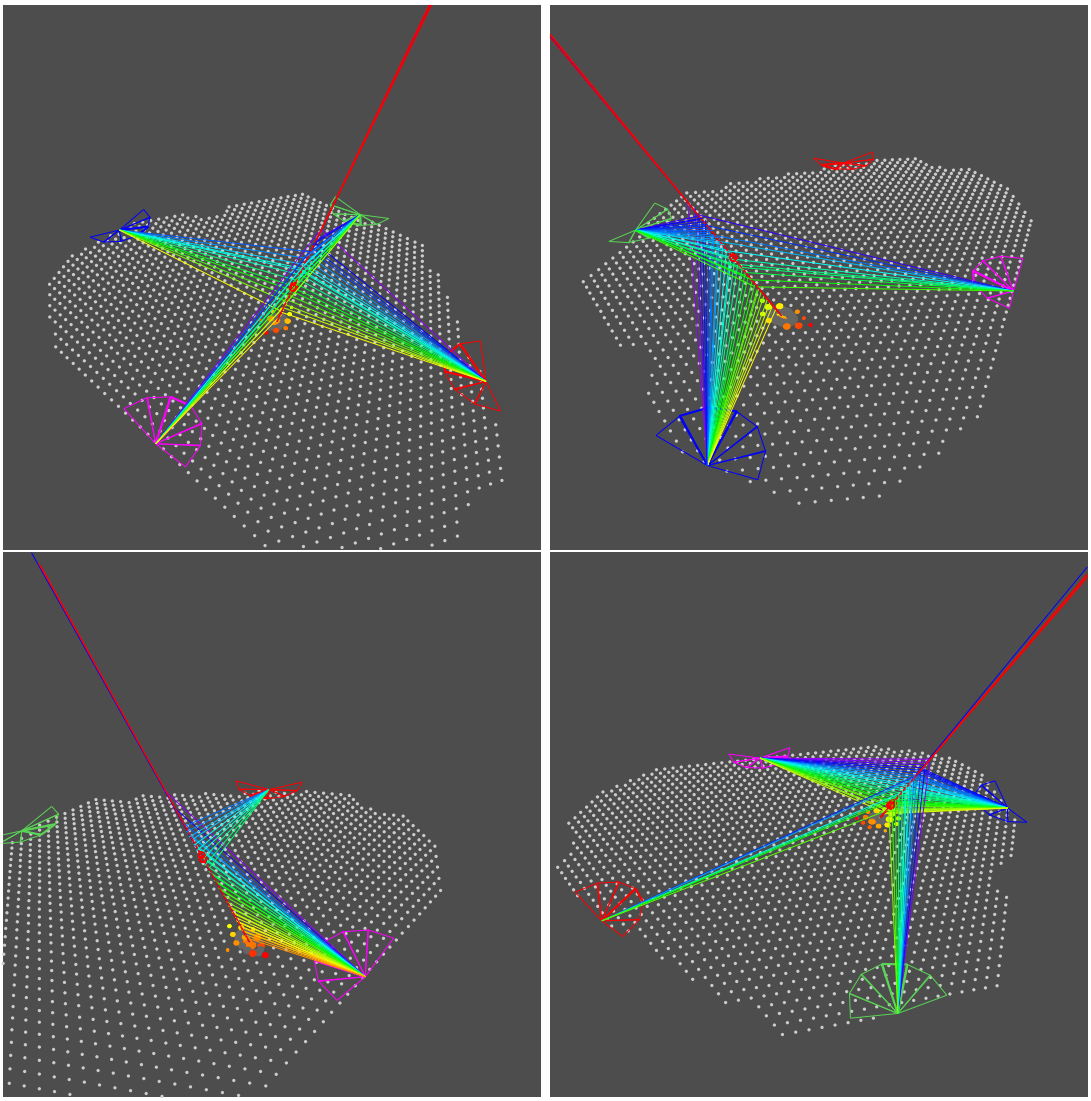

Figure 4.20: Examples of hybrid reconstruction for different events generated using QGSJETII-04 (top panels) and EPOS-LHC (bottom panels) for proton (left panels) and iron (right panels) primaries. The FD telescopes are represented by the following colours: Loma Amarilla in red, Coihueco in green, Los Morados in purple and Los Leones in blue. The straight lines represent the incoming direction of the cosmic ray reconstructed by the SD (in blue) and by each FD telescope (in red), while the red dot in the incoming direction marks the position of the reconstructed $X_{\max}$ parameter. Colours of the SD tanks follow the same pattern explained in Fig. 4.5: the yellow stations are triggered in the first place (early stations) and the red stations are the last ones (late stations).

been defined in section 3.3.1), above which the probability of single detector triggering is about 100% [167]. With respect to core position, detectors used for the analysis were required to be further than 500 m from the core of the shower to avoid signal saturation effects that prevent an accurate measurement of $t_{1/2}$ (signals saturate at average values of about 800 VEM depending on the PMT gains). Finally, to reject stations with very large uncertainties in the reconstructed risetimes it is required that the water-Cherenkov detectors are within 2000 m from the core.

4.5 Azimuthal asymmetry in the time structure

In this section the method developed in [206, 207, 229, 230, 231] will be revisited and explained in detail. To understand the azimuthal asymmetry analysis is required to study the slant depth dependence of a generic shower parameter. For that, it is easier to approximate the shower structure as an inverted cone and, as it was shown in [232, 233], the intersection of an inclined cone with a plane parallel to the ground leads to the following relationship:

$$\frac{z}{\cos\theta} - L = (z' - L)\left(1 - \frac{r'}{z' - L} \cdot \tan\theta \cdot \cos\zeta\right) . \tag{4.6}$$

In this expression, z', r' and ζ are the coordinates in the shower frame with $x' = r'\cos\zeta$, and L and θ are indicated in Fig. 4.21. Assuming a cone angle α nearly independent of z and using the fact that $\tan\alpha = r'/(z' - L)$, the equation which relates the vertical atmospheric depth and the slant depth in terms of the azimuthal angle ζ can be obtained:

$$\frac{dz}{\cos\theta} = dz'(1 - \tan\alpha \cdot \tan\theta \cdot \cos\zeta) . \tag{4.7}$$

This expression, in terms of slant depth is equivalent to:

$$\frac{X}{X'} = \cos\theta(1 - \tan\alpha \cdot \tan\theta \cdot \cos\zeta) . \tag{4.8}$$

where X is the vertical atmospheric depth at observation level and X' the slant depth traversed by the shower.

This equation can be expressed as:

$$X' = \frac{X}{\cos\theta(1 - \tan\alpha \cdot \tan\theta \cdot \cos\zeta)} = X \cdot \sec\theta \cdot \frac{1}{1 - \tan\alpha \cdot \tan\theta \cdot \cos\zeta} . \tag{4.9}$$

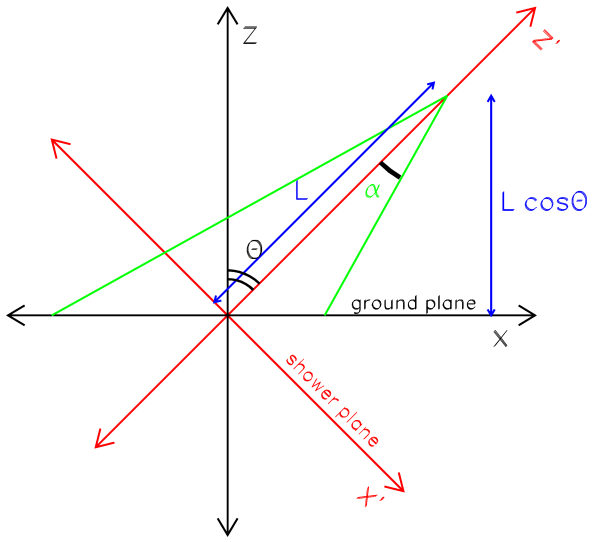

Figure 4.21: Intersection of a cone with the ground plane. Figure taken from [207]

Using the approximation $1/(1-x) \simeq 1+x$, X' is given by:

$$X' \simeq X \cdot \sec\theta(1 + \tan\alpha \cdot \tan\theta \cdot \cos\zeta) \,. \tag{4.10}$$

Thus, the expression for the azimuthal dependence of the slant depth X' can be expressed as:

$$X' = X_s + \Delta X_s \simeq X \cdot \sec\theta(1 + B \cdot \cos\zeta) \,, \tag{4.11}$$

where the slant depth along the shower axis X_s, ΔX_s and B are:

$$X_s = X \cdot \sec\theta \,, \tag{4.12}$$

$$\Delta X_s = X_s \cdot B \cdot \cos\zeta \,, \tag{4.13}$$

$$B = \tan\alpha \cdot \tan\theta \equiv B_0 \cdot \tan\theta \,. \tag{4.14}$$

Using equation (4.11) it is possible to study the dependence of a generic temporal variable τ with ζ. While for vertical showers τ depends only on the core distance r and

the atmospheric depth X, for inclined showers the slant depth depends also on ζ and θ angles, i.e., $\tau(r, X'(\zeta, \theta))$. Following [234], this dependence can be described using a Taylor expansion around $X_s = X \cdot \sec\theta$:

$$\tau(r, X') = \tau(r, X_s + \Delta X_s) = \tau(r, X_s) + \left.\frac{\partial \tau}{\partial X'}\right|_{X_s} \cdot \Delta X_s + \left.\frac{\partial^2 \tau}{\partial X'^2}\right|_{X_s} \cdot \Delta X_s^2 + ... \quad (4.15)$$

Introducing the value previously obtained of $\Delta X_s(\zeta)$, this expression is equivalent to:

$$\tau(r, X') = \tau(r, X_s) + \left.\frac{\partial \tau}{\partial X'}\right|_{X_s} \cdot X_s \cdot B \cdot \cos\zeta + \left.\frac{\partial^2 \tau}{\partial X'^2}\right|_{X_s} \cdot X_s^2 \cdot B^2 \cdot \cos^2\zeta + ... \quad (4.16)$$

So, in first order approximation, the slant depth dependence is equivalent to using a linear function in $\cos\zeta$:

$$\tau(r, X') = a + b \cdot \cos\zeta \ . \quad (4.17)$$

Factoring out $\tau(r, X')$ in the expression (4.16), in first order approximation the above equation can be expressed as:

$$\tau(r, X') = \tau(r, X_s) \left(1 + \left.\frac{\partial \ln \tau}{\partial \ln X'}\right|_{X_s} \cdot B \cdot \cos\zeta\right) \ , \quad (4.18)$$

so a and b are defined as:

$$a = \tau(r, X_s) \ , \quad (4.19)$$

$$b = \tau(r, X_s) \cdot \left.\frac{\partial \ln \tau}{\partial \ln X'}\right|_{X_s} \cdot B \ . \quad (4.20)$$

In order to check the validity of approximation (4.17) for the risetime, its dependence with ζ has been studied for sets of simulated showers with fixed energy and zenith angle, since, as it was explained in section 4.3, this analysis cannot be carried out for individual showers because of the small number of triggered stations per shower. In the first place for given ζ values the average $\langle t_{1/2}/r \rangle$ has been evaluated for each set of showers, and the corresponding uncertainty is calculated as the RMS of the distribution divided by the squared root of the number of traces. Hereafter the τ variable will be equivalent to $\langle t_{1/2}/r \rangle$. As explained above the risetime is divided by r to reduce the dependence with core distance. In Fig. 4.22 some examples are shown for a sample

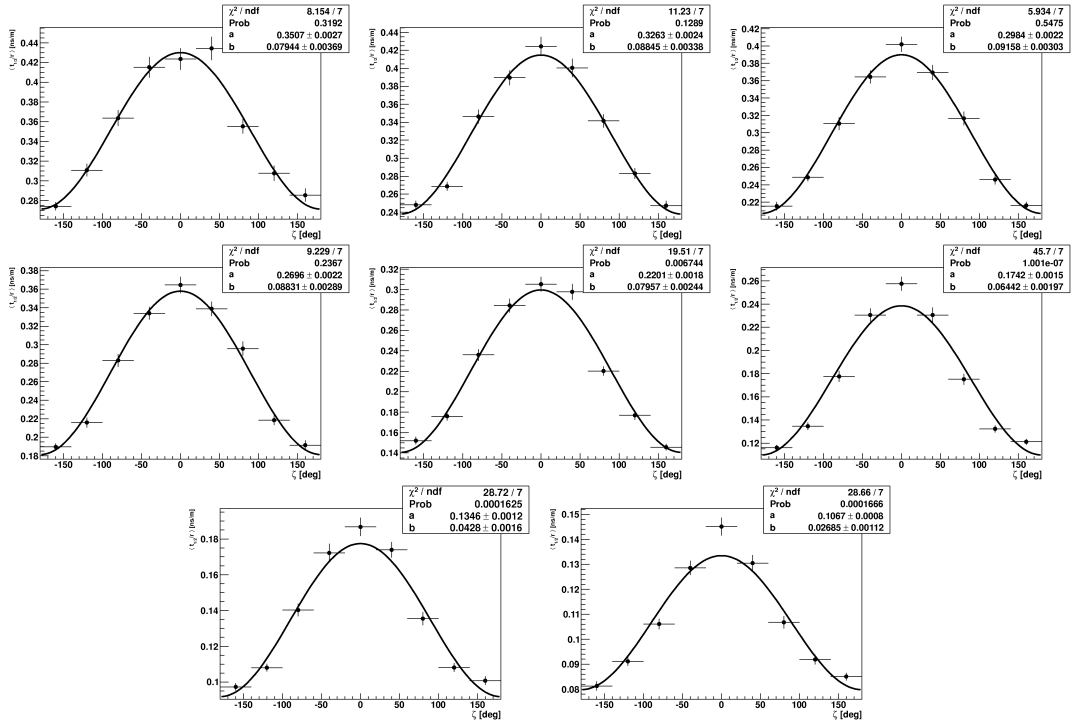

Figure 4.22: Distribution of $\langle t_{1/2}/r \rangle$ vs ζ fitted following the equation (4.17) given by the first order approximation in the Taylor expansion. Showers correspond to EPOS-LHC proton simulated showers with a mean energy of $\log(E/\mathrm{eV}) = 19.2$ and $\theta = 32°$, $\theta = 36°$, $\theta = 41°$, $\theta = 45°$, $\theta = 49°$, $\theta = 53°$, $\theta = 57°$ and $\theta = 60°$ from upper left to bottom right. The horizontal bar represents the with of the angular bin and the vertical bar is the statistical uncertainty of the corresponding $\langle t_{1/2}/r \rangle$ value.

of EPOS-LHC showers initiated by protons at several zenith angles. As can be seen, approximation (4.17) represents properly the dependence of $\langle t_{1/2}/r \rangle$ with ζ for small θ values, but for very inclined showers the first-order Taylor expansion does not suffice to properly represent the $\langle t_{1/2}/r \rangle$ vs ζ dependence. For these cases it is required to include a quadratic term in $\cos\zeta$:

$$\tau(r, X') = a + b \cdot \cos\zeta + c \cdot \cos^2\zeta \; . \tag{4.21}$$

As an example of the improvement of the fit when including the second order, in Fig. 4.23 two examples of $\langle t_{1/2}/r \rangle$ vs ζ are shown alongside with the fit to the linear and second-order polynomial approximations for QGSJETII-04 iron simulated showers: top panels correspond to $\log(E/\mathrm{eV}) = 18.7$ and $\theta = 36°$ while bottom ones correspond to

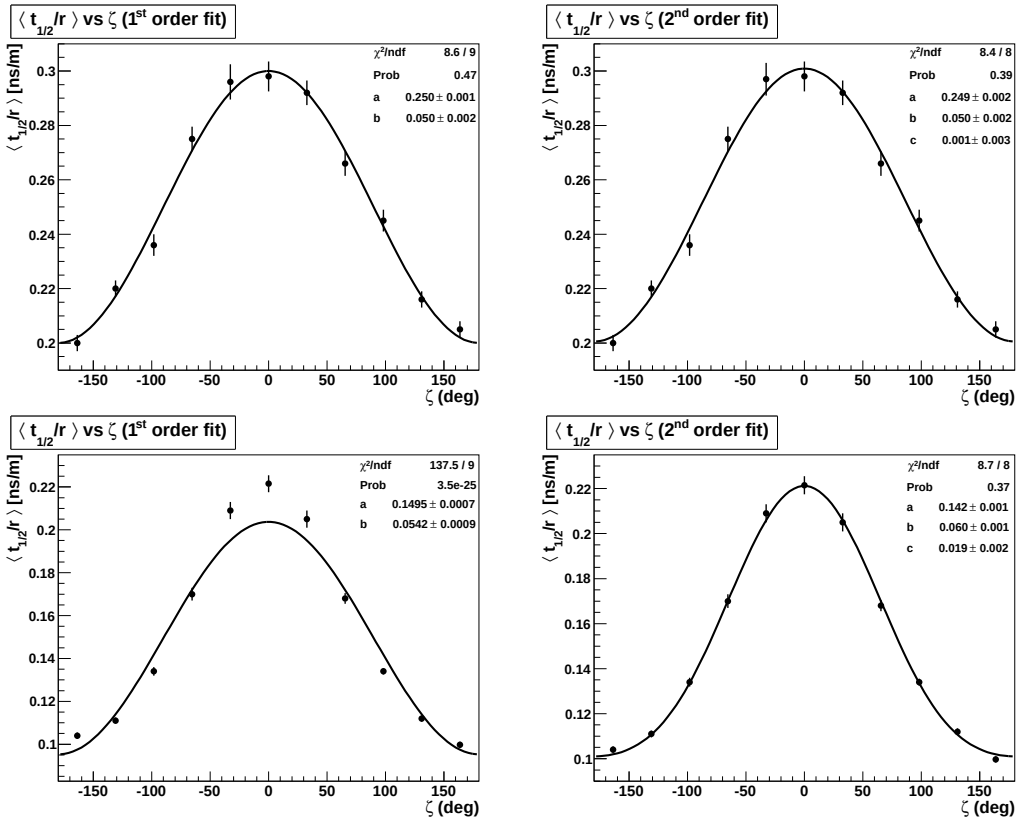

Figure 4.23: Linear fit (left panels) vs. second-order polynomial fit (right panels) for two different cases of QGSJETII-04 iron simulated showers. Top: $\log(E/\mathrm{eV}) = 18.7$ and $\theta = 36°$. Bottom: $\log(E/\mathrm{eV}) = 20.2$ and $\theta = 53°$. Vertical bars are the statistical uncertainties.

$\log(E/\mathrm{eV}) = 20.2$ and $\theta = 53°$. As can be seen, the first order is a good approximation for low energy and zenith angles, but for larger zenith angle and higher energy values, for which the asymmetry is larger, the fit is improved including a quadratic term.

To quantify the asymmetry, a parameter, the asymmetry factor, is defined as:

$$\text{Asymmetry factor} = \frac{\tau_{\text{early}} - \tau_{\text{late}}}{\tau_{\text{early}} + \tau_{\text{late}}} \,, \tag{4.22}$$

where τ_{early} and τ_{late} are the values of $\langle t_{1/2}/r \rangle$ at $\zeta = 0$ and $\zeta = \pm\pi/2$ respectively. In the linear approximation (4.17), the asymmetry factor equals b/a and represents the relative amplitude of the asymmetry (see left panel of Fig. 4.24). Taking into account (4.18) this parameter is related to the logarithmic variation of the risetime

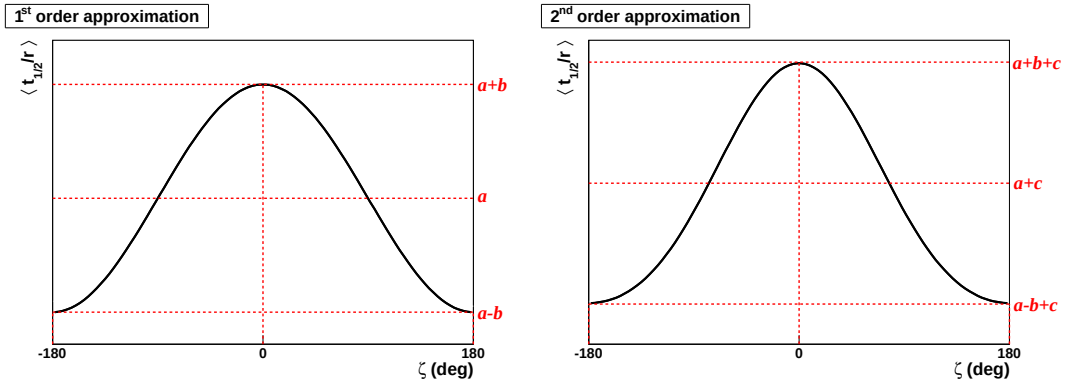

Figure 4.24: Asymmetry factor for first order approximation (left panel) and second order approximation (right panel). The factor is given by the difference between the values of the temporal distribution in early and late regions divided by the sum of both values.

with X:

$$\frac{b}{a} = B \left. \frac{\partial \ln \tau}{\partial \ln X'} \right|_{X_s} . \tag{4.23}$$

Using the same definition (4.22) for the second order approximation (4.21), the asymmetry factor equals $b/(a+c)$ and also represents the relative asymmetry amplitude (see right panel of Fig. 4.24).

The asymmetry factor contains information about the variation with the slant depth of the ratio between the electromagnetic and the muonic component. As it will be discussed in the following, for a given energy E, the variation of the asymmetry factor with $\sec\theta$ shows a correlation with the average longitudinal development of the shower. Hence the azimuthal asymmetry in the time structure is sensitive to the average mass of the primary cosmic ray.

4.6 Mass composition from the asymmetry in risetime

As was previously pointed out in 4.3, the azimuthal asymmetry of $t_{1/2}$ cannot be measured on a shower-by-shower basis because the whole range of ζ values from early to late regions cannot be sampled in a single event. Therefore the method relies on a statistical analysis of the azimuthal asymmetry of the risetime in intervals of energy and zenith angle.

This section will explain step by step the procedure to determine the mass composition using Monte Carlo simulations with the latest hadronic interaction models. If not stated otherwise, the analysis described in this section will be carried out using the risetime information of stations in the radial interval 500 - 2000 m. However, as mentioned before in section 4.2.2, the azimuthal asymmetry of $\langle t_{1/2}/r \rangle$ is expected to grow with the radial interval. The dependence of the risetime asymmetry on r and the potential impact for mass composition will be discussed in section 4.6.4.

4.6.1 Azimuthal dependence on the average $t_{1/2}/r$

The first step is to split the event sample in subsamples of showers of energy and zenith angle within intervals as narrow as possible keeping a reasonable statistics. Then, as described in section 4.5, for each subsample the average value $\langle t_{1/2}/r \rangle$ and its uncertainty have to be evaluated for intervals of ζ and fitted to equations (4.17) and (4.21) (according to the need of considering or not the second order) to obtain the asymmetry factor.

As an example, the results for samples of MC proton and iron showers with an average energy of $\log(E/\text{eV}) = 19.2$ and different zenith angles is shown in Fig. 4.25. The asymmetry of risetime with respect to ζ (and its dependence with θ) is evident: for early region ($\zeta \sim 0$) values of $\langle t_{1/2}/r \rangle$ are larger than the ones registered in late region ($\zeta \sim \pm\pi$). This asymmetry becomes smaller for increasing θ values, as explained in section 4.2.2. As it can be observed the fit of the equation (4.21) represents properly the $\langle t_{1/2}/r \rangle$ vs ζ dependence independently of the value of θ and the primary. In this figure it can also be noticed that this function is flatter for iron showers than for proton ones. This difference between primaries is due to a combination of two effects (explained in section 2.6): iron showers are shallower and have a larger number of muons than proton showers for the same primary energy and zenith angle. This leads to a total signal with a larger muonic contribution and an electromagnetic component more attenuated for iron showers, which translates into smaller values of risetime and a smaller asymmetry than the registered for proton initiated showers.

4.6.2 Mass sensitive parameter $(\sec\theta)_{\max}$

With the previously obtained values of the asymmetry factor for different values of θ in a given energy bin, it is possible to study its evolution with the zenith angle. This dependence is shown in Fig. 4.26, where the asymmetry factor is plotted against $\ln(\sec\theta)$ for a set of proton showers with average energy of $10^{18.9}$ eV simulated using the EPOS-

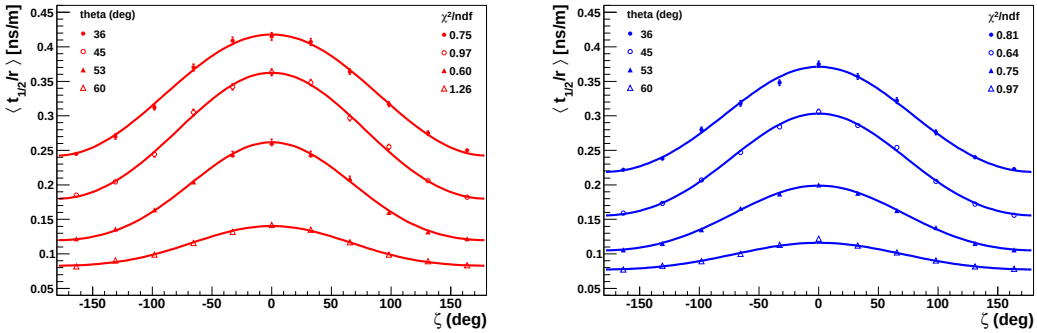

Figure 4.25: $\langle t_{1/2}/r \rangle$ vs ζ for simulated showers with EPOS-LHC hadronic model, a primary energy of $10^{19.2}$ eV and different zenith angles for proton (left panel) and iron nuclei (right panel).

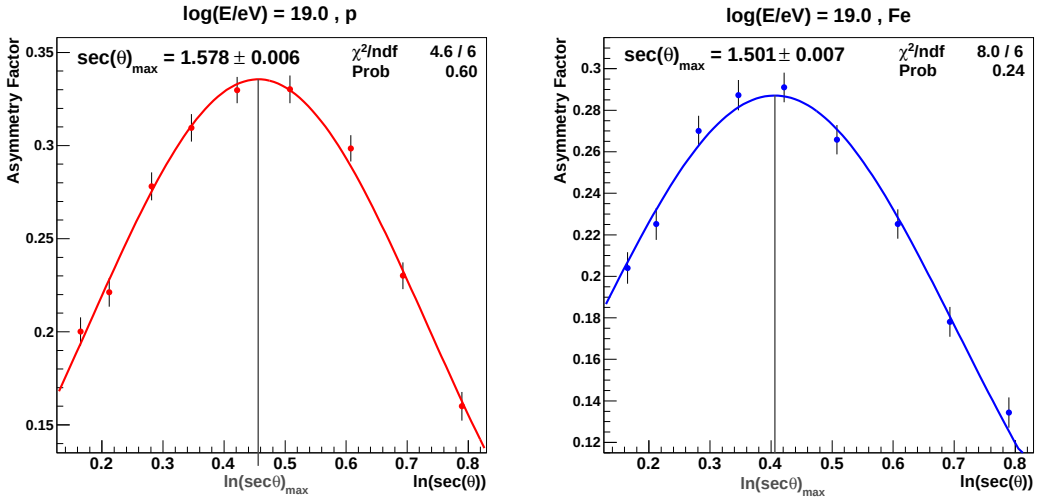

Figure 4.26: Dependence of the asymmetry factor with $\ln(\sec\theta)$ for a sample of EPOS-LHC proton (iron) initiated shower in the left (right) panel with a mean energy of $10^{19.0}$ eV. Vertical error bars are the statistical uncertainties of the asymmetry factor. The definition of $(\sec\theta)_{\max}$ is illustrated.

LHC model. Note that the asymmetry factor is related to the logarithmic variation of $\tau(r, X \cdot \sec\theta)$ with X' (see equation (4.23)) and thus the asymmetry factor is represented versus $\ln(\sec\theta)$ because with this variable the function is found to be symmetric. In this figure the expected behaviour is observed: the asymmetry grows with the atmospheric

depth (represented by $\sec\theta$), reaches a maximum and then decreases. In this figure the vertical error bar is the statistical uncertainty of the asymmetry factor inferred from the fit of the $\langle t_{1/2}\rangle$ vs ζ plots to expressions (4.17) and (4.21). The mass sensitive parameter $(\sec\theta)_{\max}$ is defined as the value of $\sec\theta$ that maximizes the asymmetry. To obtain $(\sec\theta)_{\max}$ and the corresponding statistical uncertainty this distribution is fitted to a Gaussian function as shown in the examples of Fig. 4.26.

This parameter is related to the primary mass, as can be seen in Fig. 4.27 where the evolution of the asymmetry factor with θ of proton and iron showers are compared for several energies. As can be observed in the figure, for a given primary energy, $(\sec\theta)_{\max}$ is higher for proton showers than for iron ones. This fact can be explained as a combination of the differences in the longitudinal development and the muon content between iron and proton showers. On the one hand, as has been explained previously, a proton shower penetrates deeper in the atmosphere than an iron one with the same energy, which implies a higher amount of electrons reaching the surface detector in the case of proton showers. As a consequence, for a given energy, proton showers need to be more inclined than iron showers in order to reach the point where the difference in the attenuation of the electromagnetic component between the early and late regions maximizes, and thus, $(\sec\theta)_{\max}$ becomes higher than those for iron showers. On the other hand, iron showers have more muons than proton showers, and therefore its electromagnetic component has less impact on the total signal collected in the surface detector. In addition, due to these two effects, the ratio between the electron and muon signals is smaller for iron showers, and thus also smaller the corresponding values of the asymmetry factor, as can be observed in Fig. 4.27.

4.6.3 Evolution of $(\sec\theta)_{\max}$ with the energy

Once the value of $(\sec\theta)_{\max}$ has been obtained for each energy bin, the dependence of $(\sec\theta)_{\max}$ with energy is studied in a similar way to the elongation rate analysis. In Fig. 4.28 the energy evolution of $(\sec\theta)_{\max}$ for all models of hadronic interactions of the MC library described in section 4.4 is shown. As can be observed, there is a linear dependence between $(\sec\theta)_{\max}$ and $\log E$. The fact that $X_{\max}$ increases with $\log E$ (see section 2.7.1) means that the position of the shower maximum is closer to the ground as the energy increases, and therefore a higher amount of electromagnetic particles reaches the surface detector. Consequently, as has been explained in the previous section 4.6.2, a higher number of electromagnetic particles in the detector implies a higher amount of atmosphere necessary to reach the point where the early-late attenuation maximizes, i.e., a higher value of $(\sec\theta)_{\max}$. Thus, a strong correlation between the parameters

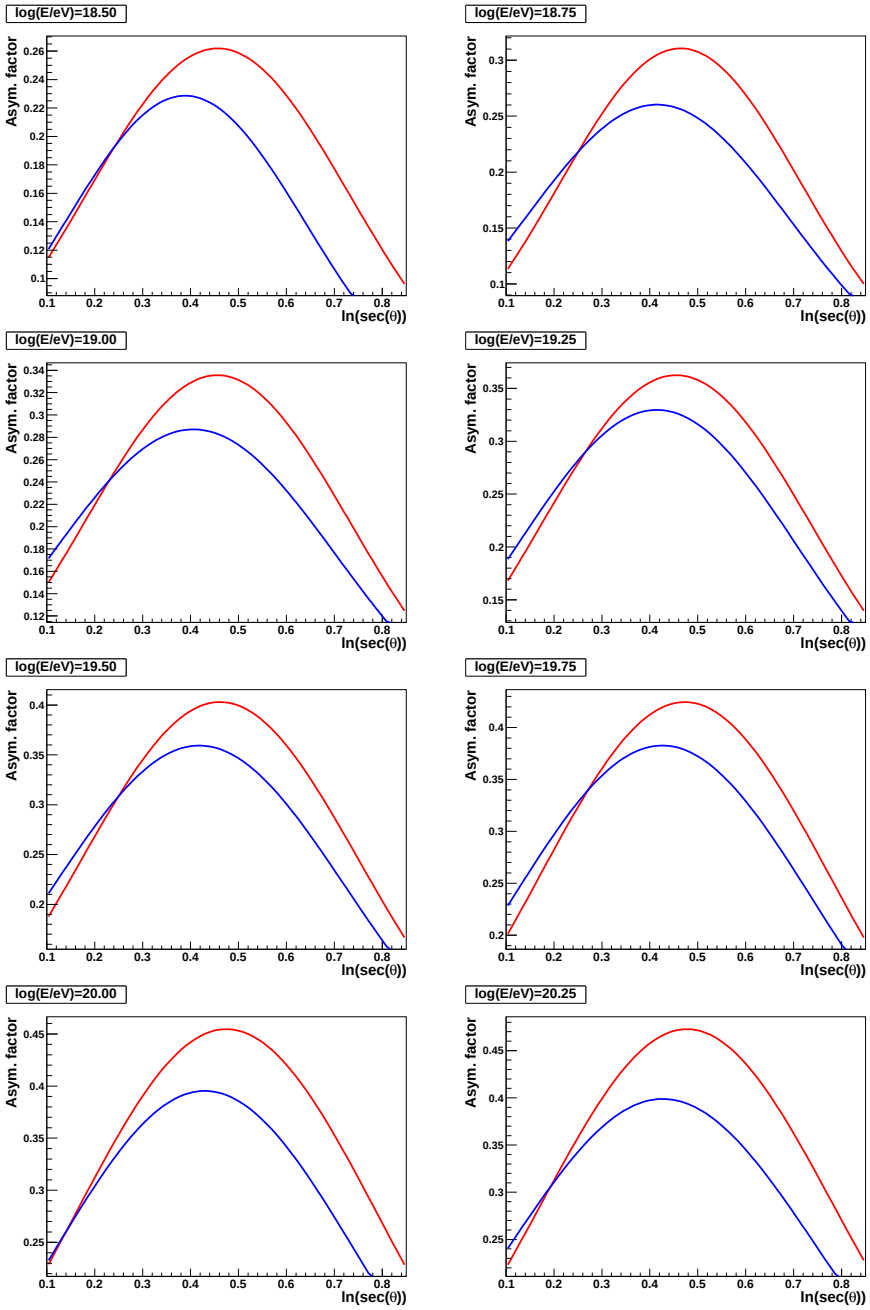

Figure 4.27: Evolution of asymmetry factor for MC sample using EPOS-LHC hadronic model for all the energy bins and two different primary species: proton (the red line) and iron (the blue one).

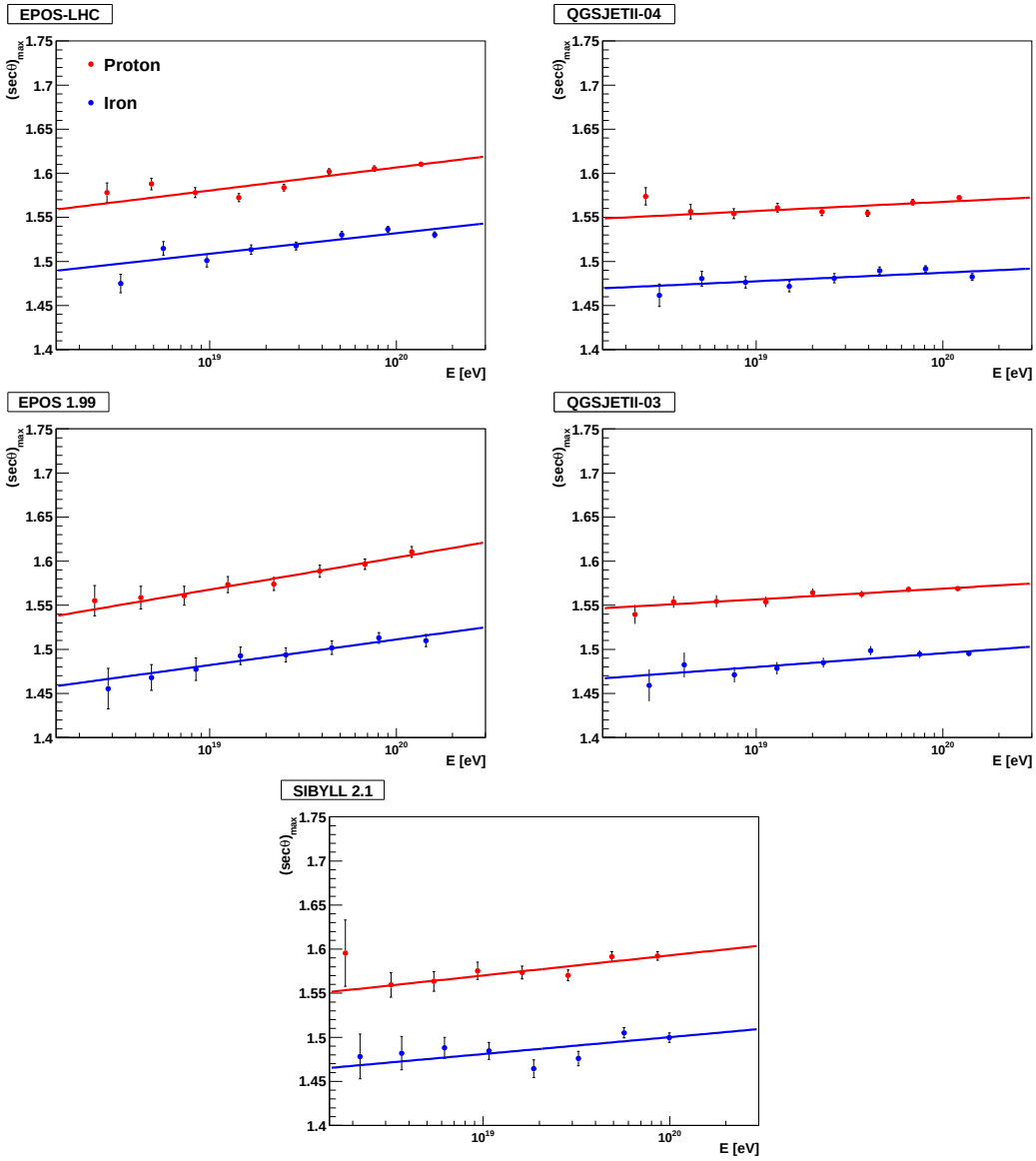

Figure 4.28: Evolution of $(\sec\theta)_{\rm max}$ with energy for EPOS-LHC (upper left panel), QGSJETII-04 (upper right panel), EPOS 1.99 (central left panel), QGSJETII-03 (central right panel) and Sibyll 2.1 (bottom panel) hadronic models showing the linear fit. Colours represent the different primary species: proton (red) and iron (blue). Vertical error bars are the statistical uncertainties of $(\sec\theta)_{\rm max}$ calculated from the fit to a Gaussian function of the asymmetry factor vs $\ln(\sec\theta)$. Stations in the radial interval 500 - 2000 m have been included. Results for other intervals will be shown in the next chapter.

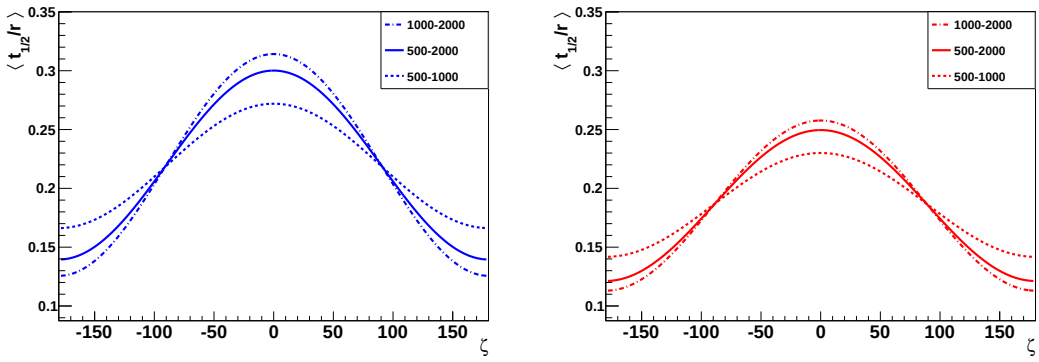

Figure 4.29: Dependence of $\langle t_{1/2}/r \rangle$ vs ζ with the chosen core distance intervals for MC simulations using EPOS-LHC hadronic model with proton (left panel) and iron (right panel) induced showers with a mean energy of $\log(E/\mathrm{eV}) = 19.2$ and $\theta = 50°$.

$(\sec\theta)_{\max}$ and $X_{\max}$ is expected. This will be studied in the next section.

As shown in Fig. 4.28, $(\sec\theta)_{\max}$ follows a linear dependence with energy and the corresponding fits for proton and iron showers are well separated, allowing thus the discrimination between light and heavy primaries. In addition, as will be discussed later in sections 4.7 and 5.5, $(\sec\theta)_{\max}$ is linearly correlated with the shower maximum depth (see also [206]) and thus it can be used to measure the mass composition of the event sample as a function of the primary energy.

From the MC results for proton ($A = 1$) and iron ($A = 56$) showers, a relationship between $(\sec\theta)_{\max}$ and the average mass of primary cosmic ray can be established by means of expression (2.28).

$$\langle \ln A \rangle = \frac{(\sec\theta)_{\max,\mathrm{p}} - (\sec\theta)_{\max,\mathrm{data}}}{(\sec\theta)_{\max,\mathrm{p}} - (\sec\theta)_{\max,\mathrm{Fe}}} \ln 56 \; . \tag{4.24}$$

In addition, deviations in the $(\sec\theta)_{\max}$ values of data can be easily transformed into deviations in $\langle \ln A \rangle$ with the expression:

$$\langle \Delta \ln A \rangle = -\frac{\Delta(\sec\theta)_{\max,\mathrm{data}}}{(\sec\theta)_{\max,\mathrm{p}} - (\sec\theta)_{\max,\mathrm{Fe}}} \ln 56 \; . \tag{4.25}$$

4.6.4 Dependence of $(\sec\theta)_{\max}$ on the radial interval

As mentioned before, the plots used in section 4.6 to explain the procedure with the assistance of MC simulations have been produced using all the tanks passing the cuts described in section 4.4 within the radial interval 500 - 2000 m. However, the azimuthal

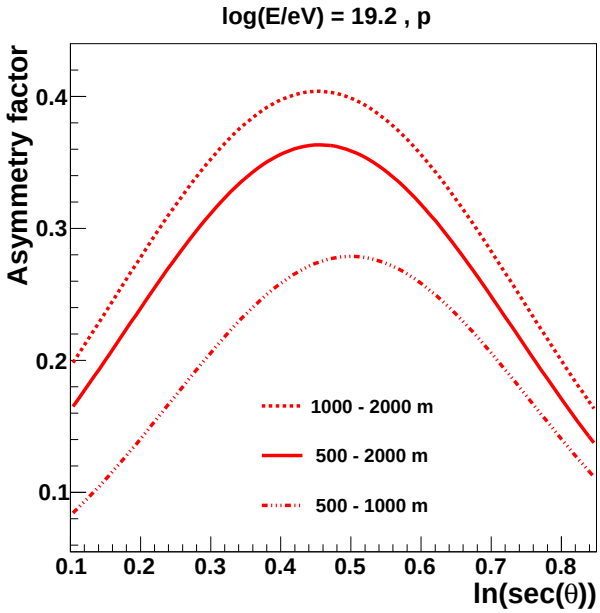

Figure 4.30: Dependence of the asymmetry factor vs $\ln(\sec\theta)$ with the chosen core distance intervals for an EPOS-LHC proton shower with a mean energy of $10^{19.2}$ eV.

asymmetry of $\langle t_{1/2}/r\rangle$ is expected to grow with the radial distance of the stations used in the analysis. If the number of available events is sufficiently large it is desirable to split the sample of stations in several radial intervals. As an example, in Fig. 4.29 the azimuthal asymmetry of the whole radial interval is compared with that obtained in two independent radial intervals (500 - 1000 m and 1000 - 2000 m) for proton and iron MC showers, corresponding to a mean energy of $10^{19.2}$ eV and $\theta = 50°$ using the EPOS-LHC hadronic model.

This dependence of the asymmetry factor with r leads to a dependence of $(\sec\theta)_{\max}$ with the r-interval, as can be seen in Fig. 4.30. As expected, it can be observed that selecting stations close to the core (500 - 1000 m) leads to systematically larger $(\sec\theta)_{\max}$ values, since the closer to the core the stations are, the weaker the asymmetry is (the electromagnetic contribution dominates). Thus, the zenith angle at which the muon component starts to dominate, and the asymmetry starts to decrease, is higher. However it is important to note that, in principle, this dependence of $(\sec\theta)_{\max}$ with the radial interval should not limit the capability of this technique for the determination of the mass composition as far as the behaviour of MC and data with respect to the radial interval is the same.

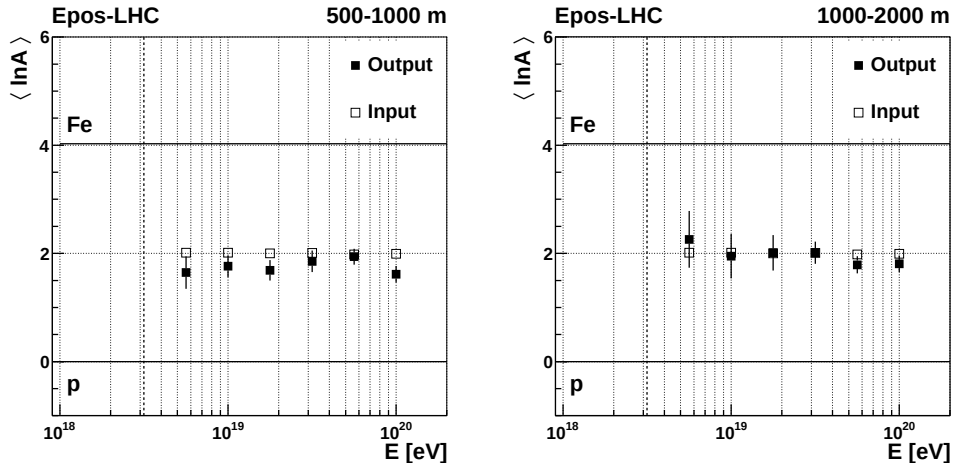

Figure 4.31: Differences of $\ln A$ between the generated values (input) and the obtained ones with the asymmetry analysis (output) for the 50%p - 50%Fe sample using EPOS-LHC hadronic model in both intervals: 500 - 1000 m (left panel) and 1000 - 2000 m (right panel).

Since the $(\sec\theta)_{\max}$ parameter will be used for the determination of the mass composition in the next chapter, it is thus very important to check that the quality cuts of this analysis do not introduce any mass-dependent bias. This is the case when stations in the 500 - 2000 m interval are used, as was demonstrated in [207]. However, since two radial subintervals will be used in this work, 500 - 1000 m and 1000 - 2000 m, the relative efficiency p/Fe has to be compared using stations in both core distance ranges. To this end three samples of mixed composition (25%p - 75%Fe, 50%p - 50%Fe and 75%p - 25%Fe) have been produced with hadronic models QJSJETII-04 and EPOS-LHC. The corresponding $(\sec\theta)_{\max}$ values have been obtained for each energy bin applying the asymmetry analysis and the results have been compared with those of the pure samples of proton and iron. Using expression (4.24), the value of $\langle \ln A \rangle$ has been obtained for the samples and compared with the real one. As an example, results for the 50%p - 50%Fe sample using the EPOS-LHC hadronic model are shown in Fig. 4.31 for both r-intervals. As can be seen, the comparison for this example in the 1000 - 2000 m interval (right panel) shows small differences in both directions, while results in the 500 - 1000 m interval (left panel) might be subjected to non-negligible bias leading to lighter compositions applying the asymmetry analysis.

These model dependent differences in the reconstructed mass can be interpreted as a systematic uncertainty of the $(\sec\theta)_{\max}$ parameter as a tool for the evaluation of

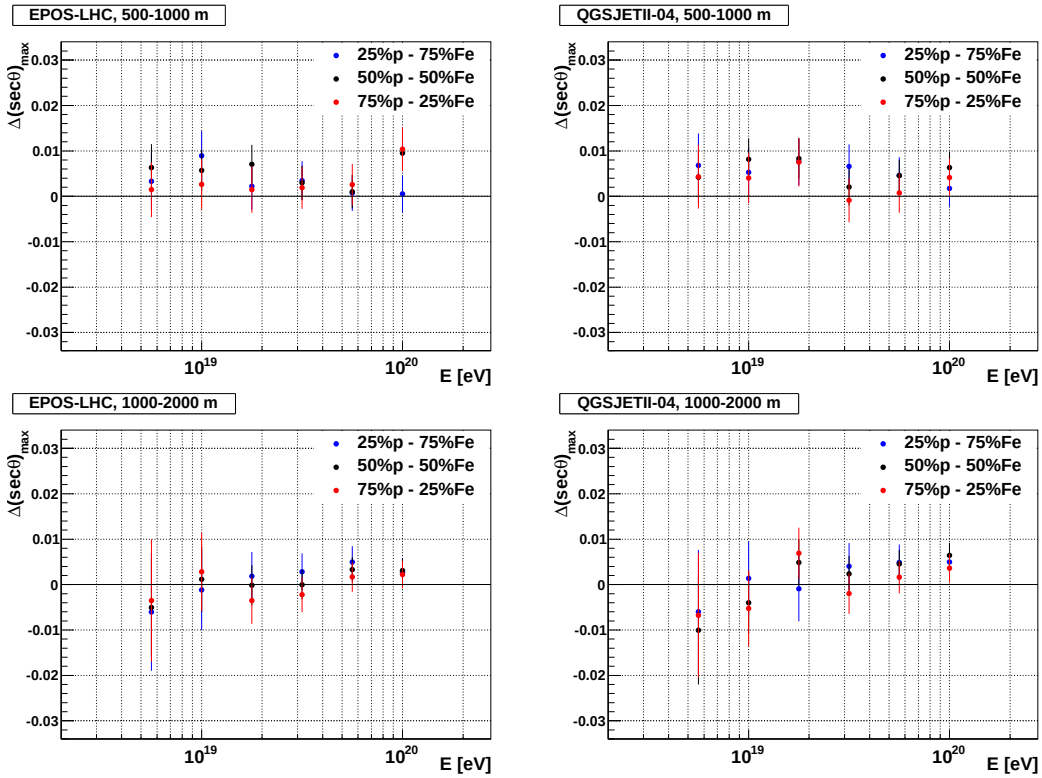

Figure 4.32: $\Delta(\sec\theta)_{\max}$ (see text) vs E for three samples with different p-Fe fractions using EPOS-LHC (left panels) and QGSJETII-04 (right panels) hadronic models in the radial intervals 500 - 1000 m (top panels) and 1000 - 2000 m (bottom panels).

the mass composition. The value of the corresponding deviation of $(\sec\theta)_{\max}$ can be calculated from those of $\langle \ln A \rangle$ using expression (4.25). The results for both models and radial intervals are shown in Fig. 4.32. As can be observed, for both core distance intervals the largest deviations $\Delta(\sec\theta)_{\max}$ take place for a 50%p - 50%Fe composition and are of about 0.01 units of $(\sec\theta)_{\max}$. It should be stressed that these deviations are not systematic uncertainties of the $(\sec\theta)_{\max}$ parameter itself but they give the corresponding uncertainties in mass units due to the dependence of the selection efficiency on the composition when using equations (4.24) and (4.25).

4.7 Correlation between $(\sec\theta)_{\max}$ and $X_{\max}$

As has been already explained, there is a similarity between the behaviour of the SD parameter $(\sec\theta)_{\max}$ and the FD observable $X_{\max}$. These parameters, measured

with two different techniques, are expected to be correlated because both depend on the speed of the shower development (and hence on primary mass), as it was shown in [235].

To study the relationship between both observables, the generated value of the shower maximum depth of MC showers simulated using the EPOS-LHC and QGSJETII-04 models was considered. Using these values the showers are grouped within bins of $X_{\max}$, with widths chosen to have enough statistics to perform accurately the asymmetry analysis. These bins will be different for proton and iron showers because the covered $X_{\max}$ range is different for both primaries: iron populates the lower region (lower $X_{\max}$ values) while proton populates the upper region (higher $X_{\max}$ values) overlapping in a wide middle region.

With the events grouped in $X_{\max}$ bins, $(\sec\theta)_{\max}$ is obtained as a function of the corresponding mean value $\langle X_{\max}\rangle$. Note that this study cannot be carried out event by event, but on average values, obtaining a result of the $(\sec\theta)_{\max}$ parameter for each $\langle X_{\max}\rangle$ value. In Fig. 4.33 the relationship between $(\sec\theta)_{\max}$ and $X_{\max}$ is shown for all the hadronic models and for both primaries. As can be seen in this figure, there is a strong linear correlation between both observables independently of the primary type and for all the hadronic models. The results confirm that the $(\sec\theta)_{\max}$ parameter obtained through the analysis of the observed azimuthal asymmetry is a reliable mass estimator. This figure has been produced using stations in the 500 - 2000 m interval. As will be shown in the next chapter, the results in the intervals 500 - 1000 m and 1000 - 2000 m also show a strong correlation between $(\sec\theta)_{\max}$ and $X_{\max}$ in good agreement with data.

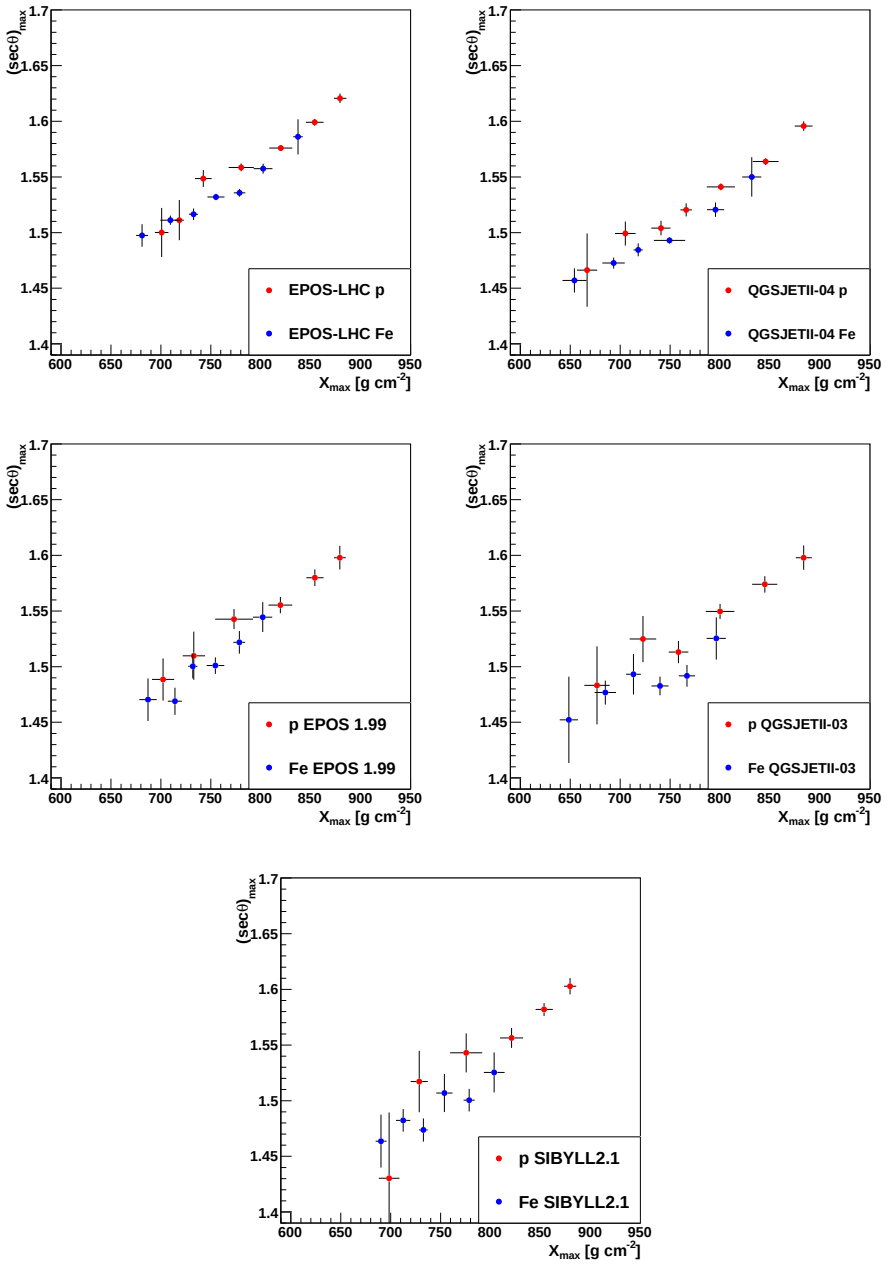

Figure 4.33: Correlation between the SD parameter $(\sec\theta)_{\max}$ and the FD parameter $X_{\max}$ for EPOS-LHC (upper left panel), QGSJETII-04 (upper right panel), EPOS 1.99 (central left panel), QGSJETII-03 (central right panel) and Sibyll 2.1 (bottom panel) hadronic models. $(\sec\theta)_{\max}$ has been obtained using stations in the 500 - 2000 m.

Chapter 5

Mass composition from the azimuthal asymmetry of the risetime

5.1 Introduction

As stated in chapter 2, direct detection of ultra-high-energy cosmic rays is not feasible and therefore their properties have to be obtained from the extensive air showers developed in the atmosphere. In particular, inferring the nature of the primary particle is a complicated task. In principle, neutrinos and photons can be easily distinguished from nuclei; however, discriminating between different nuclei according to their mass is extremely difficult. It is well known that, on average, showers initiated by heavier nuclei develop higher in the atmosphere and they have, at ground level, a larger number of muons. However these differences are difficult to observe because of the large statistical fluctuations of the shower development. On the other hand all methods for mass composition rely on the comparison with simulations that use models for the hadronic interactions based on accelerator data at centre of mass energies much smaller than those of the interactions of UHECRs in the atmosphere. As will be discussed later, this is the main source of systematic uncertainty that presently limits our capability to measure the composition at these energies.

Mass composition can be determined from the average and variance of the $X_{\max}$ distributions recorded by fluorescence telescopes (see section 2.7.1 for details). Unfortunately, as it has been pointed out in chapter 3, these telescopes have a duty cycle of about 13% that severely limits the size of the data sample. For this reason, meth-

ods based on the information provided by the surface detectors, which have a ∼100% duty cycle, are being developed by the Auger collaboration, like the one based on the azimuthal asymmetry of the SD signals that is presented in this thesis. This method has been described in the previous chapter with the help of MC simulations. Here, it will be applied to data of the Pierre Auger Observatory to extract information on the mass composition. In section 5.2 the steps of the analysis are shown. In section 5.3 the systematic uncertainties in the measurement of $(\sec\theta)_{\max}$ are described. In section 5.4 the results of mass composition versus primary energy obtained from the analysis in several radial intervals for two models of hadronic interactions will be shown, and inconsistencies with models will be discussed. Finally, in section 5.5 the expected correlation between $(\sec\theta)_{\max}$ and $X_{\max}$ is studied using hybrid events collected by the Observatory, pointing to check the feasibility of the method. These results have been published in [236].

5.2 Obtaining $(\sec\theta)_{\max}$ for real events

After the description of the sample of data used in the analysis, the values of $(\sec\theta)_{\max}$ are obtained as a function of the primary energy. As explained previously in 4.6.4, analyses are carried out separately using the signal of stations in different intervals of the core distance. Finally, experimental results are compared with MC predictions carried out with several hadronic interaction models.

5.2.1 The event sample

Events collected with the SD of the Pierre Auger Observatory from January 2004 to October 2014 excluding the so-called bad periods (periods of instabilities defined in chapter 3) have been reconstructed with the $\overline{\text{Off}}\underline{\text{line}}$ version v2r9p3.

As already mentioned, this asymmetry analysis cannot be performed on an event by event basis and therefore the sample has to be split in bins of energy and zenith angle. The sample of MC showers used in the previous chapter had fixed values of both E and θ. On the contrary, in real showers both parameters can obviously have any value on a continuous distribution. The sample used for the analysis contains events with zenith angle between 30° and 62° and energy larger than $10^{18.5}$ eV with the following binning:

- θ in 10 bins of equal size: [30.0,33.2), [33.2,36.4), [36.4,39.6), [39.6,42.8), [42.8,46.0), [46.0,49.2), [49.2,52.4), [52.4,55.6), [55.6,58.8), [58.8,62.0).

- $\log(E/\text{eV})$ in 6 bins of different widths: [18.55,18.70), [18.70,18.85), [18.85,19.00), [19,00,19.20), [19.20,19.50) and one last bin with $\log(E/\text{eV}) \geq 19.50$.

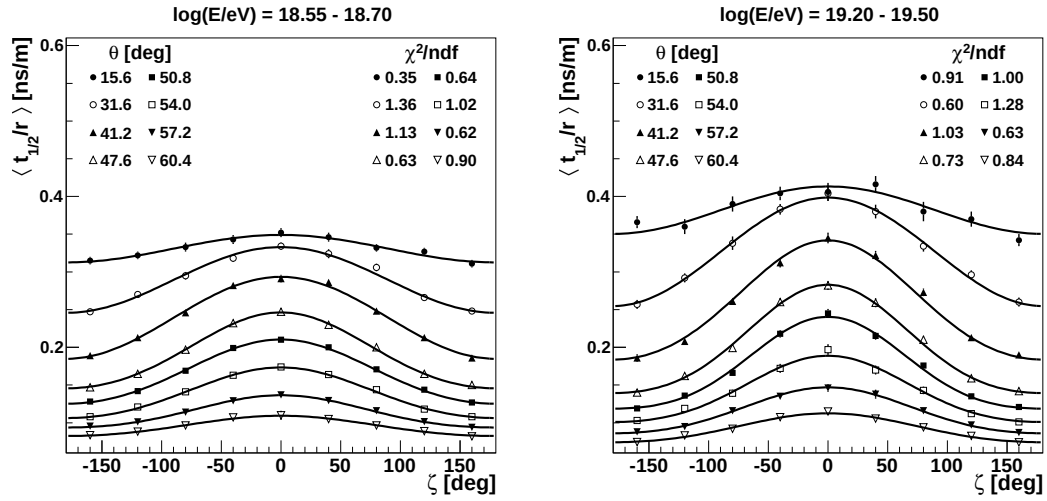

Figure 5.1: $\langle t_{1/2}/r\rangle$ vs ζ angle in the shower plane for primary energy $\log(E/\mathrm{eV}) = 18.55 - 18.70$ (left) and $\log(E/\mathrm{eV}) = 19.2 - 19.5$ (right) at different zenith angle bands. Each data point represents an average (with the corresponding uncertainty) over all stations surviving the selection criteria.

These intervals are selected to keep a reasonable statistics in each interval, allowing good quality fits in the various steps of the analysis.

After applying the quality cuts defined in section 4.4, a total of 191534 FADC signals from 54584 events were available. The most energetic event registered in the data sample has an energy of 1.26×10^{20} eV.

5.2.2 Measurement of the azimuthal asymmetry

The first step is to measure the azimuthal asymmetry from the dependence of $\langle t_{1/2}/r\rangle$ on ζ for each of the above-defined bins of E and θ. As mentioned in 4.5, the risetime of the stations are split in several intervals of ζ angle, and the average $\langle t_{1/2}/r\rangle$ and RMS of the corresponding distributions are calculated. As an example, in Fig. 5.1 the results for the bin with mean energies $\log(E/\mathrm{eV}) = 18.6$ (left panel) and $\log(E/\mathrm{eV}) = 19.4$ (right panel) are shown for several θ intervals[1]. The vertical bars represent the statistical error of the average $\langle t_{1/2}/r\rangle$, that is, the RMS of the distribution divided

[1]Including $\theta = 15.6^\circ$ as a comparison with a zenith interval where the asymmetry due to the longitudinal evolution of the shower does not dominate. This zenith angle is not used in the asymmetry analysis.

Fraction (%) of stations		
$\log(E/\text{eV})$	500-1000m	1000-2000m
18.6	70%	30%
18.8	56%	44%
18.9	45%	55%
19.1	36%	64%
19.3	26%	74%
19.6	20%	80%

Table 5.1: Fraction of stations distributed in each r-interval for each E bin.

by the squared root of the number of triggered stations contributing to the histogram. The asymmetry between risetime values of early and late region is clearly observed. As already explained in 4.6, in general, the relationship between $\langle t_{1/2}/r\rangle$ and ζ can be fitted to a linear function in $\cos\zeta$ (equation (4.17)) although at large θ and E values a quadratic function (equation (4.21)) is necessary. In Fig. 5.2 both fits are compared for the case of $\log(E/\text{eV}) = 18.8$. It can be noticed that the quadratic term becomes more important as the zenith angle increases.

In the above examples, all stations in the radial interval 500 - 2000 m were used. Since the number of events collected by the SD passing the cuts of this analysis is large enough to allow the analysis in two independent subintervals of r, the same calculation has also been carried out separately for stations in the 500 - 1000 m and 1000 - 2000 m intervals. This selection leads to a total of 102123 FADC signals from stations passing the cuts for the 500 - 1000 m interval, and 89411 FADC signals for the 1000 - 2000 m interval. The fraction of the stations for each r-interval and energy bin is detailed in Table 5.1. As an example, the results for these intervals are compared with that of the 500 - 2000 m for $\theta = 51^\circ$ and $\log(E/\text{eV}) = 19.1$ in Fig. 5.3, showing the same features observed in the MC simulations (Fig. 4.29), that is, the azimuthal asymmetry grows with the radial distance of the stations used in the analysis.

5.2.3 $(\sec\theta)_{\max}$ versus energy

The asymmetry factor and its uncertainty are calculated for all energy and angular bins from equations (4.17) and (4.21) like in the analysis of MC events. In Fig. 5.4 their values are represented as a function of the azimuthal angle for all energy bins using the traces of all stations in the 500 - 2000 m interval are presented alongside with the fit

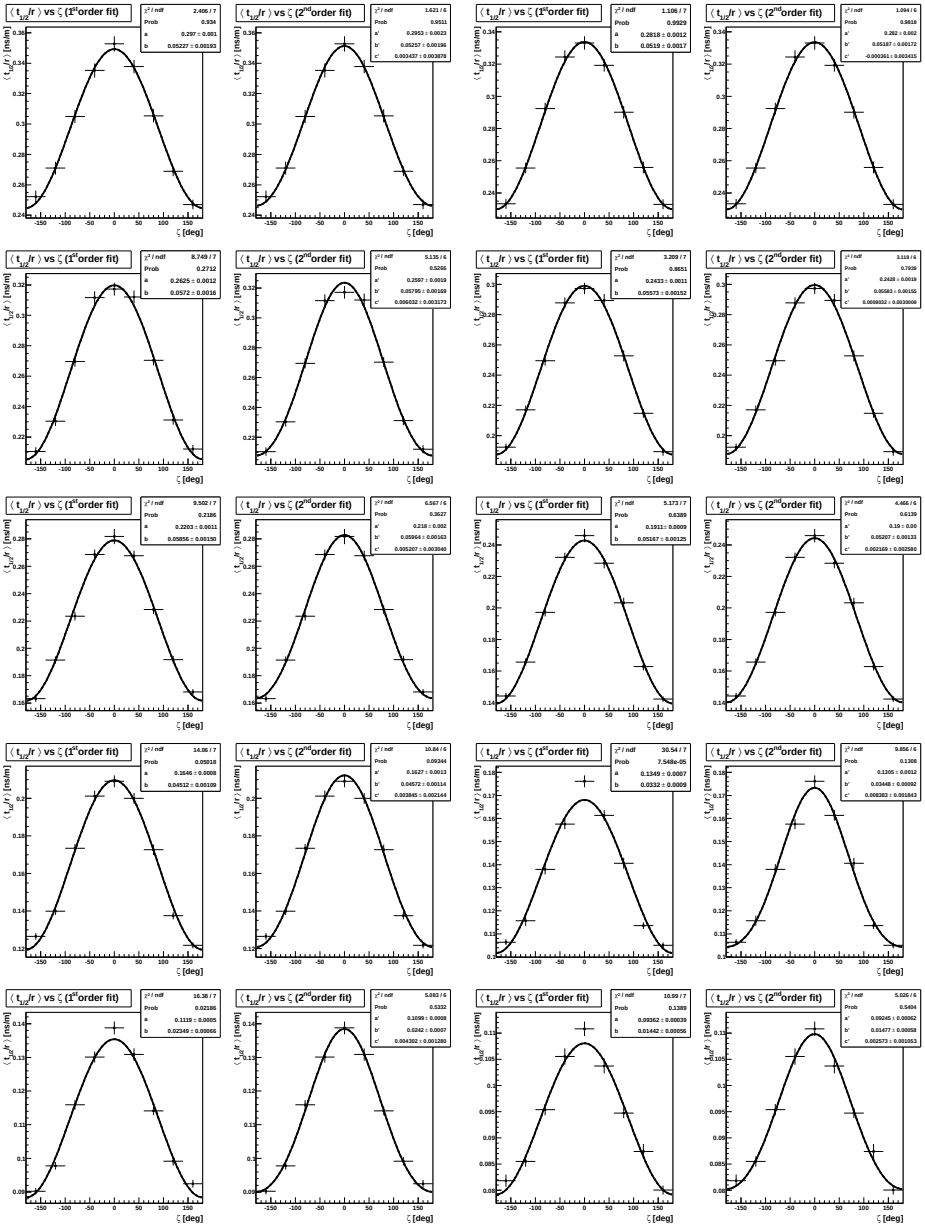

Figure 5.2: $\langle t_{1/2}/r \rangle$ vs ζ for data with an energy bin of mean value $\log(E/\mathrm{eV})= 18.8$. The average value of the θ angle are: 31.6°, 34.8°, 38.0°, 41.2°, 44.4°, 47.6°, 50.8°, 54.0°, 57.2°and 60.4°, increasing from upper left to bottom right. Linear (first and third columns) and second order (second and fourth columns) fits are compared. The second order one is necessary at large zenith angles.

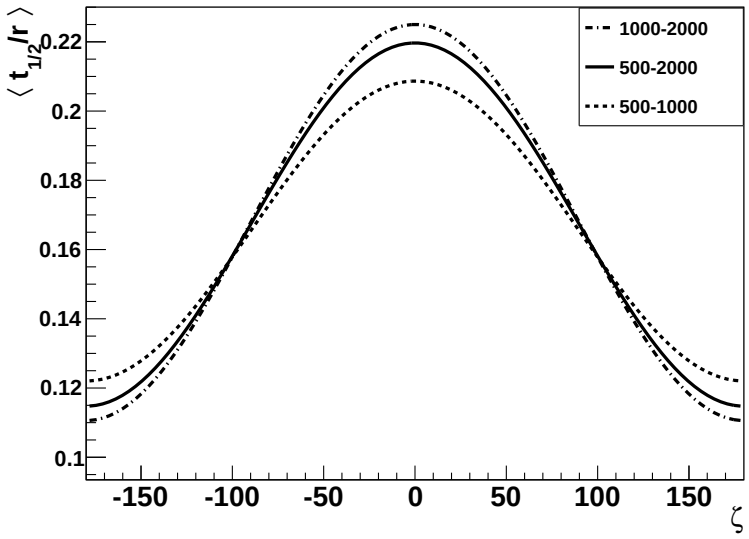

Figure 5.3: Dependence of $\langle t_{1/2}/r \rangle$ vs ζ with the chosen core distance intervals for data with $\theta = 51°$and $\log(E/\mathrm{eV}) = 19.1$.

to a Gaussian function. The expected dependence of the asymmetry parameter with $\sec\theta$ is found, that is, it reaches a maximum at a $(\sec\theta)_{\max}$ value that will be used as the observable for mass determination. The $(\sec\theta)_{\max}$ results obtained from the fits for each energy bin are represented against the corresponding average value of the reconstructed energy in Fig. 5.5. The vertical error bars are the statistical uncertainties evaluated in the same way than for the MC samples.

The same analysis has been repeated for the r-intervals 500 - 1000 and 1000 - 2000 m. The evolution of the asymmetry factor for both intervals with the zenith angle is represented in Figs. 5.6 and 5.7 respectively. The results of $(\sec\theta)_{\max}$ vs E for both intervals are represented in Fig. 5.8, showing the expected features mentioned in the previous chapter, that is, the closer to the core the stations are, the weaker the azimuthal asymmetry is, and the zenith angle at which the muon component starts to dominate (and the asymmetry starts to decrease) is higher. As already pointed out, this dependence of $(\sec\theta)_{\max}$ with the chosen r-interval should not limit the capability of this observable for mass composition as far as the MC simulations follow the same behaviour.

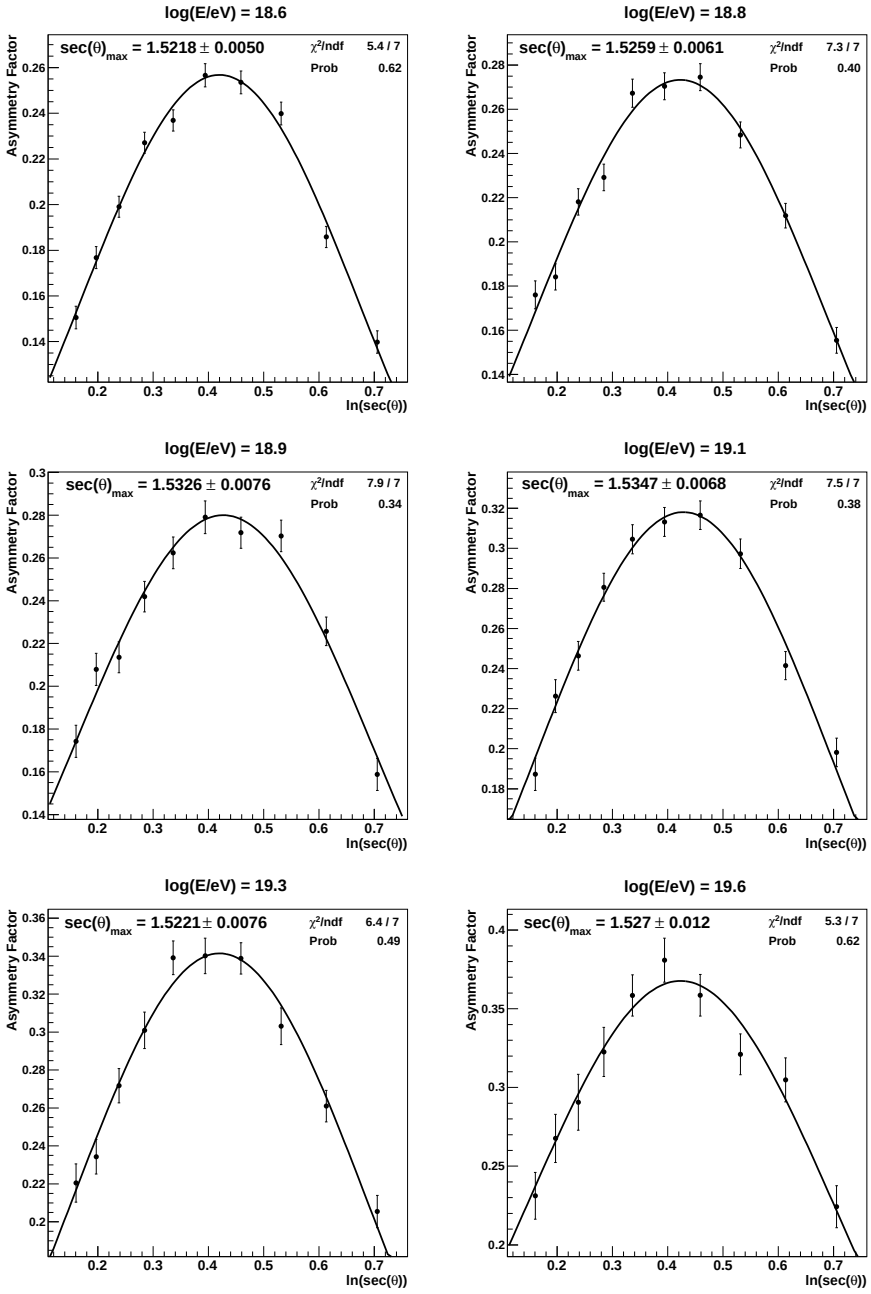

Figure 5.4: Asymmetry factor vs $\ln(\sec\theta)$ for data in all energy bins. The energy increases from upper left to bottom right. The Gaussian fit reaches a maximum at an angle $(\sec\theta)_{\max}$ that defines the mass sensitive parameter. All stations in the 500 - 2000 m interval have been used. Statistical error bars are evaluated as in Fig. 4.26.

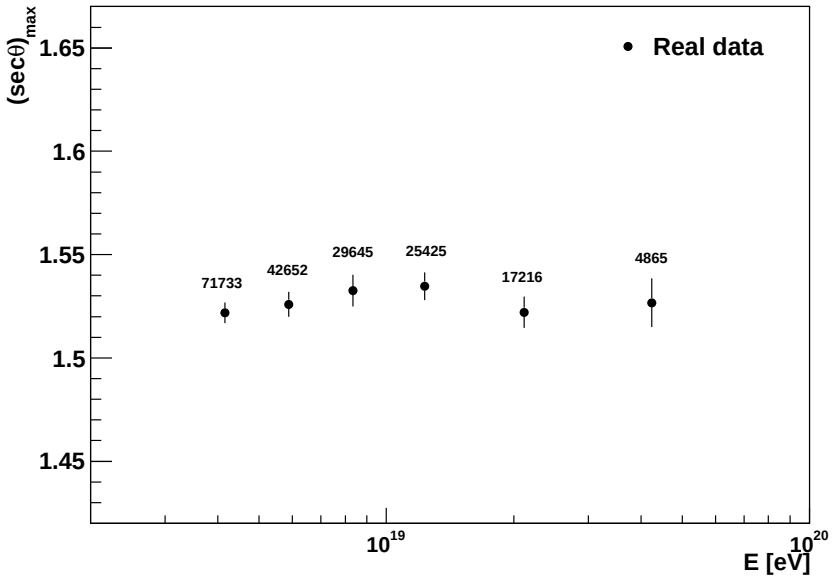

Figure 5.5: $(\sec\theta)_{\max}$ vs $\log(E/\mathrm{eV})$ for real events. Number of stations in the 500 - 2000 m interval available for the analysis are indicated. Vertical bars are statistical uncertainties obtained from the fits to a Gaussian function in plots of Fig. 5.4.

5.2.4 Comparison with MC simulations

In this section, results of $(\sec\theta)_{\max}$ versus energy for both real and simulated showers (proton and iron primaries) will be compared. Details of the libraries and analyses of the MC events have been explained in chapter 4. In Fig. 5.9 it is shown the comparison for proton (red) and iron (blue) simulations using the following hadronic models: EPOS 1.99, QGSJETII-03, SIBYLL 2.1, EPOS-LHC and QGSJETII-04. In both data and MC simulations, all stations in the 500 - 2000 m r-interval are used. As can be observed, data are bracketed by the predictions of proton and iron showers for all the hadronic models.

Results using only stations in the core distance intervals 500 - 1000 m or 1000 - 2000 m have also been compared with MC results in the corresponding radial interval. For these comparisons, only the most recent hadronic models, EPOS-LHC and QGSJETII-04, have been used. The results are shown in Fig. 5.10. From these plots it is difficult to draw strong conclusions; however, in both cases, there is an indication that the mean mass increases slowly with energy in line with other Auger studies [99, 109]. In

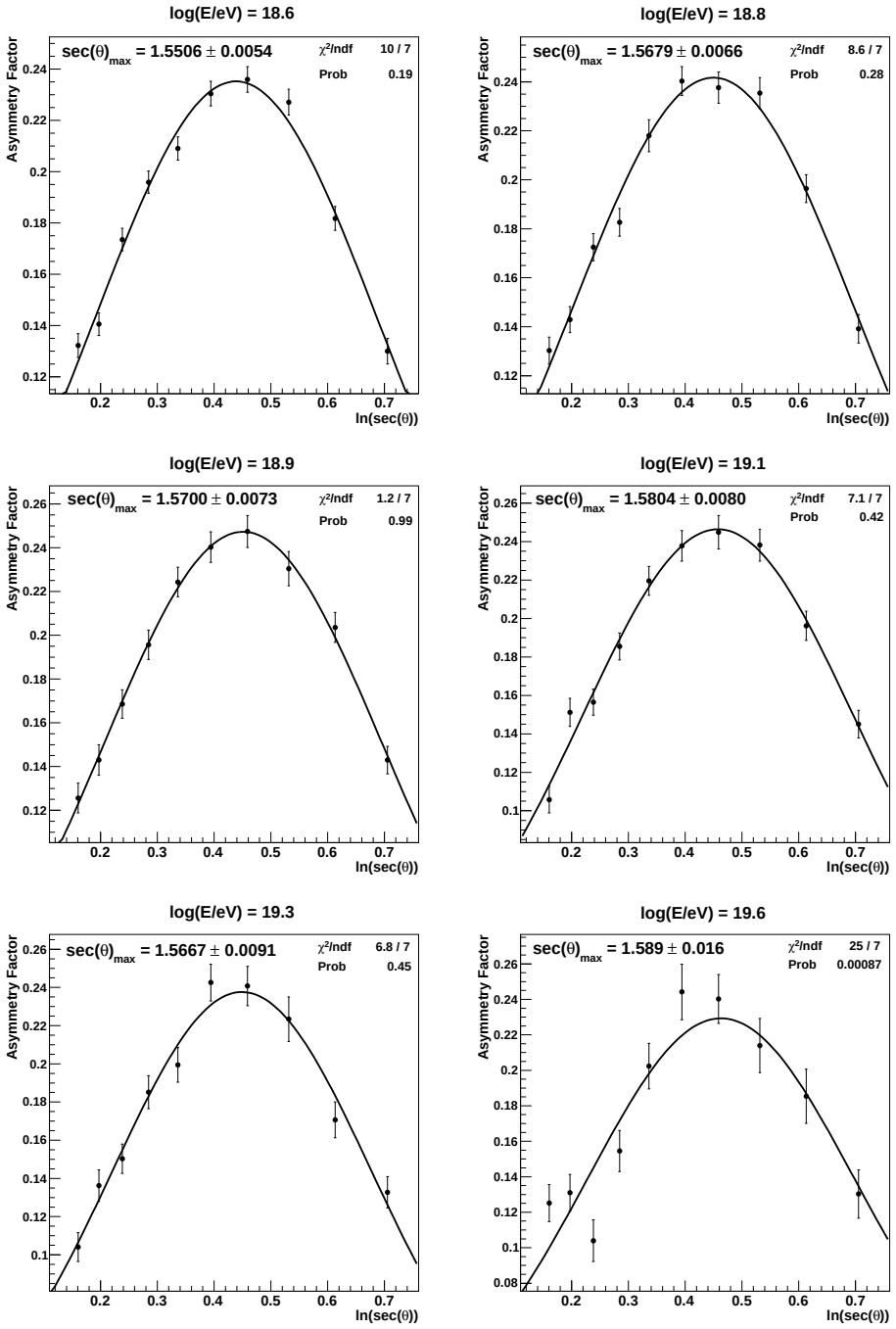

Figure 5.6: Asymmetry factor vs $\ln(\sec\theta)$ for data in all the energy bins for the 500 - 1000 m r-interval. The energy increases from upper left to bottom right.

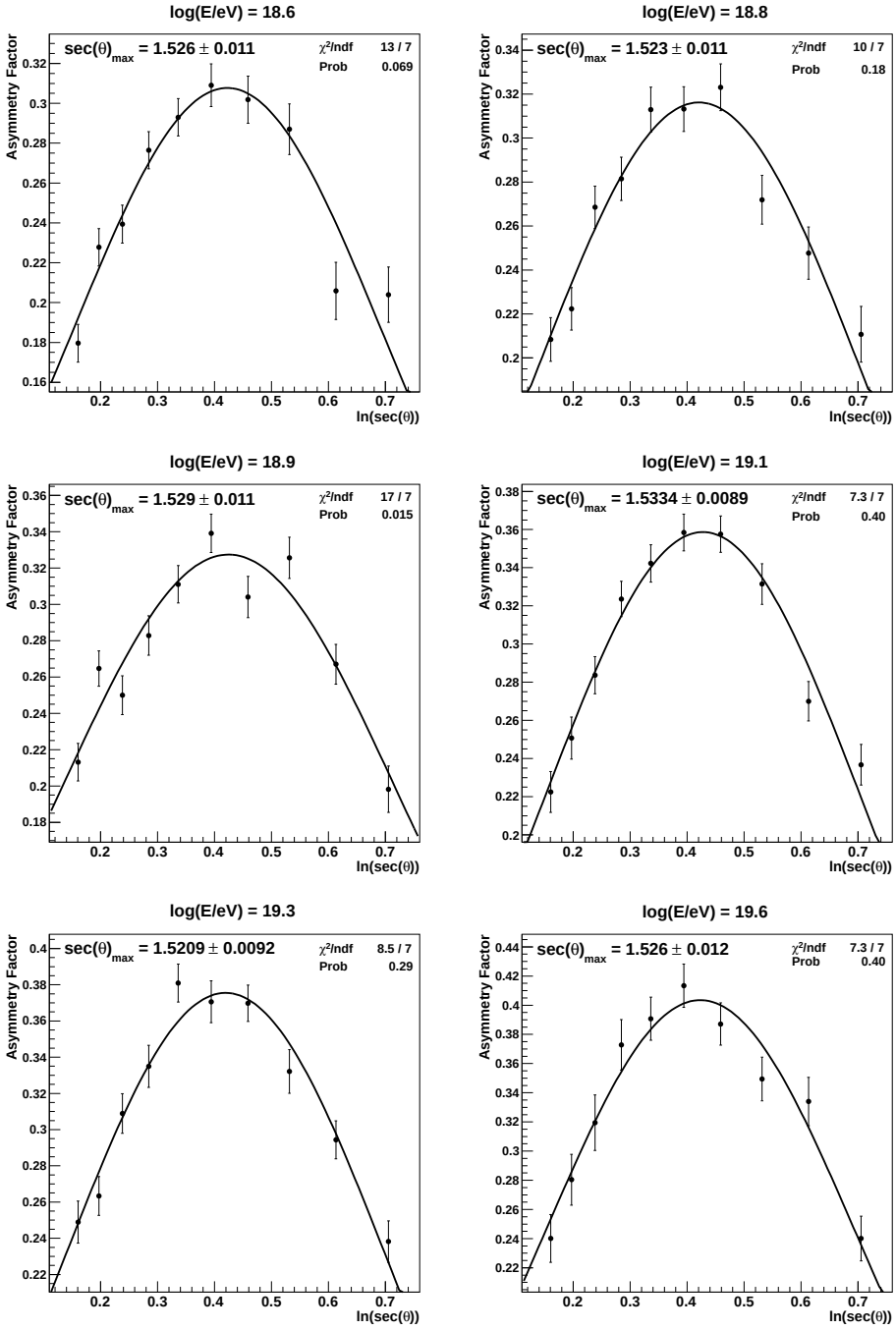

Figure 5.7: Asymmetry factor vs $\ln(\sec\theta)$ for data in all the energy bins for the 1000 - 2000 m r-interval. The energy increases from upper left to bottom right.

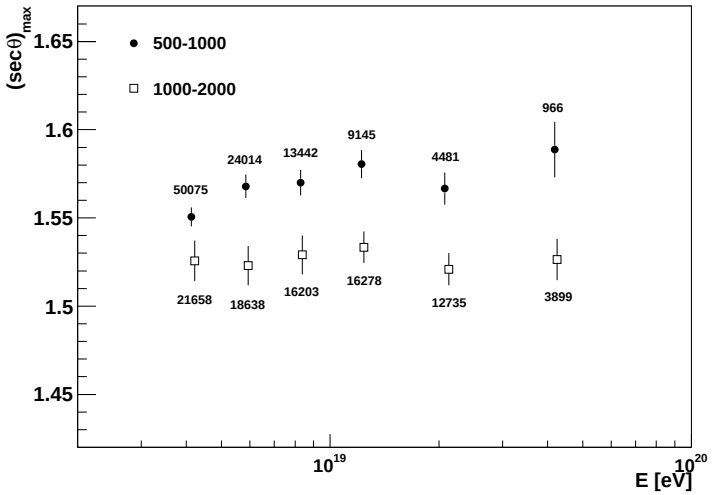

Figure 5.8: Energy dependence of $(\sec\theta)_{\max}$ for both intervals of core distance 500 - 1000 m and 1000 - 2000 m. The number of stations available for the analysis is indicated.

addition, in these plots it can also be noticed a possible inconsistency of results between both intervals when they are compared with the predictions of QGSJETII-04, that is, the comparison with MC shows a heavier composition in the 500 - 1000 m range than in the 1000 - 2000 m interval. This unphysical result points to a discrepancy between the radial features of real EASs and the predictions of QGSJETII-04 that will be analysed later. In order to quantify this effect, an analysis in terms of mass composition has been carried out in both intervals, and the results will be shown in section 5.4.

5.3 Systematic uncertainties

There are several contributions to the uncertainty in the determination of the mass sensitive parameter $(\sec\theta)_{\max}$.

In particular it has been studied the impact of the uncertainty in the reconstruction of the core position (5.3.1), the assumed parameterization for the radial dependence of $t_{1/2}$ (5.3.2), the effect of the systematic uncertainty in the risetime measurement (5.3.3) and the systematic uncertainty in the energy scale of the Auger experiment (5.3.4). In the first place, each of the above parameters that could contribute to the systematic uncertainty in $(\sec\theta)_{\max}$ has been modified individually and the full analysis has been

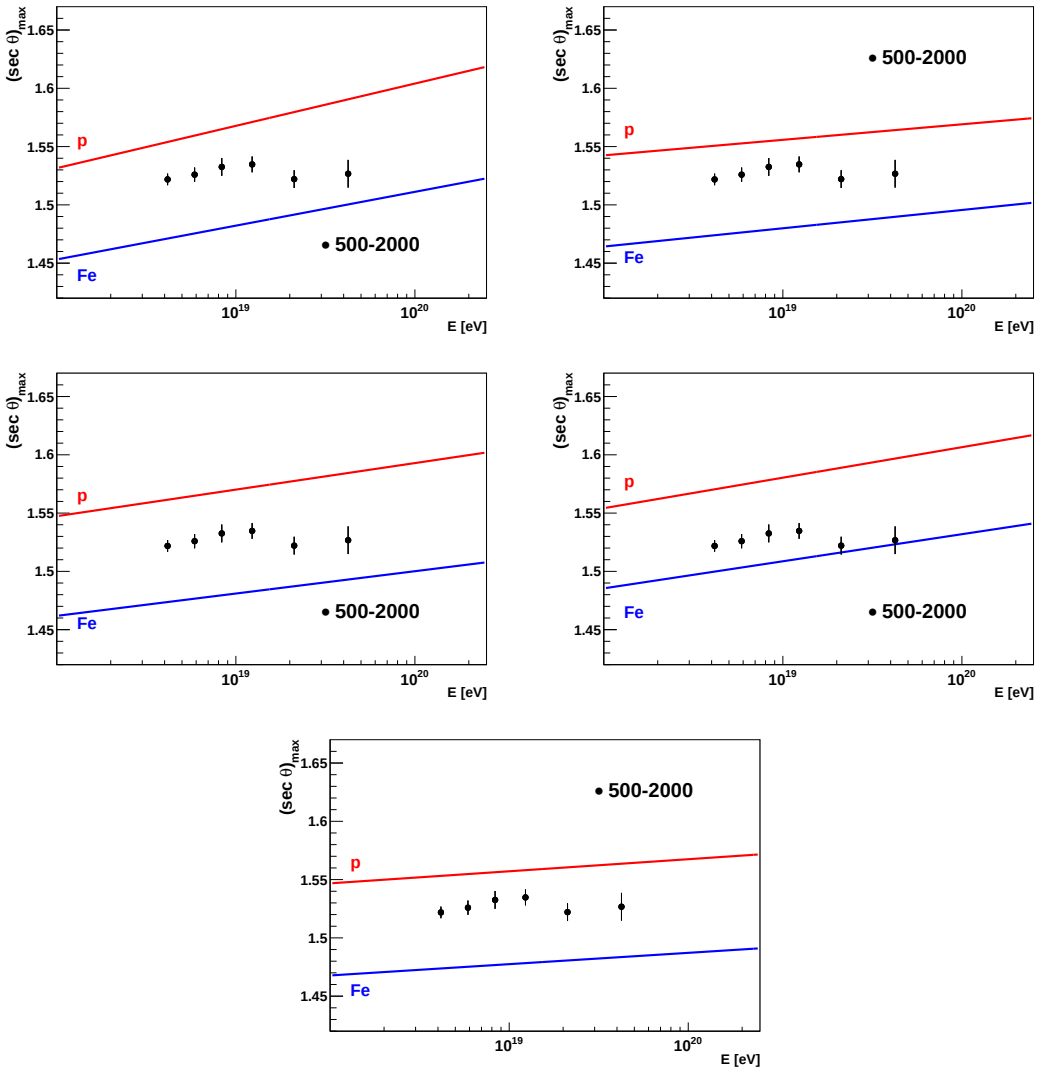

Figure 5.9: Comparison of data results (black dots) of $(\sec\theta)_{\max}$ versus energy with MC predictions for protons (red line) and iron nuclei (blue line) in the r-interval 500 - 2000 m assuming the following models of hadronic interactions: EPOS 1.99 (upper left panel), QGSJETII-03 (upper right panel), Sibyll 2.1 (central left panel), EPOS-LHC (central right panel) and QGSJETII-04 (bottom panel). Vertical bars are statistical uncertainties.

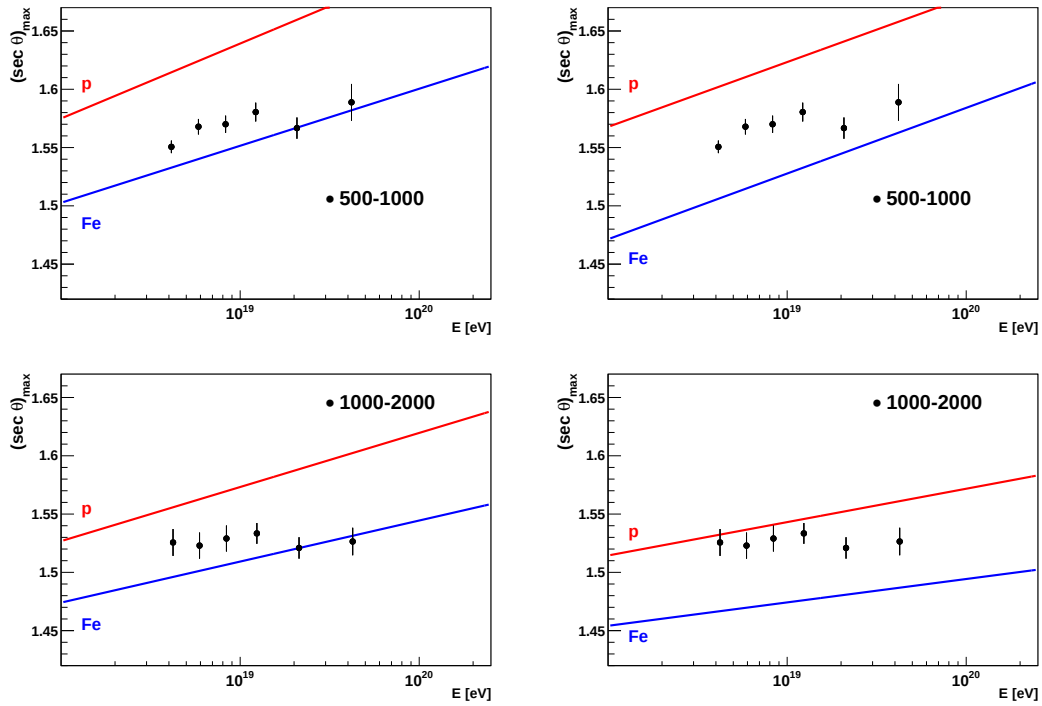

Figure 5.10: Comparison of data results (black dots) of $(\sec\theta)_{\max}$ versus energy with MC predictions for protons (red line) and iron nuclei (blue line) in the r-intervals 500 - 1000 m (upper panels) and 1000 - 2000 m (bottom panels) for EPOS-LHC (left panels) and QGSJETII-04 (right panels) hadronic models. Vertical bars are statistical uncertainties.

repeated for all energy bins. Then, the corresponding deviation in $(\sec\theta)_{\max}$ is represented as a function of the energy, and a linear fit is performed. The maximum positive and negative values taken by the fit in the whole energy interval are conservatively used to estimate the systematic uncertainty. This study has been carried out for the two radial intervals used in the analysis.

In addition several cross checks have been carried out (5.3.6) to confirm that other elements of the analysis, e.g., selection cuts in both the signal intensity and the zenith angle, seasonal-dependent weather effects, etc., do not lead to additional uncertainties.

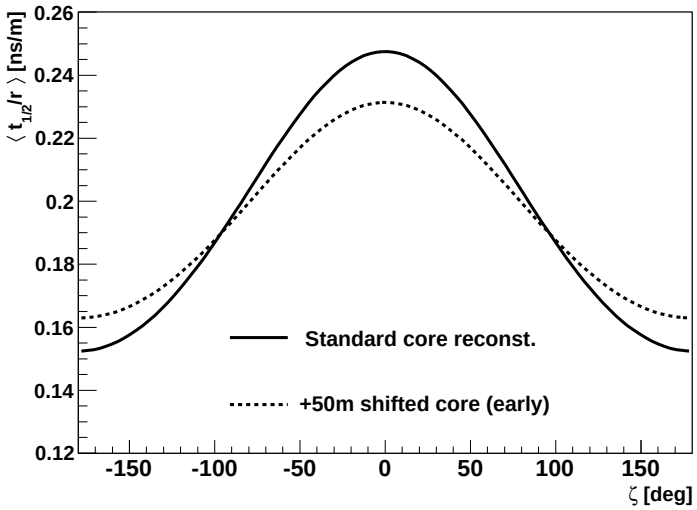

Figure 5.11: Example of differences in $\langle t_{1/2}/r \rangle$ vs azimuth angle in the shower plane using the original core position (solid line) and the modified one (dashed line) shifting the core 50 m towards the late region for $\log(E/\mathrm{eV}) = 19.1$ eV and $\theta = 47.6°$ in the 500 - 1000 m radial interval.

5.3.1 Core position reconstruction

As it was explained in section 4.2.3, the reconstructed position of the core is shifted with respect to the real one towards the early region. Note that this systematic uncertainty in the core position is translated to the ratio $\langle t_{1/2}/r \rangle$ used in the evaluation of the asymmetry factor (see Fig. 5.11), and therefore the value of $(\sec\theta)_{\max}$ is expected to be correspondingly affected. In order to study its contribution to the total systematic uncertainty, the position of the core is shifted in the late direction by 50 m to compensate the systematic shift due to the reconstruction. The value of 50 m is chosen because it corresponds to the typical uncertainty in the reconstructed core position [144]. Then, the whole chain of analysis is repeated to obtain the new values of the position of the maximum of the asymmetry, and the difference with the nominal $(\sec\theta)_{\max}$.

In Fig. 5.12 the difference in $(\sec\theta)_{\max}$ values are shown in both intervals of core distance. The linear fit is represented by a red dashed line, and the maximum and minimum values considered are numerically shown and also represented with horizontal solid lines. As can be observed, the systematic uncertainty from the reconstruction of

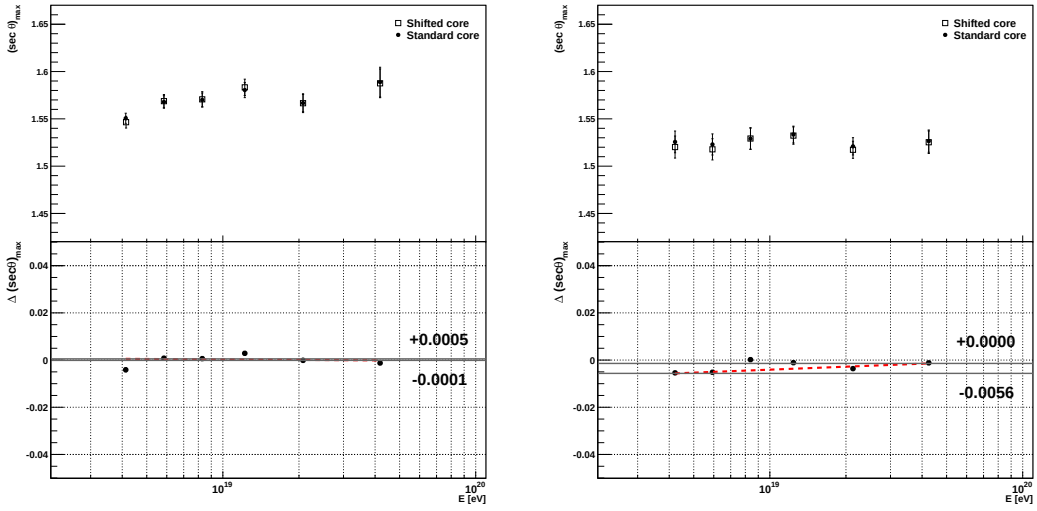

Figure 5.12: Differences between values of $(\sec\theta)_{\max}$ when the core position is modified 50 m towards the late region in the core distance ranges of 500 - 1000 m (left panel) and 1000 - 2000 m (right panel). The dashed red line represents the linear fit.

the core position in units of $(\sec\theta)_{\max}$ are $+0.0005/-0.0001$ for the 500 - 1000 m interval and $+0/-0.0056$ for the 1000 - 2000 m one.

5.3.2 Parametrization of $t_{1/2}$ as a function of r

The selection of the parametrization used to describe the dependence of the risetime with the core distance can also contribute to the uncertainty of $(\sec\theta)_{\max}$. In the analysis a linear function in r has been assumed (see section 4.3). In order to evaluate the effect of using a quadratic function in r, the average value $\langle t_{1/2}/(a + b\,r + c\,r^2)\rangle$ instead $\langle t_{1/2}/r\rangle$ has been used and the deviations in the corresponding $(\sec\theta)_{\max}$ values have been obtained. The results are shown in Fig. 5.13. The estimated systematic uncertainty results are $+0.0019/-0.0012$ for the interval 500 - 1000 m and $+0.0031/-0.0005$ for the interval 1000 - 2000 m.

5.3.3 Risetime uncertainties

Another possible source of systematic uncertainty is that from the measurement of the risetime itself. To evaluate the effect of this uncertainty, the risetime is shifted randomly around a Gaussian distribution with standard deviation σ given by the uncertainty in the measurement of the risetime (equation (4.3)). Then, the analysis is repeated using

these new values of risetime. Differences in $(\sec\theta)_{\rm max}$ between the standard analysis and the one using these risetime values are shown in Fig. 5.14. Systematic uncertainties in $(\sec\theta)_{\rm max}$ are $+0.0008/-0.0063$ for the 500 - 1000 m interval and $+0.0032/-0.0076$ for the 1000 - 2000 m interval.

5.3.4 Energy scale

As it was explained in section 3.2.3, the absolute energy calibration of the observatory is affected by a total systematic uncertainty of 14% [189]. To study the corresponding effect on $(\sec\theta)_{\rm max}$, the energy values assigned to each event are shifted by the corresponding percentage in both directions (i.e., $E + 0.14\,E$ and $E - 0.14\,E$) and the full chain of the analysis is repeated in each case. Results are shown in Fig. 5.15. From the linear fit, the maximum positive and negative deviations observed in each radial interval lead to an uncertainty of $+0.0078/-0.0095$ for the 500 - 1000 m interval and $+0.0090/-0.0030$ in units of $(\sec\theta)_{\rm max}$ for the 1000 - 2000 m interval.

5.3.5 Total systematic uncertainty of $(\sec\theta)_{\rm max}$

In Table 5.2 the various contributions to the systematic uncertainty discussed in the previous subsections are shown for the analysis in both radial intervals. The result of

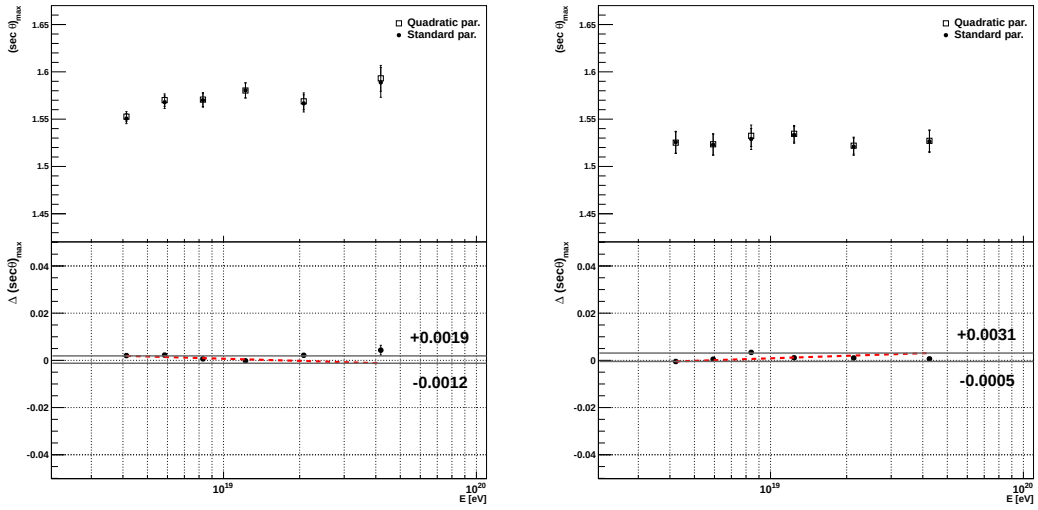

Figure 5.13: Differences between values of $(\sec\theta)_{\rm max}$ using a quadratic parametrization of risetime with r and using a linear one as a function of the energy. Left panel: core distance range of 500 - 1000 m. Right panel: core distance range of 1000 - 2000 m.

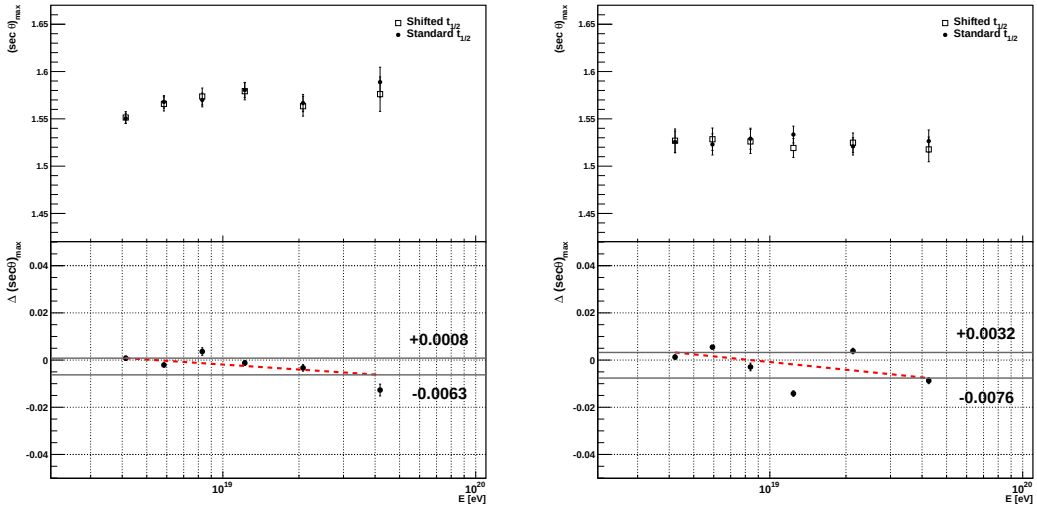

Figure 5.14: Differences between values of $(\sec\theta)_{\max}$ using risetime values shifted randomly around a Gaussian distribution with standard deviation σ given by the uncertainty in the measurement of the risetime. Left panel: core distance range of 500 - 1000 m. Right panel: core distance range of 1000 - 2000 m.

a quadratic sum of the above contributions give a total systematic uncertainty in the $(\sec\theta)_{\max}$ parameter of $+0.008/-0.011$ for the r-interval 500 - 1000 m and $+0.010/-0.010$ for 1000 - 2000 m.

However when the $(\sec\theta)_{\max}$ parameter is used as mass discriminator, the dependence of the efficiency of the cuts on the primary mass has to be included, leading to an additional contribution discussed in section 4.6.4 and shown in the last row of the table. When this contribution is included the total uncertainty increases to a final value of $+0.013/-0.015$ and $+0.014/-0.014$ for the 500 - 1000 m and 1000 - 2000 m respectively. These values can be compared with the corresponding statistical uncertainties; for example, at a mean energy of $10^{19.1}$ eV, for 500 - 1000 m, $(\sec\theta)_{\max} = 1.580 \pm 0.008(\text{stat})^{+0.013}_{-0.015}(\text{sys})$, while for 1000 - 2000 m, $(\sec\theta)_{\max} = 1.533 \pm 0.009(\text{stat})^{+0.014}_{-0.014}(\text{sys})$, showing larger systematic uncertainties than statistical ones. The systematic uncertainty on the measured $(\sec\theta)_{\max}$ amounts to less than 16% (500 - 1000 m) and 21% (1000 - 2000 m) of the predicted separation between proton-iron $(\sec\theta)_{\max}$ for both models.

In Fig. 5.16 the final results on $(\sec\theta)_{\max}$ versus energy have been represented for both radial intervals including the systematic uncertainties.

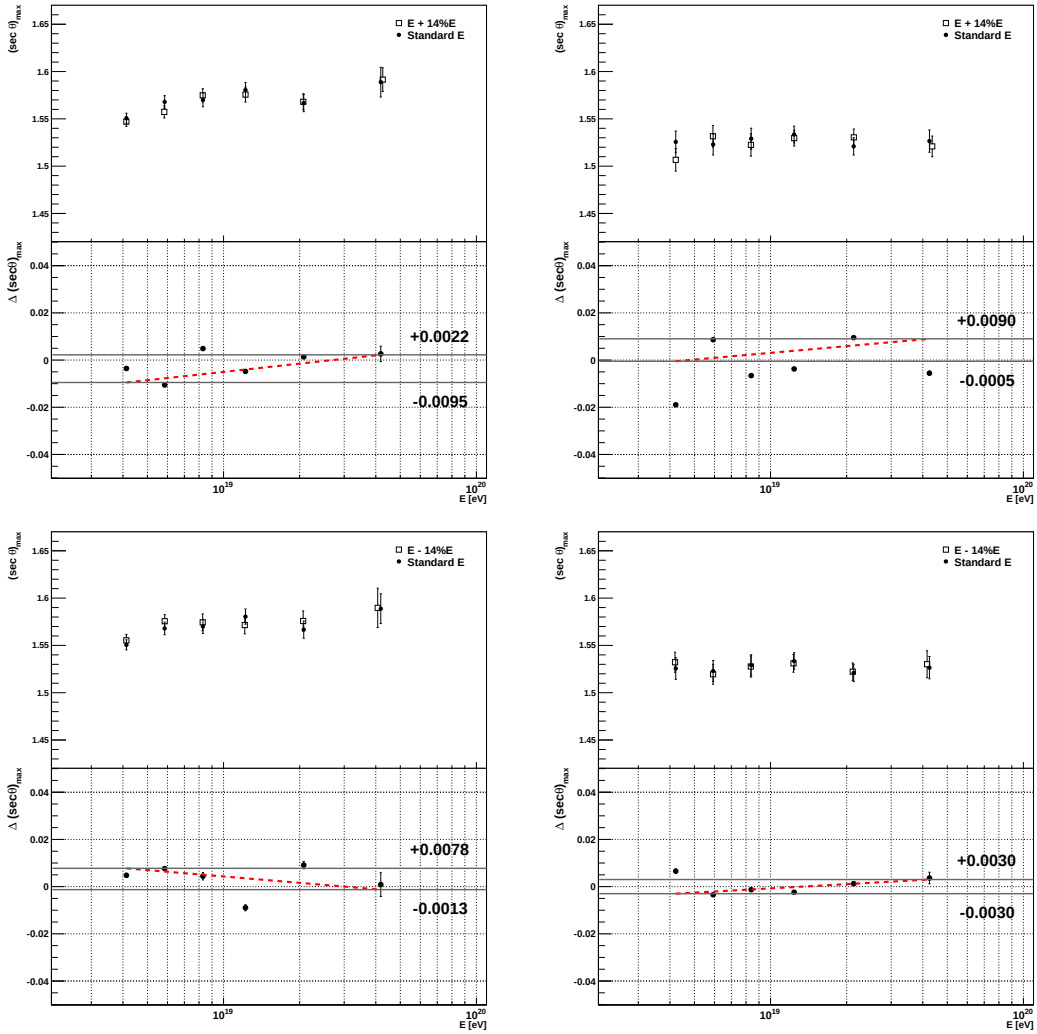

Figure 5.15: Differences between values of $(\sec\theta)_{\max}$ when the energy scale is considered shifting the energy values by +14% (top panels) and -14% (bottom panels) for 500 - 1000 m (left panels) and 1000 - 2000 (right panels) r-intervals.

5.3.6 Additional cross-checks

The asymmetry analysis has been validated by performing numerous cross-checks that demonstrate the stability of the results within the above systematic uncertainties. These checks include the potential effects in the various selection cuts, changes due to the use of the risetime uncertainties in a weighted mean of $t_{1/2}/r$ as well as possible effects due to the atmospheric weather and the ageing of the SD stations.

Source of systematic uncertainty	500 – 1000 m		1000 – 2000 m	
Core position reconstruction	+0.0005	−0.0001	+0	−0.0056
Risetime uncertainties	+0.0008	−0.0063	+0.0032	−0.0076
Energy scale	+0.0078	−0.0095	+0.0090	−0.0030
Risetime parametrization	+0.0019	−0.0012	+0.0031	−0.0005
Selection efficiency	+0.010	−0.010	+0.010	−0.010

Table 5.2: Contributions to systematic uncertainty of $(\sec\theta)_{\max}$ for all sources in both core distance intervals. In the last row the expected uncertainty due to the dependence of the selection efficiency with the primary cosmic ray is shown in $(\sec\theta)_{\max}$ units.

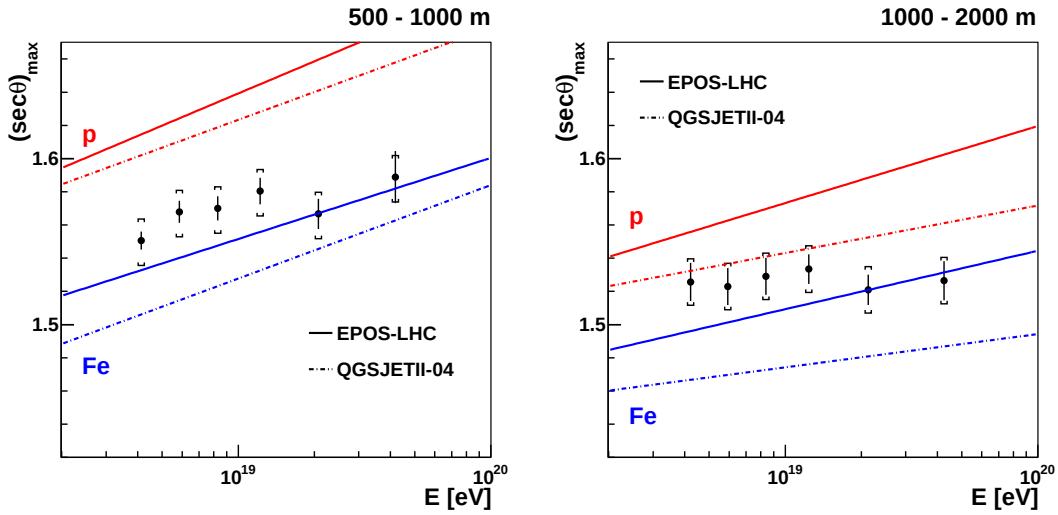

Figure 5.16: Comparison of data results (black dots) of $(\sec\theta)_{\max}$ versus energy with MC predictions for protons (red line) and iron nuclei (blue line) in the r-intervals 500 - 1000 m (left panel) and 1000 - 2000 m (right panel) for EPOS-LHC (solid lines) and QGSJETII-04 (dashed lines) hadronic models. Brackets represent the systematic uncertainty.

Selection cuts in signal and zenith angle

The effect of changing limits in selection cuts cannot be considered as a source of systematic uncertainty but it is a helpful consistency check [237, 238]. In this cross-check, a potential effect on $(\sec\theta)_{\max}$ due to the selection cuts in the signal intensity is studied by shifting the usual lower cut in the signal size of $S > 10$ VEM up ($S > 12$

VEM) and down ($S > 8$ VEM). Also, the effect of the cuts on the lower angular interval of the sample is also studied by varying the angular limits of the nominal interval of 30 $-$ 62° to 27 $-$ 62°. The effects of these variations in $(\sec\theta)_{\max}$ are shown in Fig. 5.17 for both 500 - 1000 m (left panels) and 1000 - 2000 m (right panels) core distance intervals. These studies yield an estimate of the maximum variation of 0.0044 in $(\sec\theta)_{\max}$, which is well within the systematic uncertainties.

Weighted mean of $t_{1/2}/r$

As already described in 4.6.1 the average value $\langle t_{1/2}/r\rangle$ and its corresponding error for the sample of stations inside a given interval of E, θ, and ζ have been calculated without taking into account the uncertainties in the risetime of individual stations. This is justified because the corresponding fluctuations are dominated by the intrinsic differences of the showers in the sample. Nonetheless the analysis has been repeated weighting the risetimes with their uncertainties calculated with the parameterizations used in [223, 224]. The effect on $(\sec\theta)_{\max}$ is displayed in Fig. 5.18. No relevant effect on the final results is observed.

Weather effects

Changes in the atmospheric conditions (i.e. the pressure P and temperature T) affect the development of EASs [239]. Then, the number of particles at ground, in particular those from the electromagnetic component, is sensitive to the atmospheric conditions. A possible bias affecting the risetime measurements and hence $(\sec\theta)_{\max}$ is evaluated splitting the data into "hot" (summer and spring) and "cold" (winter and autumn) periods and repeating the whole analysis chain for each case. These two samples are independent of each other, and then there is no correlation between them. The results, shown in Fig. 5.19, indicate that weather effects, if any, are within the statistical fluctuations.

Ageing of the SD detectors

Since the analysis is performed with more than 10 years of data, a possible effect of ageing of the SD detectors on the results is studied. For that, the data sample is separated in two equal sets, namely "old" (Jan.2004 - Jan.2011) and "new" (Jan.2011 - Oct.2014). Differences of $(\sec\theta)_{\max}$ between both periods are represented in Fig. 5.20. Results show that differences are compatible with zero within the statistical uncertainties of each sample.

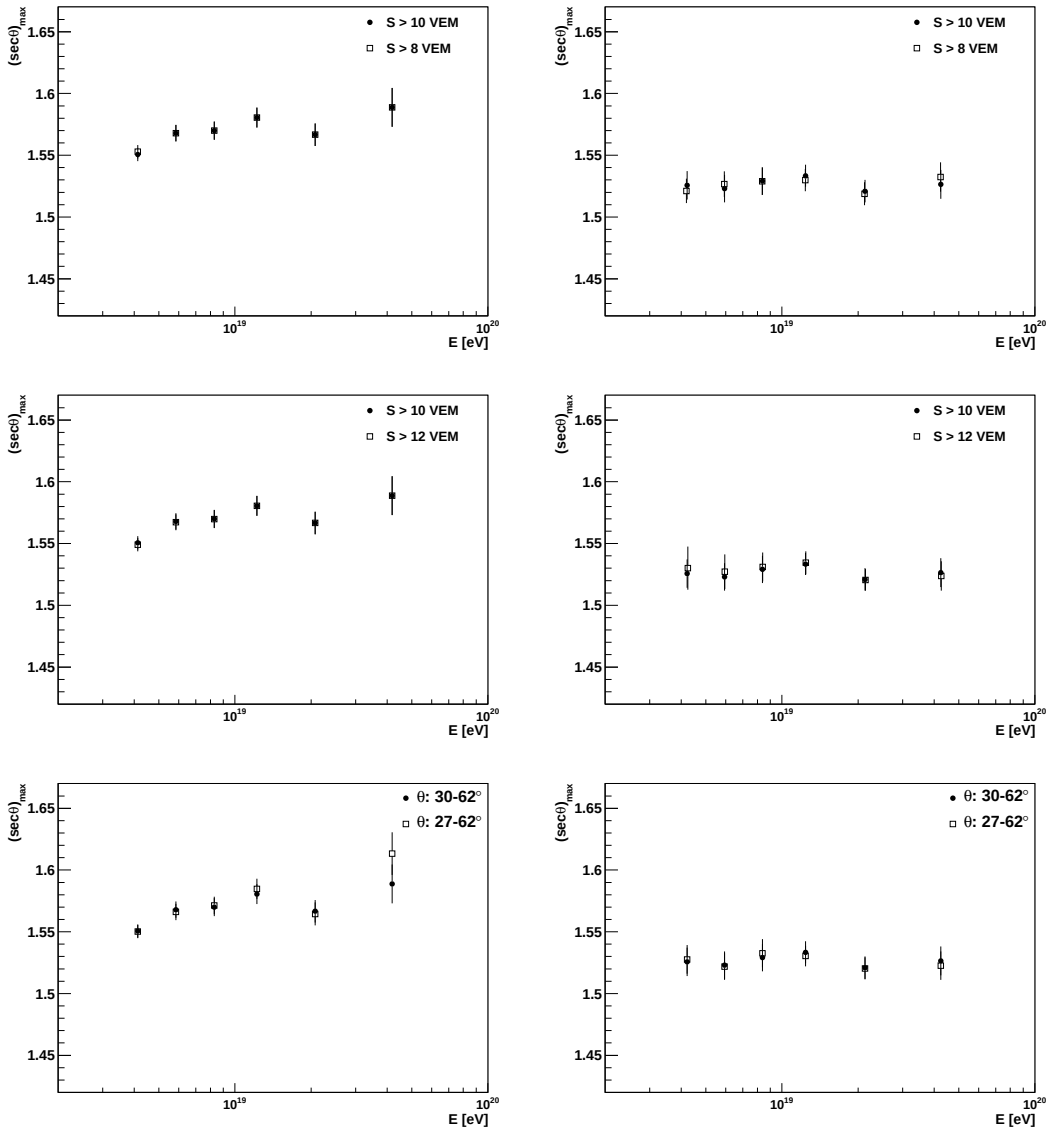

Figure 5.17: Differences between values of $(\sec\theta)_{\max}$ for standard cuts and the modified signal selection as a function of the energy, using the 500 - 1000 m (left panels) and the 1000 - 2000 m (right panels) core distance intervals. Upper panels: $S > 10$ VEM vs $S > 8$ VEM. Central panels: $S > 10$ VEM vs $S > 12$ VEM. Bottom panels: θ between $30 - 62°$ vs $27 - 62°$

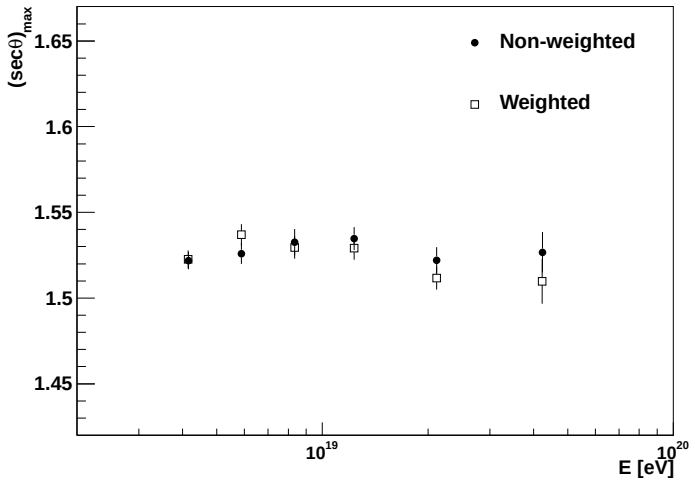

Figure 5.18: $(\sec\theta)_{\max}$ values obtained with and without using weights.

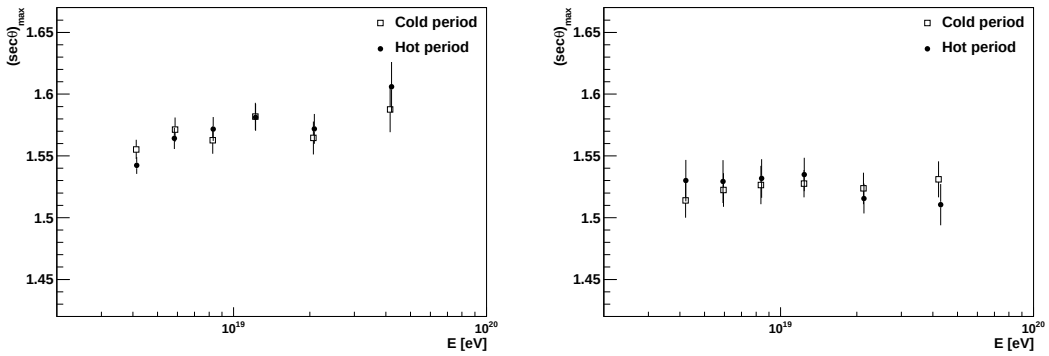

Figure 5.19: Differences between values of $(\sec\theta)_{\max}$ for different periods considering weather effects: "hot" (summer and spring) and "cold" (winter and autumn) periods. Comparisons are shown for 500 - 1000 m (left panels) and 1000 - 2000 m (right panels) core distance intervals.

Saturation problems in the high gain channel

As explained in section 3.3, two signals are extracted from each PMT of the SD stations: one from the anode (the low gain channel) and another one from the last dynode (the high gain channel), which is amplified by a factor 32 to match the dynamic range [159, 160]. Both extracted signals are read by the CDAS (see 3.2.2) but only the one obtained

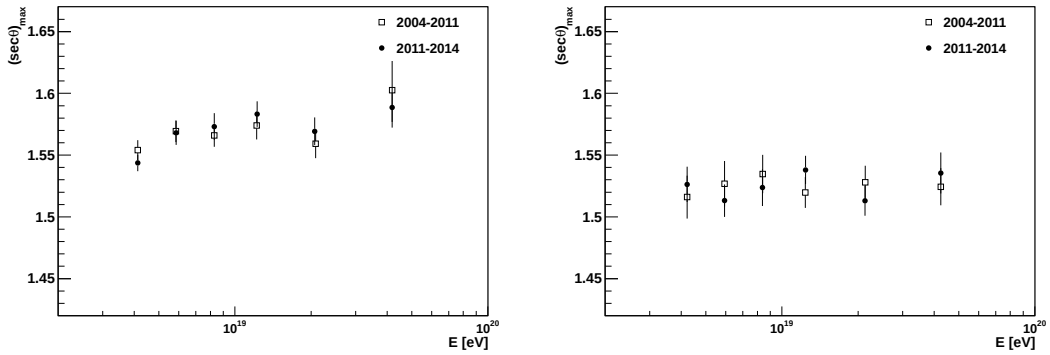

Figure 5.20: Differences between values of $(\sec\theta)_{\max}$ for different periods considering the ageing of the detectors: "old" (Jan.2004 - Jan.2011) and "new" (Jan.2011 - Oct.2014). Results are shown for 500 - 1000 m (left panels) and 1000 - 2000 m (right panels) r-intervals.

from the high gain channel is selected. However, if the signal from the high gain channel is saturated, the low gain one is used. Finally, if the low gain channel is also saturated, the signal cannot be recovered anymore (see [184] for a detailed explanation of the saturation recovery in the SD traces). Nevertheless, a problem that affected the reconstruction of the risetime measured in the low gain channel was identified [240]. The baseline was sometimes overestimated in such a way that the reconstruction algorithm generates negative signals. Consequently, the integrated traces are underestimated with the corresponding effect on the risetime.

In order to evaluate the variation on $(\sec\theta)_{\max}$ due to this problem, the full analysis has been repeated using an algorithm implemented in the software $\overline{\text{Off}}\underline{\text{line}}$ which aims to correct the saturation problem (also used in [241, 242]). The corresponding values of $(\sec\theta)_{\max}$ are presented in Fig. 5.21 for the 500 - 1000 m (left panel) and 1000 - 2000 m (right panel) core distance intervals. The maximum deviations from this contribution are $+0.0073$ and -0.0048, which are within the systematic uncertainties.

5.4 Mass composition versus energy

As explained in section 4.6.3, the transformation of $(\sec\theta)_{\max}$ into $\langle \ln A \rangle$ allows extracting information on the mass composition of cosmic rays as a function of the energy. For each interaction model the value of $\langle \ln A \rangle$ can be computed from the predicted difference in $(\sec\theta)_{\max}$ between both primaries using the relationships (4.24) and (4.25).

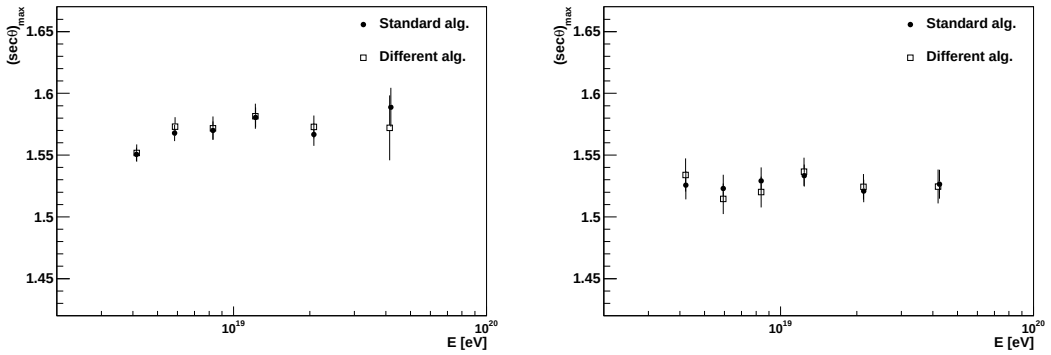

Figure 5.21: Differences between values of $(\sec\theta)_{\max}$ obtained using the algorithm of [240] for the risetime in the 500 - 1000 m (left panel) and 1000 - 2000 m (right panel) core distance intervals.

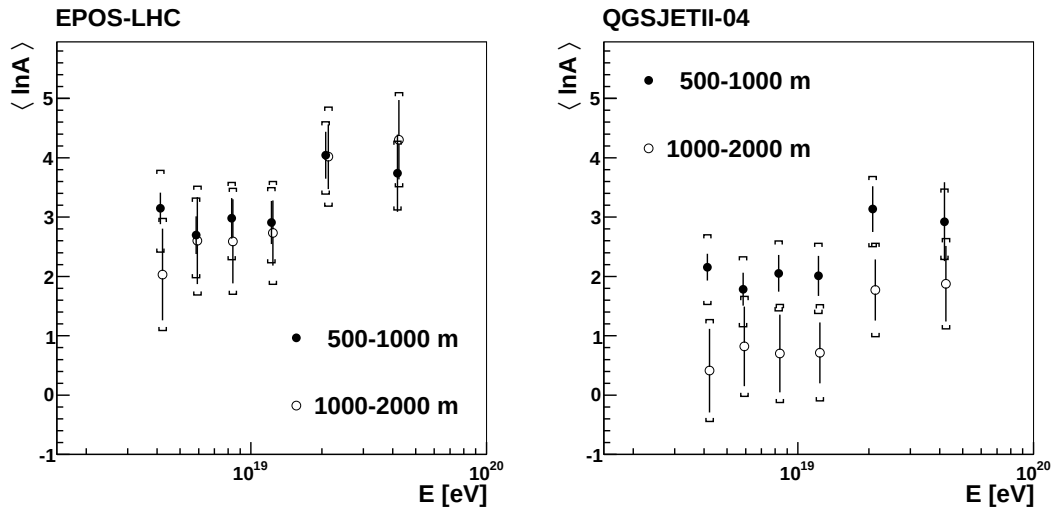

Figure 5.22: Comparison of $\langle \ln A \rangle$ values from the asymmetry analysis vs E between both radial intervals assuming the EPOS-LHC (left) and QGSJETII-04 (right) hadronic interaction models.

In this way, experimental values of $(\sec\theta)_{\max}$ (and their corresponding error bars) can be transformed into mass units.

In Fig. 5.22 the results of $\langle \ln A \rangle$ obtained in both radial intervals are compared. As can be observed, assuming the EPOS-LHC model of hadronic interactions (left panel), the results in both intervals are fully compatible. However, the results obtained

with QGSJETII-04 (right panel) seem to depend on the radial interval chosen for the analysis, which has non-physical meaning.

The statistical and systematic uncertainties in both radial intervals are partly correlated. Note that on the one hand, for a given energy, the same events are used in both r-intervals but using the risetime information at different core distances. In regard with systematic uncertainties, for instance, the error in the core position cannot affect in a similar way in both intervals. Taking into account that all the six $\langle \ln A \rangle$ values of 500 - 1000 m are larger than those of 1000 - 2000 m and that uncertainties are only partly correlated, the compatibility of the mass composition results in both radial intervals is significantly weak.

As already mentioned, the Pierre Auger Observatory has published results on mass composition from the shower maximum depth measured by the FD [99]. Also the MPD method (see section 2.7.2) provides information of mass composition by measuring the position of the maximum of the muon production depth $X^{\mu}_{\rm max}$ [109]. Both methods rely on MC simulations and thus the results might depend on the assumed model of hadronic interaction. The results obtained in this work in both radial intervals are compared with those from $X_{\rm max}$ and $X^{\mu}_{\rm max}$ in Fig. 5.23 for EPOS-LHC and in Fig. 5.24 for QGSJETII-04.

The asymmetry analysis under the EPOS-LHC hadronic model leads to a mass composition heavier than that obtained from the $X_{\rm max}$ measurements. The MPD method under this model leads to an unrealistically heavy composition pointing out a serious limitation of EPOS-LHC to account of the $X^{\mu}_{\rm max}$ distributions observed in data. It is important to note that the shower maximum depth is a feature of the electromagnetic shower, while the MPD fully relies on the muon cascade. However, the complex nature of the zenith angle behaviour of the azimuthal asymmetry is a reflection of the contributions of both components, and thus gives a combined information of the electromagnetic and muonic components. The fact that the mass composition of the asymmetry analysis is in between the results of the $X_{\rm max}$ and the $X^{\mu}_{\rm max}$ might be a clue to understand the origin of the difficulties of EPOS-LHC to describe accurately the measurements of UHECRs.

In regard with the results under the QGSJETII-04 model, the $(\sec\theta)_{\rm max}$ values are different in the two radial interval, as pointed out before. The mass composition obtained with the asymmetry analysis in the 1000 - 2000 m interval is fully compatible with the results obtained from the shower maximum depth but heavier if the analysis is carried out in the 500 - 1000 m. The MPD method leads to a composition heavier than that obtained from the $X_{\rm max}$ distributions although it could be compatible with

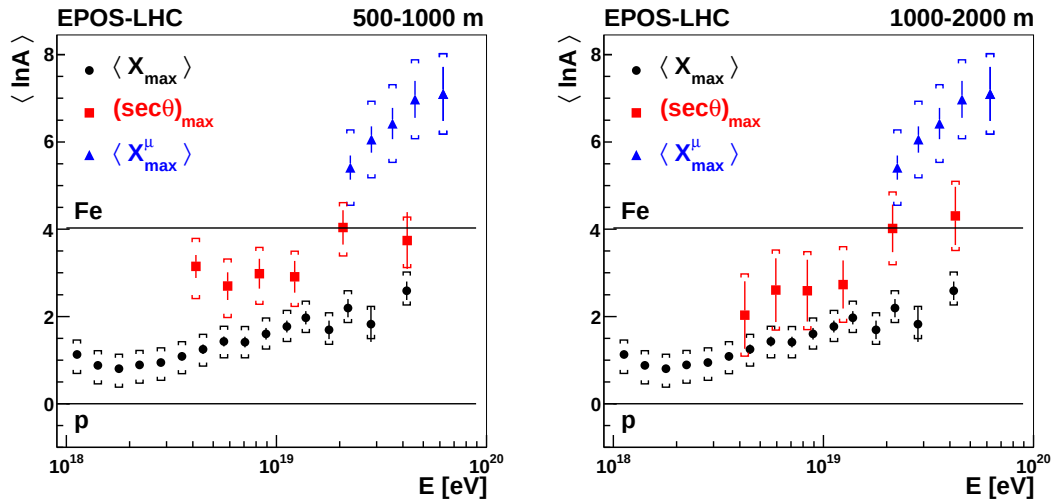

Figure 5.23: $\langle \ln A \rangle$ against energy as predicted by the EPOS-LHC hadronic interaction model. Results from the asymmetry analysis using stations in the 500 - 1000 m (left) and 1000 - 2000 m (right) core distance interval are compared with those from the elongation curve and MPD method assuming the same model for hadronic interactions.

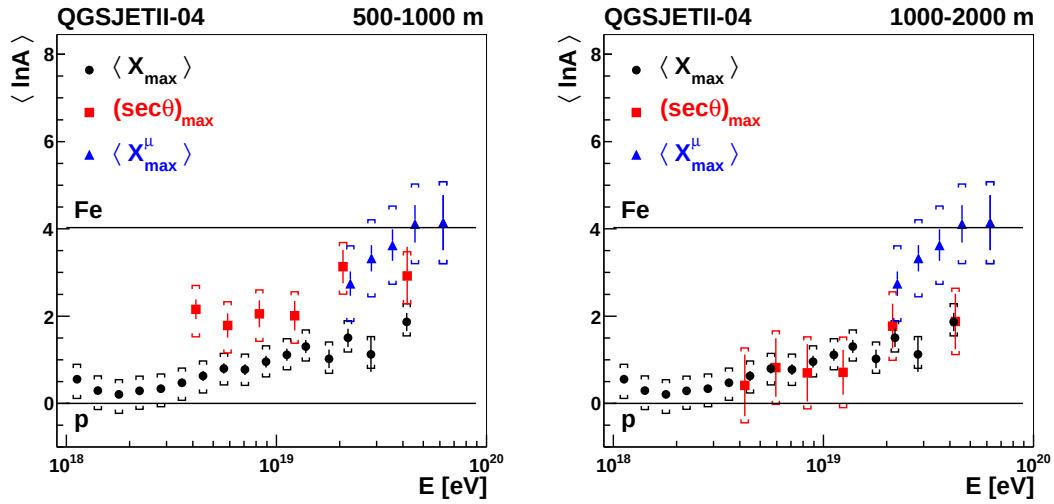

Figure 5.24: $\langle \ln A \rangle$ against energy as predicted by the QGSJETII-04 hadronic interaction model. Results from the asymmetry analysis using stations in the 500 - 1000 m (left) and 1000 - 2000 m (right) core distance interval are compared with those from the elongation curve and MPD method assuming the same model for hadronic interactions.

that from $(\sec\theta)_{\rm max}$ in 500 - 1000 m. It is important to remember that this hadronic model also showed problems to describe in a consistent way the first two moments of $\ln A$ distribution using the $X_{\rm max}$ measurements [105].

Thus, while the EPOS-LHC is favoured over QGSJETII-04, neither model provides an accurate description of muons in air-showers, and as a consequence no model describes satisfactorily the wide range of data using the Auger Observatory. A similar conclusion has been drawn from the study of inclined showers made at the Pierre Auger Observatory [243] from which it was deduced that showers contain more muons than predicted by EPOS-LHC model.

In order to progress on the mass composition analysis through $(\sec\theta)_{\rm max}$, these deficiencies in the understanding of shower modelling must be resolved. Aiming to get the origin of this incompatibilities, several tests of the MC simulations have been performed and will be described in the following section.

5.4.1 Dependence of composition results with r

Obviously, the mass composition results should be independent of the distance to the core of the stations used in the analysis. However, while the results in both r-interval assuming EPOS-LHC are fully compatible, those of QGSJETII-04 in 500 - 1000 m lead to a heavier composition than those in 1000 - 2000 m. In order to understand the origin of this behaviour, several studies have been carried out. As is well known, the risetime of the SD signals depends on the core distance and also on the primary mass. The radial dependence of the risetime has been studied for both primaries and both models of hadronic interactions in several intervals of zenith angle and energy. As an example, in Fig. 5.25 risetime data for energies $10^{19.00} < E < 10^{19.25}$ with $1.2 < \sec\theta < 1.4$ (top panels) and $1.4 < \sec\theta < 1.6$ (bottom panels) are compared with predictions from EPOS-LHC (left panels) and QGSJETII-04 (right panels). As can be seen in the figure, according to EPOS-LHC the risetime of data is consistent with a heavy composition for all radial distances, while for QGSJETII-04 the risetime behaves as produced by a heavy composition close to the core position getting lighter at larger distances.

This anomalous behaviour points to the same direction that the one from the analysis of the asymmetry. In order to understand the origin of this discrepancy, a detailed analysis of the contribution of each shower component to the total signal has been carried out. The LDF distribution of the various components has been represented as a function of θ. The results for events with $\log(E/{\rm eV}) = 19.5$ are shown in Fig. 5.26 for four different θ bins and for both primaries. As can be observed, as θ increases the electromagnetic component is more attenuated and the muonic component dominates

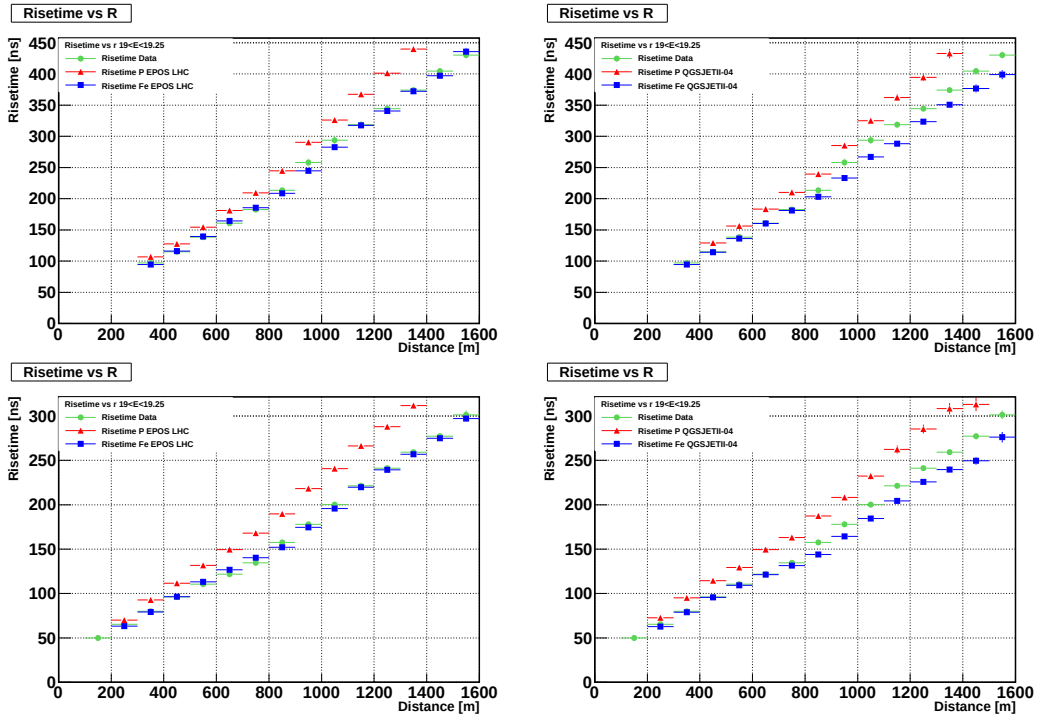

Figure 5.25: Risetime vs core distance for $1.2 < \sec\theta < 1.4$ (top panels) and $1.4 < \sec\theta < 1.6$ (bottom panels) for EPOS-LHC (left panels) and QGSJETII-04 (right panels). Iron showers are represented in blue, proton showers in red, and data in green. The energy range corresponds to $19.00 < \log(E/\mathrm{eV}) < 19.25$.

the total signal, as it was explained in section 4.2.2. Also, the iron distributions show a larger muonic component that proton distributions, as expected. However, both models present a similar behaviour and therefore inconsistencies in the LDF of the different shower components can be discarded. As an additional test, the ratio of electromagnetic and muonic signals over the total one have been plotted. The results for the same energy and θ bins are shown in Fig. 5.27. Again, the results do not provide any clue to understand the origin of the discrepancies.

At present, this is still an open question, and more work is being developed in order to find the origin of this anomaly.

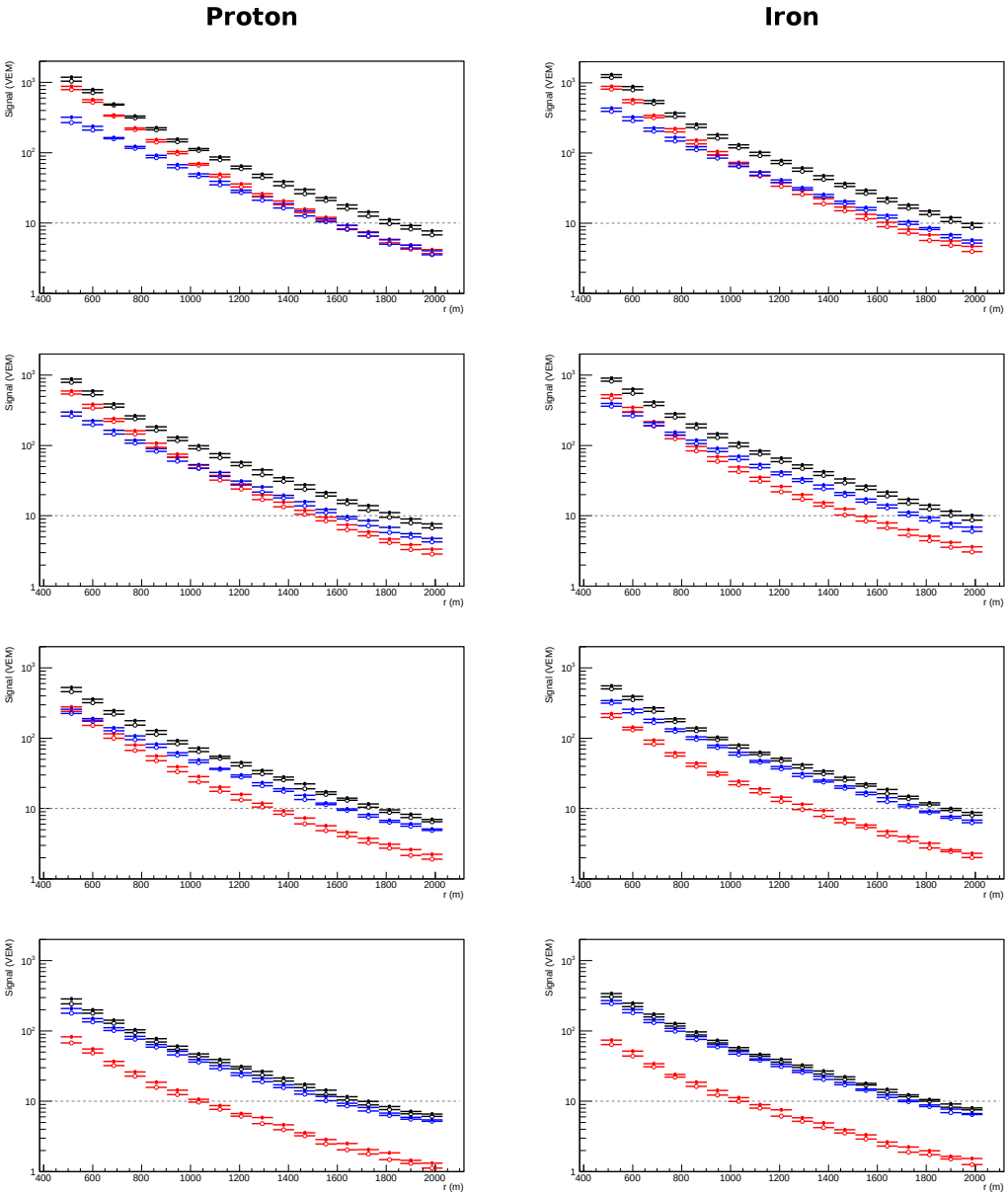

Figure 5.26: LDFs corresponding to EPOS-LHC (full dots) and QGSJETII-04 (empty dots) simulated events with $\log(E/\text{eV}) = 19.5$ and $\theta = 36°$, 45°, 53°and 60°(from top to bottom) for proton (left panels) and iron (right panels) primaries. The total signal (black dots) is divided into its components: the muonic component (blue dots) and the electromagnetic component (red dots).

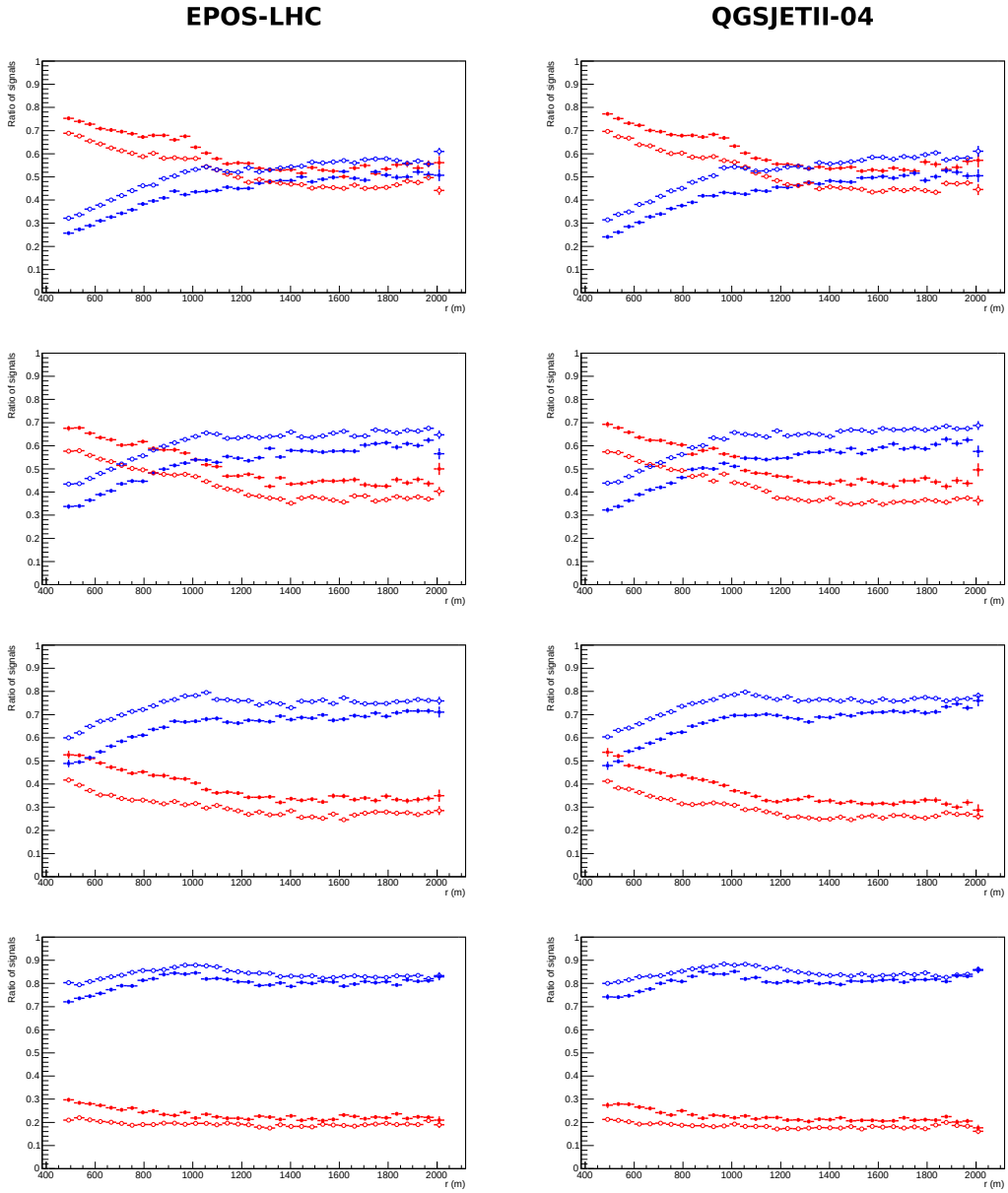

Figure 5.27: Ratios between electromagnetic and total signal (red points) and between muonic and total signal (blue points) corresponding to EPOS-LHC (left panels) and QGSJETII-04 (right panels) simulated events with $\log(E/\text{eV}) = 19.5$ and $\theta = 36°$, $45°$, $53°$and $60°$(from top to bottom). Proton and iron primaries are represented with full and open dots respectively.

5.5 Correlation with $X_{\max}$

As it has been explained previously, since the $(\sec\theta)_{\max}$ parameter is sensitive to mass composition it is expected to be correlated with the shower maximum depth. In section 4.7 the correlation between both magnitudes according to the predictions of MC simulations using stations in the radial interval 500 - 2000 m was shown (see Fig. 4.33).

In this section, the correlation will be studied using the Auger data. However, since $(\sec\theta)_{\max}$ is an SD parameter and $X_{\max}$ is an FD observable, only hybrid events (that is, those recorded and reconstructed by the FD and SD simultaneously) can be used to study the correlation between both parameters. Therefore, the size of the data sample for this analysis is significantly smaller due to the duty cicle of the FD. In addition, selection cuts similar to those used in [244] have been required. These cuts include the condition that the reconstructed $X_{\max}$ lies within the field of view of the telescopes; showers must be well-fitted to a Gaisser-Hillas function; uncertainties in the reconstructed energy and $X_{\max}$ have to be constrained to a maximum value of 20% (relative uncertainty) and 40 $\mathrm{g\,cm^{-2}}$ respectively; the minimum viewing angle (light emission angle towards the FD) must be larger than 20°, and the reduced χ^2 of the Gaisser-Hillas fit is required to be smaller than 2.5.

After applied all the cuts, 4759 events were selected and then grouped within bins of $X_{\max}$. For each interval of $X_{\max}$ the asymmetry factor has been measured as a function of $\sec\theta$, and $(\sec\theta)_{\max}$ has been determined as previously described. In Fig. 5.28 the results in the 500 - 1000 m and 1000 - 2000 m intervals are shown. As can be seen, there is a clear linear correlation between both observables and in good agreement with MC predictions independently of the primary mass. This result strengthens the reliability of the $(\sec\theta)_{\max}$ parameter as a mass estimator. However, it can be easily noticed a discrepancy between data and MC for QGSJETII-04 in the 1000 - 2000 m interval, since data points are systematically above the predictions. This discrepancy takes place in the same radial interval and for the same hadronic model than the one observed in the results of $\langle \ln A \rangle$ vs E (see Fig. 5.22), which supports the fact that this hadronic model has problems to accurately describe the data in that specific core distance range.

The asymmetry analysis provides a mass estimator itself with systematic uncertainties independent of those of the shower maximum depth measured by the FD. However, the results shown in Fig. 5.28 could also be used to convert $(\sec\theta)_{\max}$ into $X_{\max}$ units. It is important to point out that this transformation will be done only as a consistency check of the method, since the analysis of the azimuthal asymmetry does not aim to

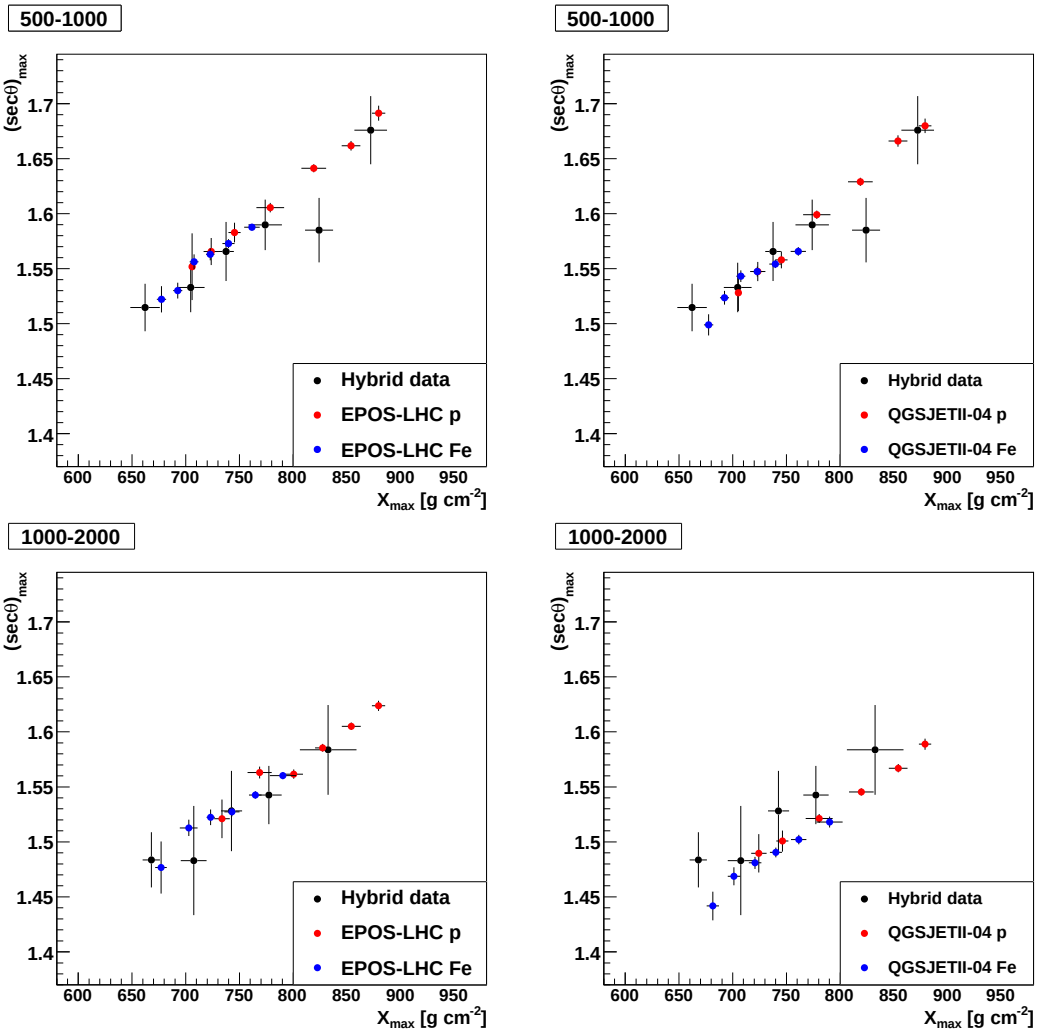

Figure 5.28: Correlation between $(\sec\theta)_{\max}$ and $X_{\max}$ evaluated in the 500 - 1000 m (upper plots) and 1000 - 2000 m (bottom plots) for data (black dots) and MC simulations using EPOS-LHC (left) and QGSJETII-04 (right). MC results are shown for protons (red) and iron nuclei (blue).

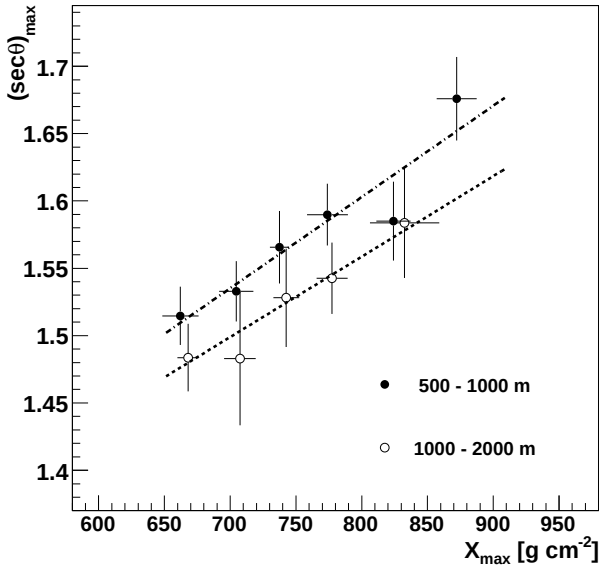

Figure 5.29: Correlation between $(\sec\theta)_{\max}$ and $X_{\max}$ for hybrid events evaluated in the 500 - 1000 m (full dots) and 1000 - 2000 m (empty dots). The linear fit to each interval show two parallel lines, as it is expected (see text).

measure $X_{\max}$ with SD. A linear fit to data:

$$(\sec\theta)_{\max} = a + b \cdot X_{\max} \ , \tag{5.1}$$

allows obtaining the $X_{\max}$ parameter from the $(\sec\theta)_{\max}$ value. Also, both the statistical and systematic uncertainty in $X_{\max}$ can be translated from those of $(\sec\theta)_{\max}$ as:

$$\Delta X_{\max} = \frac{\Delta(\sec\theta)_{\max}}{b} \ , \tag{5.2}$$

In Fig. 5.29 the linear fit (equation (5.1)) is represented for both radial intervals, leading to near parallel straight lines, that is, the a parameter depends on the radial interval while b is nearly independent. Since $(\sec\theta)_{\max}$ from stations in both intervals are well correlated with $X_{\max}$, the inferred results of $X_{\max}$ versus energy should be independent of the radial interval.

Equation (5.1) can be used to measure the $X_{\max}$ parameter using the SD data sample. The results for both radial intervals are displayed in Fig. 5.30 as a function of

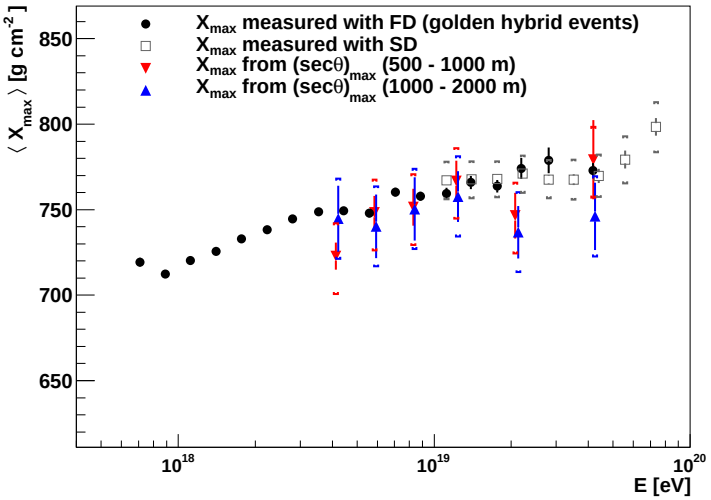

Figure 5.30: $\langle X_{\max} \rangle$ versus energy from data of the Pierre Auger Observatory. Results from FD measurements (full dots), SD data [245] (open squares) and those inferred from $(\sec\theta)_{\max}$ of this work (coloured triangles) for the 500 - 1000 m (red) and 1000 - 2000 m (blue) core distance intervals are compared.

the energy reconstructed with the SD. These results are compared with those from the direct measurements of $X_{\max}$ values obtained with the FD using the golden hybrid data sample of [99] and other analysis based on the SD data [245] with a resolution of 32 $\mathrm{g\,cm^{-2}}$ above 50 EeV. As can be observed, both the absolute value and the dependence on energy of the $\langle X_{\max} \rangle$ parameter inferred from $(\sec\theta)_{\max}$ for both radial intervals are in agreement with other $\langle X_{\max} \rangle$ measurements within uncertainties. Note that the uncertainties of the asymmetry analysis are underestimated here because the error of the parameters of the linear fit of the correlation has not been included.

This plot demonstrates that $(\sec\theta)_{\max}$ is a robust parameter for mass composition studies. If the $X_{\max}$ values from the hybrid sample are used to interpret $(\sec\theta)_{\max}$, the same composition is obtained in both r-intervals. However, when the hadronic models are used to interpret $(\sec\theta)_{\max}$, the composition changes with r for the QGSJETII-04 model. Therefore, since hadronic models are required to extract information about the mass composition, the deficiencies in the understanding of shower modelling have to be resolved before the mass composition can be inferred from $(\sec\theta)_{\max}$. On the other hand, these results probe that the reach of the $(\sec\theta)_{\max}$ observable extends to providing a test of hadronic interactions models.

Chapter 6

Conclusions

The Pierre Auger Observatory has measured with unprecedented accuracy the energy spectrum of ultra-energetic cosmic rays ($E > 10^{18}$ eV) identifying two major features, that is, the ankle at $E \sim 4 \cdot 10^{18}$ eV and a GZK-like suppression at $E \sim 6 \cdot 10^{19}$ eV. Nonetheless, in order to solve the problem of the origin of these cosmic rays in the framework of the proposed theoretical scenarios it is necessary to measure the mass composition. At these energies the only established procedure relies on the measurement of $X_{\rm max}$ that it is performed by means of the FD with a duty cycle of $< 13\%$.

This thesis is related with a novel method for mass analysis that is based on the azimuthal asymmetry of the risetime of the signals recorded by the SD with a duty cycle $\sim 100\%$. The dependence of the amplitude of this asymmetry with the zenith angle of the primary cosmic ray is related with the longitudinal evolution of the shower and therefore the parameter $(\sec\theta)_{\rm max}$ is sensitive to the mass of cosmic rays. Since the SD only samples a very small fraction of the shower front, the number of stations triggered in a single event is not enough to carry out the analysis and thus this technique cannot be applied to individual showers but to samples of events within intervals of energy and zenith angle.

In this work, a significant progress on this technique has been carried out with the assistance of Monte Carlo simulations. More than 4.5×10^5 showers initiated by protons and iron nuclei have been produced with the CORSIKA code using five hadronic models: EPOS 1.99, SIBYLL 2.1, QGSJETII-03 and the most recent ones QGSJETII-04 and EPOS-LHC. The detector simulation as well as the reconstruction of the events has been performed with the tools of the Offline Software Framework of the Auger Collaboration.

This method has been applied to the data of the Pierre Auger Observatory recorded

in the period from January 2004 to October 2014. After applying the appropriate quality cuts, the sample contains 191534 FADC signals from more than 5×10^4 showers with energies $E > 10^{18.5}$ eV in the angular interval $30^\circ < \theta < 62^\circ$.

As expected from simple geometrical considerations, the $(\sec\theta)_{\max}$ parameter increases when using stations at lower core distances. This effect is observed in MC simulations and confirmed by Auger data, and in principle it should not limit the capability for mass composition as far as the behavior of MC showers were identical to the one of data. To better account for this dependence on the core distance, the analysis has been carried out independently using stations in two core distance intervals: 500 - 1000 m and 1000 - 2000 m.

The systematic uncertainties in the experimental measurement of $(\sec\theta)_{\max}$ have been evaluated taking into account the uncertainty in the reconstruction of the core position, the parameterization of the risetime, the uncertainty in the energy scale, etc. The total systematic uncertainty in units of $(\sec\theta)_{\max}$ is $+0.013/-0.015$ in the 500 - 1000 m core distance range and $+0.014/-0.014$ in 1000 - 2000 m, that expressed in terms of mass units corresponds to less than 16% (500 - 1000 m) and 21% (1000 - 2000 m) of the difference between pure proton and pure iron composition.

Mass composition can only be obtained from comparison of data with MC predictions using the available models of hadronic interactions. Using the MC results for p and Fe nuclei, the measurements of $(\sec\theta)_{\max}$ have been converted into mass units and compared with those from other composition studies. This comparison has lead to several conclusions:

- There are indications that the composition of UHE cosmic rays get heavier with energy in line with other results of the Pierre Auger Collaboration.

- Assuming the EPOS-LHC model the mass predictions are independent, within the uncertainties, of the core distance of the stations. Under this model, it is inferred a composition heavier than that obtained from the $X_{\max}$ method, but lighter than the one obtained from the MPD method.

- The mass analysis using the QGSJETII-04 model for hadronic interactions lead to an inconsistency, since the mass composition seems to depend on the core distance. In this case, while the result in the 1000 - 2000 m interval is fully compatible with that obtained from $X_{\max}$, the composition in the 500 - 1000 m range is heavier and could be compatible with the one predicted by the MPD.

The MPD method relies solely in the information of the muon content of the shower and the $X_{\max}$ observations are dominated by the electromagnetic component. However, the complex nature of the zenith angle behavior of the time-asymmetry is a reflection

of the contributions from both components. Therefore there are three analyses of the Pierre Auger Collaboration where the muon component plays rather different roles and, at the same time, they provide contrasting inferences for $\langle \ln A \rangle$ values. This can be interpreted as evidence that no model offers a completely satisfactory description of the wide range of data, in line with other Auger studies.

Therefore, the results obtained in this work give further support to possible inconsistencies between real data and predictions using the available models of hadronic interactions. This is a clear indication that further deficiencies in the modelling of showers must be resolved before $(\sec\theta)_{\max}$ can be used to make inferences about mass composition. Once models of hadronic interactions reliable at these energies are available, the asymmetry analysis should be performed using stations in a wide radial range, e.g., 500 - 2000 m, since in this way both the statistical and the systematic uncertainties in the determination of the mass composition would be reduced. On the other hand, these results show that the reach of the $(\sec\theta)_{\max}$ observable extends to providing a test of hadronic interactions models.

Finally, to study the reliability of $(\sec\theta)_{\max}$ as a mass composition estimator, the correlation between $(\sec\theta)_{\max}$ and $X_{\max}$ has been studied using Monte Carlo simulations as well as hybrid events. The analysis performed here confirms this correlation with both data and simulation samples, which is independent on the primary particle. Besides, leaving aside the hadronic models aiming to check the feasibility of the method without considering simulations with the current hadronic models, the correlation between $(\sec\theta)_{\max}$ and $X_{\max}$ for the hybrid events allow the transformation of $(\sec\theta)_{\max}$ values into $X_{\max}$ values in both r-intervals. The results confirm that the energy dependence of $X_{\max}$ values obtained from $(\sec\theta)_{\max}$ is compatible (within uncertainties) not only between both core distance intervals but also with the $X_{\max}$ values obtained obtained with the FD and those obtained with other studies using the SD. Therefore, these results give consistency to the method described in this thesis, confirming thus that the $(\sec\theta)_{\max}$ parameter is a reliable estimator of mass composition.

Bibliography

[1] V.F. Hess. Über Beobachtungen der durchdringenden Strahlung bei sieben Freiballonfahrten. *Phys. Zeitschr.*, XIII:1084, 1912. 4

[2] R.A. Millikan and G.H. Cameron. High Frequency Rays of Cosmic Origin III. Measurements in Snow-Fed Lakes at High Altitudes. *Phys. Rev.*, 28:851–868, Nov 1926. 4

[3] C.D. Anderson. The Positive Electron. *Phys.Rev.*, 43:491–494, 1933. 4

[4] S.H. Neddermeyer and C.D. Anderson. Note on the Nature of Cosmic Ray Particles. *Phys.Rev.*, 51:884–886, 1937. 4

[5] J.C. Street and E.C. Stevenson. New Evidence for the Existence of a Particle of Mass Intermediate Between the Proton and Electron. *Phys.Rev.*, 52:1003–1004, 1937. 4

[6] C.M.G. Lattes, H. Muirhead, G.P.S. Occhialini, and C.F. Powell. Processes Involving Charged Mesons. *Nature*, 159:694–697, 1947. 4

[7] P. Auger, P. Ehrenfest, R. Maze, J. Daudin, and A.F. Robley. Extensive cosmic ray showers. *Rev.Mod.Phys.*, 11:288–291, 1939. 4

[8] B. Rossi. Misure sulla distribuzione angolare di intensita della radiazione penetrante all'Asmara. *Ric. Sci. Suppl.*, 1:288, 1934. 4

[9] J. Linsley. Evidence for a primary cosmic-ray particle with energy 10^{20} eV. *Phys.Rev.Lett.*, 10:146–148, 1963. 4

[10] J. Linsley. Measurement of multiply charged cosmic rays by a new technique. *Phys.Rev.*, 97:1292–1302, 1955. 4

[11] M.A. Lawrence, R.J.O. Reid, and A.A. Watson. The Cosmic ray energy spectrum above 4×10^{17} eV as measured by the Haverah Park array. *J.Phys.*, G17:733–757, 1991. 4, 30

[12] V.P. Artamonov *et al.* Present state and outlook of the Yakutsk EAS array. *Bull.Russ.Acad.Sci.Phys.*, 58:2026–2031, 1994. 4

[13] M.M. Winn, J. Ulrichs, L.S. Peak, C.B.A. Mccusker, and L. Horton. The Cosmic Ray Energy Spectrum Above 10^{17} eV. *J.Phys.*, G12:653–674, 1986. 4

[14] N. Chiba *et al.* Akeno giant air shower array (AGASA) covering 100 km^2 area. *Nucl.Instrum.Meth.*, A311:338–349, 1992. 4

[15] I. Allekotte *et al.* The Surface Detector System of the Pierre Auger Observatory. *Nucl.Instrum.Meth.*, A586:409–420, 2008. 4

[16] T. Abu-Zayyad *et al.* The surface detector array of the Telescope Array experiment. *Nucl.Instrum.Meth.*, A689:87–97, 2012. 4

[17] K. Suga. *Proc. 5th Interamerican Seminar on Cosmic Ray, La Paz, Bolivia.*, vol.II:49, 1962. 4

[18] A.E. Chudakov. *Proc. 5th Interamerican Seminar on Cosmic Ray, La Paz, Bolivia.*, vol.II:44, 1962. 4

[19] T. Hara *et al. Acta Phys. Acad. Sci. Hung.*, 29, suppl.3:361, 1970. 4

[20] H.E. Bergeson *et al.* Measurement of Light Emission from Remote Cosmic Ray Air Showers. *Phys.Rev.Lett.*, 39:847–849, 1977. 4

[21] T. Abu-Zayyad *et al.* The prototype high-resolution Fly's Eye cosmic ray detector. *Nucl.Instrum.Meth.*, A450:253–269, 2000. 5

[22] J. Abraham *et al.* Properties and performance of the prototype instrument for the Pierre Auger Observatory. *Nucl.Instrum.Meth.*, A523:50–95, 2004. 5, 35, 71

[23] S. Ogio *et al. Proceedings of the 30th International Cosmic Ray Conference (ICRC2007), Merida, Mexico*, 2007. 5

[24] Y. Takahashi. The JEM-EUSO mission. *New J.Phys.*, 11:065009, 2009. 5

[25] W. Hanlon. Cosmic ray spectrum of various experiments, http://www.physics.utah.edu/∼whanlon/spectrum.html. 6

[26] E.S. Seo, J.F. Ormes, R.E. Streitmatter, S.J. Stochaj, W.V. Jones, S.A. Stephens, and T. Bowen. Measurement of cosmic-ray proton and helium spectra during the 1987 solar minimum. *Astrophys.J.*, 378:763–772, September 1991. 5

[27] M. Aguilar *et al.* Relative Composition and Energy Spectra of Light Nuclei in Cosmic Rays. Results from AMS-01. *Astrophys.J.*, 724:329–340, 2010. 5

[28] M. Aguilar *et al.* Isotopic Composition of Light Nuclei in Cosmic Rays: Results from AMS-01. *Astrophys.J.*, 736:105, 2011. 5

[29] M. Nagano *et al.* Energy Spectrum of Primary Cosmic Rays Between $10^{14.5}$ eV and 10^{18} eV. *J.Phys.*, G10:1295, 1984. 5

[30] M. Nagano *et al.* Energy spectrum of primary cosmic rays above 10^{17} eV determined from the extensive air shower experiment at Akeno. *J.Phys.*, G18:423–442, 1992. 5, 6

[31] S. Yoshida *et al.* The Cosmic ray energy spectrum above 3×10^{18} eV measured by the Akeno Giant Air Shower Array. *Astropart.Phys.*, 3:105–124, 1995. 5

[32] M. Takeda *et al.* Extension of the cosmic ray energy spectrum beyond the predicted Greisen-Zatsepin-Kuzmin cutoff. *Phys.Rev.Lett.*, 81:1163–1166, 1998. 5, 11

[33] R.U. Abbasi *et al.* First observation of the Greisen-Zatsepin-Kuzmin suppression. *Phys.Rev.Lett.*, 100:101101, 2008. 5

[34] P. Sokolsky. Recent results from the High Resolution Fly's Eye experiment. *Nucl.Phys.Proc.Suppl.*, 175-176:207–212, 2008. 5

[35] B. Zhang and Z. Cao. The measurement of UHECR spectrum with the HiRes experiment in stereo mode. *Nucl.Phys.Proc.Suppl.*, 175-176:241–244, 2008. 5

[36] The Pierre Auger Collaboration. The Pierre Auger Observatory Design Report. March 1997. 5

[37] G. Kulikov and G. Khristiansen. On the size spectrum of extensive air showers. *Sov. Phys. JETP*, 35:441–447, 1959. 5

[38] D.J. Bird *et al.* Evidence for correlated changes in the spectrum and composition of cosmic rays at extremely high-energies. *Phys.Rev.Lett.*, 71:3401–3404, 1993. 5, 6, 8

[39] Nakamura *et al.* http://pdg.lbl.gov, JPG 37, 075021 (2010). 7

[40] R. Aloisio *et al.* A dip in the UHECR spectrum and the transition from galactic to extragalactic cosmic rays. *Astropart.Phys.*, 27:76–91, 2007. 6

[41] W.D. Apel *et al.* Kneelike structure in the spectrum of the heavy component of cosmic rays observed with KASCADE-Grande. *Phys.Rev.Lett.*, 107:171104, 2011. 6

[42] V. Berezinsky. Transition from galactic to extragalactic cosmic rays. *ArXiv e-prints*, October 2007. 7, 8, 9, 11

[43] V.S. Berezinsky, S.I. Grigoreva, and B.I. Hnatyk. Extragalactic UHE proton spectrum and prediction of flux of iron-nuclei at 10^8 GeV - 10^9 GeV. *Nucl.Phys.Proc.Suppl.*, 151:497–500, 2006. 7

[44] A.M. Hillas. Cosmic Rays: Recent Progress and some Current Questions. 2006. 7, 10, 12

[45] D. De Marco and T. Stanev. On the shape of the UHE cosmic ray spectrum. *Phys.Rev.*, D72:081301, 2005. 7

[46] D. Allard, E. Parizot, and A.V. Olinto. On the transition from galactic to extragalactic cosmic-rays: spectral and composition features from two opposite scenarios. *Astropart.Phys.*, 27:61–75, 2007. 8, 10, 11

[47] A.M. Hillas. Where do 10^{19} eV cosmic rays come from? *Nucl.Phys.Proc.Suppl.*, 136:139–146, 2004. 8

[48] A.M. Hillas. Can diffusive shock acceleration in supernova remnants account for high-energy galactic cosmic rays? *J.Phys.*, G31:R95–R131, 2005. 8

[49] D. Allard, E. Parizot, E. Khan, S. Goriely, and A.V. Olinto. UHE nuclei propagation and the interpretation of the ankle in the cosmic-ray spectrum. *Astron.Astrophys.*, 443:L29–L32, 2005. 8

[50] T. Wibig and A.W. Wolfendale. At what particle energy do extragalactic cosmic rays start to predominate? *J.Phys.*, G31:255–264, 2005. 8

[51] D. Allard, A.V. Olinto, and E. Parizot. Signatures of the extragalactic cosmic-ray source composition from spectrum and shower depth measurements. *Astron.Astrophys.*, 473:59–66, 2007. 8

[52] N. Globus, D. Allard, and E. Parizot. Propagation of high-energy cosmic rays in extragalactic turbulent magnetic fields: resulting energy spectrum and composition. *Astron.Astrophys.*, 479:97, 2008. 8

[53] W.D. Apel *et al.* Ankle-like Feature in the Energy Spectrum of Light Elements of Cosmic Rays Observed with KASCADE-Grande. *Phys.Rev.*, D87:081101, 2013. 9

[54] A.A. Penzias and R.W. Wilson. A Measurement of excess antenna temperature at 4080 Mc/s. *Astrophys.J.*, 142:419–421, 1965. 9

[55] K. Greisen. End to the cosmic ray spectrum? *Phys.Rev.Lett.*, 16:748–750, 1966. 9

[56] G.T. Zatsepin and V.A. Kuzmin. Upper limit of the spectrum of cosmic rays. *JETP Lett.*, 4:78–80, 1966. 9

[57] J.W. Cronin. The Highest energy cosmic rays. *Nucl.Phys.Proc.Suppl.*, 138:465–491, 2005. 11, 15

[58] R.U. Abbasi *et al.* Observation of the ankle and evidence for a high-energy break in the cosmic ray spectrum. *Phys.Lett.*, B619:271–280, 2005. 11

[59] T. Abu-Zayyad et al. Energy Spectrum of Ultra-High Energy Cosmic Rays Observed with the Telescope Array Using a Hybrid Technique. *Astropart.Phys.*, 61:93–101, 2015. 11

[60] J. Abraham *et al.* Measurement of the energy spectrum of cosmic rays above 10^{18} eV using the Pierre Auger Observatory. *Phys.Lett.*, B685:239–246, 2010. 11

[61] R. Aloisio, V. Berezinsky, and A. Gazizov. Transition from galactic to extragalactic cosmic rays. *Astropart.Phys.*, 39-40:129–143, 2012. 11

[62] T.K. Gaisser and T. Stanev. High-energy cosmic rays. *Nucl.Phys.*, A777:98–110, 2006. 12

[63] A.W. Strong, I.V. Moskalenko, and V.S. Ptuskin. Cosmic-ray propagation and interactions in the Galaxy. *Ann.Rev.Nucl.Part.Sci.*, 57:285–327, 2007. 12

[64] J.R. Hoerandel. Cosmic-ray composition and its relation to shock acceleration by supernova remnants. *Adv.Space Res.*, 41:442–463, 2008. 12

[65] E. Fermi. On the Origin of the Cosmic Radiation. *Phys.Rev.*, 75:1169–1174, 1949. 12

[66] L.O. Drury. An introduction to the theory of diffusive shock acceleration of energetic particles in tenuous plasmas. *Rept.Prog.Phys.*, 46:973–1027, 1983. 12

[67] V.S. Ptuskin and V.N. Zirakashvili. On the spectrum of high-energy cosmic rays produced by supernova remnants in the presence of strong cosmic-ray streaming instability and wave dissipation. *Astron.Astrophys.*, 429:755–765, 2005. 12

[68] K.H. Kampert. Ultra High-Energy Cosmic Ray Observations. *J.Phys.Conf.Ser.*, 120:062002, 2008. 12

[69] M. Nagano and A.A. Watson. Observations and implications of the ultrahigh-energy cosmic rays. *Rev.Mod.Phys.*, 72:689–732, 2000. 12

[70] D.R. Bergman and J.W. Belz. Cosmic Rays: The Second Knee and Beyond. *J.Phys.*, G34:R359, 2007. 12

[71] A.M. Hillas. The Origin of Ultrahigh-Energy Cosmic Rays. *Ann.Rev.Astron.Astrophys.*, 22:425–444, 1984. 12, 13

[72] P.L. Biermann and P.A. Strittmatter. Synchrotron emission from shock waves in active galactic nuclei. *Astrophys.J.*, 322:643–649, 1987. 12

[73] M.R. George, A.C. Fabian, W.H. Baumgartner, R.F. Mushotzky, and J. Tueller. On Active Galactic Nuclei as Sources of Ultra-High Energy Cosmic Rays. *Mon.Not.Roy.Astron.Soc.*, 388:59, 2008. 12

[74] J. Blumer, R. Engel, and J.R. Horandel. Cosmic Rays from the Knee to the Highest Energies. *Prog.Part.Nucl.Phys.*, 63:293–338, 2009. 13

[75] L.N. Epele and E. Roulet. On the propagation of the highest energy cosmic ray nuclei. *JHEP*, 9810:009, 1998. 14

[76] F.W. Stecker and M.H. Salamon. Photodisintegration of ultrahigh-energy cosmic rays: A New determination. *Astrophys.J.*, 512:521–526, 1999. 14

[77] R. Engel. *talk presented in the International School on Astroparticle Physics, Belgirate, Italy*, 2005. 14

[78] J. Abraham *et al.* Correlation of the highest energy cosmic rays with nearby extragalactic objects. *Science*, 318:938–943, 2007. 15

[79] P. Abreu *et al.* Update on the correlation of the highest energy cosmic rays with nearby extragalactic matter. *Astropart.Phys.*, 34:314–326, 2010. 15

[80] National Aeronautics and Space Administration. http://swift.gsfc.nasa.gov/results/bs58mon/. 16

[81] M.P. Véron-Cetty and P. Véron. A catalogue of quasars and active nuclei: 13th edition. *Astron.Astrophys.*, 518:A10, July 2010. 16

[82] H.R. Marquez-Falcon and L. Villasenor. Correlation of ultra-high-energy cosmic rays with nearby active galactic nuclei using distance-dependent and flux-dependent weights. *Auger Technical Note, GAP-2012-046*, 2012. 16

[83] H.R. Marquez-Falcon and L. Villasenor. Identification of potential AGN sources of UHECRs detected by the Auger Observatory using weights proportional to the inverse square distances of AGN from the VCV 13th ed. and the S-B 58m catalogs. *Auger Technical Note, GAP-2012-102*, 2012. 16

[84] L. Anchordoqui *et al.* High energy physics in the atmosphere: Phenomenology of cosmic ray air showers. *Annals Phys.*, 314:145–207, 2004. 17

[85] T. Stanev. *High Energy Cosmic Rays.* 2010. 17

[86] N.N. Kalmykov, S.S. Ostapchenko, and A.I. Pavlov. Quark-gluon string model and EAS simulation problems at ultra-high energies. *Nucl.Phys.Proc.Suppl.*, 52B:17–28, 1997. 18

[87] K. Werner and T. Pierog. Extended Air Shower Simulations Based on EPOS. *AIP Conf.Proc.*, 928:111–117, 2007. 18

[88] R.S. Fletcher, T.K. Gaisser, P. Lipari, and T. Stanev. SIBYLL: An Event generator for simulation of high-energy cosmic ray cascades. *Phys.Rev.*, D50:5710–5731, 1994. 18

[89] O. Bruning *et al.* LHC Design Report. 1. The LHC Main Ring. 2004. 18

[90] O. Bruning *et al.* LHC Design Report. 2. The LHC infrastructure and general services. 2004. 18

[91] M. Benedikt, P. Collier, V. Mertens, J. Poole, and K. Schindl. LHC Design Report. 3. The LHC injector chain. 2004. 18

[92] W. Heitler. The Quantum Theory of Radiation, 3rd. edition. *Oxford University Press London*, page p.386 (Section 38), 1954. 19

[93] J. Matthews. A Heitler model of extensive air showers. *Astropart.Phys.*, 22:387–397, 2005. 19, 21, 22, 23

[94] K. Greisen. *Progr. Cosmic Ray Physics.*, 3:1, 1956. 20, 58

[95] T.K. Gaisser and A.M. Hillas. *Proc. 15th International Cosmic Ray Conference, Plovdiv, Bulgary*, 8:353, 1977. 21, 43

[96] K. Kamata and J. Nishimura. The lateral and the angular structure functions of electron showers. *Progress of Theoretical Physics Supplement*, 6:93–155, 1958. 21, 58

[97] K. Greisen. Cosmic ray showers. *Ann.Rev.Nucl.Part.Sci.*, 10:63–108, 1960. 24, 71

[98] M. Ave, J. Knapp, J. Lloyd-Evans, M. Marchesini, and A.A. Watson. The Energy spectrum of cosmic rays above 3×10^{17} eV as measured with the Haverah Park array. *Astropart.Phys.*, 19:47–60, 2003. 24

[99] A. Aab *et al.* Depth of maximum of air-shower profiles at the Pierre Auger Observatory. I. Measurements at energies above $10^{17.8}$eV. *Phys.Rev.*, D90(12):122005, 2014. 25, 26, 28, 116, 133, 142

[100] S. Ostapchenko. Monte Carlo treatment of hadronic interactions in enhanced Pomeron scheme: I. QGSJET-II model. *Phys.Rev.*, D83:014018, 2011. 25

[101] T. Pierog, Iu. Karpenko, J. M. Katzy, E. Yatsenko, and K. Werner. EPOS LHC: Test of collective hadronization with data measured at the CERN Large Hadron Collider. *Phys. Rev.*, C92(3):034906, 2015. 25

[102] E.J. Ahn, R. Engel, T.K. Gaisser, P. Lipari, and T. Stanev. Cosmic ray interaction event generator SIBYLL 2.1. *Phys.Rev.*, D80:094003, 2009. 25

[103] T. Pierog. *Rencontres de Moriond, VHEPU, La Thuille*, March 2013. 26

[104] E.J. Ahn for the Pierre Auger Collaboration. Inferences about the mass composition of cosmic rays from data on the depth of maximum at the Auger Observatory. *Contributions to the 33rd International Cosmic Ray Conference (ICRC 2013), Rio de Janeiro, Brazil*, 2013. 25

[105] P. Abreu *et al.* Interpretation of the Depths of Maximum of Extensive Air Showers Measured by the Pierre Auger Observatory. *JCAP*, 1302:026, 2013. 25, 34, 135

[106] T. Abu-Zayyad *et al.* Evidence for Changing of Cosmic Ray Composition between 10^{17} eV and 10^{18} eV from Multicomponent Measurements. *Phys.Rev.Lett.*, 84:4276–4279, 2000. 27

[107] K. Shinozaki and M. Teshima. AGASA results. *Nucl.Phys.Proc.Suppl.*, 136:18–27, 2004. 28

[108] K. Shinozaki *et al. Proc. 28th International Cosmic Ray Conference, Tsukuba, Japan.*, 401, 2003. 28

[109] A. Aab *et al.* Muons in air showers at the Pierre Auger Observatory: Measurement of atmospheric production depth. *Phys.Rev.*, D90(1):012012, Erratum: *Phys. Rev.* **D92** (2015) 019903, 2014. 28, 29, 30, 116, 133

[110] D. García. Muon Arrival Time distributions and its relationship to the mass composition of Ultra High Energy Cosmic Rays: An application to the Pierre Auger Observatory. *Ph.D. Thesis, Auger Technical Note, GAP-2011-104*, 2011. 28, 29

[111] T. Pierog. private communication. 29

[112] A.A. Watson and J.G. Wilson. Fluctuation studies of large air showers - the composition of primary cosmic ray particles of energy e(p) approx. equal 10^{18} eV. *J.Phys.*, A7:1199–1212, 1974. 30, 84

[113] M. Ave, J. Knapp, M. Marchesini, M. Roth, and A.A. Watson. Time structure of the shower front as measured at Haverah Park above 10^{19} eV. *Proc. 28th International Cosmic Ray Conference, Tsukuba, Japan.*, 1, 2003. 30

[114] C. Wileman. The Spread in the Arrival Times of Particles in Air-Showers for Photon and Anisotropy Searches above 10 EeV. *Ph.D. Thesis, Auger Technical Note, GAP-2008-160*, 2008. 30, 84

[115] B. Smith. The Mass Composition of Cosmic Rays Above 1 EeV Inferred Using the Spread in Arrival Times of Air Showers Particles. *Ph.D. Thesis, Auger Technical Note, GAP-2008-161*, 2008. 30

[116] C. Jarne, H. Wahlberg, and M. T. Dova. Risetime at 1000 m revisited. *Auger Technical Note, GAP-2013-079*, 2013. 31

[117] C. Jarne, M.T. Dova, and H. Wahlberg. Update on the study of R1000 distributions. *Auger Technical Note, GAP-2014-116*, 2014. 31, 85

[118] D. Barnhill. Composition Analisys of Ultrahigh Energy Cosmic Rays Using the Pierre Auger Observatory Surface Detector. *Ph.D. Thesis, Auger Technical Note, GAP-2005-082*, 2005. 31

[119] R. Engel, D. Heck, and T. Pierog. Extensive air showers and hadronic interactions at high energy. *Ann.Rev.Nucl.Part.Sci.*, 61:467–489, 2011. 31

[120] G.R. Farrar for the Pierre Auger Collaboration. The muon content of hybrid events recorded at the Pierre Auger Observatory. *Contributions to the 33rd International Cosmic Ray Conference (ICRC 2013), Rio de Janeiro, Brazil*, 2013. 31, 32, 33

[121] J. Alvarez-Muniz, R. Engel, T.K. Gaisser, J.A. Ortiz, and T. Stanev. Hybrid simulations of extensive air showers. *Phys.Rev.*, D66:033011, 2002. 33

[122] A. Aab *et al.* The Pierre Auger Cosmic Ray Observatory. *Nucl. Instrum. Meth.*, A798:172–213, 2015. 35

[123] R. Gaior for the Pierre Auger Collaboration. Detection of cosmic rays using microwave radiation at the Pierre Auger Observatory. *Contributions to the 33rd International Cosmic Ray Conference (ICRC 2013), Rio de Janeiro, Brazil*, 2013. 36, 66, 67

[124] I.C. Maris, R. Engel, and S. Petrera. Expected physics performance of the upgraded Pierre Auger Observatory (AugerPrime). *Auger Technical Note, GAP-2015-046*, 2015. 36

[125] T. Paul. Prototype framework for Auger offline software. *Auger Technical Note, GAP-2002-066*, 2002. 37

[126] S. Argirò *et al.* The Offline Software Framework of the Pierre Auger Observatory. *Nucl.Instrum.Meth.*, A580:1485–1496, 2007. 37

[127] F. Arqueros, J.R. Hoerandel, and B. Keilhauer. Air Fluorescence Relevant for Cosmic-Ray Detection - Summary of the 5th Fluorescence Workshop, El Escorial 2007. *Nucl.Instrum.Meth.*, A597:1–22, 2008. 37

[128] F. Arqueros, F. Blanco, and J. Rosado. Analysis of the fluorescence emission from atmospheric nitrogen by electron excitation, and its application to fluorescence telescopes. *New J.Phys.*, 11:065011, 2009. 37

[129] J. Abraham *et al.* The Fluorescence Detector of the Pierre Auger Observatory. *Nucl.Instrum.Meth.*, A620:227–251, 2010. 37, 38, 40, 42, 44

[130] G. Borreani *et al.* The fluorescence detector prototype for the Auger project: optical system. *Nucl.Instrum.Meth.*, A461:577–578, 2001. 37

[131] M.A.L. de Oliveira, V. de Souza, H.C. Reis, and R. Sato. Manufacturing the Schmidt corrector lens for the Pierre Auger Observatory. *Nucl.Instrum.Meth.*, A522:360–370, 2004. 37

[132] B. Keilhauer for the Pierre Auger Collaboration. Rapid monitoring of the atmosphere after the detection of high-energy showers at the Pierre Auger Observatory. *Proc. 31st International Cosmic Ray Conference (ICRC 2009), Poland*, 2009. 38

[133] S.Y. BenZvi *et al.* The Lidar System of the Pierre Auger Observatory. *Nucl.Instrum.Meth.*, A574:171–184, 2007. 38

[134] S.Y. BenZvi *et al.* Measurement of the Aerosol Phase Function at the Pierre Auger Observatory. *Astropart.Phys.*, 28:312–320, 2007. 38

[135] P. Abreu *et al.* The Rapid Atmospheric Monitoring System of the Pierre Auger Observatory. *JINST*, 7:P09001, 2012. 39

[136] B. Keilhauer *et al.* for the Pierre Auger Collaboration. Atmospheric Profiles at the Southern Pierre Auger Observatory and their Relevance to Air Shower Measurement. *Proc. 29th International Cosmic Ray Conference (ICRC 2005), Pune, India*, 2005. 39

[137] P. Trávníček *et al. Proceedings of the 30th International Cosmic Ray Conference (ICRC2007), Merida, Mexico*, 2007. 39

[138] R. Cester *et al.* for the Pierre Auger Collaboration. Atmospheric aerosol monitoring at the Pierre Auger Observatory. *Proc. 29th International Cosmic Ray Conference (ICRC 2005), Pune, India*, 2005. 39

[139] J. Bäuml *et al.* for the Pierre Auger Collaboration. Measurement of the Optical Properties of the Auger Fluorescence Telescopes. *Contributions to the 33rd In-*

ternational Cosmic Ray Conference (ICRC 2013), Rio de Janeiro, Brazil, 2013. 39

[140] J.T. Brack, R. Meyhandan, G.J. Hofman, and J. Matthews. Absolute photometric calibration of large aperture optical systems. *Astropart.Phys.*, 20:653–659, 2004. 39

[141] H. Gemmeke *et al.* Design of the trigger system for the AUGER fluorescence detector. *IEEE Trans.Nucl.Sci.*, 47:371–375, 2000. 39

[142] A. Schmidt *et al.* New Third Level Trigger for the Fluorescence Telescopes. *Auger Technical Note, GAP-2007-118*, 2007. 39

[143] D. Kuempel, K.-H. Kampert, and M. Risse. Geometry reconstruction of fluorescence detectors revisited. *Astropart.Phys.*, 30:167–174, 2008. 41, 42

[144] C. Bonifazi *et al.* for the Pierre Auger Collaboration. Angular resolution of the Pierre Auger Observatory. *Proc. 29th International Cosmic Ray Conference (ICRC 2005), Pune, India*, 2005. 41, 122

[145] M. Ave *et al.* Precise measurement of the absolute fluorescence yield of the 337 nm band in atmospheric gases. *Astropart.Phys.*, 42:90–102, 2013. 43

[146] J. Rosado, F. Blanco, and F. Arqueros. Comparison of available measurements of the absolute fluorescence yield. *Astropart.Phys.*, 34:164–172, 2010. 43

[147] J. Rosado, F. Blanco, and F. Arqueros. On the absolute value of the air-fluorescence yield. *Astropart.Phys.*, 55:51–62, 2014. 43

[148] M. Monasor, J.R. Vázquez, D. García-Pinto, and F. Arqueros. The impact of the air-fluorescence yield on the reconstructed shower parameters of ultra-high energy cosmic rays. *Astropart.Phys.*, 34:467–475, 2011. 43

[149] J.R. Vázquez. Impact of the Air-Fluorescence Yield on the energy scale of the Pierre Auger Observatory. *Ph.D. Thesis, Auger Technical Note, GAP-2015-051*, 2015. 43, 62

[150] M. Ave *et al.* Measurement of the pressure dependence of air fluorescence emission induced by electrons. *Astropart.Phys.*, 28:41–57, 2007. 43

[151] J.R. Vázquez, J. Rosado, D. García-Pinto, and F. Arqueros for the Pierre Auger Collaboration. The effect of the fluorescence yield selection on the relative energy scales of the Auger and TA experiments. *Contributions to the 33rd*

International Cosmic Ray Conference (ICRC 2013), Rio de Janeiro, Brazil, 2013. 43

[152] F. Nerling, J. Bluemer, R. Engel, and M. Risse. Universality of electron distributions in high-energy air showers: Description of Cherenkov light production. *Astropart.Phys.*, 24:421–437, 2006. 43

[153] J. Pekala, P. Homola, B. Wilczynska, and H. Wilczynski. Atmospheric multiple scattering of fluorescence and Cherenkov light emitted by extensive air showers. *Nucl.Instrum.Meth.*, A605:388–398, 2009. 43

[154] M. Unger, B.R. Dawson, R. Engel, F. Schussler, and R. Ulrich. Reconstruction of Longitudinal Profiles of Ultra-High Energy Cosmic Ray Showers from Fluorescence and Cherenkov Light Measurements. *Nucl.Instrum.Meth.*, A588:433–441, 2008. 43

[155] H. Barbosa, F. Catalani, J.A. Chinellato, and C. Dobrigkeit. Determination of the calorimetric energy in extensive air showers. *Astropart.Phys.*, 22:159–166, 2004. 44

[156] A.G. Mariazzi and M.J. Tueros. Estimating the missing energy of Extensive Air Showers at the Pierre Auger Observatory. *Auger Technical Note, GAP-2013-026*, 2013. 44, 45

[157] M.J. Tueros for the Pierre Auger Collaboration. Estimate of the non-calorimetric energy of showers observed with the fluorescence and surface detectors of the Pierre Auger Observatory. *Contributions to the 33rd International Cosmic Ray Conference (ICRC 2013), Rio de Janeiro, Brazil*, 2013. 44, 45

[158] D. Barnhill *et al.* Testing of photomultiplier tubes for use in the surface detector of the Pierre Auger Observatory. *Nucl.Instrum.Meth.*, A591:453–466, 2008. 45

[159] T. Suomijärvi for the Pierre Auger Collaboration. Surface detector electronics for the Pierre Auger Observatory. *Proc. 27th International Cosmic Ray Conference (ICRC 2001), Hamburg, Germany*, 2011. 45, 130

[160] B. Genolini *et al.* Low power high dynamic range photomultiplier bases for the surface detectors of the Pierre Auger observatory. *Nucl.Instrum.Meth.*, A504:240–244, 2003. 45, 130

[161] T. Suomijärvi. The surface detectors of the Pierre Auger Observatory. *Nucl.Phys.Proc.Suppl.*, 136:393–398, 2004. 46

[162] C. Bonifazi for the Pierre Auger Collaboration. The monitoring system of the Pierre Auger Observatory: on-line and long-term data quality controls. *Contributions to the 33rd International Cosmic Ray Conference (ICRC 2013), Rio de Janeiro, Brazil*, 2013. 46, 47

[163] J. Rautenberg *et al.* Online Monitoring of the Pierre Auger Observatory. *Proceedings of the 30th International Cosmic Ray Conference (ICRC2007), Merida, Mexico*, 2007. 46

[164] X. Bertou *et al.* Calibration of the surface array of the Pierre Auger Observatory. *Nucl.Instrum.Meth.*, A568:839–846, 2006. 48, 49, 50

[165] M. Aglietta *et al.* for the Pierre Auger Collaboration. Response of the Pierre Auger Observatory Water Cherenkov Detectors to Muons. *Proc. 29th International Cosmic Ray Conference (ICRC 2005), Pune, India*, 2005. 48

[166] A. Etchegoyen *et al.* Muon-track studies in a water Cherenkov detector. *Nucl.Instrum.Meth.*, A545:602–612, 2005. 49, 50

[167] J. Abraham *et al.* Trigger and aperture of the surface detector array of the Pierre Auger Observatory. *Nucl.Instrum.Meth.*, A613:29–39, 2010. 50, 52, 91

[168] Z. Szadkowski and D. Nitz. Implementation of the first level surface detector trigger for the Pierre Auger Observatory Engineering Array. *Nucl.Instrum.Meth.*, A545:624–631, 2005. 50

[169] P. Billoir. Proposition to improve the local trigger of the Surface Detector for low energy showers. *Auger Technical Note, GAP-2009-179*, 2009. 50

[170] P. Billoir, P. Ghia, D. Nitz, and R. Sato. First results of the ToTd trigger in the test hexagon. *Auger Technical Note, GAP-2011-032*, 2011. 51

[171] P Billoir. New proposal to improve the local trigger of the Surface Detector. *Auger Technical Note, GAP-2011-089*, 2011. 51

[172] D. Veberič and M. Roth. SD Reconstruction; Offline Reference Manual. *Auger Technical Note, GAP-2005-035*, 2005. 53, 54, 56, 57, 58

[173] M. Horvat and D. Veberič. On shower-front start-time variance. *Auger Technical Note, GAP-2007-057*, 2007. 55

[174] A.M. Hillas. *Acta Phys. Acad. Sci. Hung.*, 29, suppl.3:355, 1970. 57

[175] A.M. Hillas. *Proc. 12th International Cosmic Ray Conference (ICRC 1971), Tasmania, Australia*, 1971. 57

[176] D. Newton, J. Knapp, and A.A. Watson. The Optimum Distance at which to Determine the Size of a Giant Air Shower. *Astropart.Phys.*, 26:414–419, 2007. 57, 58

[177] M. Ave *et al.* The accuracy of signal measurement with the water Cherenkov detectors of the Pierre Auger Observatory. *Nucl.Instrum.Meth.*, A578:180–184, 2007. 57

[178] R.N. Coy, G. Cunningham, C.L. Pryke, and A.A. Watson. Lateral Distribution of Extensive Air Showers Produced by Cosmic Rays above 10^{19} eV as Measured by Water-Cherenkov Detectors. *Auger Technical Note, GAP-1996-030*, 1996. 58

[179] T. Schmidt, I.C. Mari, and M. Roth. Fine Tuning of the LDF parameterisation and the Influence on S1000. *Auger Technical Note, GAP-2007-106*, 2007. 58

[180] M. Roth. The Lateral distribution function of shower signals in the surface detector of the Pierre Auger Observatory. *Proc. 28th International Cosmic Ray Conference (ICRC 2003), Tsukuba, Japan.*, 1:333–336, 2003. 58

[181] T. Schmidt. Measurement of the Flux of Ultra High Energy Cosmic Rays using very inclined Extensive Air Showers measured at the Pierre Auger Observatory. *Auger Technical Note, GAP-2010-046*, 2010. 58

[182] F. Arneodo, S. Maldera, and G. Navarra. A procedure to derive the anode charges for saturated signals from the dynode and anode undershoots. *Auger Technical Note, GAP-2005-025*, 2005. 59

[183] I.C. Maris, M. Roth, and T. Schmidt. A Phenomenological Method to Recover the Signal from Saturated Stations. *Auger Technical Note, GAP-2006-012*, 2006. 59

[184] I. De Mitri, S. Maglio, and D. Martello. A method for SD traces saturation recovery. *Auger Technical Note, GAP-2006-075*, 2006. 59, 131

[185] J. Abraham *et al.* Observation of the suppression of the flux of cosmic rays above 4×10^{19}eV. *Phys.Rev.Lett.*, 101:061101, 2008. 60

[186] J. Hersil, I. Escobar, D. Scott, G. Clark, and S. Olbert. Observations of Extensive Air Showers near the Maximum of Their Longitudinal Development. *Phys.Rev.Lett.*, 6:22–23, 1961. 60

[187] A. Schulz for the Pierre Auger Collaboration. The measurement of the energy spectrum of cosmic rays above 31017 eV with the Pierre Auger Observatory. *Contributions to the 33rd International Cosmic Ray Conference (ICRC 2013), Rio de Janeiro, Brazil*, 2013. 60, 61

[188] I. Valino for the Pierre Auger Collaboration. A measurement of the muon number in showers using inclined events recorded at the Pierre Auger Observatory. *Contributions to the 33rd International Cosmic Ray Conference (ICRC 2013), Rio de Janeiro, Brazil*, 2013. 61

[189] V. Verzi for the Pierre Auger Collaboration. The Energy Scale of the Pierre Auger Observatory. *Contributions to the 33rd International Cosmic Ray Conference (ICRC 2013), Rio de Janeiro, Brazil*, 2013. 61, 62, 124

[190] R. Pesce for the Pierre Auger Collaboration. Energy calibration of data recorded with the surface detectors of the Pierre Auger Observatory: an update. *Proc. 32nd International Cosmic Ray Conference (ICRC 2011), Beijing, China*, 2, 2011. 61

[191] F. Suárez for the Pierre Auger Collaboration. The AMIGA muon detectors of the Pierre Auger Observatory: overview and status. *Contributions to the 33rd International Cosmic Ray Conference (ICRC 2013), Rio de Janeiro, Brazil*, 2013. 63, 64

[192] AMIGA Task. AMIGA Status Report. *Auger Technical Note, GAP-2014-002*, 2014. 63

[193] F. Sanchez for the Pierre Auger Collaboration. The AMIGA detector of the Pierre Auger Observatory: an overview. *Proc. 32nd International Cosmic Ray Conference (ICRC 2011), Beijing, China*, 2011. 63

[194] C. Meurer and N. Scharf. HEAT - a low energy enhancement of the Pierre Auger Observatory. *Astrophys.Space Sci.Trans.*, 7:183–186, 2011. 64

[195] S. Falk *et al.* A First Look at HEAT Data. *Auger Technical Note, GAP-2010-123*, 2010. 64

[196] T. Hermann for the Pierre Auger Collaboration. The HEAT Telescopes of the Pierre Auger Observatory Status and First Data. *Proc. 32nd International Cosmic Ray Conference (ICRC 2011), Beijing, China*, 2011. 65

[197] G.A. Askaryan. Excess Negative Charge of an Electron-Photon Shower And Its Coherent Radio Emission. *Soviet Journal of Experimental and Theoretical Physics*, 14:441–443, 1962. 64

[198] G.A. Askaryan. Coherent Radio Emission from Cosmic Showers in Air and in Dense Media. *Soviet Journal of Experimental and Theoretical Physics*, 21:658, September 1965. 64

[199] J.L. Kelley for the Pierre Auger Collaboration. *Proc. 32nd International Cosmic Ray Conference (ICRC 2011), Beijing, China*, 2011. 64

[200] W.D. Apel *et al.* Lateral Distribution of the Radio Signal in Extensive Air Showers Measured with LOPES. *Astropart.Phys.*, 32:294–303, 2010. 64

[201] D. Ardouin *et al.* Geomagnetic origin of the radio emission from cosmic ray induced air showers observed by CODALEMA. *Astropart.Phys.*, 31:192–200, 2009. 64

[202] F.G. Schroder for the Pierre Auger Collaboration. Radio detection of air showers with the Auger Engineering Radio Array. *Contributions to the 33rd International Cosmic Ray Conference (ICRC 2013), Rio de Janeiro, Brazil*, 2013. 65, 66

[203] P. Abreu *et al.* Antennas for the Detection of Radio Emission Pulses from Cosmic-Ray. *JINST*, 7:P10011, 2012. 66

[204] P.W. Gorham *et al.* Observations of Microwave Continuum Emission from Air Shower Plasmas. *Phys.Rev.*, D78:032007, 2008. 65

[205] P. Allison for the Pierre Auger Collaboration. Microwave detection of cosmic ray showers at the Pierre Auger Observatory. *Proc. 32nd International Cosmic Ray Conference (ICRC 2011), Beijing, China*, 2011. 68

[206] M.T. Dova *et al.* Time asymmetries in extensive air showers: a novel method to identify UHECR species. *Astropart.Phys.*, 31:312–319, 2009. 69, 70, 79, 91, 102

[207] D. García-Pinto. Time Asymmetry in UHE Cosmic Ray Showers. Mass Composition Studies in the Pierre Auger Observatory. *Ph.D. Thesis, Auger Technical Note, GAP-2010-054*, 2009. 69, 70, 78, 91, 92, 104

[208] M.T. Dova, L.N. Epele, and A.G. Mariazzi. The Effect of atmospheric attenuation on inclined cosmic ray air showers. *Astropart.Phys.*, 18:351–365, 2003. 70, 77

[209] C.D. England. The Longitudinal Development of Extensive Air Showers at energies above 10^{17} eV. *Ph.D. Thesis*, 1984. 71

[210] M. Ave, J. Knapp, M. Marchesini, M. Roth, and A.A. Watson. A Preliminary Analysis of the 11-fold Event 184599. *Auger Technical Note, GAP-2002-020*, 2002. 71

[211] M.T. Dova. Asymmetries observed in giant air showers using water Cherenkov detectors. *Proc. 28th International Cosmic Ray Conference (ICRC 2003), Tsukuba, Japan.*, 1:369–372, 2003. 72

[212] E.W. Kellermann and L. Towers. The electromagnetic component of large air showers. *J.Phys.*, A3:284–295, 1970. 72

[213] D. Heck, G. Schatz, T. Thouw, J. Knapp, and J.N. Capdevielle. CORSIKA: A Monte Carlo code to simulate extensive air showers. *FZKA 6019*, 1998. 74

[214] X. Bertou and P. Billoir. On the Origin of the Asymmetry of Ground Densities in Inclined Showers. *Auger Technical Note, GAP-2000-017*, 2000. 74, 77

[215] P. Billoir, P. Da Silva, and X. Bertou. Checking the Origin of the Asymmetry of the Surface Detector Signals. *Auger Technical Note, GAP-2002-074*, 2002. 77

[216] D. Allard *et al.* A guide-line to the Auger-Surface-Detector Analysis. *Auger Technical Note, GAP-2006-024*, 2006. 80

[217] Sergey Ostapchenko. Status of QGSJET. *AIP Conf. Proc.*, 928:118–125, 2007. 81

[218] E. García. *Degree Thesis of the Universidad Complutense de Madrid*, 2008. 82, 83

[219] M.T. Dova, F.G. Monticelli, and H. Wahlberg. Influence of the reconstructed core position on S(1000) for inclined showers. *Auger Technical Note, GAP-2006-035*, 2006. 82

[220] C. Jarne. *Degree Thesis of the Universidad Nacional de La Plata*, 2010. 83

[221] C. Fracchiolla, C. Bonifazi, A. Letessier-Selvon, and O.B. Bigas. Angular Resolution with the Super-Hexagon. *Auger Technical Note, GAP-2008-095*, 2008. 84

[222] K.S. Caballero-Mora. Composition studies of Ultra High Energy Cosmic Rays using Data of the Pierre Auger Observatory. *Ph.D. Thesis, Auger Technical Note, GAP-2010-037*, 2010. 84, 86

[223] K. Arisaka J. Lee M. Healy, D. Barnhill and P. Boghrat. A Study of Composition Trends Using Rise Time and Curvature Data. *Auger Technical Note, GAP-2006-092*, 2006. 84, 128

[224] C. Wileman B. Smith and A.A. Watson. Can the risetime be used to infer the position of shower maximum? *Auger Technical Note, GAP-2007-092*, 2007. 84, 128

[225] H.L. Cook. Limit to the Ultra-High Energy Gamma-Ray Flux Using Data from the Surface Detectors of the Pierre Auger Observatory. *Ph.D. Thesis, Auger Technical Note, GAP-2012-107*, 2012. 84

[226] Leeds Private communication. Parametrization implemented on Risetime1000LLL module for Offline version before Rev25278. 86

[227] C. Jarne, M.T. Dova, H. Wahlberg, D. García-Pinto, I.A. Minaya, and F. Arqueros. An update to the asymmetry correction of risetime with data from 2004 to 2013. *Auger Technical Note, GAP-2014-042*, 2014. 86

[228] T. Pierog and K. Werner. EPOS Model and Ultra High Energy Cosmic Rays. *Nucl. Phys. Proc. Suppl.*, 196:102–105, 2009. 88

[229] M.T. Dova, M. Mancedino, and A.G. Mariazzi. Primary composition from asymmetries in EAS - new approach. *Auger Technical Note, GAP-2005-014*, 2005. 91

[230] M.T. Dova, M. Mancedino, A.G. Mariazzi, H. Wahlberg, F. Arqueros, and D. García-Pinto. UHECR mass determination using asymmetries in time distributions. *Auger Technical Note, GAP-2007-135*, 2007. 91

[231] E. Arganda, F. Arqueros, M.T. Dova, D. García-Pinto, C. Jarne, A. Mariazzi, M. Monasor, and H. Wahlberg. Azimuthal asymmetry in risetime as estimator of mass composition of UHECR. *Auger Technical Note, GAP-2010-069*, 2010. 91

[232] C. Pryke. Asymmetry of Air Showers at Ground Level. *Auger Technical Note, GAP-1998-034*, 1998. 91

[233] M.T. Dova, L.N. Epele, and A.G. Mariazzi. Particle density distributions of inclined air showers. *Nuovo Cim.*, C24:745–750, 2001. 91

[234] A.G. Mariazzi. Asimetrías espacio-temporales en las cascadas de rayos cósmicos ultra-energéticos y composición de la partícula primaria. *Ph.D. Thesis*, 2004. 93

[235] F. Arqueros, D. García-Pinto, M. Monasor, M.T. Dova, A.G. Mariazzi, and H. Wahlberg. Inferring $X_{\max}$ from asymmetry in risetime. *Auger Technical Note, GAP-2008-179*, 2008. 106

[236] I.A. Minaya for the Pierre Auger Collaboration. Azimuthal asymmetry in the risetime of the Surface Detector signals of the Pierre Auger Observatory. *Proc. 34th ICRC, The Hague, Netherlands*, 2015; A. Aab *et al.* Azimuthal asymmetry in the risetime of the Surface Detector signals of the Pierre Auger Observatory (in preparation). 110

[237] R. Barlow. Systematic errors: Facts and fictions. *Advanced statistical techniques in particle physics. Proceedings, Conference, Durham, UK, March 18-22, 2002*, pages 134–144, 2002. 127

[238] R. Barlow. Statistics: A Guide to the Use of Statistical Methods in the Physical Sciences. 127

[239] S. Mollerach, E. Roulet, and O. Taborda. Revisiting the effects of weather on the air shower energy reconstruction. *Auger Technical Note, GAP-2014-047*, 2014. 128

[240] R. Bruijn. *Pierre Auger Observatory Internal Presentation*, 2011. 131, 132

[241] A. Bueno, P. Sánchez-Lucas, and A.A. Watson. The Delta-Method revisited. *Auger Technical Note, GAP-2013-078*, 2013. 131

[242] A. Bueno, P. Sánchez-Lucas, and A.A. Watson. Risetime Studies Using Monte-Carlo Simulations. *Auger Technical Note, GAP-2014-119*, 2014. 131

[243] A. Aab *et al.* Muons in air showers at the Pierre Auger Observatory: Mean number in highly inclined events. *Phys. Rev.*, D91:032003, 2015. 135

[244] J. Abraham *et al.* Measurement of the Depth of Maximum of Extensive Air Showers above 10^{18} eV. *Phys. Rev. Lett.*, 104:091101, 2010. 139

[245] G. van Aar and C. Timmermans. Xmax measured with the SD detector. *Auger Technical Note, GAP-2015-032*, 2015. 142